École doctorale Science de l'ingénierie et des systèmes (ENGSYS-632)
Génie Civil, Énergétique, Matériaux (MGCEM)

THÈSE

présentée par

Xufei ZHAO

Domaine

GÉNIE CIVIL

Sujet de la thèse

Étude expérimentale sur le processus d'auto-colmatage des roches argileuses fissurées

Experimental study on the self-sealing process of cracked clayey rocks

pour obtenir le grade de

DOCTEUR DE L'UNIVERSITÉ DE LILLE

Soutenue le **1 JUILLET 2026**

Devant le jury composé de :

Mme **Sandrine ROSIN-PAUMIER**	Professeure, Université de Lorraine	Président
M. **Pierre BESUELLE**	Directeur de recherche (CNRS), UGA	Rapporteur
M. **Jean SULEM**	Professeur, ENPC	Rapporteur
Mme **Nathalie CONIL**	Ingénieur de recherche, INERIS	Examinateur
M. **Jean TALANDIER**	Ingénieur de recherche, Andra	Examinateur
M. **Jianfu SHAO**	Professeur, Université de Lille	Directeur de thèse
M. **Matthieu BRIFFAUT**	Professeur, Centrale Lille Institut	Co-directeur de thèse
M. **Nicolas GAY**	Docteur, Centrale Lille Institut	Co-encadrant

LAMCUBE - UNIVERSITÉ DE LILLE

ABSTRACT

The self-sealing process of fractures in clayey rocks is considered an essential mechanism for long-term confinement performance in the deep geological disposal of radioactive waste. Swelling of clay minerals in these rocks plays a pivotal role in fracture closure. In this work, we investigate the fracture closure process and its impacts on transport properties in pre-cracked samples of Callovo-Oxfordian claystone (COx). The novelty is to create an indirect fracture hydration process, which is close to field conditions. For this purpose, two original experimental setups are designed. In the first experiment, three sets of mock-ups are prepared, and all samples are drilled along the parallel direction to bedding planes. Swelling pressure and water permeability are measured during water injection, following by gas breakthrough pressure after fracture sealing. Experimental results indicate that, in comparison to samples with direct water penetration into the main fracture, cracked samples with an impermeable joint preventing direct water penetration into the fracture exhibit a higher swelling pressure. Swelling deformation is more important in samples parallel to bedding planes than those perpendicular to them. It is obtained that the gas breakthrough pressure of the cracked sample is strongly correlated with its swelling pressure. Water permeability after gas breakthrough test is further observed to be that the gas-induced channels can be closed by water saturation. For the second experiment, an innovative mini-triaxial cell is designed for in situ monitoring of fracture evolution under X-ray micro-tomography. Changes in gas permeability, fracture opening, and sample diameter are measured, and the effects of fracture geometry and initial opening on self-sealing behavior are discussed. After analyzing the deformation fields, microscale mechanisms associated with fracture closure and anisotropic swelling are discovered. From the results obtained using two experimental setups, it is found that fractures in pre-cracked claystone could be closed by matrix swelling during indirect hydration.

Keywords: Swelling, self-sealing, fracture closure, gas breakthrough pressure, permeability, X-ray, fracture opening, deformation filed, clayey rocks

RÉSUMÉ

Le processus d'auto-colmatage des fractures dans les roches argileuses est considéré comme un mécanisme essentiel pour assurer le confinement à long terme dans le cadre du stockage géologique profond des déchets radioactifs. Le gonflement des minéraux argileux joue un rôle déterminant dans la fermeture des fractures. Dans ce travail, nous étudions le processus de fermeture des fractures ainsi que ses effets sur les propriétés de transport dans des échantillons pré-fissurés d'argilite du Callovo-Oxfordien (COx). L'originalité de cette étude réside dans la mise en place d'un processus d'hydratation indirecte des fractures, proche des conditions in situ. À cette fin, deux dispositifs expérimentaux originaux sont conçus. Dans la première expérience, trois ensembles de maquettes sont préparés, et tous les échantillons sont carottés parallèlement aux plans de stratification. La pression de gonflement et la perméabilité à l'eau sont mesurées pendant l'injection d'eau, puis la pression de percée du gaz est déterminée après auto-colmatage des fractures. Les résultats expérimentaux indiquent que les échantillons fissurés munis d'un joint imperméable empêchant la pénétration directe de l'eau dans la fracture principale développent une pression de gonflement plus élevée que les échantillons permettant cette pénétration directe. Les déformations de gonflement sont plus importantes dans les échantillons orientés parallèlement aux plans de stratification que dans ceux orientés perpendiculairement. La pression de percée du gaz des échantillons fissurés est fortement corrélée à leur pression de gonflement. Les mesures de perméabilité à l'eau réalisées après l'essai de percée du gaz indiquent que les voies de migration induites par le gaz peuvent se refermer lors de la resaturation en eau. Dans la seconde expérience, une cellule triaxiale miniature innovante est conçue pour suivre in situ l'évolution des fractures par microtomographie à rayons X. Les variations de la perméabilité au gaz, de l'ouverture des fractures et du diamètre des échantillons sont mesurées, et les effets de la géométrie des fractures et de leur ouverture initiale sur le comportement d'auto-colmatage sont examinés. L'analyse des champs de déformation permet d'identifier des mécanismes à l'échelle microscopique associés à la fermeture des fractures et au gonflement anisotrope. Les ré-

sultats obtenus avec les deux dispositifs expérimentaux montrent que les fractures des échantillons d'argilite pré-fissurés peuvent être refermées par le gonflement de la matrice lors de l'hydratation indirecte.

Keywords: Gonflement, auto-colmatage, fermeture de fractures, pression de percée du gaz, perméabilité, rayons X, ouverture de fracture, champ de déformation, roches argileuses

ACKONWLEDGEMENTS

This acknowledgment is dedicated to all who have influenced and supported me throughout the journey of this thesis.

First and foremost, I would like to express my thanks to my supervisors, Prof. Jianfu SHAO and Prof. Matthieu BRIFFAUT, for your careful and patient guidance throughout my doctoral research. It has been a great honor to be one of your PhD students. Your insightful guidance helped me clarify my research direction during times of confusion. Your patient mentorship taught me how to conduct meaningful academic research and played a vital role in the completion of this thesis. I am also sincerely grateful to Dr. Nicolas GAY for his valuable suggestions, encouragement, and support during my studies.

I would like to sincerely thank the jury members of my thesis for their constructive comments and thoughtful discussions. Their valuable feedback has significantly improved the quality of this work and provided me with new perspectives for future research.

Special thanks to Mr. Thierry DUBOIS and Dr. Chuanrui WANG for your help throughout my experiments. I would like to thank all the members of laboratory: Thierry DUBOIS, Zhibo DUAN, Ludovic POTIER, Marie-Claude WILLEMETZ and Laurent LECONTE for their critical laboratory technical assistance.

To my friends that I met during my study in France and the good moments shared with them: Dr. Zhenxin LI, Dr. Hailing SHI, Dr. Yue SUN, Dr. Zhan YU, Dr. Meng WANG, Dr. Yudan JIN, Dr. Jing XUE, Dr. Yuhao ZHANG, Dr. Yue SHI, Dr. Yushu WANG, Dr. Yunlong WU, Dr. Yu SUN, Dr. Xingxing QI, Dr. Yunchang DU, Dr. Wei XU, Xinyue ZHU, Xiaolin LIN, Wen YANG, Rongfei LIU, Wenyong LIU, Kuan ZHANG, Jianping ZHANG, Xiangyu ZHANG, Ming WU, Feihu TONG and Jun WU. These reunions with familiar in unfamiliar places brought warmth and joy to my journey, creating memories I will always treasure.

Also, I would like to thank the China Scholarship Council (CSC) and French national agency for radioactive waste management (Andra) for financial support during my

research period.

Most importantly, I would like to express my deepest gratitude to my parents and sister. Their unwavering support for my decision to study in France, both emotionally and financially, has been the foundation that enabled me to explore a wider, more diverse world. It is through their encouragement that I have had the privilege to grow, learn, and experience life from new perspectives.

To dear myself, finally, truly and sincerely. This journey, while not filled with endless hardship, had its fair share of obstacles. I thank myself for every effort made, every decision not to give up, and for continuing to move forward despite fear and uncertainty. This marks the end of my PhD journey, but it is also the beginning of a new chapter in my life.

Xufei ZHAO

June 22, 2026

CONTENTS

Abstract i

Résumé iii

Ackonwledgements v

Contents ix

List of Figures xi

List of Tables xvii

General Introduction 1

CHAPTER 1: State of the Art 5

1 Introduction 5
2 Characteristics of COx claystone 5
2.1 Mineralogical composition and microstructure 5
2.2 Porosity and moisture characteristics 9
2.3 Fluid transfer properties 11
3 Self-sealing behaviour of cracked COx claystone 14
3.1 Transport properties during resaturation 15
3.2 Swelling deformation and mechanism 17
3.3 Process and characteristics of fracture closure 25
4 Influencing factors of the self-sealing process 27
4.1 Effect of mineralogical composition 28
4.2 Effect of fracture orientations and sizes 29
4.3 Effect of external loads 31
4.4 Effect of thermal impact 33
5 Gas breakthrough pressure: concepts and measurements 34
5.1 Definitions of capillary pressure 35
5.2 Methodology for gas breakthrough pressure 36
6 Microstructure observation in cracked claystone 41
7 Conclusion 44

CHAPTER 2: Hydro-mechanical behavior of intact and cracked COx claystone **47**

1 Introduction 47

2 Materials and experimental equipment 49
2.1 Sample preparation 49
2.2 Mock-ups design 51
2.3 Tube calibration 54
2.4 Experimental system 55
3 Experimental procedures 57
3.1 Permeability measurement techniques 57
3.2 Swelling pressure test 58
4 Gas transport of composite sample 60
5 Self-sealing process of composite sample 61
5.1 Apparent water permeability 61
5.2 Apparent swelling pressure of mock-up II 64
5.3 Apparent swelling pressure of mock-up III 66
5.4 Swelling mechanism of clay minerals 69
6 Conclusions 71

CHAPTER 3: Characterization of gas migration and water transport in sealed cracked claystone 73

1 Introduction 73
2 Materials and methods 75
2.1 Sample Characterization 75
2.2 Experimental apparatus 76
2.3 Experimental procedures 77
3 Gas migration behavior after sealing 78
3.1 GBP of saturated samples in mock-up I 79
3.2 GBP of saturated samples in mock-up II 83
3.3 GBP of saturated samples in mock-up III 84
3.4 GBP comparison in intact and cracked samples 87
3.5 Analysis of GBP related to swelling pressure 88
4 Resealing of gas-induced pathways 89
4.1 Resealing effects on the fracture closure 90
5 Conclusions 92

CHAPTER 4: Self-sealing investigation in pre-cracked claystone using X-ray micro-tomography and digital volume correlation 95

1 Introduction 95
2 Sample preparation and equipment 96
2.1 Materials and model design 96
2.2 Experimental device 98

2.3 X-ray micro-tomography acquisition 100
3 Experimental methods and procedure 101
3.1 Gas permeability measurements 101
3.2 Data reconstruction and processing 101
3.3 Digital Volume Correlation (DVC) 106
4 Image-based analysis of sealing processes 108
4.1 Effect of fracture geometry 109
4.2 Effect of initial fracture opening 115
5 Gas permeability results 119
6 Deformation field analysis and discussion 124
6.1 Displacement evolution during complete fracture closure 125
6.2 Deformation analysis during partial fracture closure 129
6.3 Analysis of anisotropic swelling results 132
7 Gas migration behavior after sealing 135
8 Conclusions 137

Conclusions and perspectives **139**
1 Conclusions 139
2 Perspectives 141

References **143**

LIST OF FIGURES

I Geological diagram of the Meuse / Haute Marne site (Andra, 2023). . . . 1
II 3D visualization of the fractures network (Armand et al., 2014). 2

1.1 Lithology and mineralogy of the Callovian-Oxfordian formation (Yven et al., 2007). 6
1.2 Vertical variations of mineral contents (a) clay content, (b) carbonate content and (c) tectosilicate content along the bedding plane (Conil et al., 2018). 7
1.3 Spatial distribution of mineral content visualized (a) 2D SEM section parallel to the bedding planes; (b) 3D micro-CT subvolume (EST26095) (Robinet et al., 2012). 8
1.4 Definition of loading angle between bedding planes and sample axis ($\alpha = 0°, 45°, 90°$ corresponding to parallel, inclined and perpendicular orientations, respectively) (Shi et al., 2020). 9
1.5 Schematic diagram of the porosity organization in claystone (Yven et al., 2007). 10
1.6 Vertical distribution of water content across the thickness of the COx formation (Conil et al., 2018). 11
1.7 Sketch of the experimental apparatus for permeability measurement. (a) water permeability test (Yuan et al., 2023); (b) gas permeability test (Liu et al., 2015). 13
1.8 Apparent permeability as a function of mean gas pressure ($1/P_m$): (a) COx claystone (394 refers to core EST27394 and 480 refers to core EST30480) (Yuan et al., 2023); (b) cement-based material (Lion et al., 2005). 14
1.9 Evolution of gas permeability of (a) intact COx samples as a function of water content (Zhang and Rothfuchs, 2004); (b) damaged samples before and after water re-saturation (Zhang and Rothfuchs, 2008). 15
1.10 Evolution of water permeability of (a) UA sample as a function of time (Giot et al., 2019); (b) parallel sample EST63744-7 and perpendicular sample EST63744-11 during a self-sealing test (Agboli et al., 2024). 16
1.11 Methods for swelling pressure determination, (a) swelling-consolidation, pre-swell, zero-swell and constant-volume method, (b) loading-wetting method, (c) unloading-reloading loop method (Cui et al., 2013). 18
1.12 Swelling pressure measurements from the self-sealing experiment: (a) schematic of the experimental setup; (b) evolution of apparent swelling pressure (Wang et al., 2022a). 19
1.13 Comparison of strain measurements from different mock-ups: (a) schematic illustration of the mock-up with epoxy resin (up) and with silicone (down); (b) measured strain on the tube external surface after water injection into the sample (Wang et al., 2022a, 2024). 19

1.14 Comparison of swelling strain in radial and axial directions under unconfined conditions to humidity change: (a) intact sample with its axis perpendicular to the bedding plane (Zhang et al., 2010), (b) intact sample with its axis parallel to the bedding plane (Zhang, 2018). 20
1.15 Comparison of the two principal loading orientations in terms of (a) creep behavior (Zhang and Rothfuchs, 2004) and (b) evolution of elastic modulus with relative humidity obtained from mini-compression tests (Zhang et al., 2012). 21
1.16 Schema of the swelling of clayed rock, (a) showing the corresponding porosity micrtstructure (Menaceur et al., 2016), (b) change in pores with the relative humidity (Wang et al., 2017). 22
1.17 Swelling mechanism of clayed rock (a) interpreted by Saiyouri et al. (2000), (b) investigated through X-ray diffractometry (Saiyouri et al., 2000, 2004; Menaceur et al., 2016). 23
1.18 Conceptual model of the multi-scale swelling behavior of COx claystone. (a) and (b) show the unsaturated R1-I/S and R0-I/S interstratified clay minerals; (c) and (d) show the crystalline swelling of R1-I/S and R0-I/S, corresponding to 100% RH; (e) and (f) are the osmotic swelling of R1-I/S and R0-I/S; (g) and (h) are the samples with high R1-I/S content and high R0-I/S content after swelling (Wang, 2021a). 24
1.19 Cracks on the COx sample surface before and after water flowing (Ghayaza et al., 2013). 25
1.20 X-ray imaging and quantitative tracking of discontinuity evolution: (a) X-ray image and grey-value histogram of sample AV1112; (b-d) evolution of equivalent discontinuity size for COx claystone sample (b) AV1112 and AH1112 from core EST57243 under V-W loading path, (c) 3132 from core EST53644 under V-W-D loading path, and (d) 9192 from core EST53644 under D-W loading path (Di Donna et al., 2022). 26
1.21 (a) Vertical swelling strain versus time for (b) intact sample T1, horizontally fractured sample TH-2 and vertically fractured sample TV-2 from core EST57190 (Wang et al., 2022b). 29
1.22 X-ray images at different steps during test sample (a) V3132 and (b) V4142 from core EST58102, with the red dotted line showing the orientation of the bedding (Di Donna et al., 2022). 30
1.23 Evolution of confining pressure (P_c), permeability (K) and crack closure (cc) (Davy et al., 2007). 32
1.24 Temperature effect on the water permeability of cracked claystone during the self-sealing process: (a) long-term measurements of water permeability at different temperatures and (b) water permeability as a function of temperature (Zhang, 2018). 34

1.25 Conceptual sketch of capillary pressure (P_c) as a function of water saturation (S_w) for saturated rock (IRWS denotes irreducible water saturation, RGS means residual gas saturation) (Hildenbrand et al., 2002; Busch and Amann-Hildenbrand, 2013). 35
1.26 Scheme description of four direct breakthrough pressure measurement methods (P, V and Q represent pressure, cumulative water volume and flow rate, respectively) in Boulin et al. (2011). 37
1.27 A typical cone-beam tomography setup (Brisard et al., 2020). 41
1.28 X-ray images at different steps during (a) test 4142 (UA), resolution 13.5 μm); (b) test AV1112 (U.T.), resolution 7 μm) (Di Donna et al., 2019). 42
1.29 The evolution of crack volume in COx claystone (UA sample) by 3D tomography (Giot et al., 2019). 43
1.30 X-ray 3D tomography images of parallel sample EST63744-7 showing the evolution of the crack volume with time during a self-sealing test at 20 °C (Agboli et al., 2024). 44

2.1 Steps of the sample preparation: (a) original core; (b) cored sample. . . . 49
2.2 Designed mock-ups: (a) schematic of experimental mock-up I; (b) cross-section of "stainless steel tube-epoxy-sample" composite; (c) schematic of experimental mock-up II; (d) schematic of experimental mock-up III. . 51
2.3 Orientations of strain gauges and main fractures: (a) three assembled configurations (Schemes A-C), (b) summary of orientations for each sample. Orientations are defined with respect to the bedding planes, where $\perp$ for perpendicular and $\parallel$ for parallel. 52
2.4 Cracked samples prepared for Brazilian tests, (a) perpendicular to the bedding plane; (b) parallel to the bedding plane. 53
2.5 Relation between the inner pressure and surface strain of tube. 55
2.6 The experimental apparatus for self-sealing test (a) permeability test of mock-up I; (b) swelling test of mock-up II and mock-up III. 56
2.7 Main experimental procedure in the self-sealing test. 59
2.8 Apparent gas permeability values K_{ag} for different $1/P_m$ by the Klinkenberg equation: (a) S0-C, (b) S0-S and S0. 61
2.9 Apparent water permeability of the composite samples using mock-up I and mock-up II measured over the duration of the self-sealing test. 62
2.10 Apparent water permeability of the composite samples using mock-up III measured over the duration of the self-sealing test. 63
2.11 Apparent swelling pressures (P_{app}) using mock-up II. 65
2.12 Apparent swelling pressures (P_{app}) using mock-up III. 67

3.1 Photos of re-saturated and resealed samples after self-sealing test. 75
3.2 Experimental apparatus for gas breakthrough test and resealing test. . . . 77

3.3 GBP of (a) intact sample S0-S and (b) cracked sample S0-C under 3 MPa confining pressure. 79
3.4 Photograph of the experimental phenomenon at the downstream valve. . . 80
3.5 GBP of (a) intact sample S0-S and (b) cracked sample S0-C under 12 MPa confining pressure. 81
3.6 GBP performance of re-compacted claystone under varying confining pressure (Zhang, 2015; Wang et al., 2024). 82
3.7 GBP of cracked sample S1-C (a) gas pressure, (b) relationship between increasing rate of $P_{\text{downstream}}$ and P_{upstream}. 83
3.8 Gas pressure evolution during the gas breakthrough test for resealed samples (a) S3-C, (c) S4-C and (e) S5-C, and re-saturated samples (b) S3-S, (d) S4-S and (f) S5-S. 85
3.9 Relationship between increasing rate $dP_{\text{downstream}}/dt$ and P_{upstream} for resealed samples (a) S3-C, (c) S4-C and (e) S5-C, and re-saturated samples (b) S3-S, (d) S4-S and (f) S5-S. 86
3.10 Comparison of GBP experimental values from this study and reference values (Zhang, 2015; Song et al., 2016b; M'Jahad et al., 2017; Chen et al., 2022; Wang et al., 2022a). 87
3.11 Gas breakthrough pressure as a function of apparent swelling pressure. . . 88
3.12 Water permeability of cracked and intact samples after GBP test. 89
3.13 Equivalent fracture aperture evolution of cracked sample. 91
3.14 Post-test dried samples comparison using mock-ups: cracked sample and intact sample. 92

4.1 Schematic illustration of artificially cracked geometries: (a) crack CG1, (b) splitting crack CG2, (c) cutting crack CG3, and (d) artificial hole CG4. 97
4.2 Preparation procedure (a) and schematic configuration (b) of the indirectly injected water model. 98
4.3 Schematic views and photographs of the triaxial compression cell and the gas–water injection system: (a) triaxial compression cell, (b) gas–water injection system, (c) triaxial cell components, and (d) experimental setup. 99
4.4 The triaxial compression cell enclosed within the X-ray micro-tomography scanner. 100
4.5 3D reconstruction of sample EST 66747-2 and resampled 8-bit X-ray tomographic image at slice 650. 102
4.6 3D reconstruction of sample EST 66747-3 and resampled 8-bit X-ray tomographic image at slice 650. 102
4.7 3D reconstruction of sample EST 66747-4 and resampled 8-bit X-ray tomographic image at slice 650. 103
4.8 3D reconstruction of sample EST 727937-1 and resampled 8-bit X-ray tomographic image at slice 650. 103

4.9 3D reconstruction of sample EST 727937-2 and resampled 8-bit X-ray tomographic image at slice 650. 103
4.10 Resampled 8-bit X-ray tomography image (a) and gray-level histogram (b) of sample EST 66747-4, with fracture region of interest (ROI) in (c). . 104
4.11 The procedure adopted for the edge segmentation from the X-ray 3D image: (a) resampled Image; (b) image segmentation; (c) enclosed holes; (d) sobel edge detection. 105
4.12 The image registration scheme of YaDICs platform. 107
4.13 Three-dimensional distribution of mineral phases and main fracture (a) and variation of DVC displacement uncertainty as a function of element size for the three displacement components (b). 108
4.14 Evolution of tomographic reconstructions of selected horizontal (XY) slice 650 under 0.3 MPa confining pressure in sample EST 66747-4. . . . 109
4.15 Time-dependent relative diameter change ($\Delta D/D_0$) across different slices in sample EST 66747-4 (a) and EST 66747-2 (b). 110
4.16 Evolution of tomographic reconstructions of selected horizontal (XY) slice 1100 under 0.3 MPa confining pressure in sample EST 66747-2. . . 111
4.17 Evolution of tomographic reconstructions of selected horizontal (XY) slice 655 under 0.3 MPa confining pressure in sample EST 66747-3. . . . 112
4.18 Time-dependent relative diameter change ($\Delta D/D_0$) across different slices in sample EST 66747-3 (a) and EST 72793-2 (b). 113
4.19 Evolution of tomographic reconstructions of selected horizontal (XY) slice 650 under 1.0 MPa confining pressure in sample EST 72793-2. . . . 114
4.20 Evolution of tomographic reconstructions of selected horizontal (XY) slices 200, 650 and 1100 under 1 MPa confining pressure in sample EST 72793-1. 116
4.21 3D fracture opening evolution maps for sample EST 66747-4 over time. . 117
4.22 3D fracture opening evolution maps for sample EST 72793-1 over time. . 118
4.23 3D fracture opening evolution maps for sample EST 72793-2 over time. . 119
4.24 Time-dependent evolution of gas permeability in sample EST 66747-4. . . 120
4.25 Schematic diagram of the flow between two parallel plates. 121
4.26 Evolution of average fracture opening and equivalent fracture aperture of sample EST 66747-4. 122
4.27 Time-dependent evolution of the gas permeability in (a) samples EST 66747-2, EST 72793-1 and EST 72793-2, and (b) sample EST 66747-3. . 123
4.28 Evolution of the 3D horizontal displacements (U_x) measured with DVC in sample EST 66747-4 under 0.3 MPa confining pressure. 125
4.29 Spatial distribution and temporal evolution of horizontal displacement U_x at three cross-sections in the middle of the sample EST 66747-4. 126
4.30 Evolution of the 3D horizontal displacements (U_x) measured with DVC in sample EST 66747-3 under 0.3 MPa confining pressure. 127

4.31 Spatial distribution and temporal evolution of horizontal displacement U_x at three cross-sections in the middle of the sample EST 66747-3. 128
4.32 Evolution of the 3D horizontal displacements (U_x) measured with DVC in sample EST 72793-1 under 1.0 MPa confining pressure. 129
4.33 Spatial distribution and temporal evolution of horizontal displacement U_x at three cross-sections in the middle of the sample EST 72793-1. 130
4.34 Evolution of the 3D horizontal displacements (U_x) measured with DVC in sample EST 66747-2 under 0.3 MPa confining pressure. 131
4.35 Spatial distribution and temporal evolution of horizontal displacement U_x at three cross-sections in the middle of the sample EST 66747-2. 132
4.36 Evolution of the 3D horizontal displacements (U_x) measured with DVC in sample EST 72793-2 under 1.0 MPa confining pressure. 133
4.37 Evolution of the 3D vertical displacements (U_y) measured with DVC in sample EST 72793-2 under 1.0 MPa confining pressure. 133
4.38 Spatial distribution and temporal evolution of horizontal displacement U_x at three cross-sections in the middle of the sample EST 72793-2. 134
4.39 Gas breakthrough pressure of sealed sample EST 66747-4 under 3 MPa confining pressure: (a) evolution of P_{upstream} and $P_{\text{downstream}}$ over time, (b) relationship between the increasing rate of $P_{\text{downstream}}$ and P_{upstream}. 135
4.40 Gas breakthrough pressure of all tested samples versus confining pressure. 136

LIST OF TABLES

1.1 Mineralogical analyses on different cores of the COx claystone from literature. 7
1.2 Summary of GBP values on the COx claystone from literature. 40

2.1 Size and initial water content of tested samples. 50
2.2 Chemical composition of the synthetic water from ANDRA. 50
2.3 Apparent gas permeability under different gas pressures. 60
2.4 Apparent water permeability results of mock-ups I and II. 62
2.5 Apparent water permeability results of mock-up III. 64

3.1 Summary of apparent swelling pressure and test duration for mock-up samples. 76
3.2 Results of gas breakthrough tests on mock-up I. 80
3.3 Results of gas breakthrough test on mock-up II. 84
3.4 Results of gas breakthrough test on mock-up III. 84

4.1 Initial conditions and geometric characteristics of testing samples. 97

General Introduction

Many countries are facing the issue of finding a solution to store radioactive waste coming from nuclear power plants. In France, the high-level radioactive waste (HLW) storage possibilities in deep geological formations were studied by the French National Radioactive Waste Management Agency (ANDRA) (Andra, 2005). Since 2000, ANDRA launched the construction of Underground Research Laboratory (URL), at the border of the Meuse and Haute-Marne site on the township of Bure (Eastern France) (Fig. I). The laboratory is located in the Callovo-Oxfordian formation (COx), at a depth ranging from 420 to 550 m below ground. The COx formation comprises clay, calcite, quartz and other secondary minerals. Based on its different mineralogy content, the COx formation was further divided into three lithological units (Armand et al., 2017b), i.e., the clay unit (UA), the transition unit (UT) and the silty-carbonated unit (USC). More precisely, the UA is richer in clays, the USC is richer in carbonates and the UT is a transition between the two others.

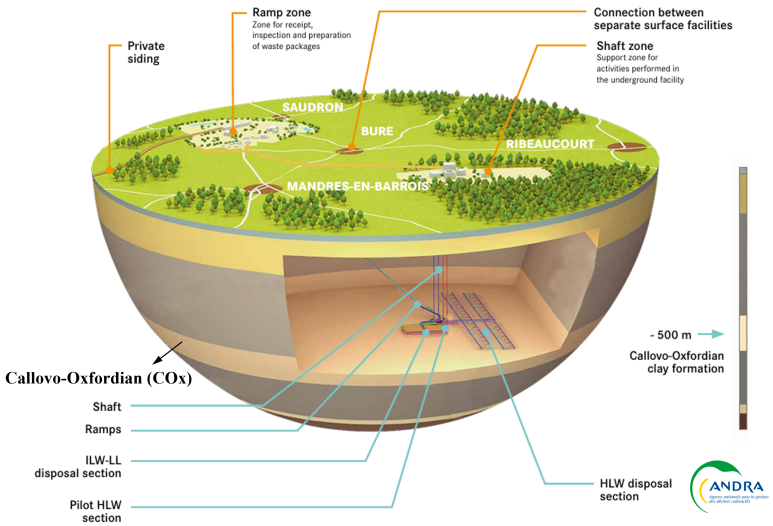

Figure I: Geological diagram of the Meuse / Haute Marne site (Andra, 2023).

The COx claystone is selected as the geological host formation thanks to its favorable major properties for repositories such as stable geological structure, extremely low permeability, favorable mechanical properties and retention capacity for radionuclides and certain self-sealing potential (Zhang, 2011, 2013; Di Donna et al., 2019). During construction of the repository tunnels, an Excavation Damage Zone (EDZ) was generated

in the COx formation, inducing tensile and shear fractures around shafts and galleries (Armand et al., 2014), seen in Fig. II. This network of fractures would provide preferential pathways for water flow and radionuclide migration. However, the EDZ would be re-saturated after the closure of the repository due to natural hydration from the surrounding rock mass, making it less conductive and eventually hydraulically insignificant. This phenomenon is commonly termed "self-sealing" (Bock et al., 2010; Bastiaens et al., 2007; Van Geet et al., 2008).

Similarly to COx claystone considered in the French project for radioactive waste disposal, self-sealing processes of excavation-induced cracked zones are investigated in other clay-rich host formations, notably Opalinus Clay in Switzerland and Boom Clay in Belgium. The recovery of the initial water permeability and gas pathway closure during the re-saturation process have indicated an excellent self-sealing and the regaining of the hydraulic barrier function of Boom clay (Gonzalez-Blanco et al., 2024). In Opalinus Clay, the time-dependent evolution of hydraulic properties in excavation-induced damaged zones is investigated, showing strong coupling between stress, fracture transmissivity and sealing process (Bossart et al., 2002; Cuss et al., 2011b; Hale et al., 2021). Self-sealing is observed even after gas breakthrough in Boom clay (Bock et al., 2010; Dao et al., 2015; Gonzalez-Blanco et al., 2024).

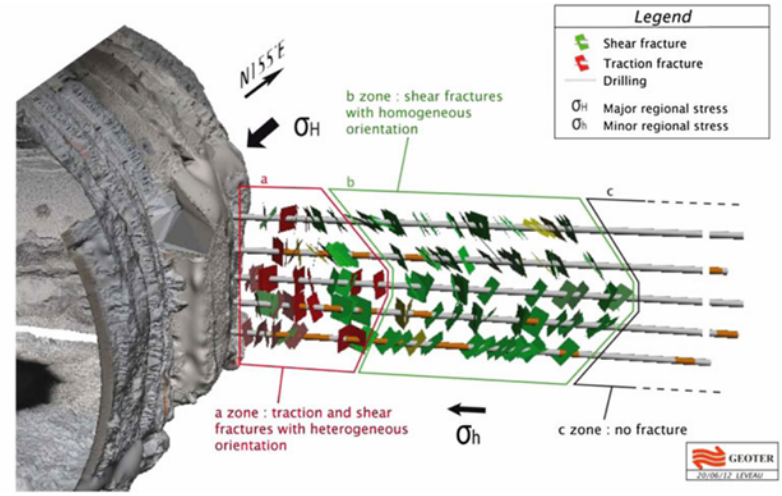

Figure II: 3D visualization of the fractures network (Armand et al., 2014).

Most researchers are currently interested in the self-sealing mechanism of cracks under hydraulic and mechanical loading (Bossart et al., 2019; Di Donna et al., 2022; Zhang

and Talandier, 2023; Quacquarelli et al., 2024; Wang et al., 2024). Experimental studies have shown that main fractures are considered the preferential pathways for water flow, while hydration involves firstly clay minerals around the fractures which clog and swell, leading to fracture closure and permeability recovery (Giot et al., 2019; Agboli et al., 2024). At the microscale, clay swelling is controlled by hydration mechanisms that can be interpreted using molecular-level insights (Karaborni et al., 1996), and it remains a key issue in applied geo-engineering contexts where swelling may alter transport properties (Anderson et al., 2010). To the authors' knowledge, most experiments have been conducted under confining conditions with direct water flow through fractures. In contrast, relatively few works have investigated the sealing behavior primarily induced by swelling within the rock matrix. Thus, the primary motivation of this thesis is to develop and implement experimental techniques following an indirect percolation path, without direct injection of liquid water into the fracture, for representing possible in situ conditions.

To achieve this objective, two types of laboratory experiments are designed and performed on cracked COx samples to characterize their sealing behavior. The first experiment involves a series of tests performed in a hydrostatic triaxial cell, where changes in swelling pressure and water permeability are measured over several months. In addition, the gas breakthrough pressure (GBP) of water-saturated samples is investigated to evaluate their sealing capacity. The second experiment employs X-ray micro-tomography to investigate the spatial evolution of claystone swelling and crack closure. Concurrently, gas permeability measurements are conducted to evaluate the evolution of crack closure and its impact on flow properties. All tests are carried out in the Laboratoire de Mécanique Multiphysique Multiéchelle (LaMcube). The following part gives a general introduction of this thesis:

In Chapter 1, the state of the art on the topic of this thesis is summarized. First, the characteristics of Callovo-Oxfordian claystone, including its mineralogical composition, porosity, moisture content, and fluid transport properties, are briefly introduced. Then, previous research on the self-sealing behavior of cracked COx claystone and its influencing factors is reviewed. The following part introduces the concepts and measurement of gas breakthrough pressure (GBP) for evaluating sealing efficiency. Finally, current studies employing imaging techniques to investigate the microstructural features of cracked claystone are presented, providing visual insights into the crack closure process. These studies primarily focus on self-sealing behavior under conditions where water directly

infiltrates cracks and serve as the foundation for the current work.

In Chapter 2, an improved experimental device is developed to characterize the self-sealing behavior of pre-cracked COx claystone under indirect water injection. Three mock-ups are designed. One is used to investigate transport properties by measuring the apparent gas and water permeabilities of the composite sample. The other two are developed specifically to investigate the apparent swelling pressure of cracked and intact samples under low confinement and injection pressure to assess the single effect of swelling. The temporal evolution of apparent water permeability during self-sealing is also analyzed.

In Chapter 3, gas migration and hydraulic transport in water-saturated COx claystone (cracked and intact samples) from Chapter 2 are investigated. First, gas breakthrough pressure tests are performed on the cracked and intact samples using the step-by-step method. The upstream and downstream gas pressures are measured and analyzed to characterize the effects of re-compaction on gas breakthrough. Finally, the resealing mechanisms of gas-induced pathways during subsequent hydration are investigated.

In Chapter 4, an innovative mini-triaxial cell is designed for in situ monitoring of crack evolution under X-ray micro-tomography. Scanning tests with high spatial resolution are performed before, during, and after testing, while gas permeability measurements are continuously taken throughout all tests. To achieve the indirect water infiltration, a cylindrical model is designed with two lateral injection channels oriented perpendicular to the main fracture. The effects of crack geometry and initial crack opening on the self-sealing behavior are discussed. Based on the tomographic images, the temporal evolution of crack opening and average sample diameter is quantitatively analyzed. In addition, Digital Volume Correlation (DVC) is used to evaluate the deformation fields in order to better understand the microstructural mechanics of crack closure.

Finally, the general conclusions are presented, together with some perspectives on further work.

CHAPTER 1

State of the Art

1 Introduction

Over the past decades, the self-sealing behavior of cracked Callovo-Oxfordian claystone has been significantly studied by many researchers (Giot et al., 2019; Wang et al., 2022a; Zhang and Talandier, 2023; Wang et al., 2024; Agboli et al., 2024). These studies have investigated the clay mineral swelling and crack closure process, ranging from macroscopic mechanisms and the evolution of transport properties to microstructural reorganization (Zhang, 2011, 2013; Giot et al., 2019). This chapter provides an overview of current knowledge about the basic physical and mechanical properties of COx claystone, transport characteristics during the self-sealing process, associated swelling mechanisms, crack closure features, and the main factors influencing these processes. Experimental methodologies of gas breakthrough pressure (GBP) are presented to evaluate sealing performance, as well as current advances in characterizing crack closure processes and microstructural mechanisms during self-sealing using imaging techniques.

2 Characteristics of COx claystone

2.1 Mineralogical composition and microstructure

Callovo-Oxfordian formation exhibits a complex mineralogical composition that has been studied at the Bure site to determine the mineralogical composition of the host rock. With an overall thickness of around 130 m, the COx claystone is located be-

tween 420 and 550 m below the ground surface (Lerouge et al., 2011; Armand et al., 2014). On the basis of mineralogical contrasts, it is subdivided into three lithological units (Armand et al., 2017a), i.e., the clay unit (UA), the transition unit (UT) and the silty-carbonated unit (USC), whose geological distribution is illustrated in Fig. 1.1. More precisely, the UA is located at the bottom of the COx formation, at about 460 m depth, comprising two-thirds of the COx layer thickness. It is the most clayey unit, with a clay content of about 45-50% (Gaucher et al., 2004). Above this layer is the UT, located at depths ranging approximately from 440 to 460 m. It exhibits a contrasting mineralogy (Conil et al., 2018). The USC is on the top of the COx layer, located at depths ranging from 420 to 440 m, with higher carbonated content. Its mineralogical composition is variable and heterogeneous, with progressive carbonate enrichment (Armand et al., 2017b). Fig. 1.2 presents a clear illustration of the mineral content distribution with depth.

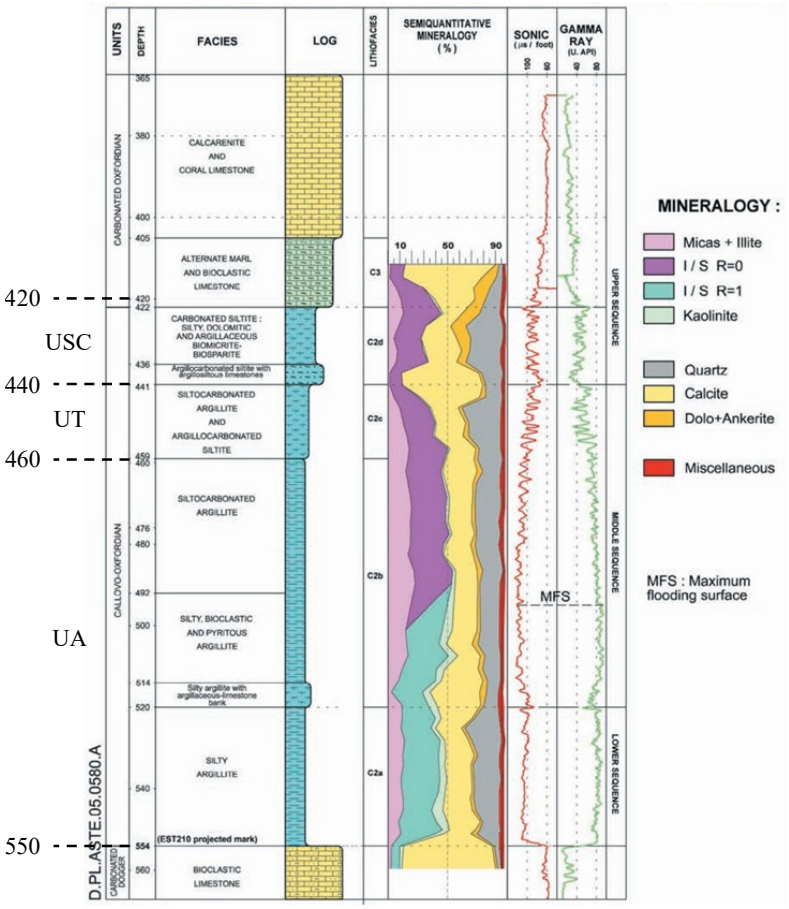

Figure 1.1: Lithology and mineralogy of the Callovian-Oxfordian formation (Yven et al., 2007).

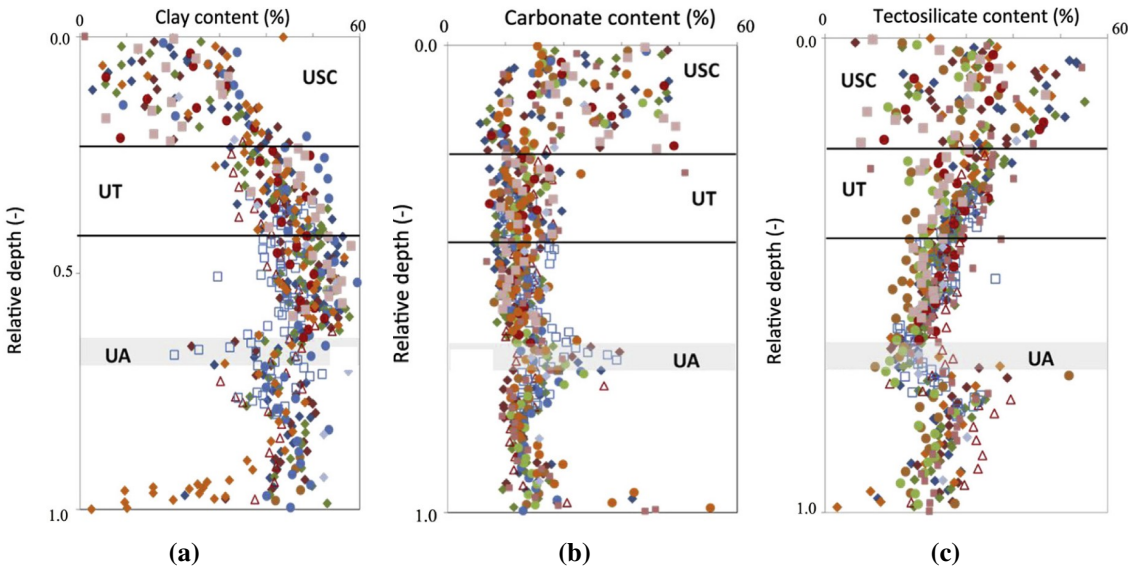

Figure 1.2: Vertical variations of mineral contents (a) clay content, (b) carbonate content and (c) tectosilicate content along the bedding plane (Conil et al., 2018).

Table 1.1
Mineralogical analyses on different cores of the COx claystone from literature.

Sample	Content(%)			
	Tectosilicates	Carbonates	Clay	Others
UA (Conil et al., 2018)	24.0	27.0	46.0	<3.0
UA_EST58128 (Wang et al., 2022a)	26.9	21.0	50.0	2.1
UA_EST58145 (Wang et al., 2022a)	28.6	22.7	46.7	2.0
UT_EST57243 (Di Donna et al., 2022)	34.7	38.0	25.7	1.1
UT_EST57261 (Di Donna et al., 2022)	11.8	78.1	9.5	0.4
USC (Conil et al., 2018)	30.0	42.0	26.0	<2.0

In general, the COx claystone consists mainly of phyllosilicates, carbonates, tectosilicates and ancillary minerals throughout the whole formation. The averaged distribution of mineral groups is tectosilicates of 25±8% of minerals, carbonates of 30±12% of minerals, clay fraction (phyllosilicates) of 42±11% of the rock and ancillary minerals constitute less than 4% (Conil et al., 2018). At the main level of the Meuse/Haute-Marne URL at a depth of 490 m, the proportions of tectosilicates, carbonates, clay minerals with subordinate pyrite and iron oxides are respectively 20%, 20-25%, 50-55% and 3% (Armand et al., 2014). The relative proportions of these mineralogical compositions vary

in different lithological units. Table 1.1 summarized the mineral contents of different cores from three typical units. Although mineralogical composition varies between cores from the same unit, particularly in the relative proportions of carbonates and tectosilicates, the overall differences are slight. It shows significant mineral content in vertical variations but low variability in the bedding plane.

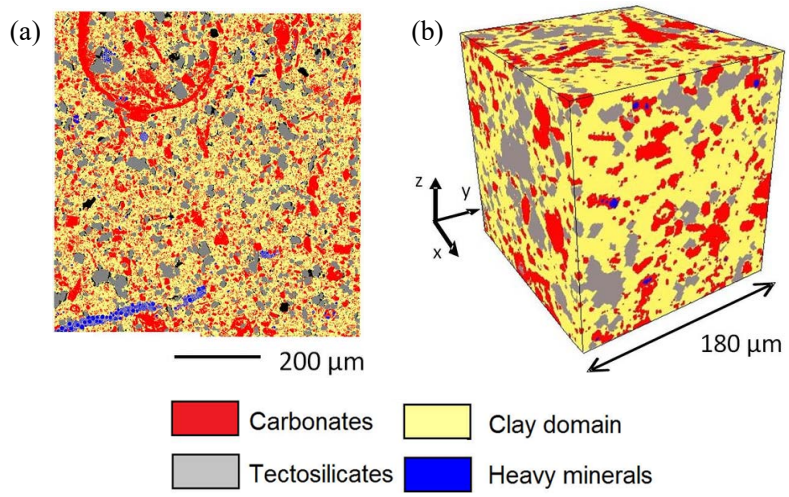

Figure 1.3: Spatial distribution of mineral content visualized (a) 2D SEM section parallel to the bedding planes; (b) 3D micro-CT subvolume (EST26095) (Robinet et al., 2012).

The predominant COx claystone could be considered as a clay matrix with inclusions of carbonate and tectosilicate grain, with grain sizes ranging from 0.1 to 100 nm (Armand et al., 2017b). Microstructural investigations are essential for improving the understanding of the macroscopic behavior and physical properties of clay-rich rocks. Fig. 1.3 presents the mineral groups, spatial distribution and mineral morphology from 2D and 3D images obtained from the analyses of Scanning Electron Microscopy (SEM) and X-ray Computed micro-Tomography (micro-CT). Robinet et al. (2012) observed an anisotropic feature of the Callovo-Oxfordian mesostructure, characterized by the preferential orientation of elongated carbonate and tectosilicate inclusions parallel to the bedding, whereas the orientation of clay particles and aggregates with respect to the bedding plane was less pronounced.

The structural anisotropy of claystone is revealed with various kinds of uniaxial compression tests (Grgic et al., 2019), triaxial compression and extension tests (Zhang et al., 2019; Wang et al., 2025) and creep tests (Shi et al., 2020) on samples drilled in different orientations with respect to the bedding plane, namely parallel, inclined and perpendic-

ular, as shown in Fig. 1.4. In these tests, its structural anisotropy has also proven to have an important effect on the mechanical responses. The elastic modulus is greater in the orientation parallel to the bedding planes than in the perpendicular orientation (Wang et al., 2025) and its sensitivity to water saturation is also higher in the parallel direction. Zhang et al. (2012) found that the axial strain in the perpendicular direction was higher than that in the parallel one in various relative humidities. The progressive compaction of bedding planes leads to large axial strains (Shi et al., 2020). However, the mechanical strength under nearly saturated conditions was nearly identical for two loading orientations and then not affected by the structural anisotropy. It is noted that the smallest strength is found in the loading orientations around $45°$ regarding the bedding planes (Niandou et al., 1997).

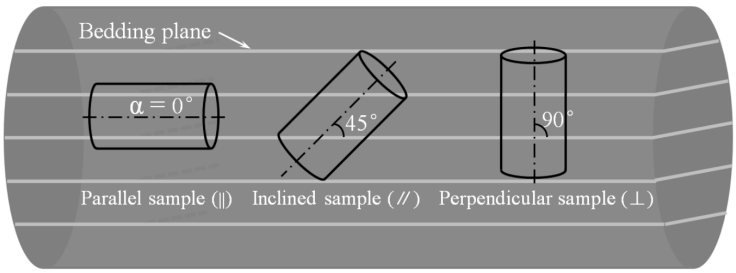

Figure 1.4: Definition of loading angle between bedding planes and sample axis ($\alpha = 0°, 45°, 90°$ corresponding to parallel, inclined and perpendicular orientations, respectively) (Shi et al., 2020).

2.2 Porosity and moisture characteristics

The spaces between the solid particles of claystone are called pores, filled with interstitial fluids such as small amounts of water. According to the classification of the International Union of Pure and Applied Chemistry (IUPAC), pores are divided into macropores (pore size $>$ 50 nm), mesopores (2 nm $<$ pore size $<$ 50 nm) and micropores (pore size $<$ 2 nm) (Sing, 1985). The porosity can be determined by the mercury injection porosimetry (MIP) and nitrogen adsorption methods. In COx claystone, porosity consists of macroporosity, mesoporosity and microporosity, as illustrated in Fig. 1.5. Macroporosity accounts for 20-40% of the total porosity and is mostly associated with detrital minerals and clay aggregates, forming inter-aggregate and inter-particle pores, with a significant proportion being isolated. In particular, the micrometric pores often occur at the interface between the clay matrix and quartz, whereas sub-micrometric pores are found

between the clay matrix and carbonates. Mesoporosity forms the dominant fraction, accounting for 60-80% of the total porosity, while being mainly located within the clay matrix, around clay aggregates and particles. Microporosity represents less than 2% of the total porosity, corresponding to intraparticle porosity. Furthermore, Yven et al. (2007) found that the total porosity ranges from 14% in the most carbonated levels to 19.5% in the clay-rich levels. At a depth of 490 m, the porosity measured by Andra is 17.5±1.2% (Conil et al., 2018).

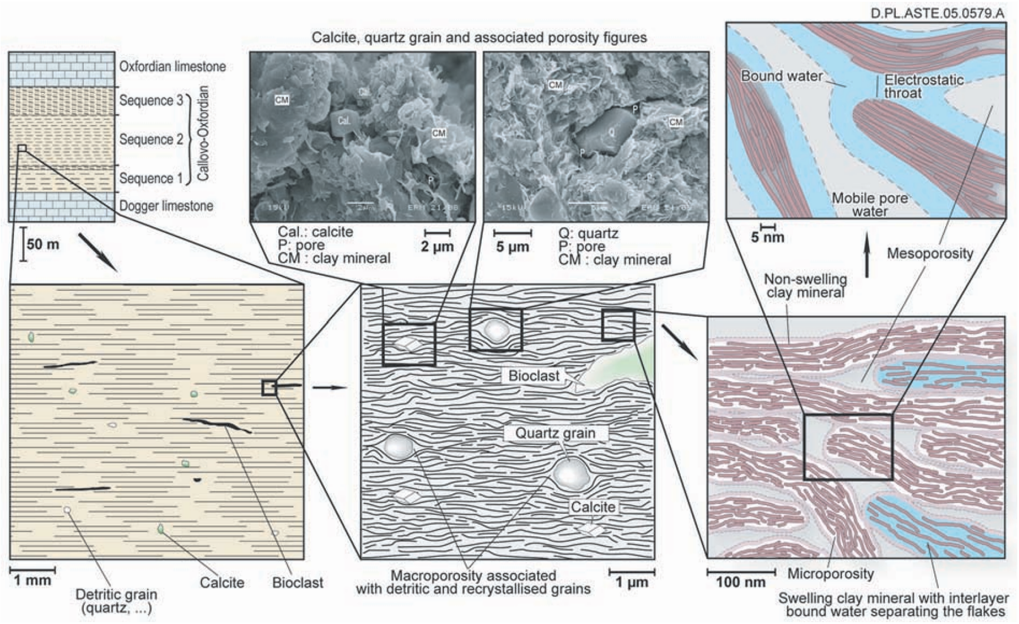

Figure 1.5: Schematic diagram of the porosity organization in claystone (Yven et al., 2007).

Another important parameter frequently mentioned in the literature (Duan et al., 2021) is the water content of claystone. The natural water content (ω) of COx claystone, referred to as the water content under in situ conditions, plays a critical role in governing fluid transport (Wan et al., 2013; Charlier et al., 2013), swelling behavior (Zeng et al., 2021; Di Donna et al., 2022), and mechanical behavior (Chiarelli et al., 2000; Hu et al., 2014; Liu and Shao, 2016). It is determined by the mass of the sample in its wet state (m_ω) and its dry mass (m_d), the latter being obtained after drying at a temperature of 105°C for 48 h.

$$\omega = \frac{m_\omega - m_d}{m_d} \tag{1.1}$$

Fig. 1.6 presents a vertical distribution of water content at the MHM URL. In the UA

level, water contents are measured between 5% and 8% and the reference value at a depth of 490 m is 7.9±0.6% (Conil et al., 2018).

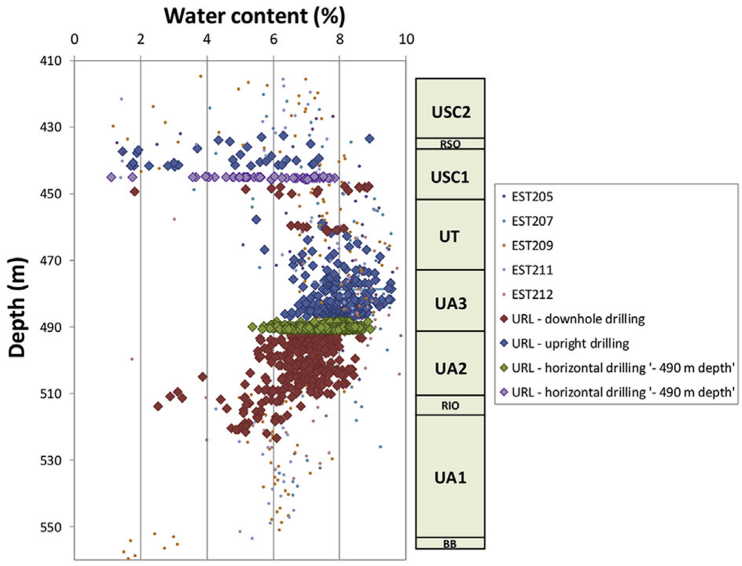

Figure 1.6: Vertical distribution of water content across the thickness of the COx formation (Conil et al., 2018).

2.3 Fluid transfer properties

Permeability is considered a main parameter for evaluating the transport properties of porous media and is critical for understanding fluid migration in COx claystone. Early studies mainly focused on the determination of intrinsic permeability. Homand et al. (2004) used two types of methods to measure the permeability of saturated and partially saturated argillites based on the hydromechanical equation. The pulse test on saturated samples was carried out by comparing the pressure evolutions of two reservoirs with theoretical curves, while the drying test measured weight loss and deformation to assess the permeability of partially saturated samples. Similarly, Jougnot et al. (2010) carried out a series of experiments on very low permeability COx claystone and demonstrated that the relative permeability can be described by a simple power law relationship with water saturation.

However, these studies mainly emphasized intrinsic permeability without considering the difference between gas permeability and water permeability. Davy et al. (2007) compared the gas permeability value determined from steady-state gas flow tests with the water permeability value obtained from transient water flow tests. They found that gas

permeability was on the order of 10^{-14} m^2, while water permeability ranges from 10^{-18} to 10^{-21} m^2, a difference attributed to swelling-induced crack closure of water-saturated rock. Further experiments indicated that gas permeability of partially saturated samples is very sensitive to water saturation, especially for highly saturated samples, while water permeability is more influenced by injected water pressure than by confining pressure Yuan et al. (2023). Under steady-state conditions, the Darcy's law describes the flow across a porous medium caused by a pressure gradient:

$$q = -\frac{K}{\mu}\nabla P \tag{1.2}$$

where q is the mean speed of the fluid (m/s), K is the intrinsic permeability of the material (m^2), μ is the dynamic viscosity of the fluid (Pa s) and ∇P is the fluid pressure gradient (Pa). The application of Darcy's law differs between incompressible fluids (e.g., water) and compressible fluids (e.g., gas), with both devices described in Fig. 1.7. For water transport, the permeability is calculated from the volume of inject water measured. Taking into account the flow due to the pressure gradient across the sample. The water permeability is as following

$$K_w = \frac{Q_w \mu_w L}{A(P_1 - P_0)} \tag{1.3}$$

where Q_w is the flow rate of the water $(\mathrm{m}^3/\mathrm{s})$, μ_w is the dynamic viscosity of the water (Pa s), L is the length of the sample (m), A is the cross-sectional area of the sample (m^2), P_1 and P_0 are respectively the pressures at the upstream and downstream sides of the sample (Pa). For gas transport, Meziani and Skoczylas (1999) designed and validated an original "quasi-stationary" flow method in order to derive K from measuring volume flow rate. More information related to this method can also be found in previous studies (Dana and Skoczylas, 1999; Liu et al., 2015, 2018b). Gas flows steadily from a buffer reservoir to the upstream side of the sample, where the pressure P_1 is recorded, while the downstream side of the sample is maintained at atmospheric pressure P_0. During the injected time $\triangle t$, the upstream gas pressure decreases from P_1 to P_1-$\triangle P$. It is assumed that steady flow occurs at a constant mean injection pressure, P_{mean}=P_1-$\triangle P/2$. The gas is assumed to be perfect and the test is conducted under constant temperature conditions. Here, μ_g denotes the dynamic viscosity of the gas and V is the volume of the buffer reservoir. Based on these assumptions, the gas permeability can be given by

$$K_{ag} = \frac{\mu_g V}{A} \frac{2L\triangle P}{(P_{mean}^2 - P_0^2)\triangle t} \tag{1.4}$$

The difference between gas and water permeability values can also be explained by the gas slippage theory (Loosveldt et al., 2002; Tanikawa and Shimamoto, 2006; Yuan et al., 2023; Gay et al., 2026), commonly referred to as the Klinkenberg effect. This theory states that when the mean free path of the gas molecules is sufficiently large compared to the pore diameter, the frequency of gas-solid collisions decreases, resulting in slip flow along the pore walls. Gas transport deviates from the classic Darcy's law but exhibits significant slip flow characteristics. This effect is particularly significant in micro/nano-porous media (Sabet et al., 2019), such as clayed rocks (Boulin et al., 2008; Duan et al., 2020), fault

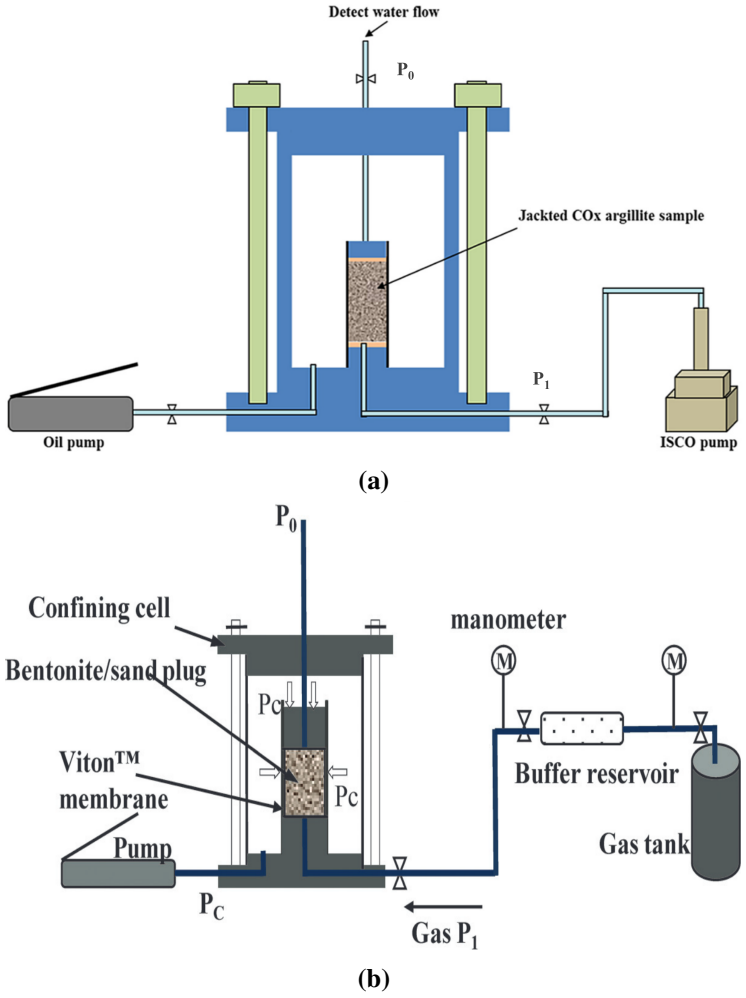

Figure 1.7: Sketch of the experimental apparatus for permeability measurement. (a) water permeability test (Yuan et al., 2023); (b) gas permeability test (Liu et al., 2015).

rocks (Duan and Yang, 2014), cement-based media (Lion et al., 2005; Benachour et al., 2008; Ezzedine El Dandachy et al., 2024). To quantify this phenomenon, Klinkenberg proposed the following correction for gas permeability (Klinkenberge, 1941)

$$K_{ag} = K_{int}\left(1 + \frac{b}{P_m}\right) \tag{1.5}$$

where K_{ag} is the apparent permeability measured at different injection pressures, K_{int} is the intrinsic permeability, P_m is the mean pressure of the sample $(P_{inj} + P_{atm})/2$ and b the Klinkenberg coefficient.

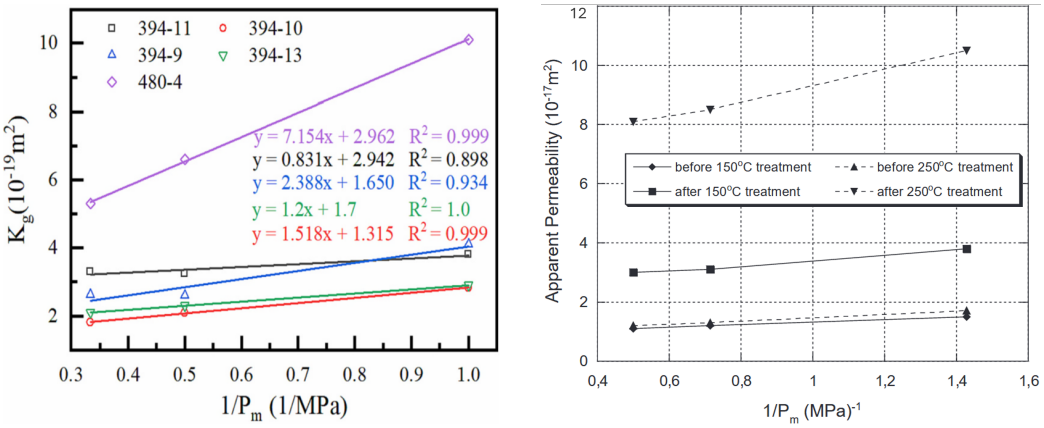

(a) **(b)**

Figure 1.8: Apparent permeability as a function of mean gas pressure $(1/P_m)$: (a) COx claystone (394 refers to core EST27394 and 480 refers to core EST30480) (Yuan et al., 2023); (b) cement-based material (Lion et al., 2005).

3 Self-sealing behaviour of cracked COx claystone

Self-sealing might be described as, at least partial, closing of fractures generated in claystone during excavation or induced by other processes such as drying (Bock et al., 2010; Wang et al., 2021, 2022c; Gonzalez-Blanco et al., 2024). It would delay the radionuclide migration in the EDZ. Understanding the self-sealing mechanisms and their quantification is consequently an important factor to consider in the performance assessment for nuclear waste repositories in clay formations. The self-sealing capacity of COx claystone is mainly evidenced by the water permeability reduction and crack closure due mostly to water-induced clay swelling.

3.1 Transport properties during resaturation

Gas and water permeability tests are widely conducted to study the efficiency of self-sealing behavior of cracked COx claystone in the laboratory (Zhang, 2011, 2013; Al Reda et al., 2020; Wang et al., 2024). In order to provide a reference, the permeability of intact COx claystone has also been extensively studied (Song et al., 2016a; Wang et al., 2022a). Results show that gas permeability decreases with increasing water content, reaching values on the order of $10^{-20} - 10^{-21}$ m^2 at water contents exceeding 4% (Zhang and Rothfuchs, 2004; Yuan et al., 2020). The gas permeability parallel to the bedding plane is about one order of magnitude higher than that perpendicular to the bedding, as seen in Fig. 1.9(a), reflecting the intrinsic anisotropy of the material. This permeability can be considered a parameter reflecting the change in transport mechanism and the evolution of deformation for claystone. When gas permeability tests were performed on re-saturated cracked COx claystone, Zhang and Rothfuchs (2008) observed that the gas permeability values were about five orders of magnitude lower than the values before water re-saturation. More precisely, as shown in Fig. 1.9(b), the gas permeability of two damaged samples (MSE00953-4 and MSE00953-2) significantly decreased from initial values of 1×10^{-16} and 1×10^{-17} m^2 to 5×10^{-22} and 1×10^{-21} m^2 upon full saturation during the saturation process. Because the fractures created in the damaged sample MSE00953-3 were not appreciably interconnected, its permeability was comparable to that of the undamaged reference sample MSE00953-1. After water re-saturation, however, the gas permeability of all damaged samples became similar to that of the undamaged sample.

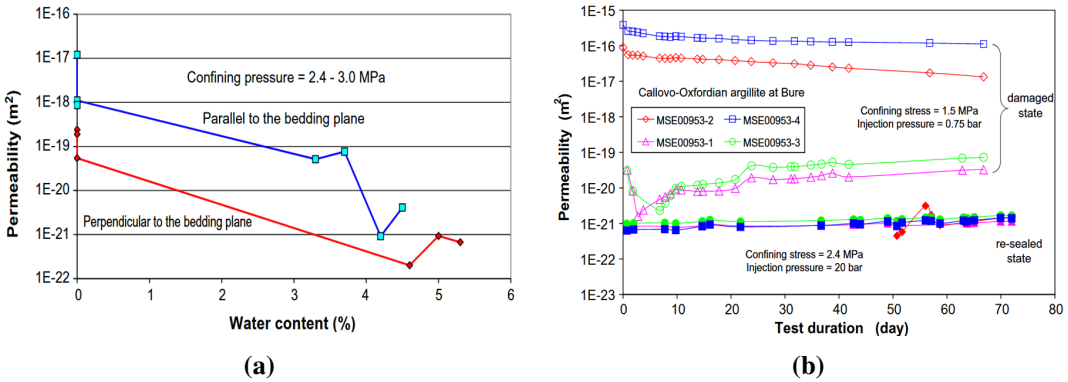

(a) (b)

Figure 1.9: Evolution of gas permeability of (a) intact COx samples as a function of water content (Zhang and Rothfuchs, 2004); (b) damaged samples before and after water re-saturation (Zhang and Rothfuchs, 2008).

Notably, water permeability is 2-8 orders of magnitude lower than gas permeability during the self-sealing process (Davy et al., 2007). The gas permeability was on the order of $10^{-13} - 10^{-16}$ m^2, whereas water permeability varied from 10^{-18} to 10^{-21} m^2. The water permeability of the sample from different units during the self-sealing process was compared by Wang et al. (2022a). The final water permeability of cracked samples from the UA core was reduced by five orders of magnitude and close to that of the intact sample around 10^{-20} m^2, while that of the cracked sample from the UT core was reduced by four orders of magnitude and stabilized at 10^{-18} m^2. Zhang (2018) indicated that the water permeability of fractured COx samples decreased gradually under low confining stresses of 2-3.5 MPa, reaching final values at $3 \times 10^{-20} - 7 \times 10^{-21}$ m^2, being the same order of magnitude as that of the undisturbed clay rock. Furthermore, Ghayaza et al. (2013) indicated that the most rapid and pronounced decrease in water permeability occurred during the first days of water injection. Similarly, Giot et al. (2019) observed a high decrease in the permeability during the first hours of water injection, followed by a more constant decrease, as seen in Fig. 1.10(a). Agboli et al. (2024) further compared the water permeability of sample orientation and found both permeabilities were moderately decreased, as shown in Fig. 1.10(b). However, the mechanical closure was not more efficient for the cracked sample parallel to the bedding plane, contrary to what was supposed (Auvray et al., 2015). These studies provided that after water re-saturation, the permeability of cracked claystone decreased and approached that of intact ones. This reduction is likely due to water flow inducing swelling, slacking, or disintegration of the clay matrix, resulting in clogging and sealing the crack interstices, thereby reducing permeability.

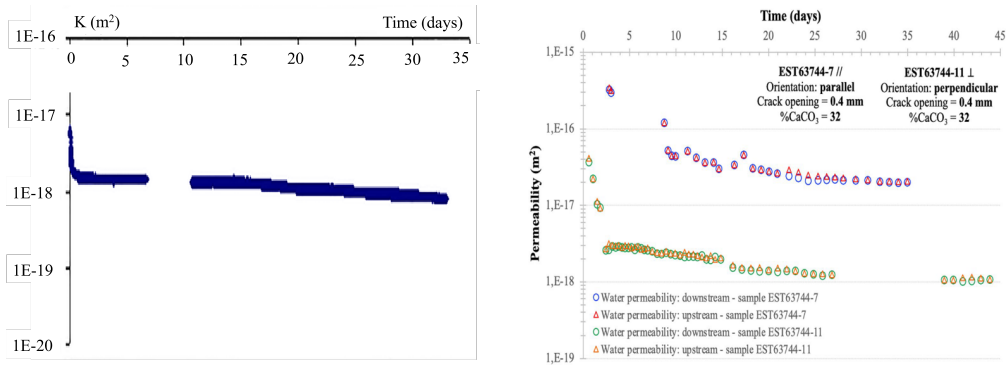

(a) **(b)**

Figure 1.10: Evolution of water permeability of (a) UA sample as a function of time (Giot et al., 2019); (b) parallel sample EST63744-7 and perpendicular sample EST63744-11 during a self-sealing test (Agboli et al., 2024).

3.2 Swelling deformation and mechanism

The self-sealing behavior of cracks, apparently due to the expansion of the hydrated clay mineral (Yven et al., 2007; Zhang and Rothfuchs, 2008; Menaceur et al., 2016), has been experimentally evidenced. This phenomenon strongly depends on the applied stress, the clay fraction, and the hydration level, mainly characterized by changes in swelling pressure and swelling strain. For the swelling pressure determination in the laboratory, it was found that different experimental methods could give different swelling pressures due to the difference in the loading conditions in each method (Sridharan et al., 1986; Villar and Lloret, 2008; Tang et al., 2011; Wang et al., 2012; Cui et al., 2013). The existing methods mainly include the swelling-consolidation, pre-swell, zero-swell and constant-volume methods (see Fig. 1.11(a)), the loading-wetting method (see Fig. 1.11(b)), and the unloading-reloading loop method (see Fig. 1.11(c)). These methods have been commonly applied to the various composite materials, but not to assess them together with one material. With regard to this, Zhang et al. (2020) determined the swelling pressure of intact COx claystone samples extracted in the direction perpendicular to the bedding plane by these methods. The results were compared and further analyzed, allowing higher swelling pressure with the swell-consolidation method, the swelling pressures determined by other methods to be comparable. The swelling line defining the swelling limit being lower than the consolidation curve further confirms the limitation of the swell-consolidation method for determining swelling pressure. For the purpose of measuring swelling pressure under different conditions, Zhang et al. (2010) designed two swelling cells, one under volume constraints and the other under axially fixed and laterally unconstrained conditions. The measured high swelling pressure reflected the capability of the interparticle absorbed water-films in the claystone to bear external loads and carry the lithostatic stress. The swelling pressure acting on interparticle water-films was validated to be equal to the effective stress in claystones by the test observations. The fluctuations of measured swelling pressure may be caused by the local changes in the stiffness of clays during the change of water content.

In order to reproduce the in situ swelling conditions, Davy et al. (2009) designed one setup version with an instrumented and calibrated tube instrumented with four strain gauges for the bentonite swelling kinetics and pressure characterization. The tube is made of a ductile material less prone to failure than argillite, such as aluminum, Plexiglas^{TM}

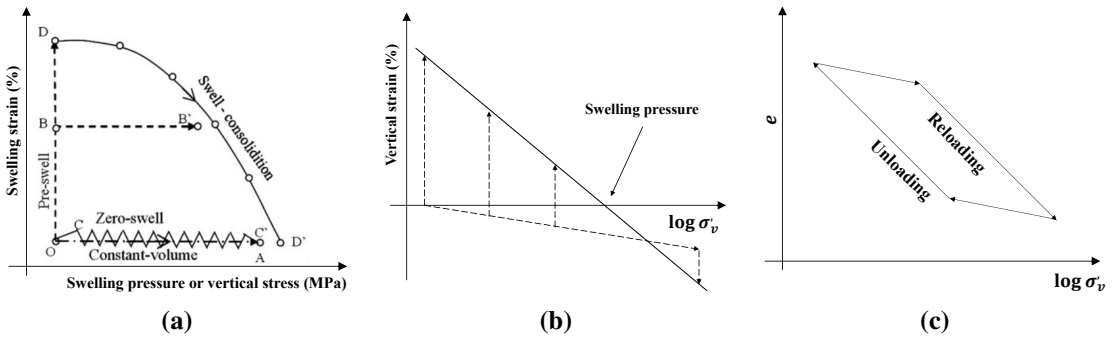

Figure 1.11: Methods for swelling pressure determination, (a) swelling-consolidation, pre-swell, zero-swell and constant-volume method, (b) loading-wetting method, (c) unloading-reloading loop method (Cui et al., 2013).

or aluminum–Plexiglas^{TM}. Through evaluating the tube material variability on the deformation, it was observed that the highest deformability is obtained with Plexiglas^{TM}, but Plexiglas^{TM} is proven to display creep after several hours of confinement and inner pressurizing. The aluminum–Plexiglas^{TM} tube is seven times more deformable than the aluminum tube, making it more sensitive and reliable. The tube material has been chosen to allow for sufficient deformation while avoiding significant creep. Liu et al. (2014) further proposed two types of tubes for constant volume swelling, one aluminum–Plexiglas^{TM} tube with a smooth inner surface and the other a grooved tube made of stainless steel, with a screw thread on its inner surface. As it is made of stainless steel, the swelling volume of the bentonite/sand plug in the tube is almost constant due to the high rigidity of the metallic tube preventing the sample from being subjected to confining pressure. More recently, Wang et al. (2022a) chose it to design the "stainless steel tube–epoxy–sample" system for measuring the apparent swelling pressure (P_{app}), deriving it from the strain on the outer surface of the tube. This apparent swelling pressure is the consequence of swelling combined with a limited volume expansion of claystone, enabling better assessment and comparison of swelling behavior. The results presented in Fig. 1.12 indicated that the intact sample exhibits a slightly higher P_{app} than macro-cracked samples, but the macro-crack created more water-mineral contact space inside the sample, accelerating the swelling kinetics.

Furthermore, the influence of filling material between the steel tube and macro-cracked sample on the measured lateral swelling pressure was discussed by Wang et al. (2024). The compared samples were extracted from the same geological depth of about 490 m and thus have similar mineralogical compositions and expansion capacities. The results

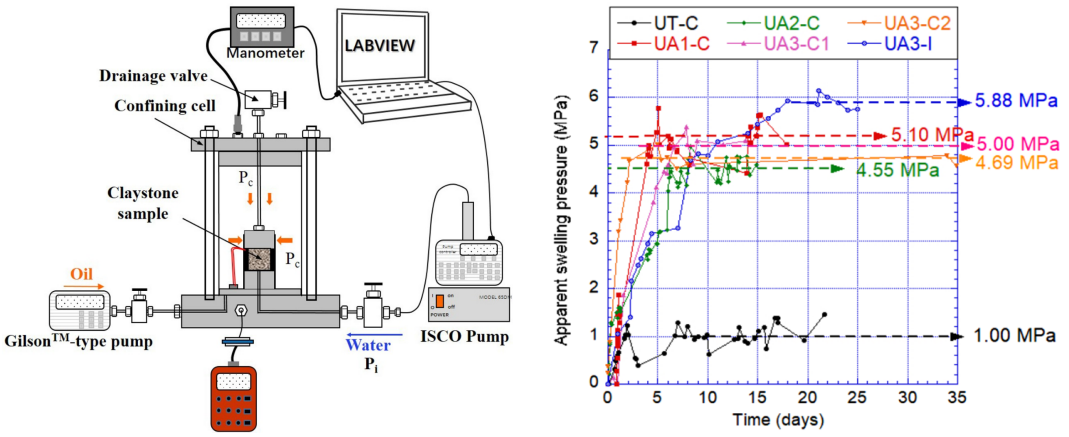

Figure 1.12: Swelling pressure measurements from the self-sealing experiment: (a) schematic of the experimental setup; (b) evolution of apparent swelling pressure (Wang et al., 2022a).

show that the lateral swelling strain with silicon as the filler is significantly lower than that obtained with epoxy resin seen in Fig. 1.13(b). This is mainly because soft silicon is of very high flexibility, enabling it to absorb most of the sample swelling deformation during re-saturation. In contrast, epoxy resin has a much higher stiffness and can effectively transmit the swelling pressure of the sample. Therefore, the steel-tube-sample system is more suitable for measuring the swelling response of the sample itself.

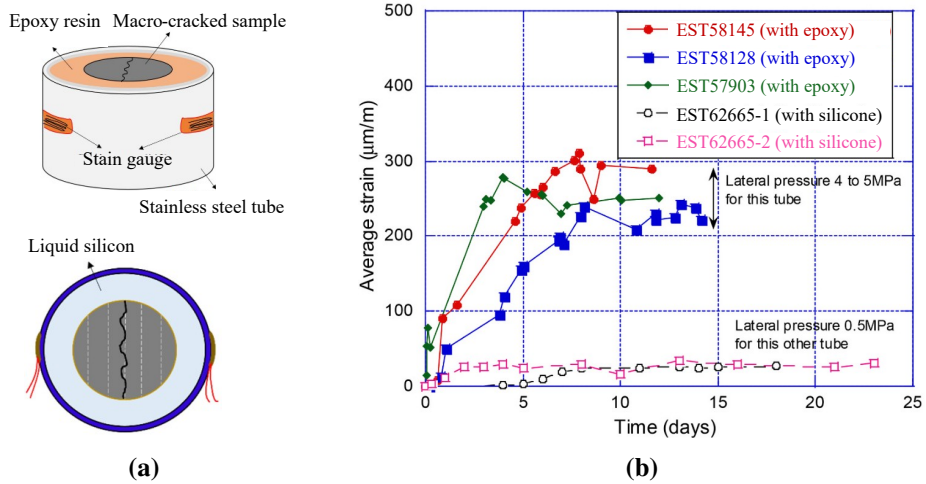

Figure 1.13: Comparison of strain measurements from different mock-ups: (a) schematic illustration of the mock-up with epoxy resin (up) and with silicone (down); (b) measured strain on the tube external surface after water injection into the sample (Wang et al., 2022a, 2024).

From a macroscopic perspective, swelling behavior is pronouncedly anisotropic due to

the bedding plane observed by some research groups (Yang et al., 2013; Wan et al., 2013). Its mechanism is mainly related to water content and the externally applied stress. During the observation of strain response to drying and wetting on the unconfined sample, it is obvious that drying caused evaporation and release of bound pore water, resulting in collapse of the pore structure to macroscopic shrinkage, as in Fig. 1.14. The subsequent wetting increased the water content, resulting in an expansion of the unconfined sample in all directions. Regarding swelling orientations with the bedding plane, Zhang et al. (2010) observed a larger swelling strain in the direction perpendicular to the bedding plane, as in Fig. 1.14(a). For the cored sample in Fig. 1.14(b), its radial strain ($\varepsilon_r^{\perp}$) normal to bedding was larger compared to the axial strain ($\varepsilon_a^{\parallel}$) parallel to bedding. Although the strain-gauge orientations relative to the bedding plane differ between the experiments conducted by Zhang et al. (2010) and Zhang (2018), the intact samples in both studies consistently exhibited this anisotropic regularity under unconfined conditions to humidity change. Under a confining pressure of 14 MPa and water injection at 5 MPa, Duan et al. (2021) observed that either intact samples or cracked samples exhibited significantly higher radial (lateral) strain perpendicular to bedding than axial (longitudinal) strain parallel to bedding. Another reason for the difference in swelling strain is that perpendicular loading causes progressive mechanical compression of the bedding plane. This process may be closely related to the stiffness degradation induced by water uptake. In other words, as the water content increases, the Young's modulus gradually decreases, resulting in greater compressive deformation under the same stress level. It is confirmed by Chiarelli et al. (2003) who has illustrated that Young's modulus is very sensitive to the water content of COx

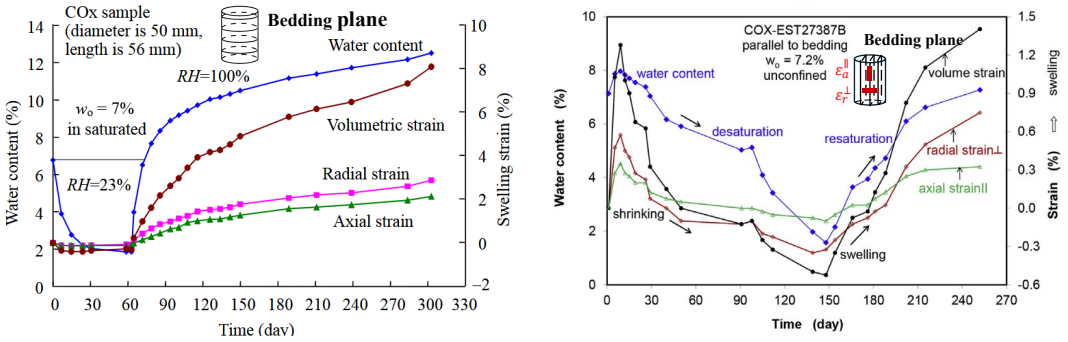

Figure 1.14: Comparison of swelling strain in radial and axial directions under unconfined conditions to humidity change: (a) intact sample with its axis perpendicular to the bedding plane (Zhang et al., 2010), (b) intact sample with its axis parallel to the bedding plane (Zhang, 2018).

claystone. More precisely, they have illustrated that Young's modulus decreases with water content. Ibrahim (2008) also shows Young's modulus decrease with relative humidity based on micro-indentation tests.

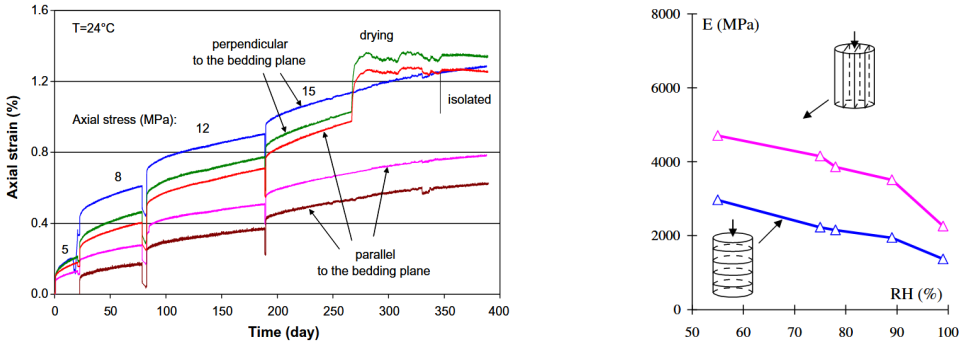

(a) (b)

Figure 1.15: Comparison of the two principal loading orientations in terms of (a) creep behavior (Zhang and Rothfuchs, 2004) and (b) evolution of elastic modulus with relative humidity obtained from mini-compression tests (Zhang et al., 2012).

Thanks to the microstructure analyses, the swelling behavior primarily related to the presence of smectites in clay minerals is evidenced by Di Donna et al. (2019, 2022). Some experiments on the clay unit (UA) COx richer in smectite clay and the transition unit (UT) COx richer in carbonates with different orientations between the bedding plane and cracks have conducted using X-ray tomography. It was found that a peeling phenomenon in the area adjacent to the crack induced the filling of the main crack, and a diffuse swelling around the peeling zone induced the sealing of the main crack. This phenomenon is more common in smectite clay-rich samples. The smectite is a typical 2:1 layered silicate, and its swelling response mainly consists of crystal swelling at the microscopic scale and osmotic swelling at the mesoscopic scale, as shown in Fig. 1.16. Swelling at the lower water contents is dominated by crystal swelling (Norrish, 1954). Many studies (Laird et al., 1995; Anandarajah and Chen, 1997) have shown that crystalline swelling is governed by a balance of attraction (Coulomb and van der Waals interactions) between clay layers and repulsion arising from interlayer cation hydration and negative surface charge sites on clay surfaces. Crystal swelling is essentially a progressive interlayer hydration process. As water molecules penetrate into the interlayer space, discrete water layers form sequentially, causing the clay platelets to separate (see Fig. 1.17(a)) and the interparticle spacing to increase. This leads to the formation of structures containing 0, 1, 2, 3, up to a maximum of 4 water layers (Barshad, 1949; Menaceur et al., 2016). The

inter-basal spacing of smectite is approximately 9.6 Å (Mitchell and Soga, 2005). As hydration progresses, X-ray diffraction (XRD) measurements show that the inter-basal spacing of smectites is known to increase in an orderly fashion, with successive adsorption of one, two, and three water layers corresponding to interlayer spacings of 12.6, 15.6, and 18.6 Å (Ferrage et al., 2005; Dazas et al., 2014) (see Fig. 1.17(b)), respectively. It is limited to four water layers and not beyond, corresponding to a layer spacing of 21.6 Å (Saiyouri et al., 2004). This process shows the sequential insertion of water molecules initially through cation hydration, followed by the formation of successive water layers up to the interlayer structure reaching its maximum hydration state.

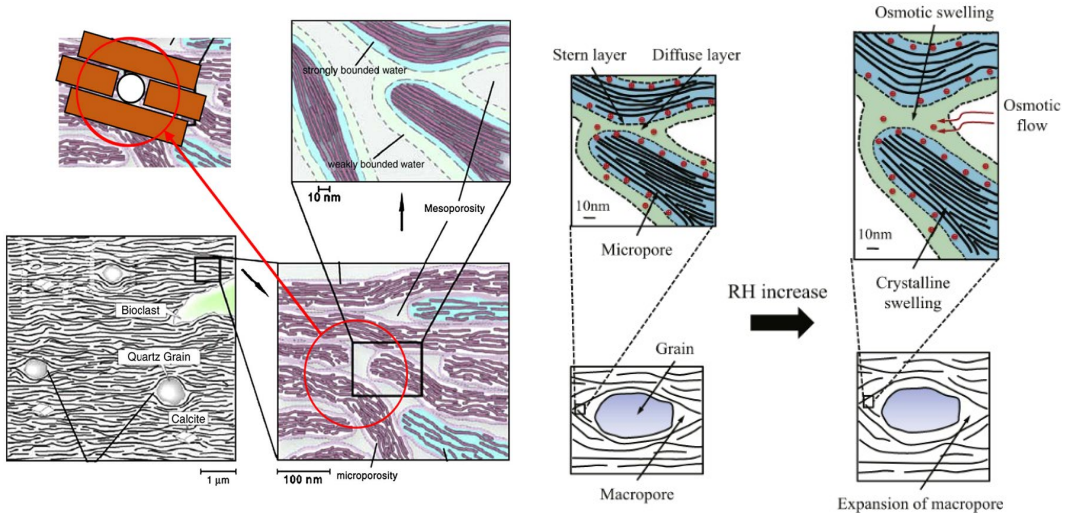

Figure 1.16: Schema of the swelling of clayed rock, (a) showing the corresponding porosity micrtstructure (Menaceur et al., 2016), (b) change in pores with the relative humidity (Wang et al., 2017).

In addition to crystalline swelling, another swelling mechanism that occurs during hydration is called osmotic swelling (see Fig. 1.16(b)). This swelling occurs in clay minerals containing exchangeable cations in the interlayer region at high water content. The difference in cation concentration between the pore water and the clay particle surfaces drives water into the spaces between particles (Anderson et al., 2010). The electrostatic repulsion is generated in the diffuse double layer around the particle surfaces, further increasing both interlayer and interparticle spacing. At higher hydration, this repulsive force may propagate to the interparticle domain, contributing to macroscopic volume increase. The magnitudes of osmotic swelling depend on several factors, including the surface charge

density and its spatial distribution, the type and concentration of cations in the pore water, and the potential swelling space (Laird, 2006; Daab et al., 2018). Osmotic swelling in sufficient swelling space can generate significantly larger volume increases than crystalline swelling, with typical spacings up to approximately 130 Å(Anderson et al., 2010). Compared to crystalline swelling, osmotic swelling accounts for the majority of macroscopic volumetric changes during high hydration.

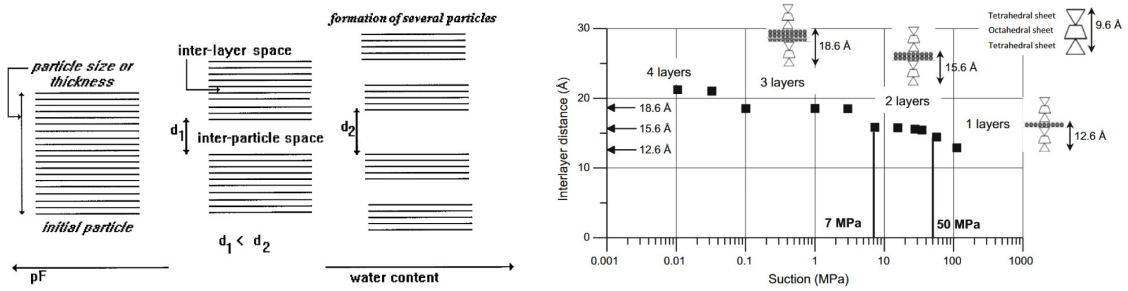

Figure 1.17: Swelling mechanism of clayed rock (a) interpreted by Saiyouri et al. (2000), (b) investigated through X-ray diffractometry (Saiyouri et al., 2000, 2004; Menaceur et al., 2016).

After extensive studies of the smectite swelling mechanism, Wang (2021a) conducted supplementary research on the multi-scale swelling behavior of COx claystone with a focus at the macroscopic level. It is commonly agreed that the macro-scale swelling of COx claystone is directly determined by smectite content (Menaceur et al., 2016). However, smectite does not appear as a single phase but rather as illite/smectite aggregates (I/S) in COx claystone. The clay minerals in COx claystone include illite, muscovite, interstratified illite/smectite aggregates, and small amounts of kaolinite and chlorite, of which the I/S aggregates are the only swelling mineral (Wang et al., 2022a). After a series of specially designed swelling tests, Wang (2021a) proposed a conceptual model to give insights into the swelling process of COx claystone, see Fig. 1.18. The inter-platelet region of smectite (in R1-I/S and R0-I/S) initially contains different layers of water molecules at different RH. As RH increases, crystallite swelling firstly occurs by increasing the inter-platelet water layers up to the maximum base spacing value (21.6 Å) at 100% RH, indicating complete crystallite swelling without structural damage. Then, at high saturation, osmotic swelling occurs, driven by the diffusion of free water into the interlayer region and electrostatic repulsion between electrical double layers on opposing clay surfaces, resulting in the delamination of stacked interstratified I/S along the smectite

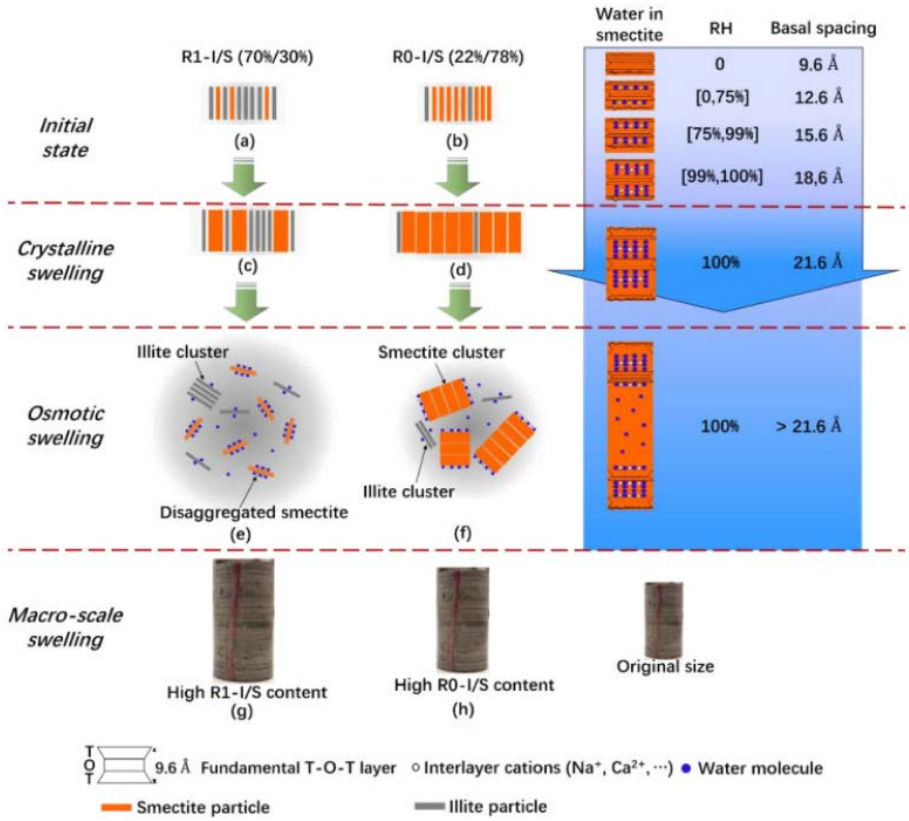

Figure 1.18: Conceptual model of the multi-scale swelling behavior of COx claystone. (a) and (b) show the unsaturated R1-I/S and R0-I/S interstratified clay minerals; (c) and (d) show the crystalline swelling of R1-I/S and R0-I/S, corresponding to 100% RH; (e) and (f) are the osmotic swelling of R1-I/S and R0-I/S; (g) and (h) are the samples with high R1-I/S content and high R0-I/S content after swelling (Wang, 2021a).

inter-platelets and a significant volume increase. Because of their larger pore volume and fewer smectite particles, the stacked R1-I/S layers separate more easily into numerous smectite "fragments" (Fig. 1.18(e)), which develop more surface area and adsorb more water molecules, resulting in stronger osmotic swelling. In contrast, R0-I/S only partially disaggregates to illite clusters and smectite clusters (Fig. 1.18(f)) and thus has a much smaller swelling magnitude. Consequently, at the centimeter scale, samples with higher R1-I/S content exhibit more swelling than those with higher R0-I/S content.

Based on these observations, the self-sealing processes related to the swelling of clay minerals are: (i) interlayer swelling of the smectitic phases (crystalline swelling), (ii) interparticle swelling by osmotic effect (osmotic swelling), and (iii) crack obstruction by clay particle aggregation (clogging).

3.3 Process and characteristics of fracture closure

Since the above summary, the self-sealing phenomenon results from the closure of cracks due to mineral hydration, structural rearrangement, and the migration and clogging associated with crack edges. As can be seen in Fig. 1.19, the fractures became noticeably narrower, the sharp wall edges smoothed out, and the interstices were filled and clogged by swelling and slaking or disintegration of the clay matrix after loading and water flowing (Zhang, 2011; Ghayaza et al., 2013). The presence of these filled fractures provides clear evidence of self-sealing. Previous studies (Bock et al., 2010) proposed that the grade of sealing depends on the initial fracture aperture, clay mineral content, confining stress, the duration of consolidation, etc. The fracture opening decreased with increasing confining pressure, and Ghayaza et al. (2013) noted that the fracture with more uniform and rougher edges is easier to self-seal. In his studies, the sample fractured with the Brazilian test with an aperture of 50 to 600 μm has an irregular shape and rough surfaces, whereas the sample made by saw cutting with an aperture of 50 to 70 μm has a regular shape and smooth surfaces. Water passage is more difficult and slow in rough fractures, which promotes clay matrix swelling as well as fine-grained particle slaking and clogging within the fracture. Water flows more smoothly through a regular fracture surface, relying highly on the swelling mechanism for sealing.

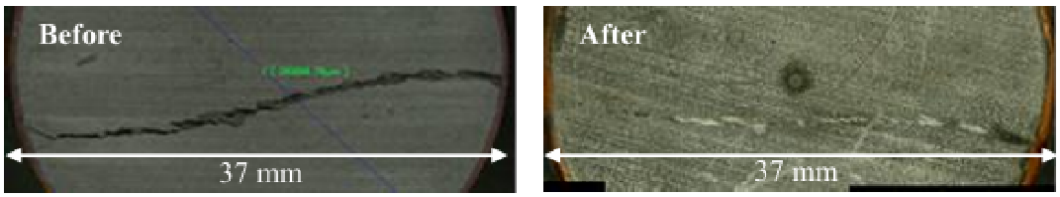

Figure 1.19: Cracks on the COx sample surface before and after water flowing (Ghayaza et al., 2013).

In addition to the crack shape, the aperture is an important parameter in the self-sealing phenomenon (Bock et al., 2010). Zhang (2011) observed that the larger fracture apertures closed more rapidly in the initial hydrostatic loading stage and then the closure rate decreased with increasing fracture stiffness at reduced apertures. According to the hyperbolic function associated with the fracture closure (Bandis et al., 1983; Bock et al., 2010; Zhang et al., 1993), Zhang (2011, 2013) proposed an exponential model for describing the normal stress-fracture closure relation. The fracture closure is also closely linked

to the intrinsic permeability of the rock mass when the aperture is very low. For a set of parallel fractures of equal aperture that are oriented parallel to the flow direction, a "cubic law" for fractured porous media was used to approximate the permeability variation with fracture aperture (Olivella and Alonso, 2008). Following this study, an additional parameter representing the influence of the fracture features of COx claystone such as the surface roughness, tortuosity, filling and others was introduced by Zhang (2011). Additionally, Wang et al. (2022a) used Poiseuille's law to calculate the crack equivalent aperture and compare it before and after sealing.

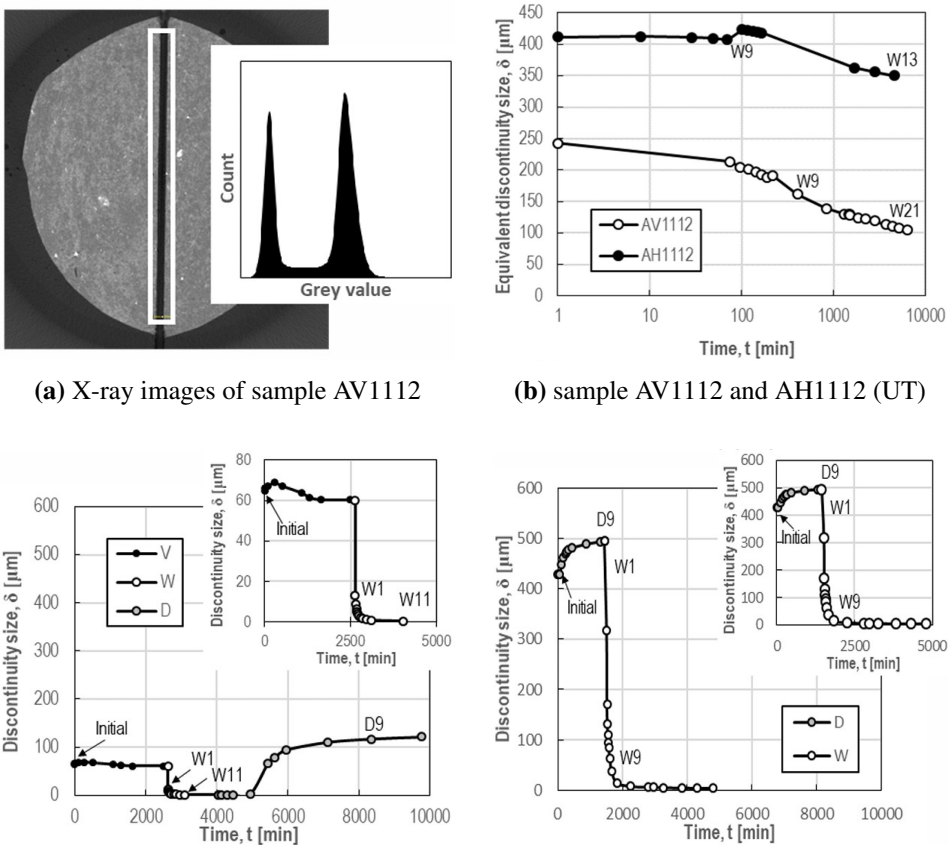

(a) X-ray images of sample AV1112 **(b)** sample AV1112 and AH1112 (UT)

(c) sample 3132 (UA) **(d)** sample 9192 (UA)

Figure 1.20: X-ray imaging and quantitative tracking of discontinuity evolution: (a) X-ray image and grey-value histogram of sample AV1112; (b-d) evolution of equivalent discontinuity size for COx claystone sample (b) AV1112 and AH1112 from core EST57243 under V-W loading path, (c) 3132 from core EST53644 under V-W-D loading path, and (d) 9192 from core EST53644 under D-W loading path (Di Donna et al., 2022).

The crack evolution was further investigated using different imaging techniques (Giot et al., 2019; Stavropoulou et al., 2019, 2020; Voltolini and Ajo-Franklin, 2020; Agboli

et al., 2024). Through visualization of the fracture evolution under x-ray tomography on the COx samples, Di Donna et al. (2019) observed the reaction of cracked COx in the different testing phases, including drying by dry air circulation (D), saturation with water vapor (V) and liquid water (W). No remarkable reaction of the samples from units UT and UA was detected during the water vapor phase. For the samples coming from unit UA, the artificial smaller crack of a 75 μm aperture closed rapidly (less than 1 μm average value) after contact with liquid water, while the largest ones with a fracture size ranging from 300 to 425 μm showed a peeling effect on the discontinuity lips. For the sample from unit UT, even if the fracture size of a 240 μm aperture reduced significantly during the phase of saturation by liquid water, the fracture was far from being sealed. Fig. 1.20(a) shows the X-ray image example of sample AV1112 at a low resolution of 7 μm. Di Donna et al. (2022) further quantified the evolution of equivalent discontinuity size based on these images. After V-W loading, the average discontinuity size was reduced but not completely closed on the same core EST57243, with a maximum closure of more than 50% of the initial fracture (240 μm) on sample AV1112 and less than 20% of the initial fracture (425 μm) on sample AH1112. Although the discontinuities of both samples from the same core EST53644 closed rapidly when in contact with liquid water, the larger initial discontinuity size lasted longer and reached 96% with respect to the aperture before the W-phase, while the other reached 99%. It was concluded that the initial size appeared to play the most important role for a given sample size in terms of the time required for closure. Moreover, the 3D images of crack volume evolution in COx claystone after water injection further evidenced the sealing phenomenon by Giot et al. (2019) and Agboli et al. (2024). The crack volume reduction is mainly induced by the clay mineral rearrangements and associated with the void closure due to clay minerals swelling near cracks (Van Geet et al., 2008; Zheng et al., 2014; Giot et al., 2019; Wang, 2021b).

4 Influencing factors of the self-sealing process

As mentioned before, the swelling and consequent self-sealing behavior of COx are closely related in several respects, for example, its mineral composition and microstructures. Under hydraulic loading, the microstructure and fracture volume can significantly change. Considering various influencing factors such as mineralogical competition, confining pressure, and thermal effect, etc., is particularly important with respect to the seal-

ing performance of COx claystone. In this section, the impact of these different parameters on the self-sealing capability of claystone is reviewed and discussed.

4.1 Effect of mineralogical composition

Several experimental studies were conducted to study the effect of different geological units on the self-sealing capacity of COx claystone (Di Donna et al., 2019; Giot et al., 2019; Zhang and Talandier, 2023). Table 1.1 presents the mineralogical composition of COx claystone from different units. Wang et al. (2022a) found that COx samples from unit UA had higher sealing efficiency and faster kinetics compared to ones from unit UT. The water permeability of UA samples was reduced by five orders of magnitude and close to that of the intact sample, while the permeability of UT samples was around one to two orders of magnitude higher than the one measured for the intact sample. Indeed, the UA samples were richer in smectite clay, while UT samples were richer in carbonates, resulting in the response to water contacts of UA samples being definitely more reactive (Di Donna et al., 2022). It has been proven that the smectite present brings to the claystone greater pore volume and larger specific surface area, in favor of water-swelling clay contact, resulting in greater swelling amplitude (Wang, 2021b). Giot et al. (2019) further discovered that the crack volume reduction of USC sample was limited, which seems to indicate that the swelling is limited and the clay plugs are unable to form or stabilize. For the UA sample, the higher the clay content, the more ability to self-seal. The rapid swelling of the clay minerals close to the cracks leads to the formation of clay plugs, and the subsequent expansion of clay minerals in the whole sample favors the plug growth and crack closure. Agboli et al. (2024) investigated the effect of calcite content on the COx self-sealing process. With a high calcium carbonate content of 52.8% or 68.1%, self-sealing was moderate, and the fracture remained globally open. However, with a very low calcium carbonate content of 5.3%, the very rapid sealing occurred after water saturation, almost instantaneously, and then the crack volume did not change and the self-sealing process stopped, probably due to the plugged capillary as a result of the collapse in the crack due to the rapid swelling of clay minerals. These findings also suggested that the higher the carbonate content, the less effective the self-sealing process, regardless of sample orientation (parallel or perpendicular).

4.2 Effect of fracture orientations and sizes

As previously noted, the initial fractures in COx claystone can be closed and thus be self-sealing due to the swelling of the clay minerals. Several laboratory tests were also conducted to demonstrate the evolution of fractures upon wetting (Pham et al., 2007; Wan et al., 2013; Menaceur et al., 2016; Giot et al., 2019), clarifying the effect of fracture orientations and sizes on the self-sealing capacity. Wang et al. (2022b) investigated the effect of fracture direction on the hydro-mechanical behavior of COx claystone, using the horizontally fractured sample TH-2, vertically fractured sample TV-2, and intact sample TI, as shown in Fig. 1.21(b). The evolution of vertical swelling strains with time in Fig. 1.21(a) could be identified as initial swell, primary swell, and secondary swell (Rao et al., 2006). Sample TV-2 had a higher swelling rate than samples TH-2 and TI during the initial swell stage, but sample TI had a higher swelling rate during the secondary swell stage. Furthermore, sample TV-2 and TI have the same infiltration path and strain rates, implying that swelling of fractured claystone is dependent on the infiltration path and direction of the initial fracture. Moreover, the swelling clearly contributed more efficiently to the sealing with the fractures parallel to the bedding plane, as reported by Di Donna et al. (2019, 2022) through 3D tomography observations. Fig. 1.22 is clearly visible for the self-sealing evolution of two samples with different fracture orientations. It can be observed that the peeling of clay particles, which appears as a dense network

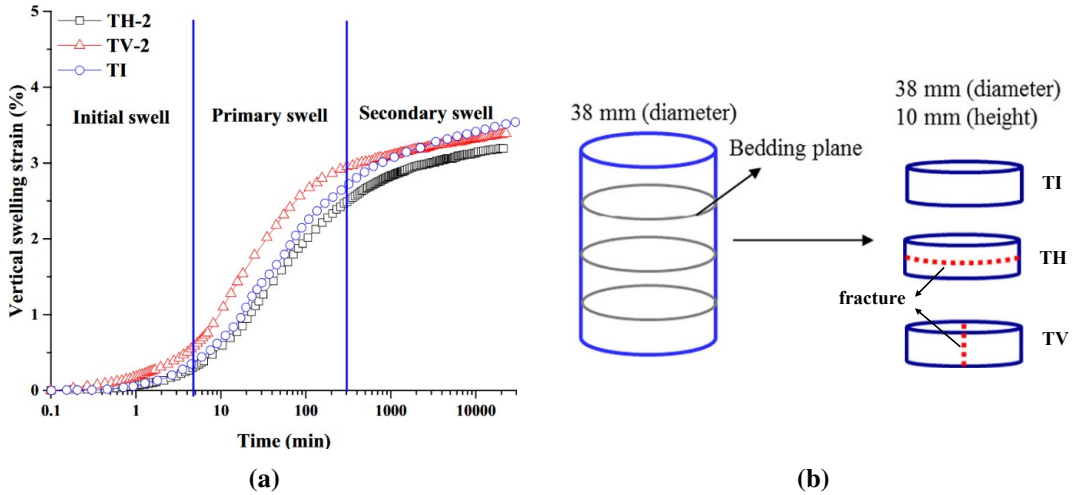

Figure 1.21: (a) Vertical swelling strain versus time for (b) intact sample T1, horizontally fractured sample TH-2 and vertically fractured sample TV-2 from core EST57190 (Wang et al., 2022b).

of parallel cracks, is strongly conditioned by the orientation of the bedding plane and mostly parallel to it. The opening of these fractures contributes to the sealing of the initial fracture. For sample V3132, with the fracture quite perpendicular to the bedding, the network of cracks was much less dense and had a lower reclosing efficiency. However, Agboli et al. (2024) found that the self-sealing process was comparably effective in both parallel and perpendicular orientations, although samples oriented in parallel to the bedding plane tended to exhibit faster swelling of crack surfaces.

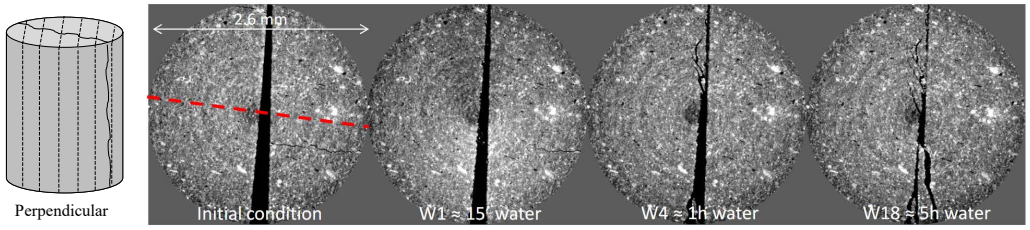

(a) fracture perpendicular to the bedding

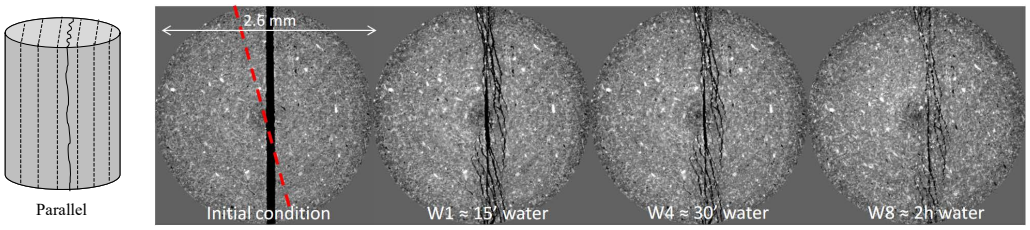

(b) fracture parallel to the bedding

Figure 1.22: X-ray images at different steps during test sample (a) V3132 and (b) V4142 from core EST58102, with the red dotted line showing the orientation of the bedding (Di Donna et al., 2022).

Fracture aperture is another parameter on which researchers are concerned about sealing effectiveness. The study by Auvray et al. (2015) proposed the maximum fracture aperture that can still effectively self-seal. The blockages and swelling of the fracture lips were also clearly visible in the tests carried out on samples with fracture apertures of approximately 400 µm and 100 µm, both for parallel (same as sample V4142 in Fig. 1.22(b)) and perpendicular (same as sample TV-2 in Fig. 1.21(b)) orientations. The results showed that self-sealing was faster in fractures with a 400 µm aperture compared to those with a 100 µm aperture. A possible explanation proposed by the authors is that the larger fracture space can accommodate clay sheets with larger surface areas, which facilitates swelling rapidly. According to previous works ((Auvray et al., 2015; Giot et al., 2019)),

Di Donna et al. (2022) conducted experiments on samples with different fracture apertures ranging between 75 and 490 μm to study the variability of the response. The self-sealing phenomenon stabilized rapidly in small fractures (75 to 150 μm), showing nearly complete closure with almost no visible peeling due to the smaller space for deformation or lower resolution. In samples with larger initial fractures, the peeling effect was much more evident at the same resolution. It also showed that the closure of the main fracture was actually associated with the disintegration of the material and the consequent creation of a network of smaller cracks. Comparing the samples with an initial fracture aperture of 400 μm and 800 μm, with almost the same low carbonate content ($\sim$20%), it was noticed that the smaller the initial fracture aperture was, the faster the water permeability decreased and the faster the closure (Agboli et al., 2024). Indeed, the fracture was more closed in the sample with an initial fracture aperture of 400 μm than in the sample with an initial fracture aperture of 800 μm. The crack volume was significantly reduced in the larger fractured sample, but it never completely closed during the test.

4.3 Effect of external loads

To simulate the EDZ conditions in laboratory tests, the sealing experiment was carried out on a cracked COx sample under external confining pressure (Zhang et al., 2007; Davy et al., 2007; Harrington et al., 2015). Indeed, both confining pressure and swelling, as sealing mechanisms (Bock et al., 2010), reduce permeability and close cracks. The evolution of measured confining pressure (P_c), permeability (K) and crack closure (cc) was analyzed for samples by Davy et al. (2007). Fig. 1.23 showed that the permeability rapidly decreased just after loading the confining pressure, and the curve revealed a linear relationship between K and P_c in the subsequent loading and unloading phases. It observed that the evolution of permeability under confining pressure is irreversible. The curves of crack closure versus permeability for three samples show identical macrocrack elastic loading-unloading phases but different crack closure amplitudes. It also indicates that cracks closed irreversibly under confining pressure and then behaved elastically. Zhang (2016) found the increase of hydrostatic stress closed up the cracks and hence decreased the permeability from two hydrostatic recompaction tests on the cracked samples. Because the subsequent unloading after hydrostatic loading led to some elastic reopening of the cracks without significant reversibility of the permeability, it suggested that parts of the cracks had been permeability closed and disconnected from the pathway.

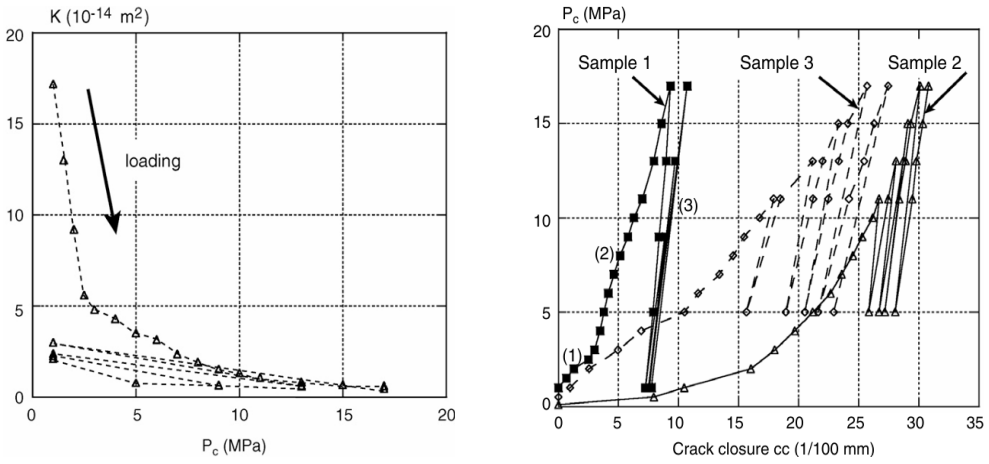

(a) K vs. P_c **(b)** P_c vs. cc

Figure 1.23: Evolution of confining pressure (P_c), permeability (K) and crack closure (cc) (Davy et al., 2007).

Moreover, Zhang and Rothfuchs (2008) performed various sealing experiments to measure gas permeability under confining pressure. The short-term re-compaction by increasing the confining pressure up to 15 MPa reduced the gas permeability from $10^{-14} - 10^{-18}$ m^2 to $10^{-19} - 10^{-20}$ m^2. The comparatively high confining stress resulted in a pronounced plastic closure of the fractures, indicated by the much lower permeability values measured. Furthermore, the high swelling capacity of the clay rocks was also confirmed by tests under low confining stress. The permeability of the cracked sample decreased more significantly to 10^{-21} m^2 under the low confining stress of 1.5 MPa during the water injection period. It noted that the effective closure of fractures mainly is caused by clay mineral and confining pressure. The clay mineral swelling can still lead to the cracked COx claystone resealing to some degree even in the absence of a high level of confinement (Wang et al., 2022a). According to the LLP test called an experiment minimizing the lateral stress on the sample, Wang et al. (2024) observed that the water permeability decreased by 2-3 orders of magnitude from the initial value of $10^{-16} - 10^{-18}$ m^2, but the gas permeability became 0 from the initial value of $10^{-14} - 10^{-16}$ m^2, meaning clay swelling itself can lead to partial recovery of the water permeability, with no possible gas transport until the gas breakthrough occurred. Comparing the water permeability and gas breakthrough pressure (GBP) of initial water-saturated samples before and after re-compaction reveals that loading with 14 MPa confining pressure resulted in a significant new decrease in water permeability, approaching that of intact material, but GBP

increased from 0.3 MPa to 1.2-1.57 MPa, implying that cracks did not disappear and remained privileged gas transport pathways, regardless of the confinement effect.

4.4 Effect of thermal impact

Thermal impact on the sealing process of cracked claystone in the EDZ is one of the most concerns (Zhang et al., 2007; Tsang et al., 2012; Marschall et al., 2017; Zhang, 2018). Temperature influence may affect the long-term safety of HLW repositories. Previous studies have investigated that the diffusive properties of COx claystone did not show any discrepancy between 21°C and 80°C, implying no observable damage to either the pore network system or the sorption properties of clay mineral (Savoye et al., 2011). Taking into account the various thermal loadings, the water permeability of cracked claystone during water flow under confining stress has been examined by Zhang (2011, 2013). As shown in Fig. 1.24(a), the cracked COx sample expanded gradually with time, but the intrinsic permeability decreased dramatically due to the water-induced effect on the hydraulic sealing of cracks during the first stage at 27°C. However, the water permeability decreased rate was less affected by the stepwise heating of the temperature up to 60°C. Further heating up to 90°C and cooling down to 60°C had no or only little effect on the permeability. From the Fig. 1.24(b), it can be more obvious that the permeabilities of the cracked claystone are slightly influenced by the heating and cooling. They decrease more or less with increasing temperature during heating and subsequently drop slightly down with cooling. Combined permeability measurements and tomographic observations (Agboli et al., 2024) revealed that temperature exerts only a slight "delaying effect" on self-sealing. Specifically, the permeability and crack volume decreased slower at 80°C than for the similar test performed at 20°C. These temperature-induced slight changes in permeability is dependent on fluid viscosity and porosity (Chen et al., 2014). In general, temperature ranging from 20°C to 90°C has no remarkable impact on the sealing capacity of cracks, and thermal effects are limited (Monfared et al., 2012; Zhang, 2018), only relevant at higher temperatures during chemical swelling due to changes in the solubilities (Pimentel, 2015). Thus, Zhang (2013) has drawn a key conclusion that thermal loading up to a maximum temperature of 90°C designed for repositories in clay rocks has no negative effects on the sealing process of fractures in the EDZ.

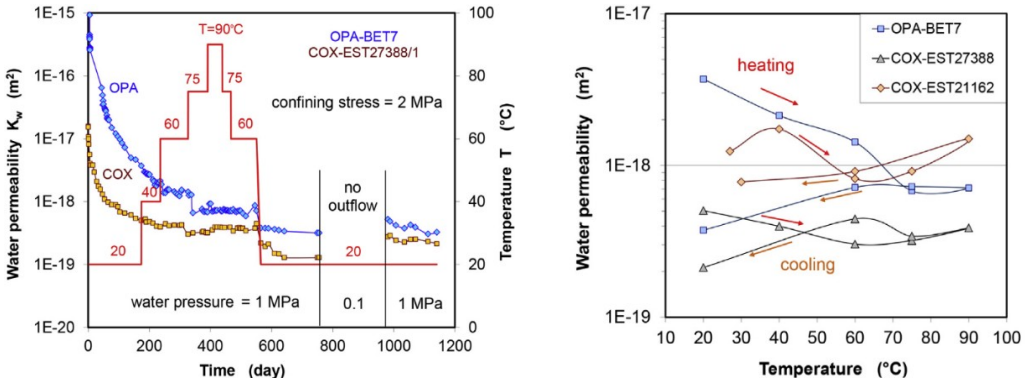

Figure 1.24: Temperature effect on the water permeability of cracked claystone during the self-sealing process: (a) long-term measurements of water permeability at different temperatures and (b) water permeability as a function of temperature (Zhang, 2018).

5 Gas breakthrough pressure: concepts and measurements

In geological disposal of radioactive waste, gases (mainly hydrogen) can be generated as a result of various processes including the radioactive decay of the waste, the radiolysis of water, the anaerobic corrosion of waste canisters and the decomposition of organic materials. If the rate of gas generation exceeds the rate of gas diffusion within the pores of the barrier or host rock, a discrete gas phase will form and accumulate (Wikramaratna et al., 1993; Ortiz et al., 2002; Cuss et al., 2011a; Harrington et al., 2012). This gas accumulation process continues until the gas pressure reaches the critical threshold to enter the surrounding material. It will eventually compromise the sealing ability of the multi-barrier system. Consequently, gas breakthrough pressure (GBP) is one of the key parameters to evaluate sealing efficiency for geological disposal of high-level radioactive waste. It is defined as the minimum gas pressure needed to overcome capillary pressure in the largest pore channel within saturated or partially saturated porous media (Egermann et al., 2006). To better understand breakthrough pressure and how it can be measured, the basic concepts derived from capillary pressure and the review of various experimental methods are introduced in this section.

5.1 Definitions of capillary pressure

Capillary pressure plays a significant role in the migration mechanism in a two-phase flow system. When two immiscible fluids, such as a wetting phase (water) and a non-wetting phase (gas), come into contact within the pore space of a rock, a pressure difference is generated at their interface due to interfacial tension (IFT) (Hassler and Brunner, 1945). This pressure difference is referred to as capillary pressure (Purcell, 1949). Put another way, capillary pressure is the resistance of the gas phase to penetrating a porous medium in the presence of a wetting fluid (Rezaeyan et al., 2015). The capillary pressure is related to the pore throat radius, interfacial tension and fluid phase properties. It can be given by Laplace's law (Washburn, 1921a,b)

$$P_c = P_g - P_w = \frac{2\sigma \cos\theta}{r} \tag{1.6}$$

where P_c denotes the capillary pressure, P_g represents the pressure of the non-wetting phase (gas), P_w is the pressure of the wetting phase (water), σ is the interfacial tension between the non-wetting phase and the wetting phase, r is the equivalent radius of the pore throat, and θ is the contact angle (CA) of the gas-liquid-solid system.

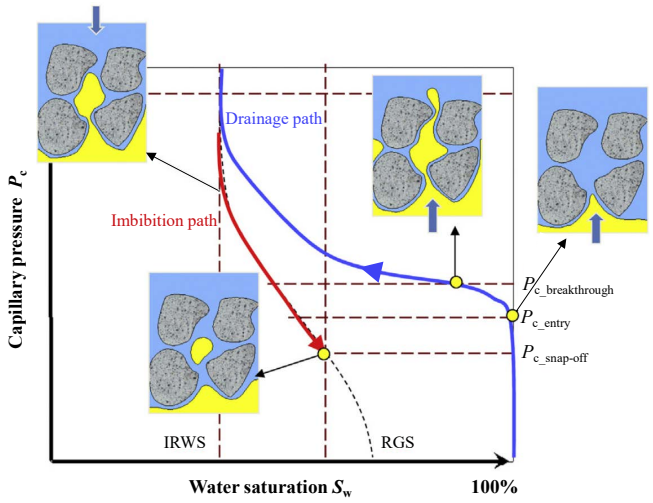

Figure 1.25: Conceptual sketch of capillary pressure (P_c) as a function of water saturation (S_w) for saturated rock (IRWS denotes irreducible water saturation, RGS means residual gas saturation) (Hildenbrand et al., 2002; Busch and Amann-Hildenbrand, 2013).

The capillary pressure has been referred to by several terms in the literature, including snap-off pressure ($P_{c_snap\text{-}off}$), breakthrough pressure ($P_{c_breakthrough}$), and entry pressure

($P_{\text{c_entry}}$). The precise definition of these terms varies depending on the author and the experiments carried out. A good perspective can be found by Hildenbrand et al. (2002); Amann-Hildenbrand et al. (2013); Wu et al. (2020). The capillary pressure curve in Fig. 1.25 provides a clearer understanding of all these concepts. Capillary pressure is path-dependent, involving an imbibition path where the wetting phase displaces the non-wetting phase and a drainage path where the non-wetting fluid displaces the wetting fluid. In the imbibition experiments, water saturation gradually increases as capillary pressure decreases until the snap-off pressure occurs where the last interconnecting capillary is sealed. $P_{\text{c_snap-off}}$ is the capillary pressure where the water phase obstructs the gas flow path. During the drainage process, the gas phase starts to displace water from the largest capillary when $P_{\text{c_entry}}$ has been overcome. $P_{\text{c_entry}}$ is the differential pressure at which a gas phase starts to penetrate a water-saturated rock (Marschall et al., 2005; Boulin et al., 2013). With further increasing capillary pressures, the gas phase will break through at the outlet of the sample ($P_{\text{c_breakthrough}}$) and be detected. At this stage, the first interconnected path for the gas flow is generated across a rock body. Subsequently, gas flow depends on the capillary pressure, with the higher the pressure difference, the higher the gas saturation and the effective permeability to the gas phase (Amann-Hildenbrand et al., 2012). Finally, the irreducible water saturation (IRWS) is reached. In general, the drainage breakthrough pressure is higher than the imbibition snap-off pressure (Amann et al., 2011).

5.2 Methodology for gas breakthrough pressure

Understanding and accurately measuring the breakthrough pressure of host rock are essential for evaluating its sealing efficiency and storage capacity. If measured breakthrough pressure is underestimated, there is a potential risk that radiolytic gases may penetrate the caprock, thereby compromising the integrity of the storage system and raising potential environmental concerns. The experimental methods for measuring breakthrough pressure can be broadly classified into two categories: indirect and direct methods (Egermann et al., 2006; Amann et al., 2011; Busch and Müller, 2011; Boulin et al., 2013; Chen et al., 2024).

Mercury injection porosimetry (MIP) is the most widely used indirect method. It was first proposed by Washburn (1921b) to measure the pore size distribution of porous media through mercury injection experiments (Mayer and Stowe, 1965), and later extended to estimate breakthrough pressure, especially when core samples are not available and only

cuttings are available (Wen et al., 2023; Soomro et al., 2025). In MIP tests, the mercury capillary pressure curves, which show the cumulative intrusion volume of mercury into the porous rock as a function of pressure on a logarithmic scale, could be used to estimate the percolation threshold (Schlömer and Krooss, 1997). However, the application of MIP for breakthrough pressure determination is subject to several limitations, including the consideration of surface roughness correction, the conversion from Hg-air to the gas-water system by assuming contact angle and surface tension values, the inability to account for breakthrough pressure anisotropy, and the impossibility of conducting under in-situ stress (Dewhurst et al., 2002; Egermann et al., 2006; Amann-Hildenbrand et al., 2013).

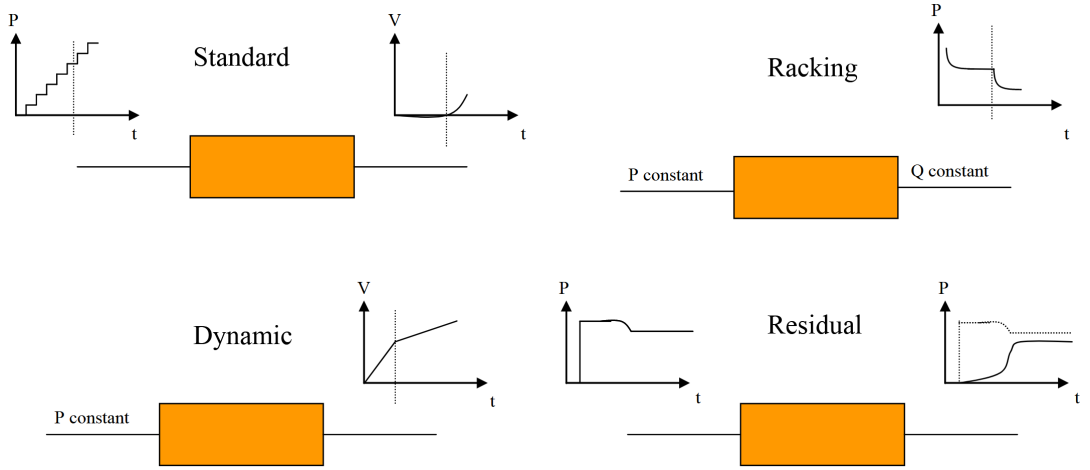

Figure 1.26: Scheme description of four direct breakthrough pressure measurement methods (P, V and Q represent pressure, cumulative water volume and flow rate, respectively) in Boulin et al. (2011).

The most commonly used measurement technique is currently direct methods, seen in Fig. 1.26, mainly including the step-by-step method, the residual capillary pressure method, the dynamic method, and the racking method (Pusch et al., 1985; Horseman et al., 1999; Zhang and Talandier, 2023). Among them, the step-by-step method, proposed in Thomas et al. (1968), is the standard approach for breakthrough pressure measurement by increasing the non-wetting phase (gas) pressure stepwise at the upstream of sample while monitoring the downstream pressure for breakthrough (Tanai et al., 1996). Prior to the testing, the rock sample is subjected to a specific water saturation level, and then gas is injected from the inlet either stepwise through constant-pressure or constant-volume control mode. When gas flow is first detected in the outlet, the pressure difference between the upstream and downstream sides is determined as the gas breakthrough pressure. It

should be noted that this method is time-consuming for low-permeability materials, and the measured value is somewhat dependent on the chosen pressure increment, usually leading to an overestimation of the real breakthrough value (Ito et al., 2011).

The residual pressure method was first proposed by Hildenbrand et al. (2002) for non-steady-state experiments after re-imbibition of the wetting phase (see Fig. 1.25). This method determines the breakthrough pressure based on the differential pressure between the upstream and downstream sides of the sample, where upstream pressure changes differently under constant-pressure or constant-volume conditions. Previous studies have observed that the breakthrough pressures obtained by the residual pressure method are generally lower than those measured by other methods on the same specimens (Boulin et al., 2013). In addition, the duration of this approach ranges from several hours to weeks, depending primarily on the sample conductivity and the initial pressure difference (Amann-Hildenbrand et al., 2012).

The dynamic method, first applied to a brine-saturated sample by Egermann et al. (2006), injected gas with a constant pressure difference higher than the breakthrough pressure. The pressure difference corresponding to the transition point between the single-phase flow rate and the two-phase flow rate is used to determine the entry pressure. This method usually takes a few days, but the measured value may be overestimated because the applied pressures are higher than the threshold pressure (Busch and Müller, 2011).

The racking method is similar to the dynamic approach, but with the difference that a high-precision syringe pump is connected to the downstream to extract water at a constant flow rate (Meyn, 1999). The upstream is linked to gas resources. When gas starts to come into the sample surface, pore pressure is still too high to allow gas to enter the sample. Due to the constant flow rate extracted by the pump, the downstream pore pressure starts to decrease, with pore pressure within the sample decreasing. When pore pressure comes low enough to permit gas penetration, gas displaces water until downstream stops decreasing. This downstream pressure drop identifies the entry pressure, as shown in Fig. 1.26. Compared with the dynamic method, this method generally takes longer (Wu et al., 2020). Boulin et al. (2013) suggested that the racking method is difficult to use in low permeability rocks, perhaps due to leakage. Given that each of these methods has its advantages and limitations, it is critical to choose an appropriate method, comprehensively considering factors such as accuracy, duration and in situ representativeness.

With regard to COx claystone, the step-by-step method is currently the most represen-

tative and widely used approach for investigating gas migration behavior in situ, and its adequacy has been validated (Zhang and Rothfuchs, 2008; Song et al., 2015a; Wang et al., 2022a). It allows identification of two typical gas migration modes at the sample outlet, namely discontinuous and continuous breakthrough (Liu et al., 2015). Previous studies have shown that gas passage occurs first by discontinuous capillary passage named snap-off, followed by continuous gas breakthrough whenever its pathway builds up sufficiently, known as permeation (Hildenbrand et al., 2002; Davy et al., 2013). This discontinuous gas migration has been experimentally confirmed on low-permeability claystone, and its mechanism may be attributed to either capillary snap-off (Rossen, 2000) or unstable dilatant pathways (Harrington et al., 2017). As mentioned previously, the pressure difference between the upstream and downstream when gas flow is formed in the outlet is recognized as the breakthrough pressure in the conventional method.

In contrast, some researchers define the gas injection pressure corresponding to the first appearance of continuous gas flow or gas bubbles at the outlet as the gas breakthrough pressure (Zhang, 2015; Liu et al., 2018a). Specifically, M'Jahad et al. (2017) progressively increased the argon injection pressure in steps of 0.5 MPa under constant confining pressures of 6 MPa and 12 MPa and identified the injected pressure when continuous gas flow was detected at the downstream. The relatively low breakthrough pressure was mainly attributed to a state of damage in the sample and the limited water saturation time. Zhang and Talandier (2023) further adopted smaller stepwise increments of 0.1-0.2 MPa per day to measure the inlet injection pressure corresponding to the first appearance of gas bubbles at the outlet, which was then taken as the breakthrough pressure. In addition, Wang et al. (2024) analyzed the gas breakthrough pressure of sealed COx sample before (lateral pressure of 0.5 MPa) and after re-compaction (lateral pressure of 14 MPa) to examine the effect of confining pressure on gas migration behavior. The results showed that the breakthrough pressure of sealed sample was around 0.3 MPa, whereas it increased to 1.2-1.57 MPa after re-compaction. This conclusion is in accordance with the studies of Zhang (2015), indicating that crack did not disappear and remained a privileged gas transport pathway regardless of the confinement effect. It is worth noting that gas breakthrough is possible in claystones at gas pressures much lower than confining pressure. In Table 1.2, gas breakthrough pressure for COx claystone is summarized, providing a reliable experimental basis for the quantitative evaluation of gas sealing performance of cracked claystone.

Table 1.2
Summary of GBP values on the COx claystone from literature.

Sample	Height (mm)	Initial state	Saturation (day)	P_c (MPa)	K_w (m^2)	GBP (MPa)	Gas	Reference
EST 30341	82	Intact	98	12.5	-	10.5	Helium	Cuss et al. (2014)
EST 28906	77		120	12	-	6		
EST 44140	30	Intact	134	6	6.90E-21	5.2–5.3	Argon	Song et al. (2015a)
EST 44331-1	20	Intact	49	6	2.60E-20	4.38		
EST 44331-2	9.5	cracked	30	6	1.90E-20	2.2		
EST 34386-1	11	macro-cracked	68	6	7.10E-21	2.25		
EST 34386-2	11		63	12	9.34E-21	1.45		
EST 34450	10	Intact	13	12	9.00E-19	0.3	Argon	M'Jahad et al. (2017)
EST 34394-4			13	12	1.50E-20	0.6		
EST 34394-6			6	6	2.30E-20	0.4		
EST 58123	40	Intact	-	12	-	5.5	Nitrogen	Chen et al. (2022)
EST 58145-3	40	Intact	15	4	1.24E-20	6.2–6.4	Argon	Wang et al. (2022a)
EST 58145-1			12		3.72E-20	1.0–1.23		
EST 57903		cracked	20		7.44E-20	0.8–0.89		
EST 58128			8		4.67E-20	1.3–1.46		
EST 52335-5	300	macro-cracked	-	4	3.00E-19	1.1	Helium	Zhang and Talandier (2023)
EST 52337-6	280		-		3.00E-19	1.2		
COx4	50	macro-cracked	>3 years	2	7.00E-21	1.0	Nitrogen	Zhang (2015)
		re-compacted		3	-	1.2		
		re-compacted		5	-	2.5		
		re-compacted		10	-	4.8		
EST 62665-1	40	cracked	18	0.5	2.48E-19	0.27	Argon	Wang et al. (2024)
		re-compacted	-	14	4.80E-20	1.2		
EST 62665-2	40	cracked	55	0.5	1.24E-19	0.3		
		re-compacted	-	14	6.10E-21	1.57		

6 Microstructure observation in cracked claystone

Microstructural studies of cracked claystone have provided valuable insights into crack formation, self-sealing behavior, and fluid transport mechanisms. Traditional imaging techniques, including scanning electron microscopy (SEM) (Keller et al., 1986; Wang et al., 2013), environmental scanning electron microscopy (ESEM) (Wang et al., 2015; Ghazy and Bassuoni, 2017), transmission electron microscopy (TEM) (Németh et al., 2016) and focused ion beam microscopy (Keller et al., 2011; Song et al., 2015b), have been widely utilized to investigate crack evolution, pore structures and mineralogical changes in claystone formations (Keller et al., 2013; Desbois et al., 2017). However, the sample preparation required for these techniques, such as cutting, grinding, polishing and high vacuum testing, can irreversibly induce microstructure. Moreover, none of these techniques track 3D visualization of the microstructure or quantitative information about the spatial distribution of its constituents throughout the total experimental process. X-ray computed tomography (XCT), by contrast, enables in-situ analysis with minimal sample preparation while delivering high-resolution, non-destructive 3D images (Cnudde and Boone, 2013; Keller and Giger, 2019; Ghazy and Bassuoni, 2017). A typical XCT setup consists of three main components: an X-ray source, a detector and a sample stage (see Fig. 1.27). Owing to the ability of X-rays to penetrate dense, opaque materials, XCT is particularly well studied for the investigation of clay-rich rocks.

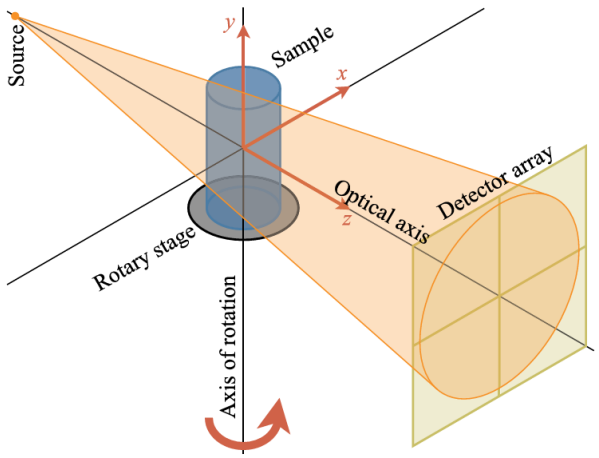

Figure 1.27: A typical cone-beam tomography setup (Brisard et al., 2020).

The early applications of X-ray computed tomography for rock research primarily fo-

cus on quantifying structural changes before and after testing (Kawakata et al., 1997). Initial studies utilized image segmentation and statistical analysis to extract key parameters such as volume fraction, spatial distribution and microstructural features, establishing relationships between structural changes and physical parameters. With the improvement of spatial resolution, X-ray micro-tomography has enabled high-resolution imaging of internal rock microstructures, significantly improving the ability to investigate damage evolution and crack propagation (Shi et al., 2021, 2023). XCT is now capable of resolving features at the microscale, while X-ray nanotomography and synchrotron-based techniques provide even higher resolution, allowing visualization at the nanometer scale (Hao et al., 2023). In addition, combined X-ray tomography and neutron radiography have been used to investigate the mechanisms of water uptake in COx clay-rocks, enabling the quantification of sample deformation, crack growth and water absorption (Stavropoulou et al., 2019).

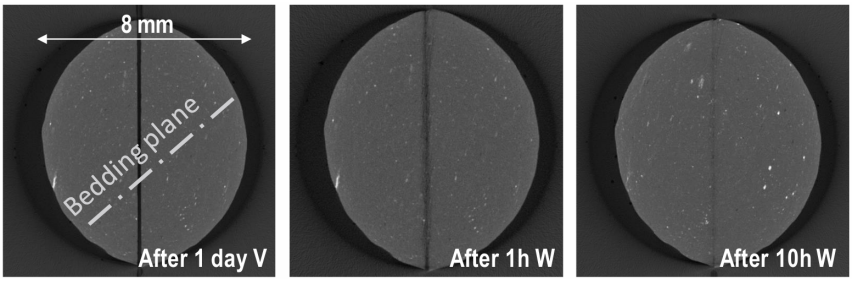

(a) test 4142 (UA), resolution 13.5 μm

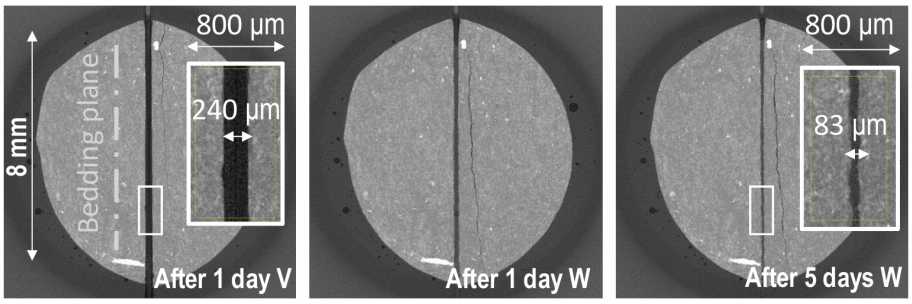

(b) test AV1112 (UT), resolution 7 μm

Figure 1.28: X-ray images at different steps during (a) test 4142 (UA), resolution 13.5 µm); (b) test AV1112 (U.T.), resolution 7 µm) (Di Donna et al., 2019).

All of these methods could capture the micro-cracking phenomenon due to water injection. Through the analysis of 2D images from X-ray tomography, as shown in Fig. 1.22, Di Donna et al. (2019, 2022) conducted some experiments on the clay unit

(UA) COx and the transition unit (UT) COx with different fracture sizes and mutual orientation of the bedding plane and fractures. The image evolution of the pre-cracked UA samples V3132 and V4142 during water injection is shown at a voxel size of 0.7 µm in Fig. 1.22. Compared to the images of UA sample 4142 under 13.5 µm resolution (see Fig. 1.28(a)), two phenomena were observed with a high voxel size of 0.7 µm: a peeling phenomenon in the area adjacent to the crack inducing filling of the main crack and a diffuse swelling around the peeling zone inducing the sealing of the main crack. The UA samples were richer in smectite clay, while UT samples were richer in carbonates. Even with the higher resolution image, the crack in the UT sample was not completely closed, though a modest closure was observed. X-ray nanotomography imaging has demonstrated that during water saturation, the crack volume of the UA sample significantly decreases in Fig. 1.29, leading to a corresponding reduction in permeability (Giot et al., 2019). This phenomenon exhibits the significant self-sealing characteristic whereby cracks progressively close due to clay mineral swelling and particle rearrangement, thus gradually reducing pore connectivity and restricting fluid migration.

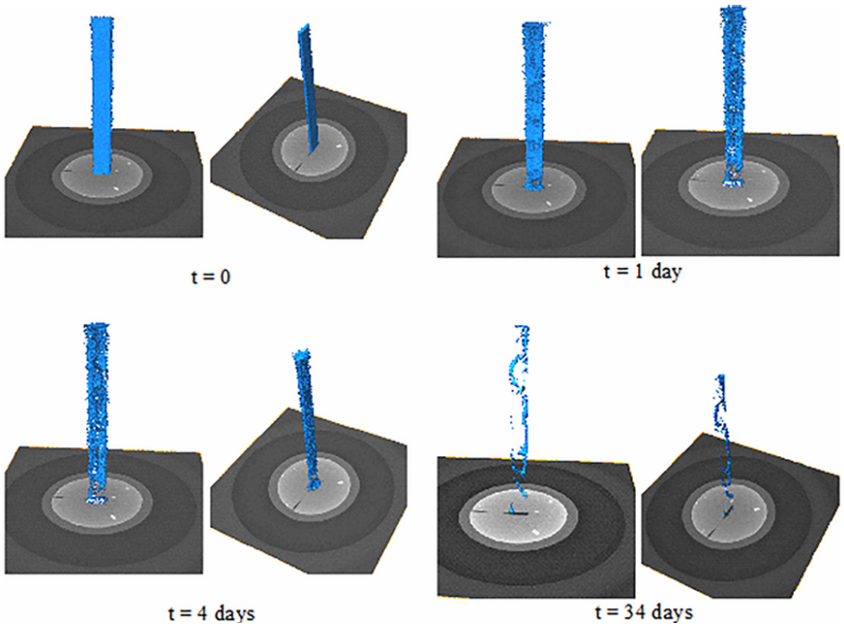

Figure 1.29: The evolution of crack volume in COx claystone (UA sample) by 3D tomography (Giot et al., 2019).

Based on this, Agboli et al. (2024) studied the evolution of crack volume using 3D X-ray images, as illustrated in Fig. 1.30, to characterize the self-sealing process under different and complex conditions. This provided the first comprehensive assessment of

the effects of temperature, calcite content, sample orientations, and initial crack openings. Regardless of the experimental conditions, self-sealing was always an effective mechanism when the clay content was high enough.

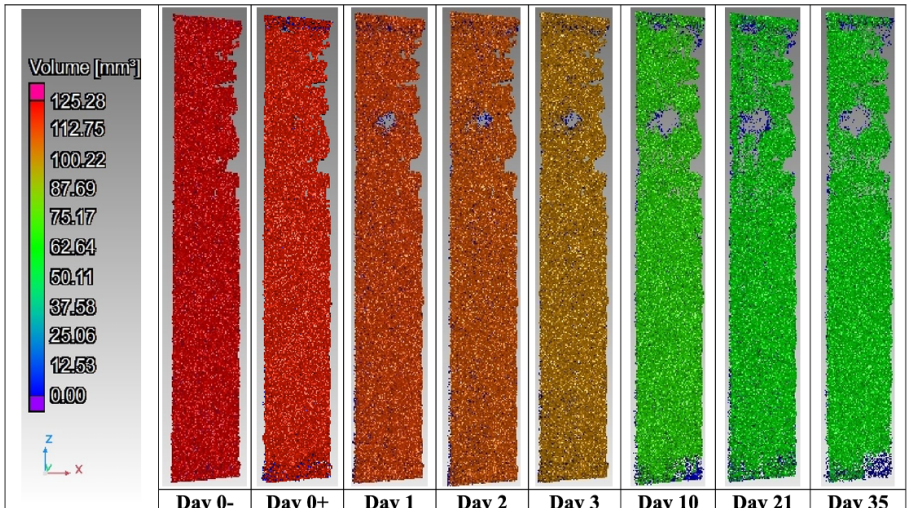

	Day 0-	Day 0+	Day 1	Day 2	Day 3	Day 10	Day 21	Day 35
Volume (mm^3)	67.7	64.9	62.1	60.2	55.8	38.5	34.2	33.5
$\%CaCO_3$	32							

Figure 1.30: X-ray 3D tomography images of parallel sample EST63744-7 showing the evolution of the crack volume with time during a self-sealing test at 20 °C (Agboli et al., 2024).

7 Conclusion

This chapter presents a short summary of the geological distribution, mineralogical composition, microstructural characteristics, and fluid transport properties of Callovo-Oxfordian claystone, with a focus on experimental studies investigating the self-sealing behavior of cracked claystone. The evolution of crack closure is thoroughly investigated by combining macroscopic responses such as permeability and swelling pressure with internal observations obtained through imaging techniques. The effects of crack geometry, orientations, and sizes, as well as external stress conditions and coupled thermo-hydromechanical processes on self-sealing behavior, are thoroughly described. In addition, gas breakthrough pressure, an important indicator for evaluating the sealing performance of cracked COx claystone, has been extensively discussed in the literature with respect to its definition, testing methods, and breakthrough values. The following key conclusions can be drawn.

COx claystone is classified into three main units based on depositional environment

and mineralogical characteristics: UA, UT, and USC. The clay mineral content and pore structure of these units vary significantly. These mineralogical and microstructural characteristics have a significant impact on the self-sealing behavior of COx claystone. Numerous studies have demonstrated that water-induced swelling causes microstructural reorganization, with the swelling potential being primarily determined by clay mineral content, particularly smectite and illite-smectite minerals.

Laboratory studies indicate that the self-sealing process of cracked claystone is mainly characterized by a progressive decrease in permeability and crack closure driven by water-induced swelling. During resaturation, the permeability of cracked samples gradually decreases over time and may eventually reach values comparable to those of intact samples once cracks are fully closed, typically in the range of 10^{-20} to 10^{-21} m^2. Increasing confining pressure also promotes crack closure and accelerates the reduction in permeability.

Crack geometry, orientation and opening are widely acknowledged as critical factors influencing the efficiency and temporal evolution of self-sealing. X-ray imaging reveals that small cracks (75 to 150 μm) typically close completely during resaturation, without visible wall peeling. In contrast, samples with larger crack openings (400 μm) more frequently exhibit crack wall peeling, fine-particle migration and clogging. For even larger apertures (800 μm), crack closure is significantly slower, with the time required to achieve complete closure significantly extended. Several studies have found that cracks oriented parallel to bedding planes have faster swelling responses and higher closure efficiency.

However, these experiments have primarily focused on scenarios where water directly infiltrated fractures, while the impact of alternative infiltration pathways (such as water first diffusing through the intact matrix before reaching the fracture) on the self-sealing process of claystone has not been sufficiently studied. The direct infiltration pathways may enhance water-fracture interactions while also causing more local swelling and clogging effects, differing from in situ conditions in which partial water gradually infiltrates fractures through the surrounding rock matrix or interfaces. Furthermore, previous research has focused on self-sealing behavior in the presence of confining stress and hydration, with little attention given to the independent contribution of matrix swelling to fracture closure. In view of these limitations, our research will investigate fracture evolution under varying infiltration pathways by designing and implementing self-sealing tests at the laboratory scale under indirect water injection conditions.

CHAPTER 2

Hydro-mechanical behavior of intact and cracked COx claystone

1 Introduction

Callovo-Oxfordian claystone is considered a potential host rock for geological disposal of radioactive waste due to its low permeability, good geological condition and suitable mechanical properties (Armand et al., 2013, 2017b). During the different stages of geological disposal of radioactive waste, the host rock is subjected to coupled mechanical loading, pore water flow, temperature change and gas transfer. In particular, damaged zones can be created by excavation of borehole and gallery (Tsang et al., 2005; Armand et al., 2014; Bossart et al., 2004). The permeability inside such excavation-induced damaged zones can be increased by several orders of magnitude (de La Vaissière et al., 2015; Hale et al., 2021; Agboli et al., 2024). The presence of such excavation-damaged zones affects both short and long term thermo-hydromechanical responses of host rock and sealing systems. Therefore, it is essential to evaluate the evolution of mechanical and transport properties of these damaged zones.

Due to the presence of clay minerals, clay-rich rocks can exhibit an important swelling deformation upon hydration. Therefore, it is of great interest to investigate the contribution of swelling deformation to progressive sealing of excavation induced cracks in clayey rocks. In order to investigate its swelling process, different experimental methods are proposed, such as swelling-consolidation, constant-volume swelling, mechanical loading-wetting coupling and hydric cycling (Sridharan et al., 1986; Villar and Lloret,

2008; Wang et al., 2012; Cui et al., 2013). Concerning the COx claystone considered in this work, it is composed of around 50% clay minerals and exhibits an important swelling potential (Robinet et al., 2012; Conil et al., 2018). Several experimental studies have been conducted to investigate its swelling deformation and self-sealing process. It mainly consists of measuring swelling strain and swelling pressure upon water injection. For example, different measuring methods of swelling pressure have been tested and compared (Zhang et al., 2020). In order to reproduce in situ swelling conditions, one special setup with a calibrated tube instrumented with strain gauges was designed for evaluating swelling kinetics and pressure (Davy et al., 2009; Liu et al., 2014). Due to the high rigidity of the metallic tube preventing the sample from confining pressure effects, that setup provides an accurate assessment of swelling behavior. Previous studies have found that cracked samples exhibit a slightly lower swelling pressure than intact samples (Wang et al., 2022a). The swelling deformation is clearly anisotropic due to the presence of bedding planes in the COx clayastone (Zhang et al., 2010; Yang et al., 2013).

An efficient way to evaluate the contribution of swelling deformation to self-sealing of fractures is measurement of permeability evolution during hydration. In general, there is a clear correlation between permeability decrease and self-sealing of cracked zones (Bock et al., 2010; Wang et al., 2022a, 2024). For example, samples with a preexisting fracture are widely tested. Water is directly injected into preexisting fracture, leading to rapid hydration of rock layers located around fracture walls. Due to swelling of clay minerals and possible particles deposit, preexisting fracture is progressively closed leading to a strong reduction in permeability (Giot et al., 2018). Despite large variability of tested samples, with different values of preexisting fracture aperture, initial water content and clay fraction, the overall permeability of fractured sample after water saturation is generally close to that of intact sample (Giot et al., 2019; Di Donna et al., 2019).

Based on these observations, this chapter aims to further investigate the swelling-driven self-sealing behavior of COx claystone under water infiltration. A dedicated experimental device is developed to monitor the self-sealing behavior of both intact and fractured samples while limiting the influence of external confinement. The evolution of water permeability and apparent swelling pressure is monitored. By comparing cracked and intact samples, the mechanisms controlling swelling-induced sealing and their impact on the hydro-mechanical integrity of COx claystone are further elucidated, with implications for the assessment of repository safety functions.

2 Materials and experimental equipment

2.1 Sample preparation

The claystone cores used in this study are collected from the Callovo-Oxfordian formation at the Bure Underground Research Laboratory (URL) operated by the French national agency for radioactive waste management (Andra). These cores designated by EST62665, EST67288, EST66747 and EST70903, are taken from horizontal boreholes in the unit A (denoted as UA) at a depth of around 490 m. The size of the original cores is around 300 mm in length and 75 mm in diameter, as shown in Fig. 2.1. Triple-tube core drilling with compressed air cooling is utilized and the samples are recovered in plastic tubes and immediately wrapped in vacuum-evacuated aluminum foil. From each original core, several cylindrical samples are retrieved in the parallel direction to the bedding planes marked with red arrows. Samples are wrapped in plastic film and sealed in vacuum bags to minimize the desaturation. The obtained samples are of a diameter of 37 mm and a length of 20 mm.

After coring, and before testing, the initial water content of different samples is measured through oven drying at 105°C for 48 h. The obtained values are summarized in Table 2.1. The water content of most samples is approximately 7%, whereas samples from EST 62665 exhibit a noticeably lower value of 4.9%. It should be noted that this sample (EST 62665) is partially desaturated and micro-cracked due to the effect of core retrieval, laboratory storage and re-coring. For reference, the in situ water content of COx formation at the Bure URL typically ranges between 6% and 8% within

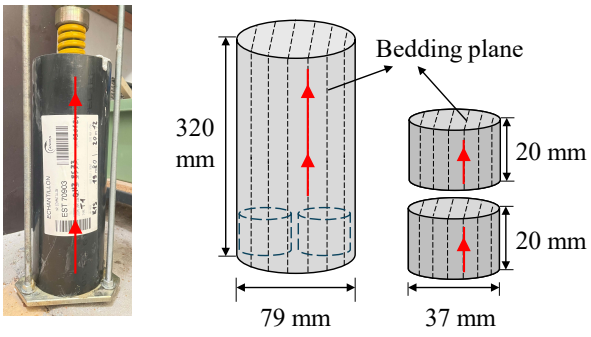

(a) original core (b) cored sample

Figure 2.1: Steps of the sample preparation: (a) original core; (b) cored sample.

Table 2.1
Size and initial water content of tested samples.

Samples Reference		Diameter (mm)	Height (mm)	Initial Water Content (%)
S0 (EST 67288-1)	S0-C	36.64	19.87	7.35
	S0-S	36.56	20.02	
S1 (EST 67288-2)	S1-C	36.42	20.87	7.35
	S1-S	36.48	19.93	
S2 (EST 62665-Wang)	S2-C	37	20	4.9
	S2-S	37	20	
S3 (EST 67288-3)	S3-C	36.38	20.07	7.23
	S3-S	36.11	20.14	
S4 (EST 66747-1)	S4-C	36.57	20.23	6.75
	S4-S	36.65	20.15	
S5 (EST 70903)	S5-C	36.43	20.11	6.91
	S5-S	36.39	20.05	

Note: All the samples are drilled along the parallel direction to bedding planes

the UA (Di Donna et al., 2022). The mineralogical compositions of UA cores consist of clay minerals (40∼50%), carbonates (21∼30%) and quartz (27∼29%). The clay minerals can be subdivided into illite-smectite mixed layers (36∼45%), chlorite (1∼2%), and kaolinite (2∼3.5%). Among them, the smectite is known as the most swelling-sensitive mineral in the illite-smectite mixed layers. Quantitative X-ray diffraction shows that the smectite content in the typical UA cores varies only slightly, in the range of 11∼13.5% (Wang et al., 2022a). Based on this, we assume that the effects of mineral compositions among the UA cores at the same depth are negligible. In order to limit possible chemical reactions, a synthetic water with a composition close to the in-situ pore water is used to saturate samples and its main components are presented in Table 2.2.

Table 2.2
Chemical composition of the synthetic water from ANDRA.

Components	NaCl	$NaHCO_3$	KCl	$CaSO_4 \cdot {}_2H_2O$	$MgSO_4 \cdot {}_7H_2O$	$CaCl_2 \cdot {}_2H_2O$	Na_2SO_4
Mass (g/L)	1.950	0.130	0.035	0.630	1.020	0.080	0.700

Note: The salt used to prepare the synthetic water is provided by ANDRA.

2.2 Mock-ups design

To simulate water infiltration, three mock-up models were designed, as shown in Fig. 2.2. Mock-up I consisted of a combination of an intact sample and a cracked sample, each measuring 20 mm in height and 37 mm in diameter. Mock-up II consists of two "stainless steel tube-epoxy-sample" composites (Wang et al., 2022a, 2024) designed to prevent the sample from external confining pressure interference. Each steel tube is 20 mm in height and 65 mm in diameter, providing a rigid kinematic constrained condition for tested samples. The samples are carefully positioned at the center of the steel tubes and fixed with epoxy resin. The solidified resin has excellent adhesion, impermeability, and compressibility, ensuring that no water or gas can flow through it during measurements while maintaining a reliable and effective seal. A layer of insulation tape is wrapped around the sample surfaces to keep the liquid epoxy resin from contacting the samples. It is noticed that with this designed mock-up, the swelling pressure of tested samples is indirectly measured by the normal force applied onto the inner surfaces of steel tubes. For this purpose, two strain gauges are glued symmetrically on each tube's external surface to measure the deformation of each tube due to swelling of samples. In order to enhance the sensitivity and accuracy of the swelling pressure measurements, artificial fractures were oriented as parallel as possible to the strain gauge.

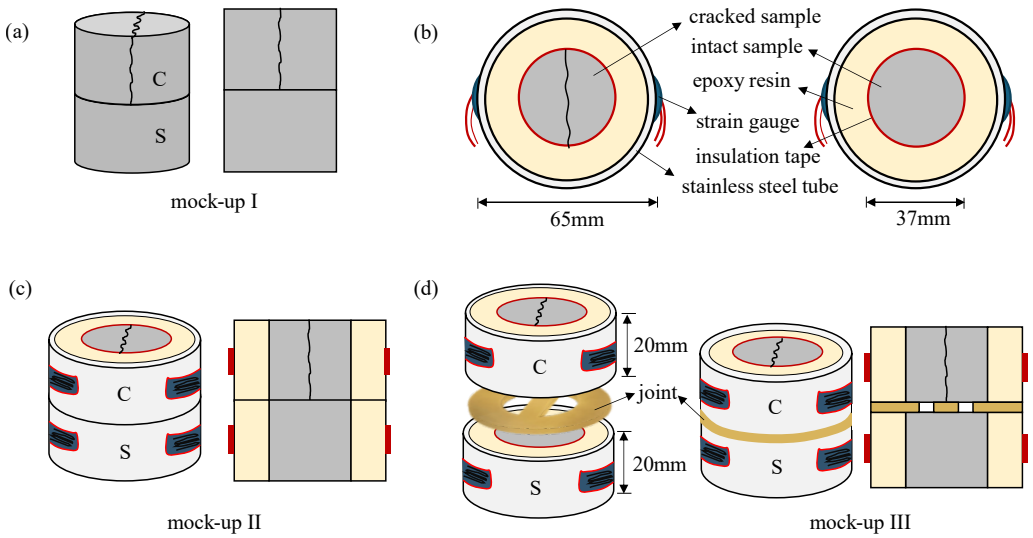

Figure 2.2: Designed mock-ups: (a) schematic of experimental mock-up I; (b) cross-section of "stainless steel tube-epoxy-sample" composite; (c) schematic of experimental mock-up II; (d) schematic of experimental mock-up III.

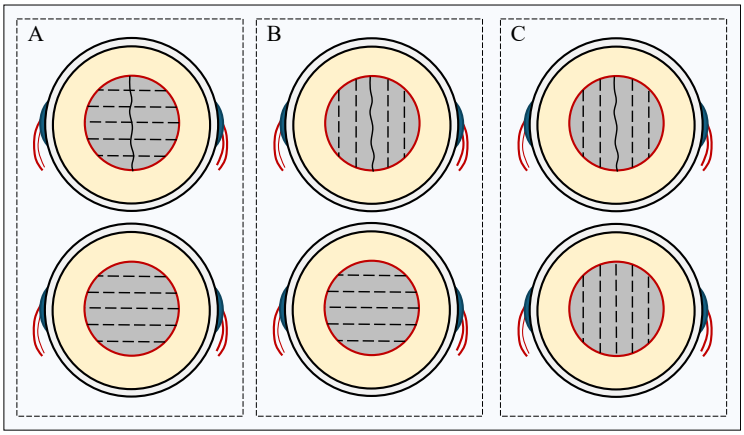

(a)

Mock-ups	Samples reference		Strain gauges orientation	Main fracture orientation in cracked samples	Illustration
mock-up I	S0 (EST 67288-1)	S0-C			
		S0-S			
mock-up II	S1 (EST 67288-2)	S1-C	⊥	⊥	A
		S1-S	⊥		
	S2 (EST 62665-Wang)	S2-C	⊥	⊥	A
		S2-S	⊥		
mock-up III	S3 (EST 67288-3)	S3-C	⊥	⊥	A
		S3-S	⊥		
	S4 (EST 66747-1)	S4-C	∥	∥	B
		S4-S	⊥		
	S5 (EST 70903)	S5-C	∥	∥	C
		S5-S	∥		

(b)

Figure 2.3: Orientations of strain gauges and main fractures: (a) three assembled configurations (Schemes A-C), (b) summary of orientations for each sample. Orientations are defined with respect to the bedding planes, where ⊥ for perpendicular and ∥ for parallel.

Mock-up III consists of two composites and an impermeable joint sheet designed to prevent direct water injection into preexisting main fracture. In this configuration, the joint is placed between the intact sample and the cracked sample, featuring two symmetric channels within the joint. This joint is fabricated with high-quality latex, known for its exceptional waterproof performance, elasticity, and durability. These properties allow it to maintain structural integrity under pressure, ensuring a reliable and effective seal. With the help of the joint, after passing through the intact sample, water could only enter the

cracked sample through the two designated channels, effectively preventing direct water penetration into the preexisting fracture. After the assembly of two parts, the silicone is applied around the exterior surfaces around the connecting zone between two steel tubes, preventing water leakage from this zone.

In this study, mock-ups are specifically designed to investigate the orientation influence of bedding plane and fracture on swelling pressure measurements. The detailed characteristics of tested samples are summarized in Table 2.1 and Fig. 2.3. The orientation refers to the relative direction between the bedding planes and the strain gauges. Among these, the strain gauges of samples S1, S2 and S3 are oriented perpendicularly to the bedding planes, whereas those of sample S5 are aligned parallel to the bedding planes. For sample S4, two conditions are considered: the strain gauges of cracked sample S4-C are arranged parallel to the bedding planes, while those of intact sample S4-S are perpendicular to the bedding planes. In all cracked samples, the strain gauges are glued symmetrically on the tube surface and consistently parallel to the fracture. In the cracked sample, a through artificial fracture is generated using Brazilian splitting test (Davy et al., 2007; Wang et al., 2022a). Prior to splitting, the bedding plane is marked to identify the fracture orientation, as shown in Fig. 2.4 and the sample is wrapped with insulation tape to maintain its intact and to avoid further damage during loading. After splitting, the fracture morphology is observed with a Keyence digital microscope (KEYENCE VH-Z100UR). The fracture aperture ranged from approximately 100 μm to 150 μm. The orientations of strain gauges and main fractures for each tested sample are summarized in Fig. 2.3.

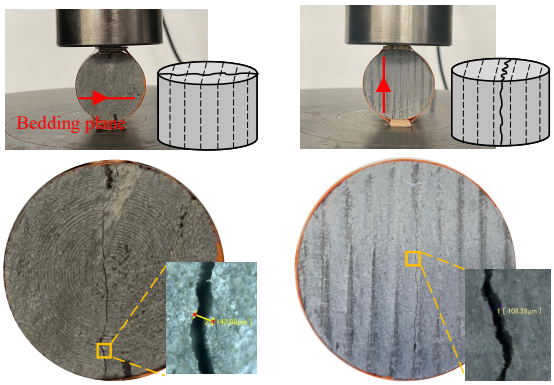

Figure 2.4: Cracked samples prepared for Brazilian tests, (a) perpendicular to the bedding plane; (b) parallel to the bedding plane.

2.3 Tube calibration

In this composite, the swelling pressure of samples can be transformed using the relationship between inner pressure and circumferential strains. This relationship is established by calibrating two instrumented tubes. To this end, before assembling this composite, a set of cyclic tests is conducted by increasing and decreasing inner pressure and measuring circumferential strains. It is noted that the silicone is applied around the exterior of the steel tube to seal it, preventing gas leakage at the connection. In order to evaluate the effect of external confining pressure, such tests are performed under confining pressure P_c of 4 to 8 MPa. It provides a relationship between the inner pressure (P_{inner}), imposed by injecting gas at various pressures inside it, and the average strain $\varepsilon = (\varepsilon_1 + \varepsilon_2)/2$ given by the two gauges on one tube surface. The thin-walled tube theory proposes that the radial stress (σ_{rr}) can be ignored when the thickness is much less than the inner radius of the tube. The theoretical strain values for the tube can be determined by the tangent stress ($\sigma_{\theta\theta}$) and elastic modulus (E). The equation for tangent stress $\sigma_{\theta\theta}$ is as follows:

$$\sigma_{\theta\theta} = \frac{(P_i - P_e)R_i}{e} \tag{2.1}$$

where P_i is the inner pressure, P_e is the external pressure, R_i is the inner radius and e is the thickness of tube. Fig. 2.5 shows the calibration results for two tubes. It is found that there is a linear relationship between inner pressure P_i and circumferential strains for both lower and upper tubes. Although the calibration results for both tubes show a slight deviation from the theoretical value, it demonstrates a linear relationship and is considered reasonable. As the stress values involved are low compared with common plastic yield threshold of steel, the two tubes exhibit a linear and elastic (reversible) behavior. At the same time, the value of Young's modulus of the steel tubes, approximately equal to 190–210 GPa, is much greater than that of confining pressure and expected swelling pressure. The deformation of tubes during sample swelling remains very small, providing a good kinematical constraint condition to accurately capture swelling pressure.

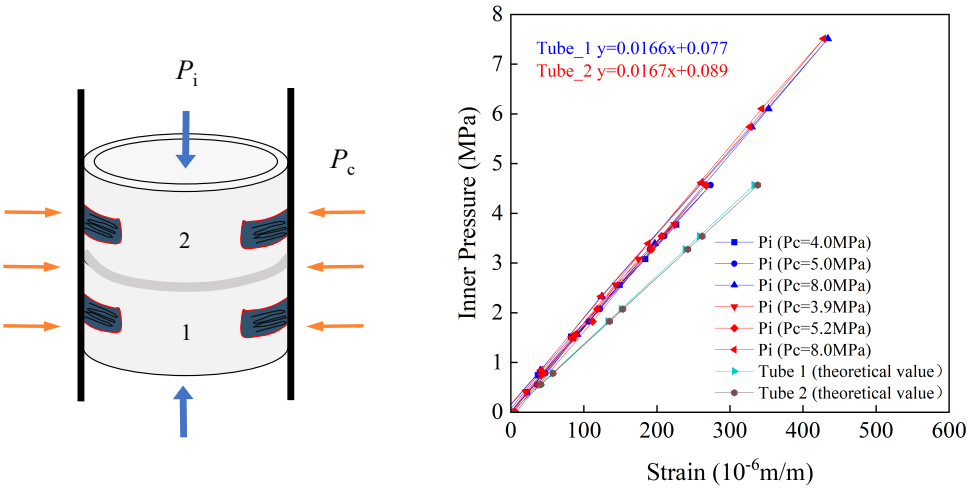

Figure 2.5: Relation between the inner pressure and surface strain of tube.

2.4 Experimental system

Two specific experimental systems are developed and shown in Fig. 2.6 for observing the self-sealing process of cracked samples. Fig. 2.6(a) illustrates the permeability test setup used for mock-up I. The apparatus consisted of five main parts: a triaxial cell with a diameter of 37 mm, a confining pressure control system, a gas pressure monitoring system, a water injection system and a data acquisition system (LabView). The confining pressure is provided by a manual hydraulic pump (model P392, Enerpac, Milwaukee, WI, USA) linked to the cell, which applied lateral and axial stresses to the sample. The gas pressure monitoring system records the pressure at both the upstream and downstream. Argon is chosen as the tested gas. The gas is injected at a constant pressure from the upstream and the gas detector (ion science) is placed at the downstream to check the gas flow. To monitor the flow more accurately, a versatile digital pressure meter with a precision of up to 0.01 % FS is installed at the downstream. A Teledyne ISCO D-series syringe pump system (Lincoln, NE, USA) is employed to deliver water from the down upwards and supply pressure in the constant pressure mode. During the permeability test, the synthetic water with a chemical composition close to that of groundwater is injected at a constant pressure of 0.5 MPa. Simultaneously, a confining pressure of 3 MPa is set to allow for sample expansion under low confining pressure conditions.

Fig. 2.6(b) shows the setup used to study the swelling behavior of mock-up II and III. It also included five main components: a triaxial cell with an internal diameter of 65 mm,

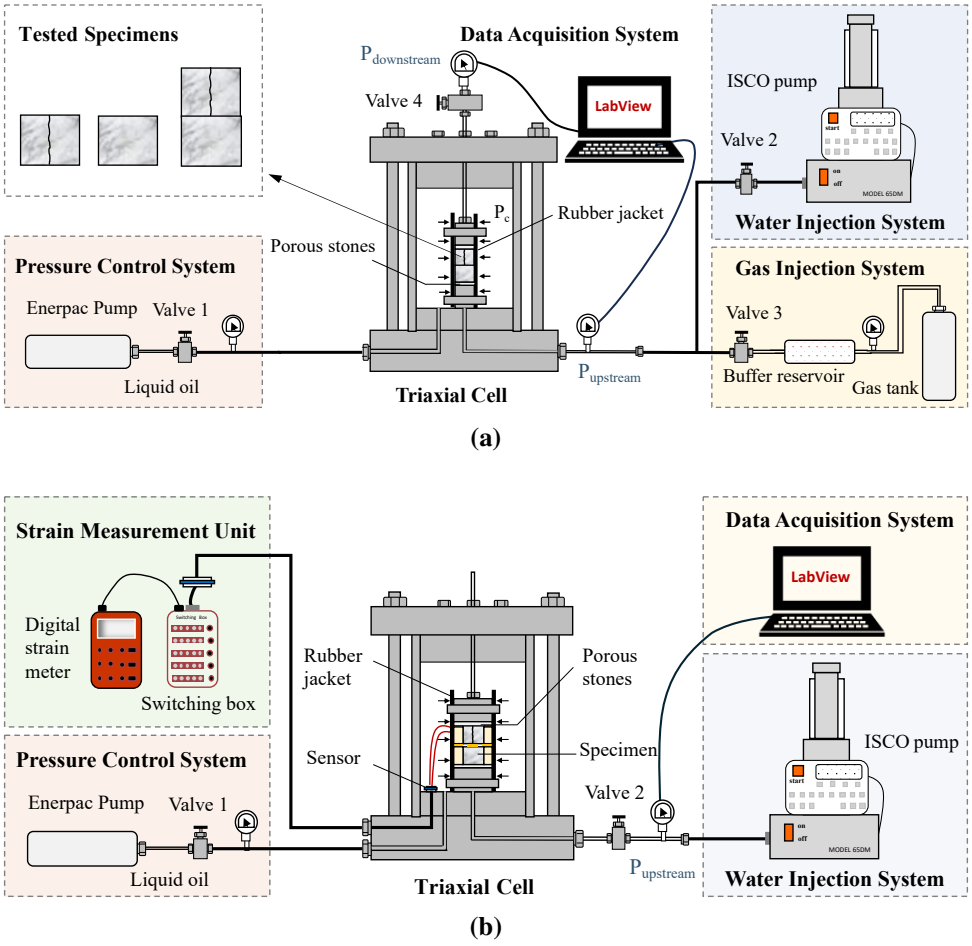

Figure 2.6: The experimental apparatus for self-sealing test (a) permeability test of mock-up I; (b) swelling test of mock-up II and mock-up III.

a confining pressure control system, a water injection system, a strain measurement unit and a data acquisition central (LabView). The strain evolutions are registered by two linear stain gauges (PFL-10-11 with 10 m length, 120.3±0.5Ω and gauge factor 2.12±1%, Tokyo, Japan) glued on each steel tube. The strain gauges are oriented along the circumference of the sample, using a strain gauge adhesive provided by the manufacturer. The strain gauge lead wires are properly isolated and secured to the surface of each tube using a quick-set adhesive to avoid any movement of the wires that may affect the accuracy of the reading. The end wires are twisted together, attached to the base of the cell and labeled to identify the location of each gauge. Through a set of electric Wheatstone bridges (CSW-5A-05 switching box, Tokyo, Japan), the strain gauges are connected with a digital strain meter (TC-31K type S238C) to convert the resistance change of the strain gauge

into a voltage output. The mock-up is placed in a triaxial cell and tested under a confining pressure of 5 MPa. This confinement is set primarily to maintain lateral confinement while allowing the sample to deform almost freely. During the experiment, the confining pressure is maintained for a period of time until the strain gauge readings stabilized, after which water is injected at the same constant pressure as in mock-up I. All tests were performed in a temperature-controlled room maintained at 21°C to exclude the influence of temperature fluctuation.

3 Experimental procedures

3.1 Permeability measurement techniques

The transfer properties of composite sample were considered, including the initial gas permeability (K_{ag}) and the initial water permeability (K_{aw}). It is a reference for fluid transport in the self-sealing process. Sample S0 (mock-up I) is chosen to measure these permeabilities under constant confining pressure. Gas permeability is determined at equilibrium using Darcy's law for compressible gas flow. According to the steady-state flow method (Loosveldt et al., 2002; Davy et al., 2007), pressure measurements are continuously recorded using a manometer, which monitors the pressure variations in the buffer reservoir and connecting tubing. The apparatus of gas permeability is shown in Fig. 2.6(a). Samples were separately placed into a 37 mm diameter triaxial under a constant oil pressure of 3 MPa using an Enerpac pump. The cell is connected to a buffer reservoir and gas tank. Argon gas is injected upstream at injection pressures of 0.2, 0.5, 1.0 and 1.5 MPa. Prior to the experiments, a precise volume calibration procedure is conducted to ensure the accuracy of the volumetric flow rate determination. The laboratory-measured gas permeability K_{ag} is calculated at equilibrium based on Darcy's law for compressible gas flow:

$$K_{ag} = \frac{\mu_g Q_g}{A} \cdot \frac{2LP_0}{P_1^2 - P_0^2} \tag{2.2}$$

where K_{ag} is apparent gas permeability (m^2), Q_g is the volume flow rate at the downstream $(\mathrm{m}^3/\mathrm{s})$, μ_g is the dynamic viscosity of Argon $(2.2 \times 10^{-5}$ Pa s), L is the length of the cylinder (m), A is the area of the injection (m^2), P_1 is the upstream pressure (Pa), and

P_0 is the downstream pressure of specimen (Pa).

In the self-sealing process of composite sample, water penetration capacity is an important concern under the effect of porewater pressure. Thus, the water permeability of all composite samples from two mock-ups is measured before and during the self-sealing experiment. The dimensions of mock-ups were different, so two triaxial cells were used, with a diameter of 37 mm for mock-up I (see Fig. 2.6(a)) and 65 mm for mock-up II (see Fig. 2.6(b)). After measuring the gas permeability of sample S0 (mock-up I) with the setups in Fig. 2.6(a), the valves 2 and 4 were disassembled while the confining pressure remained constant. The cell is then connected to the ISCO pump for hydromechanical loading. Synthetic water with a chemical composition close to that of groundwater is injected from the upstream at a relatively low constant pressure of 0.5 MPa, while the downstream is connected to the ambient air inlet (at atmospheric pressure). Based on steady-state water flow, taking into account Darcy's law rules for liquids, the water permeability of the sample is determined as follows:

$$K_{aw} = \frac{Q_w \cdot \mu_w \cdot L}{A \cdot \triangle p} \tag{2.3}$$

where K_{aw} is apparent water permeability (m^2), Q_w is the flow rate of water $(\mathrm{m}^3/\mathrm{s})$, μ_w is the dynamic viscosity of water $(1.01 \times 10^{-3}$ Pa s), L is the length of cylinder (m), A is the area of the injection (m^2) and $\triangle p$ is the pressure difference (Pa).

3.2 Swelling pressure test

The swelling pressure of the COx sample during the self-sealing process is converted by measured strain. It is called apparent swelling pressure P_{app}. The digital strain gauges connected to the strain sensors mounted at the bottom basement in Fig. 2.6(b) is used to measure the evolution of strain. According to tube calibration, it is observed that the relationship between internal pressure and measured strain remains similarly linear under different confining pressures. Detailed calibration results and validation have been discussed in the Section 2.3. This linearity indicates that, under low confining pressure conditions, the influence of confinement on the strain measurement is minimal and can be reasonably neglected. Thus, the strain measurements could be converted to apparent swelling pressure of the tested sample in subsequent experiments. The previously reported swelling pressures in re-saturated COx claystone typically range between 4 and

5 MPa, as can be seen in Fig.8 of Wang et al. (2022a). Thus, the confining pressure of 5 MPa is set primarily to maintain mechanical stability of the surrounding system while allowing the sample to deform almost freely. Prior to the experiment, the confining pressure is maintained for a period of time until the strain gauge readings stabilized, after which water is injected at a constant pressure.

The main experimental procedure in the self-sealing test is present in Fig. 2.7.

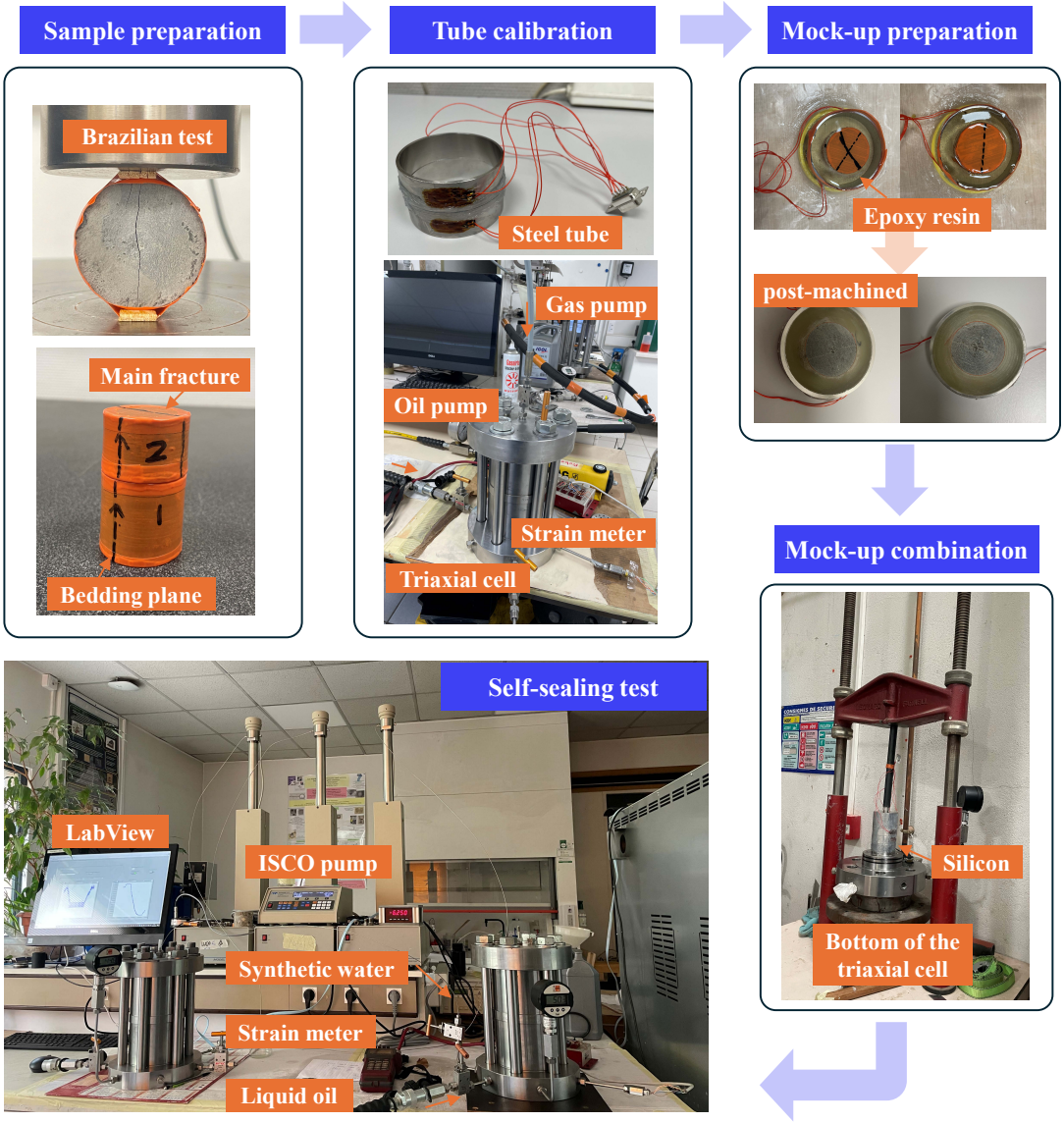

Figure 2.7: Main experimental procedure in the self-sealing test.

4 Gas transport of composite sample

The pore structure of clay-rich rocks is mainly distributed at the micrometer and nanometer scales (Boulin et al., 2008). Gas transport in such porous media deviates from the classic Darcy's law but exhibits significant slip flow characteristics, known as the Klinkenberg effect. This phenomenon has also been observed and verified in COx claystones (Yuan et al., 2023). In our study, the composite sample S0 of mock-up I is investigated for this effect on gas permeability at a confining pressure (P_c) of 3 MPa. As it is well known, Klinkenberg proposed a equation correcting the slipping effect in gas permeability (Klinkenberge, 1941)

$$K_{ag} = K_{int}\left(1 + \frac{b}{P_m}\right) \tag{2.4}$$

in which K_{ag} is the apparent permeability measured at different injection pressures, K_{int} is the intrinsic permeability, P_m is the mean pressure of the sample $(P_{inj} + P_{atm})/2$ and b the Klinkenberg coefficient.

The gas permeability results measured under four inlet gas pressures (P_i) of 0.2, 0.5, 1.0 and 1.5 MPa, respectively, are reported in Table 2.3. It is seen that lower injection pressures result in higher apparent gas permeability. Based on these experimental results, the relationship between $1/P_m$ and K_{ag} for each sample is shown in Fig. 2.8. The high linear correlation demonstrates the significant impact of the Klinkenberg effect on gas permeability, whereby gas permeability decreases with increasing gas pressure. Moreover, the intrinsic permeability and Klinkenberg coefficient can be obtained using Eq. (2.4). The K_{int} values are also reported in Table 2.3. The intrinsic permeabilities are respectively 1.67×10^{-15} m^2 for sample S0-C, 2.83×10^{-21} m^2 for sample S0-S. The lower permeability of sample S0-S reveals a dense and intact matrix with limited pore connectivity.

Table 2.3
Apparent gas permeability under different gas pressures.

P_i (MPa)		0.2	0.5	1.0	1.5	K_{int} (m^2)
K_{ag} (m^2)	S0-S	4.73×10^{-20}	2.77×10^{-20}	1.57×10^{-20}	1.50×10^{-20}	2.83×10^{-21}
	S0-C	1.42×10^{-14}	9.30×10^{-15}	6.02×10^{-15}	4.36×10^{-15}	1.67×10^{-15}
	S0	2.10×10^{-20}	1.42×10^{-20}	1.01×10^{-20}	8.89×10^{-21}	4.92×10^{-21}

Notably, the composite sample S0 exhibits an intrinsic permeability of 4.92×10^{-21} m^2, comparable to that of sample S0-S. It shows that the intact lower sample serves as the primary capillary barrier in the system, effectively restricting fluid transport regardless of the presence of fracture in the upper sample.

5 Self-sealing process of composite sample

For the evaluation of the self-sealing process, the apparent swelling pressure and apparent water permeability are measured to assess the consequences of fracture closure in the sample, driven by the swelling of clayey matrix of COx claystone.

5.1 Apparent water permeability

The evolution of apparent water permeability (K_{aw}) with time is evaluated for each set of samples during water injection using the method mentioned above. The main results of mock-ups I and II obtained are presented in Fig. 2.9 and Table 2.4 . Although the confining pressure is different, 3 MPa for mock-up I and 5 MPa for mock-up II, the apparent water permeabilities of two mock-ups are similar, with an initial value of approximately 10^{-19} m^2 measured at an injected pressure of 0.5 MPa. Under the restrained swelling condition, the increase of compressive stress (swelling pressure) induces progressive closure of the main fracture and microcracks, leading to the decrease of water permeability.

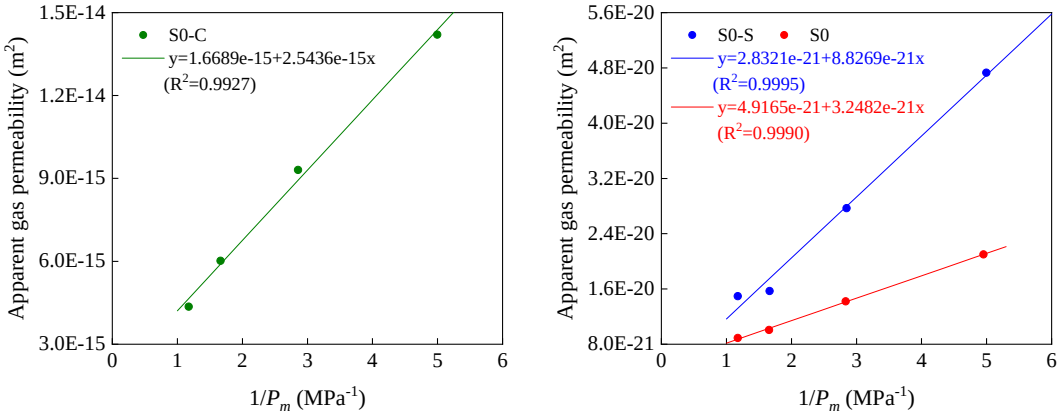

(a) S0-C **(b)** S0-S and S0

Figure 2.8: Apparent gas permeability values K_{ag} for different $1/P_m$ by the Klinkenberg equation: (a) S0-C, (b) S0-S and S0.

It is found that there is a sharp decrease of water permeability during the first days, indicating a significant closure of microcracks and main fracture. Subsequently, the closure process is progressively attenuated and reaches an asymptotic value. As a consequence, the diminution rate of water permeability becomes slower and slower. At the final stage, a stabilized residual value of permeability is obtained for each set of samples, on the order of 10^{-20} m^2. In addition, the evolution of water permeability observed in sample S1 tested with mock-up II closely resembled that of sample S0 tested without tubes. It is possible that the tubes in mock-up II effectively minimize the impact of confining pressure, providing a reliable model for observing the long-term self-sealing behavior of claystone under extremely low confinement conditions.

Table 2.4
Apparent water permeability results of mock-ups I and II.

Mock-up	**Mock-up I**	**Mock-up II**	
	S0 (EST 67288-1)	S1 (EST 67288-2)	S2 (EST 62665)
Duration (day)	121	95	89
Initial K_{aw} (m^2)	3.32×10^{-19}	6.86×10^{-19}	7.44×10^{-19}
Final K_{aw} (m^2)	1.21×10^{-20}	1.38×10^{-20}	8.68×10^{-21}

Compared to the gas permeability of sample S0 in Table 2.3, it is found that the initial

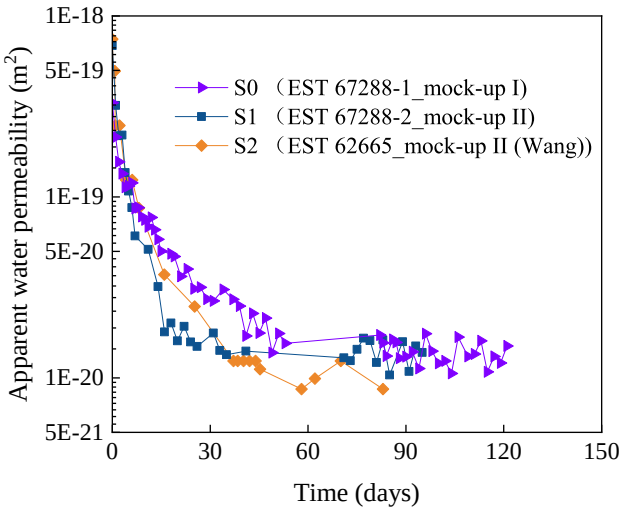

Figure 2.9: Apparent water permeability of the composite samples using mock-up I and mock-up II measured over the duration of the self-sealing test.

apparent water permeability is measured to be approximately 3.32×10^{-19} m^2, while the apparent gas permeability at an injection pressure of 0.5 MPa is about 1.42×10^{-20} m^2. Under the same injection conditions, the initial water permeability is roughly one order of magnitude higher than the corresponding gas permeability.

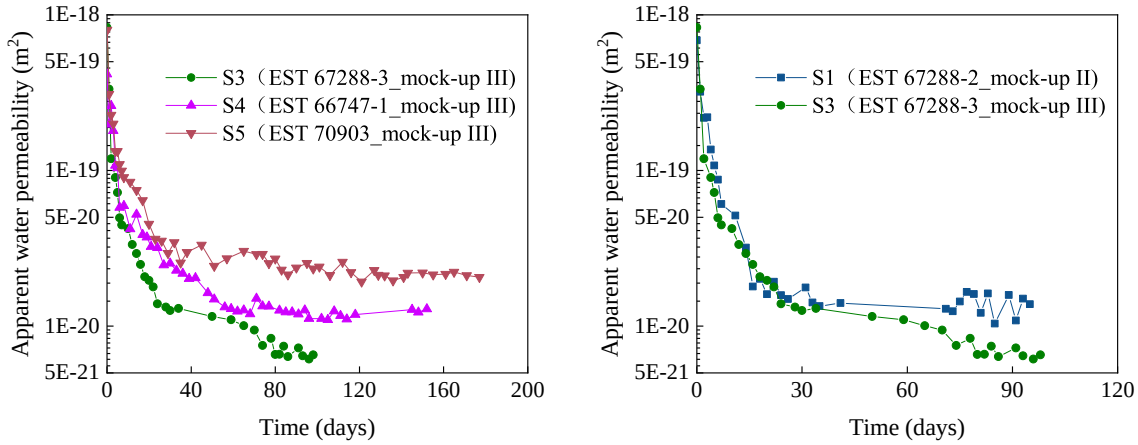

(a) mock-up III **(b)** mock-up II and III

Figure 2.10: Apparent water permeability of the composite samples using mock-up III measured over the duration of the self-sealing test.

The evolution of apparent water permeability for samples using mock-up III as a function of time is given in Fig. 2.10(a). The initial values of apparent water permeability are respectively equal to 8.29×10^{-19} m^2 for the sample S3, 4.16×10^{-19} m^2 for the sample S4 and 7.98×10^{-19} m^2 for the sample S5. All samples show a rapid decline in permeability during approximately the first days, followed by a gradual decrease and eventually stabilize at values on the order of 10^{-20} m^2. The exact values for all the sets of samples are given in Table 2.5. It is noticed that there are relatively important discrepancies between the samples S3, S4 and S5, tested in the same condition. This is likely related to the heterogeneity between samples, in particular the distribution of initial microcracks. In Fig. 2.10(b), one further compares the water permeability between the sample set with an intermediate joint (S3) and that without a joint (S1). The initial apparent water permeability of S1 is 6.86×10^{-19} m^2 and the residual value is 1.38×10^{-20} m^2. It is seen that these values are not significantly different with those of S3. This is probably due to the fact that the apparent permeability is primarily controlled by the intact sample which is located at the bottom of mock-up where water is injected.

Table 2.5
Apparent water permeability results of mock-up III.

Mock-up	**Mock-up III**		
	S3 (EST 67288-3)	S4 (EST 66747-1)	S5 (EST 70903)
Duration (day)	98	150	122
Initial K_{aw} (m^2)	8.29×10^{-19}	4.16×10^{-19}	7.98×10^{-19}
Final K_{aw} (m^2)	6.44×10^{-21}	1.41×10^{-20}	2.12×10^{-20}

5.2 Apparent swelling pressure of mock-up II

The measurement of free swelling deformation in clayey rocks is not an easy task. Alternatively, the compressive stress or swelling pressure generated under constrained swelling conditions can be measured with good accuracy. Its value can be used as a good indicator of swelling process. Therefore, the evolution of apparent swelling pressure (P_{app}) as a function of water injection time is measured in the present study. The obtained values using mock-up II are given in Fig. 2.11(a) for different samples. It is seen that there are some differences of swelling pressure in cracked and intact samples of S1 and S2. In order to compare the kinetics of swelling process, the evolution of apparent swelling pressure during the first 40 days is amplified in Fig. 2.11(b). One is the increase rate of swelling pressure in cracked sample S1-C is significantly lower than those of the intact sample S1-S during the first 40 days. Two main reasons can be evoked here. One reason is that, at the beginning of water injection from the bottom surface of mock-up, the intact sample rapidly absorbs water, leading to swelling expansion and a sharp increase in swelling pressure. But due to the very low permeability of the intact sample, the water penetration into small pores is difficult so that an asymptotic swelling pressure is quickly reached. On the other side, the penetration of water into the cracked sample is delayed by the presence of intact sample at the lower part of the mock-up. It is logical that the swelling of cracked sample occurs later than that of the intact one. In contrast, S2-S and S2-C exhibit almost simultaneous swelling behavior. It is possible that sample S2-S has numerous microcracks and is not truly intact. Water goes directly through the microcracks in sample S2-S to sample S2-C in the first days.

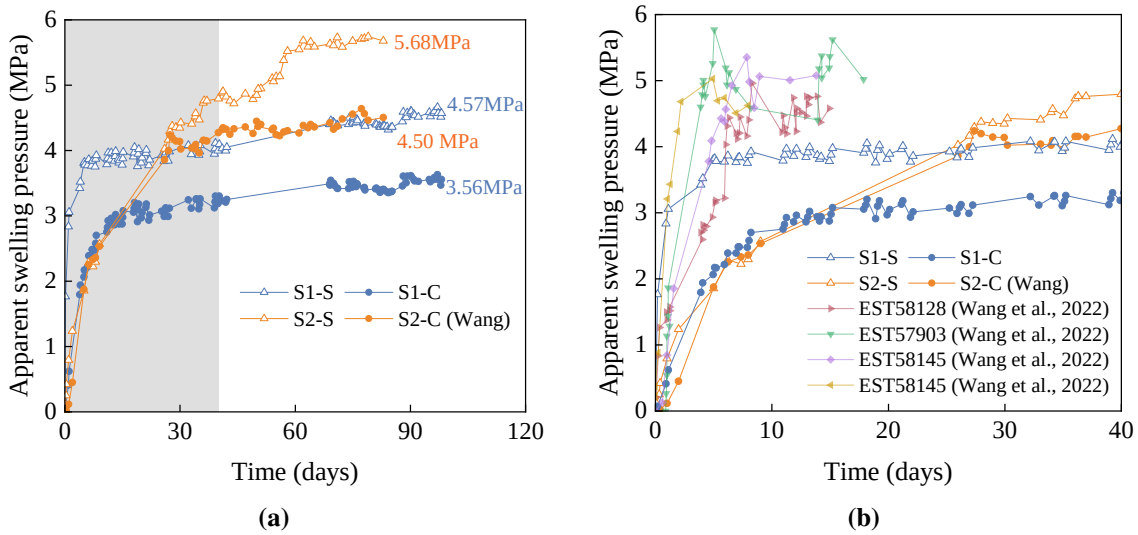

Figure 2.11: Apparent swelling pressures (P_{app}) using mock-up II.

Another can note that the final P_{app} of the cracked sample is lower than that of the intact sample. The maximum swelling pressure of S1-C and S2-C reaches 3.56 and 4.50 MPa, compared to 4.57 and 5.68 MPa for S1-S and S2-S, respectively (see Fig. 2.11(a)). The relatively low P_{app} of the cracked sample implies a high significance of the main fracture impact on its outward expansion. The water flow from the intact sample to the cracked one is facilitated and water penetrates directly into the main fracture. Thus, swelling induces this one to close quickly, resulting in a rapid stabilization of swelling pressure. In contrast, the water is more evenly distributed in the intact samples, allowing for rapid global expansion, which explains its greater lateral deformation. Furthermore, the final P_{app} of sample S1 is lower than that of sample S2, likely due to differences in mineralogical composition and initial water content. Post-coring measurements in Bure indicate water contents of about 7% for EST67288 and around 8% for EST62665, suggesting possible variability in water content. Additionally, water loss during sample preparation may have further influenced swelling behavior. In this study, the water content of sample S2, obtained from core EST62665, is about 4%, which is much lower than the post-coring water content. These differences in initial saturation state and uncontrolled water loss likely account for the observed discrepancies in swelling pressure.

In addition, the results using mock-up II in this study are compared with reference data from Wang et al. (2022a), shown in Fig. 2.11(b). The reference data were obtained from cracked samples created by the Brazilian splitting test, all originating from similar

geological depths. These cracked samples were sealed by direct water injection under the same injection and confining pressure conditions. The swelling pressures obtained in this study are similar to those measured in cracked samples subjected to direct water injection. Upon water saturation, the measured swelling pressures stabilized approximately between 4 and 5 MPa, especially for sample S2-C. The similarity in swelling behavior confirms that mock-up II effectively captures long-term swelling under low confining pressure, including fracture closure and matrix expansion.

5.3 Apparent swelling pressure of mock-up III

The swelling pressure of samples S3, S4 and S5 using mock-up III is given in Fig. 2.12. It should be noted that all samples are extracted from the same geological depth and therefore theoretically possess similar mineralogical compositions. Therefore, for the sake of simplicity, the influences of mineralogical compositions are not discussed in the analysis of results. However, we can not fully avoid some influence of the mineralogy. For instance, on Fig. 2.12(a), the two intact samples from the same borehole (S1-S and S3-S from EST 67288) give similar swelling pressures. The sample S4-S, coming from a borehole (EST 66747) which is located far from the borehole (EST 67288), shows a much high swelling pressure.

In order to compare the kinetics of swelling process, the evolution of apparent swelling pressure during the first 40 days is amplified in Fig. 2.12(b). It is seen that the increase rates of swelling pressure in the cracked samples (S3-C, S4-C, S5-C) are significantly lower than those of the intact samples (S3-S, S4-S, S5-S). The main reason has been discussed in Section 5.2. Moreover, due to the presence of main fracture and secondly cracks induced during the Brazilian test, the set-up of swelling pressure in the cracked sample is slow during the first period of water penetration. Indeed, the water penetration induces first the closure of cracks and fracture before generating swelling pressure. At the same time, with the help of the main fracture and induced secondly cracks, a large absorption of water is possible in the cracked sample. As a consequence, due to the presence of joint, the apparent swelling pressures in three cracked samples continue increasing during a longer period. Their final values become even higher that those of the intact samples. For instance, the maximum swelling pressure of S3-C, S4-C, and S5-C reach 5.08, 6.87, and 7.31 MPa, compared to 3.68, 3.72, and 6.24 MPa for S3-S, S4-S, and 55-S, respectively (see Fig. 2.12(a)). It is also noticed that there are quite large scatters between tested

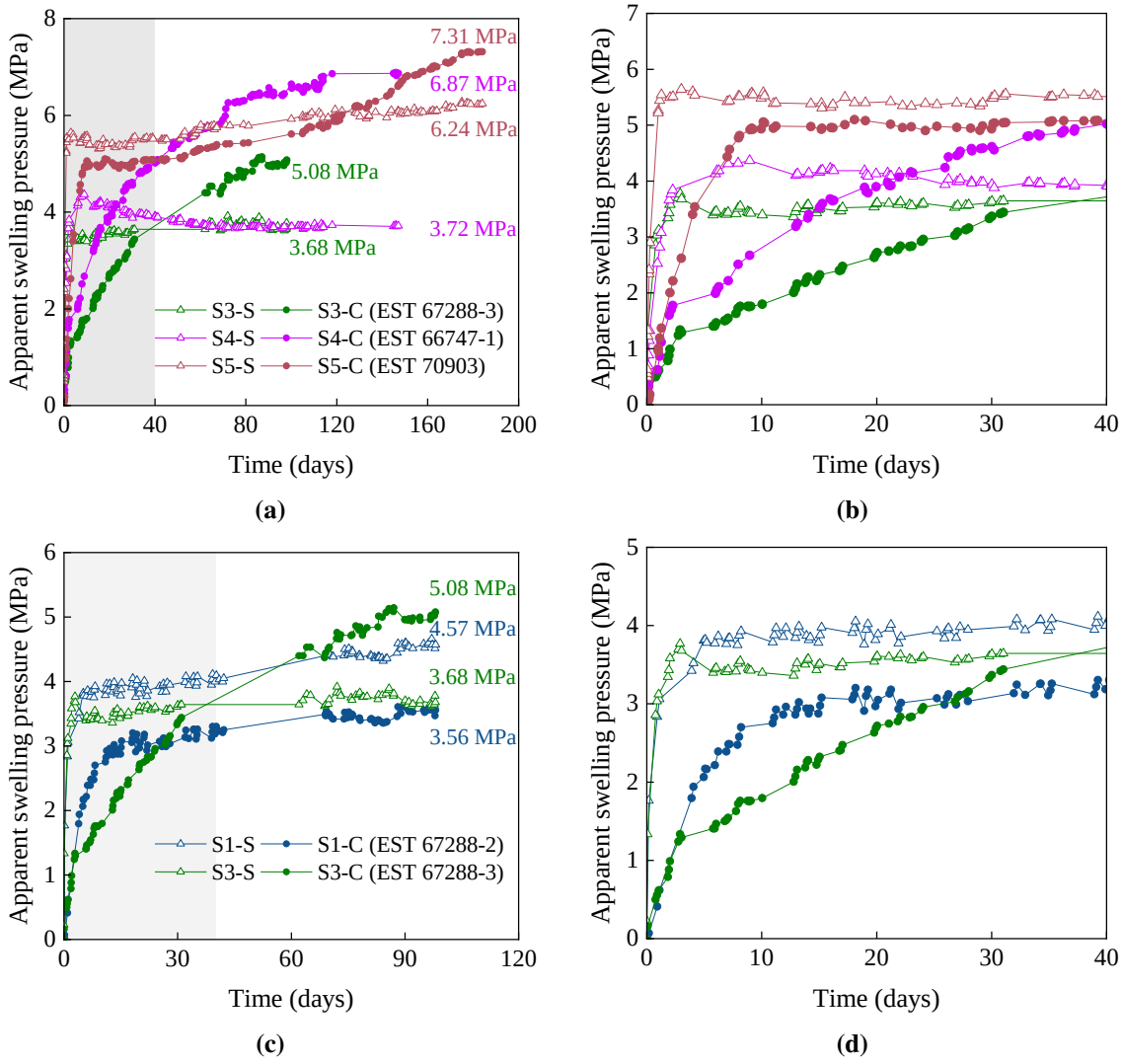

Figure 2.12: Apparent swelling pressures (P_{app}) using mock-up III.

samples, in particular for three cracked samples. In addition to the natural heterogeneity between intact samples, additional disturbances are induced in the cracked samples during the creation of the main fracture by Brazilian splitting test. This one is not easy to control in a perfect way, often resulting a number of secondly cracks around the main fracture.

As mentioned above, the apparent swelling pressure is calculated from the lateral strains measured by the gauges glued on the external surface of steel tube. Due to the presence of bedding planes and created main fracture, the lateral strains are not uniform in all directions. Therefore, the swelling pressure can be influenced by the orientations of strain gauges with respect to bedding planes, as presented in Fig. 2.3 for the different

samples. However, for the cracked samples, the strain gauges are systematically parallel to the created main fractures. It is interesting to compare the results between the samples S3 and S5. It is recalled that for the samples S3-S and S3-C, the strain gauges are perpendicular to the bedding planes while for the samples S5-S and S5-C they are parallel to the bedding place. During the water resaturation, the swelling strains in the perpendicular direction to bedding planes should be larger than that in the parallel one due to the local deformation of bedding planes. As a consequence, the swelling pressure in the sample S5-S is clearly higher than that of the sample S3-S, as shown in Fig. 2.12(a) and Fig. 2.12(b). At the same time, the samples S3-C and S5-C, the deformation of the main fracture plays an essential role in the swelling process. Although the main fracture is always parallel to the strain gauges for both samples, the sweeling pressure of the sample S5-C is higher than that of the sample S3-C. This is due to the fact that in the sample S5-C, as the main fracture is parellel to bedding planes, their effects are superposed. Indeed, in the sample S3-C, the main fracture is perpendicular to bedding planes, the lateral strains measured by the strain gauges are affected by the main fracture only, not by bedding planes. Another interesting result is about the samples S4-S and S4-C. Contrary for the other groups, the strain gauges are oriented differently for the sound and cracked samples, more precisely, perpendicular to bedding planes for S4-S and parallel to S4-C (see Fig. 2.3). As a consequence, the swelling deformation related to bedding planes is not directly measured by the strain gauges for the sample S4-S while for the sample S4-C the effects of main fracture and bedding planes are superposed. Therefore, as clearly shown in Fig. 2.12(a), the difference of swelling pressure for this couple of samples (between S4-S and S4-C) is much larger than that for the other ones, for example between S5-S and S5-C. Moreover, the swelling pressure of the sample S4-S shows a progressive decrease after its peak value. This is due to the fact that the swelling deformation of bedding planes induces a tensile lateral strain in the parallel direction to bedding planes while a compressive strain in the perpendicular direction along which the strain gauges are oriented for this sample.

As shown in Fig. 2.2, the impermeable joint can play an important role in the water flow from the intact to cracked sample. In Fig. 2.12(c) and Fig. 2.12(d), we compare the swelling pressure between the samples S1 and S3. In the mock-up S1, no impermeable joint is inserted between the intact and cracked samples while it is the case for the mock-up S3. Due to the absence of the impermeable joint, the water flow from the intact sample to the cracked one is facilitated and there is direct water penetration to the main fracture.

As a consequence, the increase of swelling pressure during the first 10 days in the sample S1-C is sharper than that in S3-C. However, due to the direct penetration of water into the main fracture in the sample S1-C, the swelling induces closure of this one leading to a quick stabilization of swelling pressure. In contrary, in the sample S3-C, the water penetration into the sound part around the main fracture takes a longer period and does not result in rapid closure of the main fracture. This produces a progressive increase of swelling pressure during a much longer period. The final value of swelling pressure for the sample S3-C becomes higher than that of S1-C.

It should be mentioned that in the present study, all the tested samples are drilled along the parallel direction of bedding planes. In some previous studies (Giot et al., 2019; Agboli et al., 2024) , the self-sealing process of the COx claystone was investigated on samples drilled in both parallel and perpendicular directions to bedding planes. No clear conclusions can be drawn so far on the influence of sample orientation on self-sealing process. Therefore, it is still an open issue to be addressed. Additional tests should be curried out in future studies to better identify the effect of COx structural anisotropy on swelling-induced self-sealing process.

5.4 Swelling mechanism of clay minerals

The swelling mechanisms of clay minerals have been investigated in previous studies at different scales (Karaborni et al., 1996; Anderson et al., 2010). In general, the swelling of clay-rich rocks involves multiple mechanisms, including crystalline swelling, osmotic swelling, and clogging-induced sealing. Giot et al. (2019) proposed that swelling begins with crystalline swelling, initiated at low water contents by the adsorption of water molecules into the interlayer spaces of the clay sheets. It first occurred in clay minerals but was mainly governed by smectite or illite–smectite. The maximum interlayer spacing associated with crystalline swelling is approximately 21.6 Å, corresponding to four water layers, as supported by multiple studies (Norrish, 1954; Karaborni et al., 1996; Saiyouri et al., 2000; Menaceur et al., 2016). This mechanism is driven by water activity and is limited in magnitude. As water continues to infiltrate, the osmotic swelling occurs in minerals containing exchangeable cations in the interlayer. The difference in cation concentration between the pore water and the clay particle surfaces drives water into the spaces between particles (Anderson et al., 2010). The electrostatic repulsion is generated in the diffuse double layer around the particle surfaces, further increasing both

interlayer and interparticle spacing. Compared with crystal swelling, the repulsion from the diffuse double layer persists longer and leads to a significantly larger volume increase. In montmorillonite-rich materials, interparticle spacing can exceed 100 Å, and swelling progresses nearly linearly with water content (Norrish, 1954; Rhaiem et al., 1987). Subsequently, as the clay matrix continues to absorb water and swell, fine particles may migrate and accumulate within crack interstices, resulting in clogging and the formation of clay plugs.

In the present study, it is shown that the swelling pressure in cracked sample can be explained by the combined effect of these mechanisms. The presence of a main fracture in the samples S1-C and S2-C of mock-up II would induce the lower swelling pressure. The water flow from the intact sample to the cracked one is facilitated and there is direct water penetration to the main fracture. Thus the swelling induces closure of this one, leading to a quick stabilization of swelling pressure. In contrast, the water was more uniformly distributed in the intact samples, allowing for rapid global expansion, which is why the lateral deformation amplitude is relatively larger. It is noteworthy that in mock-up III with an impermeable joint, the water penetration into the intact part around the main fracture takes a longer period and does not result in rapid closure of the main fracture. As a consequence, the increase of swelling pressure during the first 10 days in the sample S1-C is sharper than that in S3-C, as shown in Fig. 2.12(c). This also produces a progressive increase of swelling pressure during a much longer period. The final value of swelling pressure for the sample S3-C becomes higher than that of S1-C. In relation to the swelling mechanisms mentioned above, this can be explained by a deeper water infiltration in cracked samples leading to stronger conjugated effects of both crystal and osmotic swelling.

It is to be noted that liquid saturation of claystone increases as capillary pressure decreases during water absorption (Grgic et al., 2019), which may enhance the swelling tendency of the clayey matrix. Under confined conditions, this swelling tendency can result in an increase in swelling pressure. Unfortunately, the quantitative water content measurement is very complex and not completed in those tests. The present analysis is based on plausible reasoning and needs to be confirmed by complementary studies.

6 Conclusions

This chapter investigated the self-sealing behavior of cracked COx claystone under indirect water injection using three designed experimental mock-ups, namely mock-up I without steel tubes, mock-up II with steel tubes and mock-up III with a joint between two steel tubes. For mock-up I, gas and water permeability tests were first carried out before and after water injection. The swelling pressure of samples in mock-ups II and III was additionally determined. The presence of a joint priority in mock-up III prevented liquid flow through the fracture by further providing an indirect injection condition. All samples used in this study were obtained from COx claystone at a depth of approximately 490 m.

The permeability is an efficient measurement to identify the progressive sealing of microcracks, fractures, bedding planes and other fluid flow pathways. It is observed that gas permeability of the composite sample in the mock-up I is comparable to that of the intact sample. It suggests that its permeability is mainly governed by the lower intact sample and accompanied by a significant Klinkerberg effect. In the tested samples, the apparent water permeability of mock-ups I, II and III shows a similar trend, gradually decreasing from an initial value of approximately 10^{-19} m^2 to a stable value of 10^{-21} m^2.

Based on the results obtained, it is found that the swelling pressure is an efficient indicator of self-sealing process under the kinematically constrained condition. Compared with the intact samples, the set-up of swelling pressure of the cracked samples during the first stage of saturation is slower. But with water infiltration, there is a higher swelling potential during a longer swelling period, leading to a higher long term swelling pressure. Compared with the samples with direct water penetration into main fracture, the samples with an impermeable joint preventing direct water penetration into fracture show a larger resaturation extent and then a higher swelling pressure. However, this result should be taken with caution as no quantitative water content in tested samples is measured. Further studies can be envisaged for the confirmation of the present result.

In all experiments, self-sealing induced by swelling itself is always an effective mechanism under low confinement and low injected pressure. It validates the reasonable simulation capability of the designed experimental mock-up for the water infiltration process. However, it is useful to point out that the results presented in this work rely on a single test for each configuration, although maximum care is taken in order to minimize sample variability as much as possible. Due to the experimental complexity and long test

duration, we have not discussed the repeatability of tests. Additional tests are expected to address this important issue. Otherwise, it will be interesting to investigate the influence of initial anisotropy related to bedding planes on self-sealing process. Microscopic tests with micro-tomography images will also be developed to explicitly monitoring the progressive closure of cracks and fractures during water injection.

CHAPTER 3

Characterization of gas migration and water transport in sealed cracked claystone

1 Introduction

The gas migration behavior of Callovo-Oxfordian (COx) claystone, as well as its hydraulic-mechanical properties, is one of the most critical issues affecting the long-term safety of engineered barrier systems in deep geological disposal sites. During underground excavation and operation, fractures in the host rock are unavoidable. Even if such fractures can close under certain conditions, they still serve as the most potential gas migration pathways. Previous studies also have shown that under re-saturation conditions, COx claystone can achieve partial or complete fracture closure through multiple mechanisms, including matrix swelling induced by water uptake, migration and clogging of fine particles, and re-compaction under confining stress (Zhang, 2013; Wang, 2021b; Di Donna et al., 2022). However, it is important to emphasize that cracks do not disappear and remain the privileged gas transport capacity (Zhang and Rothfuchs, 2008; Wang et al., 2024). Gas breakthrough pressure (GBP) is most commonly used as a quantitative indicator to evaluate the sealing performance of geological storage of CO_2 and nuclear waste (Rutqvist, 2012; Andrew et al., 2014; Amann-Hildenbrand et al., 2013; Harrington et al., 2017; Zappone et al., 2020), and it is defined as the minimum gas pressure required to overcome the capillary pressure in the largest pore channel (Hildenbrand et al., 2002; Egermann et al., 2006). Some studies have demonstrated that gas migration within a sealed cracked sample first exhibits discontinuous following continuous gas flow charac-

teristics (Hildenbrand et al., 2002; Davy et al., 2013; Zhang, 2015; Liu et al., 2018a).

Although significant progress has been made in the study of gas breakthrough behavior in COx claystone (Cuss et al., 2014; Song et al., 2015a; M'Jahad et al., 2017; Wang et al., 2022a; Zhang and Talandier, 2023), most existing investigations have focused on the breakthrough pressure of intact samples or sealed cracked samples after direct water saturation. In contrast, after indirect water injection conditions, where water gradually permeates through the matrix and clay swelling induces crack closure, the characteristics of gas transport and breakthrough behavior within samples with sealed cracks are poorly understood, particularly the quantitative relationship between the degree of crack resealing and gas breakthrough pressure. In addition to the hydration swelling of clay minerals, re-compression is another important mechanism contributing to crack closure and sealing performance (Zhang and Rothfuchs, 2008). It refers to the stress redistribution within the damaged zone, which serves to re-compact pre-existing fractures and decrease its hydraulic transmissivities. At the laboratory scale, such an effect has been demonstrated. The gas permeability of the damaged sample was reduced by several orders of magnitude after short re-compaction through increasing confining pressure from 3 MPa to 15 MPa (Zhang, 2011). Moreover, the crack closure in claystone due to re-compaction has been confirmed by measurements of gas permeability or gas breakthrough pressure under impressive stresses (Zhang and Talandier, 2023; Wang et al., 2024).

This chapter focuses on sealed cracked COx claystone as investigated in Chapter 2 and examines their gas migration and hydraulic transport behavior. Gas breakthrough tests are performed on the disassembled samples from mock-ups I, II and III, enabling a comparative analysis of gas breakthrough characteristics between sealed cracked samples and re-saturated intact samples, taking account of the temperature and re-compaction effect. Furthermore, the intrinsic relationship between gas breakthrough behavior and swelling pressure is explored, and the re-sealing mechanisms of gas-induced pathways during subsequent hydration are analyzed.

2 Materials and methods

2.1 Sample Characterization

Two water-saturated samples (intact and cracked samples) after self-sealing test, a cracked sample, denoted by C, and an intact sample, denoted by S. Fig. 3.1 shows the re-saturated and resealed samples after disassembly of the mock-up used in this study. These samples are from three mock-ups described in Chapter 2, with samples S0-S and S0-C tested by mock-up I, samples S1-S and S1-C, S2-S and S2-C tested by mock-up II and samples S3-S and S3-C, S4-S and S4-C, S5-S and S5-C tested by mock-up III. Table 3.1 summarizes the saturated time and corresponding stable apparent swelling pressure. These core samples are cylinders, with a diameter of 37 mm and a height of 20 mm, from a horizontal core aligned parallel to the bedding plane. The dimension of the sample with a tube is 65 mm in diameter and 20 mm in height.

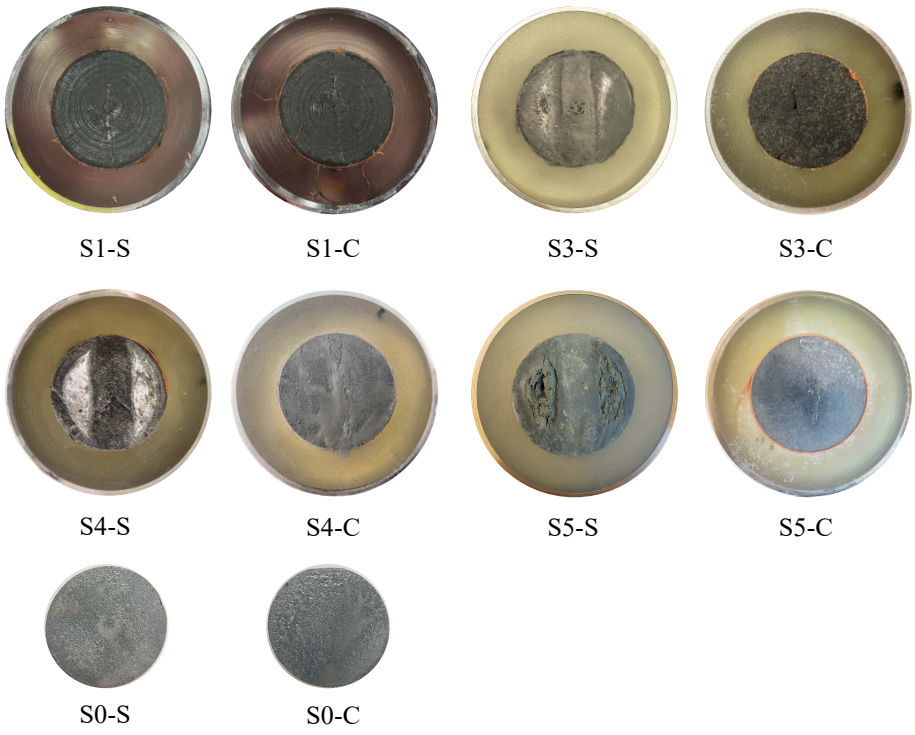

Figure 3.1: Photos of re-saturated and resealed samples after self-sealing test.

Table 3.1
Summary of apparent swelling pressure and test duration for mock-up samples.

Samples Reference		Swelling pressure (MPa)	Duration (days)	Mock-ups
S0 (EST 67288-1)	S0-C	/	121	mock-up I
	S0-S	/		
S1 (EST 67288-2)	S1-C	3.56	95	mock-up II
	S1-S	4.57		
S2 (EST 62665-Wang)	S2-C	4.50	89	
	S2-S	5.68		
S3 (EST 67288-3)	S3-C	3.68	98	mock-up III
	S3-S	5.08		
S4 (EST 66747-1)	S4-C	6.87	150	
	S4-S	3.72		
S5 (EST 70903)	S5-C	7.31	122	
	S5-S	6.24		

2.2 Experimental apparatus

The apparatus shown in Fig. 3.2 is designed for observing the breakthrough pressure and resealing process of cracked samples. The system includes five independent components: a triaxial cell with 37 mm or 65 mm diameter as a pressure chamber, an Enerpac pump for inner pressure loading, a gas injection system for continuous gas sources, an ISCO pump for hydromechanical loading and a LabView system for automated data acquisition and monitoring. Samples S0-S and S0-C from mock-up I are tested in a triaxial cell with a diameter of 37 mm, while the others used a 65 mm cell. During the gas breakthrough test, the triaxial cell is connected with the gas injection system and the data acquisition system recorded the gas pressure at both the upstream and downstream. Argon is chosen as the tested gas. The gas is injected at a constant pressure from the upstream and the gas detector (ion science) is placed at the downstream to check the gas flow. To monitor the flow more accurately, a versatile digital pressure meter with a precision of up to 0.01 $\%$ FS is installed at the downstream. During the resealing test, the cell is connected

with the water injection system and the synthetic water with a chemical composition close to that of groundwater (see Table 2.2) is injected at a constant pressure.

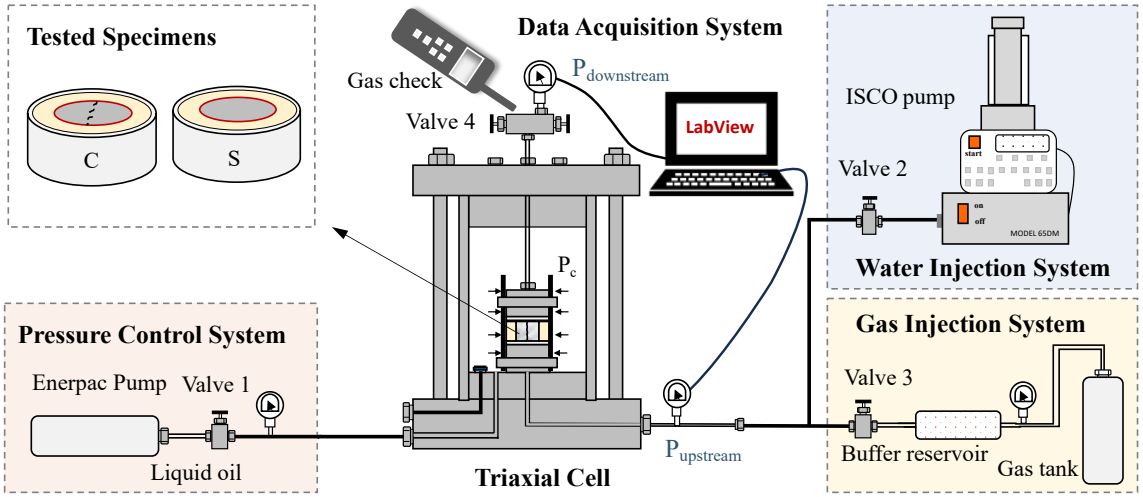

Figure 3.2: Experimental apparatus for gas breakthrough test and resealing test.

2.3 Experimental procedures

The present experimental work comprises the following two phases: the gas breakthrough test and the resealing test. All phases are briefly present hereafter. To minimize the influence of temperature on experimental results, all tests are conducted in a temperature-controlled room maintained at 21°C.

Firstly, gas is injected into water-saturated samples (resaturated and resealed samples) to evaluate gas breakthrough pressure. The GBP of the saturated intact sample is for reference. After the self-sealing process, the water-saturated composite sample is disassembled and simultaneously placed into two triaxial cells, with the confining pressure kept constant for a period before testing. This confining pressure is consistent with that during the self-sealing process. Samples from mock-up II and mock-up III are under 5 MPa confining pressure, while samples from mock-up I are introduced in the following content. Argon gas pressure is injected at the upstream side of the sample using a step-by-step method. Given the noticeable time lag typical of gas migration in clayed rocks, the upstream pressure $P_{upstream}$ is increased in small steps of 0.1 to 0.2 MPa every 24 hours for precise detection until a continuous gas flow is detected at the downstream. Before each pressure increment, the drainage valve (valve 4) at the downstream is opened to check for gas flow. Although the gas flow is quite low, detection is possible using a gas detector

with a precision of 0.1 $\mu L/s$. The breakthrough criterion is defined as the occurrence of continuous gas flow at the downstream. Specifically, the detection procedure involved opening the valve 4 once a significant increase in downstream pressure ($P_{downstream}$) is observed, while simultaneously placing an argon detector toward the opened valve to verify the presence of continuous gas flow. If such flow is confirmed, the corresponding $P_{upstream}$ is considered as GBP, otherwise, the upstream pressure is further increased. Throughout the experiment, record the breakthrough pressure and time.

As reported in other studies (Zhang and Talandier, 2023; Wang et al., 2024), re-compaction can promote the reduction of fracture aperture caused by stress redistribution. To verify this mechanism in the present work, different levels of confining pressure are applied to specimens of mock-up I. To be more specific, the first gas breakthrough test is carried out under a confining pressure of 3 MPa, identical to that used in the self-sealing process. Afterwards, the confining pressure is slowly increased to 12 MPa and maintained for a period of time so as to degas the residual argon within the specimen and allow it to reach a steady state. Once stabilized, gas pressure is applied stepwise for the test. Finally, the variation in GBP is compared between the two tests.

After the gas breakthrough test, gas-induced pathways are present within the sample. To assess whether these pathways could be sealed, the following resealing test is conducted under identical confining pressure conditions. The triaxial cell is first disconnected from the gas system for a period of time to remove the gas pressure completely and then connected to the water injection system. The synthetic water is then injected from upstream at a pressure of 0.5 MPa to reseal the pathway by monitoring the water permeability.

3 Gas migration behavior after sealing

Gas breakthrough tests are conducted on twelve water-saturated COx samples: two samples without tubes from sample S0 of mock-up I, four samples from samples S1 and S2 of mock-up II and six samples from samples S3, S4 and S5 of mock-up III.

3.1 GBP of saturated samples in mock-up I

The gas breakthrough pressures are measured on each sample at two confining pressures of 3 MPa and 12 MPa. The first test is performed on the water-saturated sample, just after disassembling the composite sample following the self-sealing test. The confining pressure remains constant at approximately 3 MPa. The variations of upstream and downstream pressure with time are presented in Fig. 3.3. The upstream gas pressure is increased by small increments of 0.1-0.2 MPa every 24 hours. The downstream gas pressure reported in these figures is calibrated as the variation with respect to atmospheric pressure. During the first period of test, no gas outlet is detected and the measured increments of downstream pressure are generated by water flow pushed by injected gas toward the outlet surface. When the upstream pressure reaches some specific value, the argon detector detects a flow rate of argon in the expelled mixture (see Fig. 3.4). The obtained values are reported in Table 3.2. As the gas detection is completed over a certain time interval during which the corresponding upstream pressure varies, the values of GBP are therefore given with a range of variation. It is observed that the GBP for cracked samples is lower than that of intact sample.

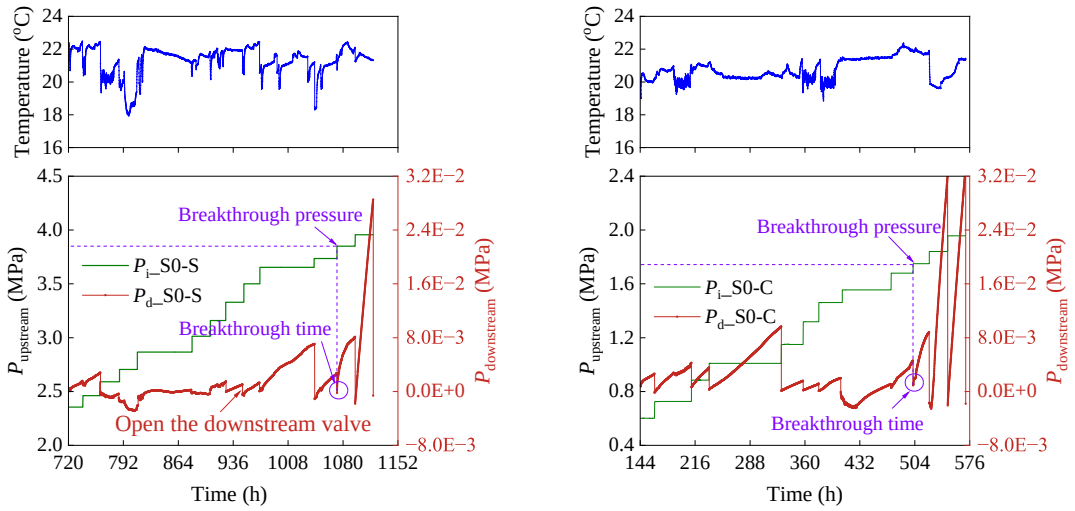

(a) intact sample **(b)** cracked sample

Figure 3.3: GBP of (a) intact sample S0-S and (b) cracked sample S0-C under 3 MPa confining pressure.

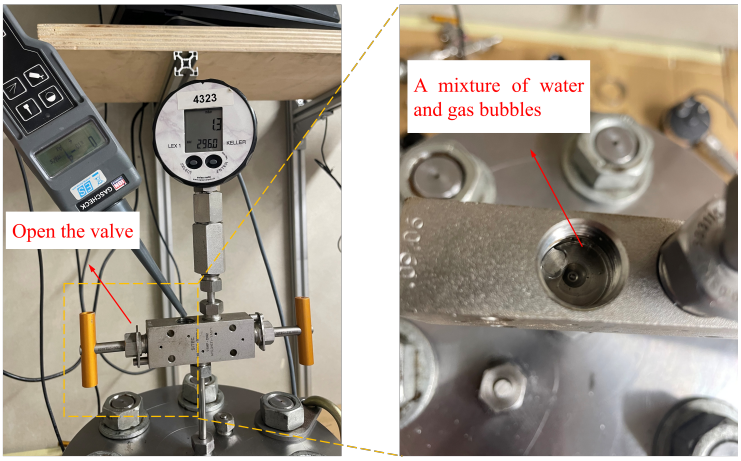

Figure 3.4: Photograph of the experimental phenomenon at the downstream valve.

Table 3.2
Results of gas breakthrough tests on mock-up I.

Mock-up	**Mock-up I (P_c=3 MPa)**		**Mock-up I (P_c=12 MPa)**	
	S0-C	S0-S	S0-C	S0-S
GBP by gas detector (MPa)	1.68-1.75	3.73-3.85	5.15-5.30	8.63-8.77

Subsequently, gas breakthrough tests are conducted on two re-compacted samples under a higher confining pressure of 12 MPa. After loading, the samples are maintained at this state for a period of time to allow the residual gas within the samples to be removed. The results show that when gas is reinjected at the upstream at the beginning, the downstream gas pressure hardly increases and no gas flow occurs. The main results obtained are presented in Fig. 3.5. It can be observed that when a continuous gas flow is detected, the peak of $P_{downstream}$ is much lower than the value recorded under 3 MPa. It is likely related to gas pathways being more tightly restricted under higher confining stress. The obtained values are reported in Table 3.2. The detected GBP values of re-compacted samples S0-C and S0-S are significantly greater than those measured under a confining pressure of 3 MPa. Notably, the higher GBP values clearly indicate that re-compaction is able to effectively seal channels induced by prior gas transport.

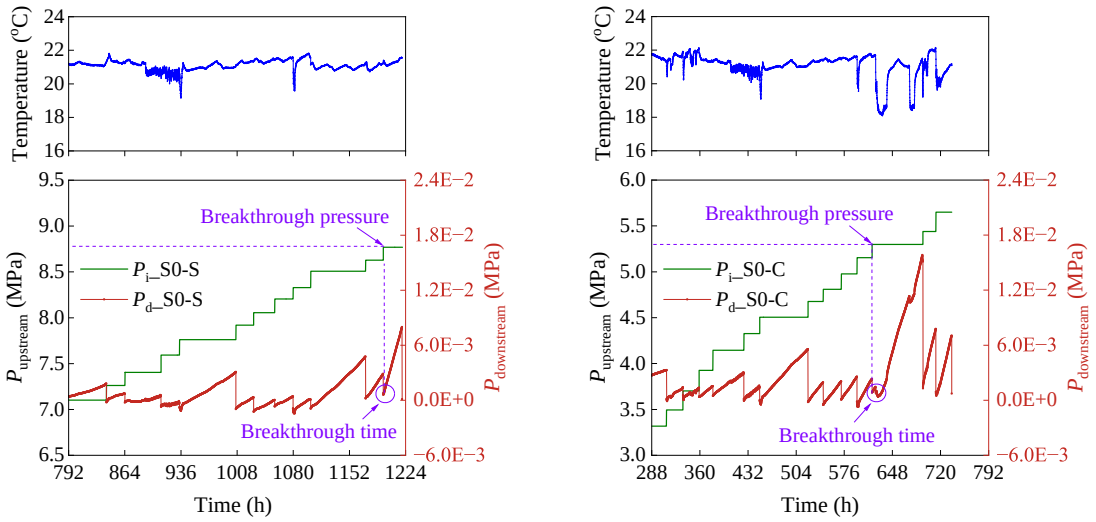

(a) intact sample **(b)** cracked sample

Figure 3.5: GBP of (a) intact sample S0-S and (b) cracked sample S0-C under 12 MPa confining pressure.

3.1.1 Thermal effect on breakthrough pressure

Combining Fig. 3.3 and Fig. 3.5, it can be observed that the $P_{downstream}$ exhibits significant fluctuations during the early stage of the test, mainly due to the influence of surrounding temperature. Such fluctuations may lead to potential misinterpretation, as it could be taken as a breakthrough signal, whereas no gas flow is detected when the downstream valve is opened. It just reflects the sensitivity to external thermal disturbances. Thus, the gas check at the downstream is essential, as relying solely on $P_{downstream}$ may result in inaccurate identification and even underestimation of breakthrough pressure. In contrast, once the formation of continuous gas pathways, $P_{downstream}$ increases stability and shows little sensitivity to temperature fluctuations. It indicates that the influence of temperature is significant before gas breakthrough occurs but limited once the pathway is formed. Although the breakthrough signal is dominated by the gas flow itself, the subsequent experiments are conducted under stable temperature conditions to avoid premature breakthrough.

3.1.2 Time-Dependent behavior of breakthrough pressure

Another important factor observed in the gas breakthrough test is the role of time dependence. Specifically, with longer duration, $P_{downstream}$ gradually increases even under

relatively low $P_{upstream}$. It is inferred that a breakthrough could occur with relatively low upstream pressure, provided that the injection time is sufficiently long. In other words, the breakthrough pressure is not only a function of the injected upstream pressure but also depends on the duration of gas migration. This time-dependent effect implies that the breakthrough pressure may be underestimated. Consequently, the influence of time should be minimized by maintaining consistent time intervals between pressure increments to ensure a reliable determination of breakthrough pressure.

3.1.3 Re-compaction effects on the crack closure

It is worth noting that previous studies by Zhang (2015) and Wang et al. (2024) investigated the effect of re-compaction on self-sealing under confining pressures ranging from 2 to 14 MPa. The more distinct pressure dependence is observed in Fig. 3.6, sample S0-S is a resaturated intact sample, whereas the others are resealed cracked samples. A clear trend is observed wherein GBP increases with confining pressure, reflecting the role of mechanical constraint on sealing performance. Notably, the GBP values of the re-compacted samples are much higher than the previous values. The sample S0-S exhibits the highest GBP under high confinement, significantly exceeding that of cracked samples under comparable conditions. The sealing behavior is likely due to enhanced microstructural uniformity and reduced pore connectivity resulting from re-compaction. In contrast,

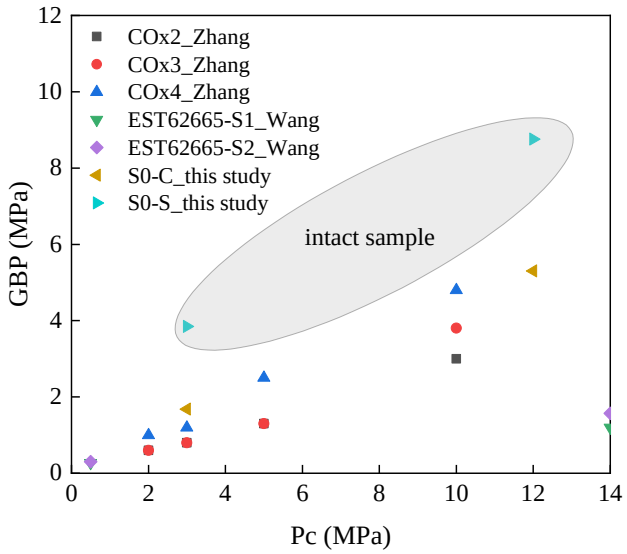

Figure 3.6: GBP performance of re-compacted claystone under varying confining pressure (Zhang, 2015; Wang et al., 2024).

cracked samples show consistently lower GBP values compared to intact samples, even at higher confining pressures, indicating that residual pathways remain despite partial self-sealing. The results align well with reported studies, confirming the critical role of compaction and confinement in governing gas migration resistance in COx claystone.

3.2 GBP of saturated samples in mock-up II

The gas breakthrough tests are conducted on saturated samples from mock-up II under a constant confining pressure of 5 MPa, consistent with the self-sealing test. The GBP value of resealed samples S1-C and S2-C is detected at 0.9-1.0 MPa, as shown in Fig. 3.7(a). As the determination of GBP by the detection of gas-water mixture flow is quite an empirical technique, we try to propose here a more optimized method. For this purpose, the relationship between the increasing rate of downstream pressure $P_{downstream}$ and the upstream pressure $P_{upstream}$ is studied and the obtained results are presented in Fig. 3.7(b). It is very interesting to observe that there is a clear change of the downstream pressure variation rate for a specific value of the upstream pressure. This specific value can be identified as the gas breakthrough pressure (GBP). The main value obtained is reported in Table 3.3. The GBP by gas pressure rate is 0.92 MPa. For sample S1-S, the breakthrough pressure could not be reliably determined, as the gas breakthrough test was not carried out in time and cracks had already developed on the surface. Moreover, the monitoring data of sample S2 is also not obtained, but the GBP values of samples S2-C and S2-S are detected at 0.92-1.15 MPa and 6.40-6.77 MPa, respectively. The value of

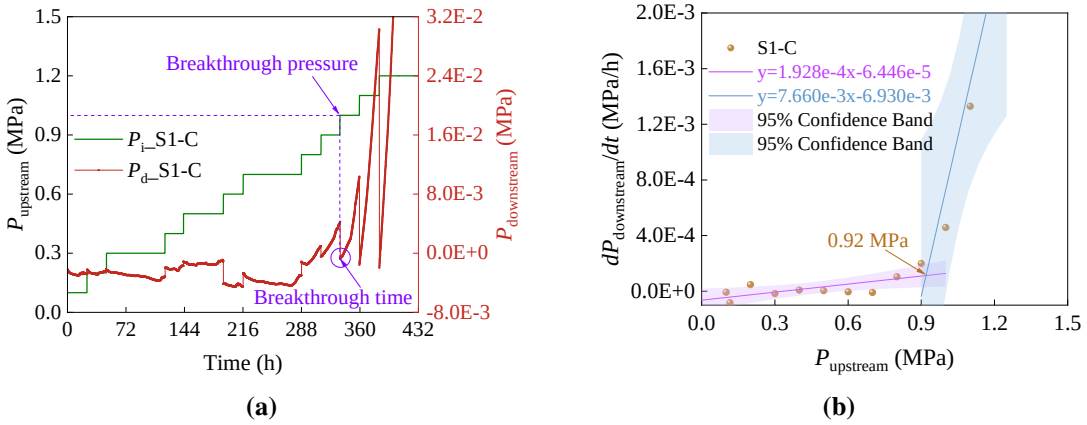

Figure 3.7: GBP of cracked sample S1-C (a) gas pressure, (b) relationship between increasing rate of $P_{\text{downstream}}$ and P_{upstream}.

sample S2-S is close to the reported value of 6.2–6.4 MPa for the intact saturated sample from EST 58145 (Wang et al., 2022a). It is observed that the GBP for cracked samples is also lower than that of intact sample.

Table 3.3
Results of gas breakthrough test on mock-up II.

Mock-up	Mock-up II			
	S1-C	S1-S	S2-C	S2-S
GBP by gas detector (MPa)	0.90-1.00	/	0.92-1.15	6.40-6.77
GBP by gas pressure rate (MPa)	0.92	/	/	/

3.3 GBP of saturated samples in mock-up III

The gas pressures at the upstream and downstream of saturated samples S3, S4 and S5 are shown in Fig. 3.8. During the test, the breakthrough time may need days or even weeks for one sample measurement depending on the degree of re-saturation and fracture closure. It is found that except for the set of samples S3, the GBP for cracked samples is higher than that of intact samples, as reported in Table 3.4. This result appears to be unconventional as the cracked samples usually contain more cracks than the intact ones and should enhance gas flow. At the same time, due to the presence of a preexisting main fracture, the hydration process upon water penetration can be facilitated for the cracked samples. This can lead to a deeper resaturation zone inside the cracked samples than the intact ones, resulting in a stronger swelling deformation and a quite complete closure of the main fracture and secondary cracks. It is therefore possible to obtain a higher GBP for the cracked samples. Unfortunately, the quantitative water content measurement is very complex and not completed in those tests. The present analysis is based on plausible

Table 3.4
Results of gas breakthrough test on mock-up III.

Mock-up	Mock-up III					
	S3-C	S3-S	S4-C	S4-S	S5-C	S5-S
GBP by gas detector (MPa)	1.52–1.61	2.52–2.65	5.45–5.59	3.30–3.42	5.81-5.91	1.71-1.86
GBP by gas pressure rate (MPa)	1.50	2.53	5.25	3.26	5.83	1.67

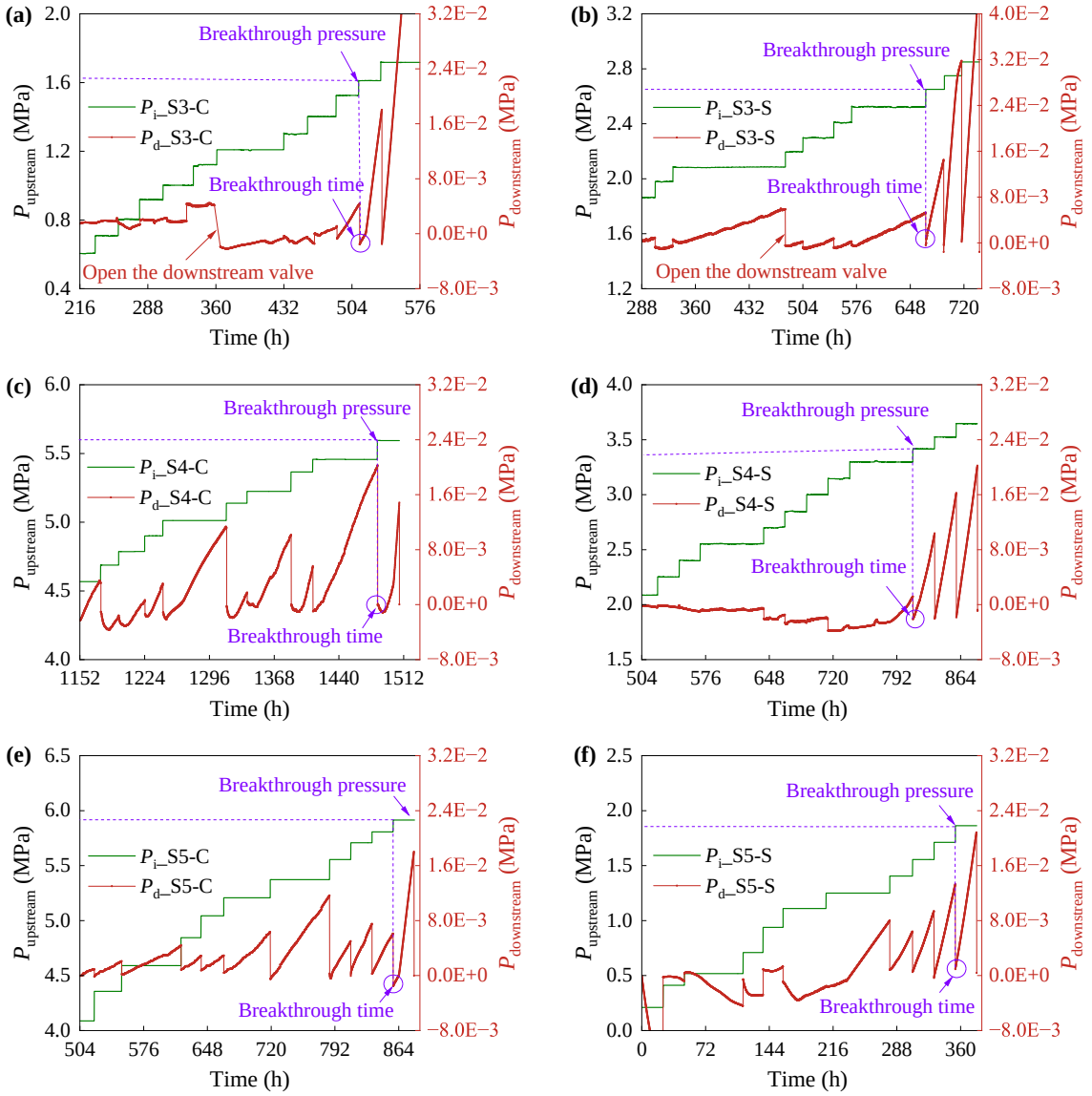

Figure 3.8: Gas pressure evolution during the gas breakthrough test for resealed samples (a) S3-C, (c) S4-C and (e) S5-C, and re-saturated samples (b) S3-S, (d) S4-S and (f) S5-S.

reasoning and needs to be confirmed by complementary studies.

The relationship between the increasing rate of downstream pressure $P_{downstream}$ and the upstream pressure $P_{upstream}$ is also studied and the obtained results are presented in Fig. 3.9. It is also observed that for each sample, there is a clear change of the downstream pressure variation rate for a specific value of the upstream pressure. The values obtained by this method are also reported in Table 3.4. It is interesting to notice that the values provided by this analytical method are quite close to those identified by the gas detection

technique. This clearly indicates that the outlet flow of gas is accompanied by a rapid increase of downstream gas pressure.

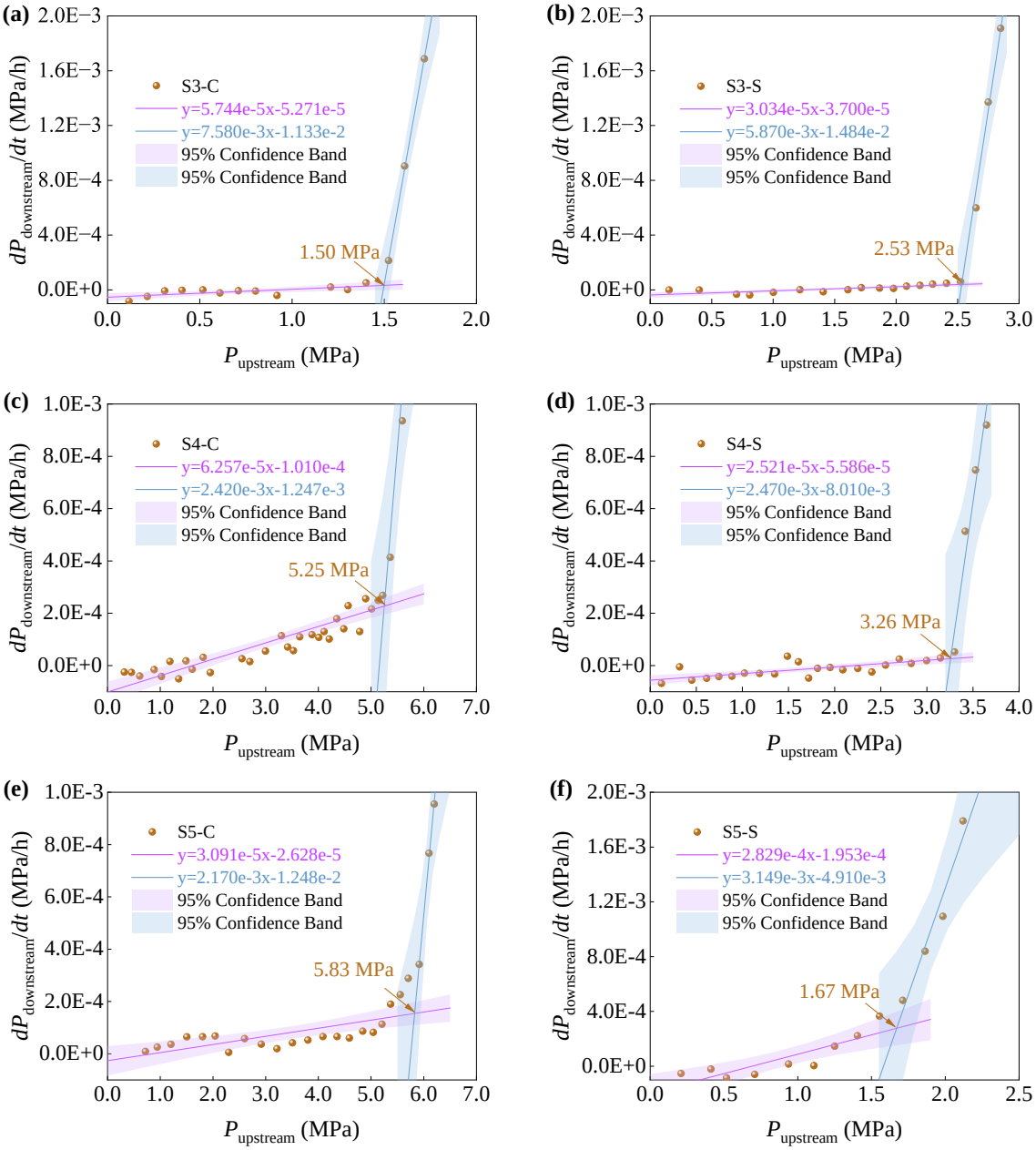

Figure 3.9: Relationship between increasing rate $dP_{\text{downstream}}/dt$ and P_{upstream} for resealed samples (a) S3-C, (c) S4-C and (e) S5-C, and re-saturated samples (b) S3-S, (d) S4-S and (f) S5-S.

3.4 GBP comparison in intact and cracked samples

Following the previous discussion, we attempt to compare the gas breakthrough pressures obtained from this study with reference values, as shown in Fig. 3.10, while accounting for factors such as sample height and confining pressure (P_c). In mock-up II and III, due to the presence of a steel tube, the sample is not subjected to external confining pressure but is instead influenced solely by internal swelling pressure. Therefore, the swelling pressure can be considered as the effective confining pressure for comparative analysis. The color scale indicates sample height, providing an additional reference for explaining GBP behavior. Generally, GBP value of cracked samples is lower than that of intact samples. Cracked samples exhibit the lowest GBP values, generally below 2 MPa, indicating that residual fractures remain preferential gas pathways despite partial self-sealing. In contrast, intact samples display significantly higher GBP values, ranging from 4 to 12 MPa.

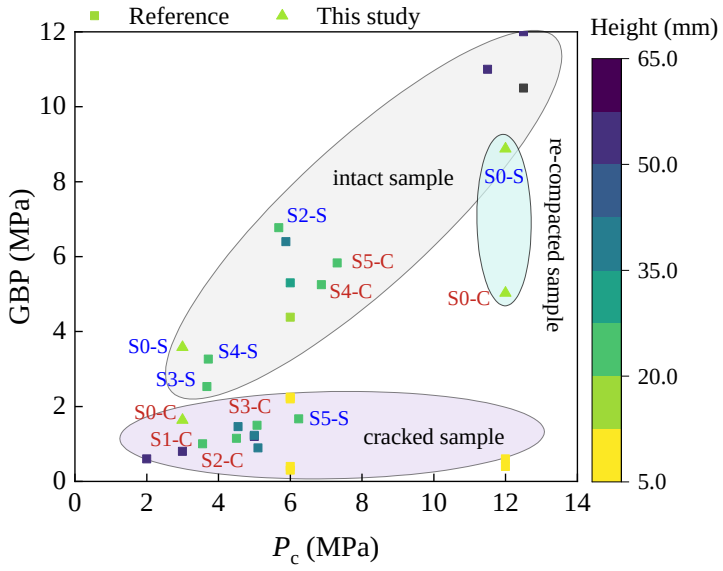

Figure 3.10: Comparison of GBP experimental values from this study and reference values (Zhang, 2015; Song et al., 2016b; M'Jahad et al., 2017; Chen et al., 2022; Wang et al., 2022a).

However, compared to literature results (Song et al., 2016b; Chen et al., 2022; Wang et al., 2022a), the gas breakthrough pressure of resaturated intact samples is relatively low in this study. It seemed that the intact sample is damaged when the composite sample is disassembled, as seen in Fig. 3.1. This could explain why there is low breakthrough

pressure of the intact sample in the gas breakthrough tests. Samples S4-C and S5-S from mock-up III have higher GBP values than others. It is possible that these resealed samples have higher swelling pressures. This feature will be discussed in a later section. Notably, in the gas breakthrough test on re-compacted samples, the GBP values of cracked samples are also lower than those of the intact samples. This suggests that although self-sealing can close the fracture, it may not be sufficient to fully restore resistance to gas migration to the level of undisturbed material. The residual weakness in the original fracture zones may still provide preferential pathways for gas migration under higher gas pressure.

Furthermore, the comparison indicates that both the confining pressure and the sample height influence the measured GBP. An overall increasing trend of GBP with confining pressure can be observed, while specimens with greater heights generally exhibit higher GBP values. This behavior can be attributed to enhanced fracture closure under higher confinement and the longer gas migration path in higher specimens. However, the considerable scatter suggests that additional factors, such as fracture geometry, self-sealing efficiency and material heterogeneity, also play important roles.

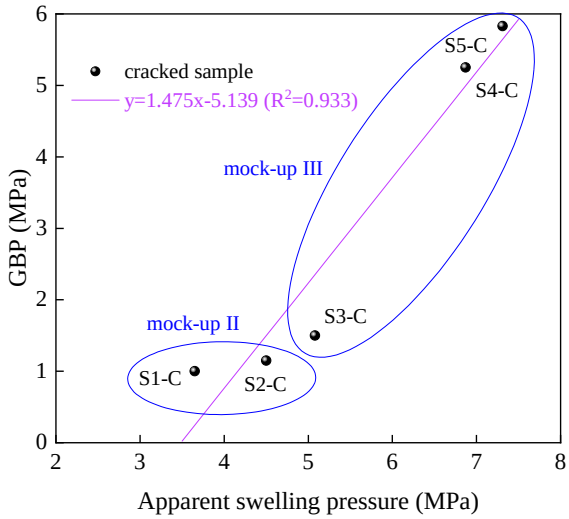

Figure 3.11: Gas breakthrough pressure as a function of apparent swelling pressure.

3.5 Analysis of GBP related to swelling pressure

As the GBP is affected by the sealing state after the water injection phase, in particular of main fracture, it is thus interesting to investigate the relationship between GBP and swelling pressure. In Fig. 3.11, the values of GBP for five cracked samples are plot-

ted versus those of apparent swelling pressure. A linear correlation line is found. It is interesting to notice that the value of GBP is positively correlated with that of swelling pressure. It indicates that under a high swelling pressure, the main fracture and secondly cracks are well sealed, leading to a high gas breakthrough pressure.

4 Resealing of gas-induced pathways

During the gas injection tests, the gas flow may induce opening of microcracks and main fracture. In order to evaluate the consequences of gas flow-induced pathways, water injection is completed at the end of gas injection tests. The water permeability values for the different samples are plotted in Fig. 3.12. In general, there is a decrease of water permeability with resaturation. This indicates that the pathways created by gas flow are progressively resealed by the rejection of water. Comparing the various samples tested, there are great differences between the samples from mock-up II and mock-up III. For mock-up I, the initial water permeability of cracked samples S1-C and S2-C is higher than those of intact samples S1-S and S2-S, as shown in Fig. 3.12(a). This implies that the main fracture can still serve as a preferential pathway for gas flow, and an important opening of the main fracture in this sample has been induced.

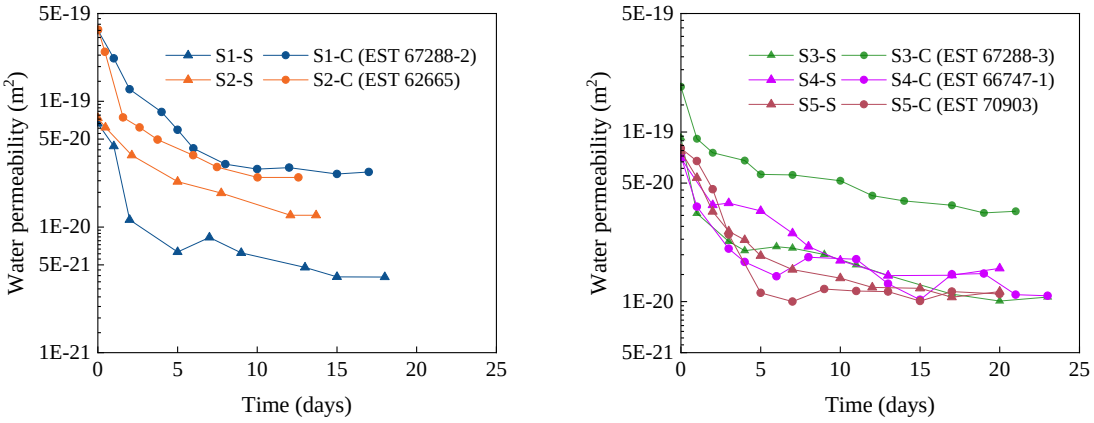

(a) samples of mock-up II **(b)** samples of mock-up III

Figure 3.12: Water permeability of cracked and intact samples after GBP test.

For mock-up II, there are small differences between the samples S4-S and S4-C as well as between S5-S and S5-C (see Fig. 3.12(b)). It seems that for these two sets of samples, the main fracture in the cracked sample is not significantly opened by gas flow

so that its presence has a negligible effect on the subsequent evolution of water permeability. However, for the mock-up S3, the sample S3-C shows a much larger initial permeability (around 1.85×10^{-19} m^2) than those of other samples ranging from 6.99 to 9.25×10^{-20} m^2. This indicates that the gas flow has induced an important opening of the main fracture in this sample. Moreover, the kinetics of permeability decrease of S3-c is also slightly slower than that of the other samples. At the end of test, its permeability is approximately equal to 3×10^{-20} m^2, whereas the value of the other samples reaches 1×10^{-20} m^2. Therefore, the re-sealing process of the sample S3-C is less complete than the other samples. This difference can be related to the morphology of main fracture created in S3-C, such as average opening and tortuosity. A quantitative morphological description of main fracture will be very helpful in future study.

As discussed in Section 3.5, the lower resaturation of intact samples than in previous studies is one of the reasons for its lower GBP value in this study. In order to check this feature, at the end of resealing the gas-induced pathways, second gas injection tests are conducted on the samples S5-S and S5-C. The breakthrough pressures are equal to 2.5 MPa and 6 MPa for S5-S and S5-C, respectively. These values are higher than those obtained in the first phase of gas injection, 1.67 MPa and 5.83 MPa, in particular for the sample S5-S. This increase can be explained by a better water resaturation of the samples after two phases of water injection.

4.1 Resealing effects on the fracture closure

Poiseuille's law is employed to calculate the equivalent fracture aperture for evaluating the resealing effect on the cracked sample. During the gas breakthrough test, gas initially migrates through the weakest or least sealed zone of the cracked sample. To this purpose, the gas flow path is assumed to lie within the fracture, and the fracture is assumed to be simply modeled as two parallel planes. This simplified representation allows the use of Poiseuille's law to estimate the equivalent fracture aperture and evaluate the extent of fracture closure (Wang et al., 2022a). For an incompressible liquid under steady-state flow conditions, the equivalent fracture aperture can be estimated

$$e = \sqrt[3]{3\pi d K_{aw}} \tag{3.1}$$

where e is the equivalent fracture aperture, d is the width of the fracture plane (per-

pendicular to the flow direction).

The results obtained are presented in Fig. 3.13. It shows that the equivalent fracture aperture of cracked samples decreases significantly during the first 7 days of hydration. The initial fracture aperture of samples S1-C and S2-C is approximately 0.40 µm and 0.41 µm, while samples S4-C and S5-C are 0.24 µm and 0.25 µm, respectively. It proved that gas flow has induced a more important opening of the main fracture in the samples S1-C and S2-C than in others. After resealing, the final residual fracture aperture is around 0.17 µm for samples S1-C and S2-C, and 0.13 µm for samples S4-C and S5-C. The aperture of sample S3-C decreases from 0.33 to 0.18 µm. This residual aperture suggests partial but effective fracture sealing in all samples.

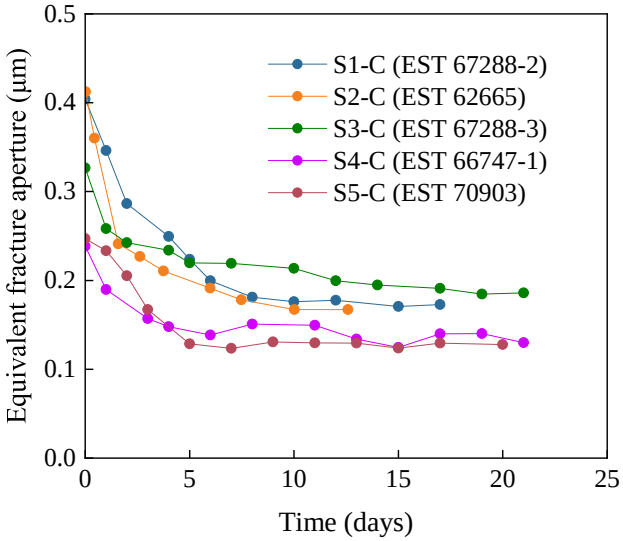

Figure 3.13: Equivalent fracture aperture evolution of cracked sample.

After all testing, the samples are disassembled from the cell and then freely dried in the air. The post-test dried samples from mock-ups II and III are presented in Fig. 3.14. The black masked line represents the orientation of a preexisting main fracture in cracked samples. The bedding plane can be seen clearly in the dried sample, which is yellow-masked. This is consistent with the Fig. 2.3. It is useful to point out that the results presented in this work relied on a single test for each configuration, although maximum care is taken in order to minimize sample variability as much as possible. Due to the experimental complexity and long test duration, we have not discussed the repeatability of tests. Additional tests are expected to address this important issue.

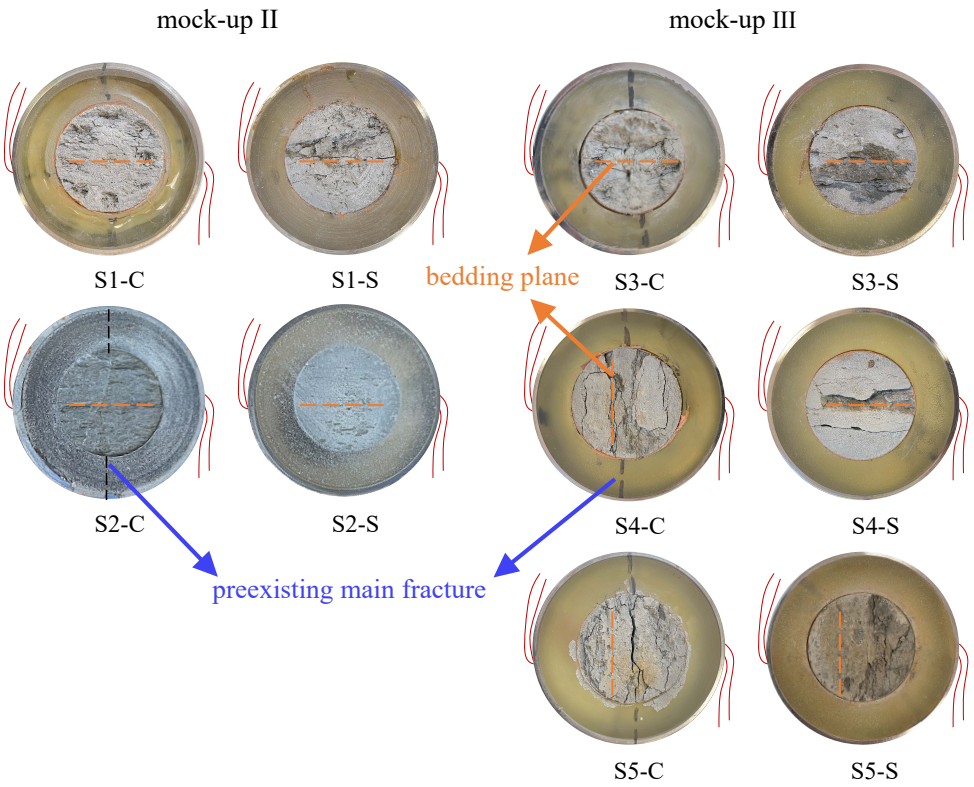

Figure 3.14: Post-test dried samples comparison using mock-ups: cracked sample and intact sample.

5 Conclusions

This chapter investigates gas migration behavior in sealed fractured COx claystone based on gas breakthrough pressure (GBP) and resealing tests conducted on water-saturated samples (intact and fractured samples) from different experimental models. Based on the above results and analysis of gas breakthrough and resealing tests, the following conclusions can be drawn:

(1) Gas breakthrough pressure provides an interesting measurement of the self-sealing state of samples. However, the gas breakthrough pressure can be affected by multiple factors, including the distribution of initial microcracks, the morphology of macroscopic fractures and mechanical loading conditions such as confining stress. With a high number of microcracks and irregular fractures, the self-sealing is more difficult to complete, and the gas breakthrough pressure of cracked sample is generally lower than that of intact one. Such results have been found in a number of previous studies. In the present studies,

some different results are obtained. Further investigations are needed by incorporating micro-structural analysis of cracked zones and varying loading conditions.

(2) Re-compaction is critical in preventing gas breakthrough and effectively compresses pathways activated after gas breakthrough. It is found that gas breakthrough has a strong time dependence, making it possible even at low injection pressures if the duration is sufficient. However, temperature variations have little effect on breakthrough pressure determination.

(3) As another interesting result, the gas breakthrough pressure is positively correlated with the swelling pressure. A higher swelling pressure, indicating a good self-sealing state, corresponds to a higher gas breakthrough pressure. The gas flow-induced pathways can be re-sealed by subsequent water injection. Water permeability can be reduced by 1 to 2 orders of magnitude.

Note: Results of Chapter 2 and Chapter 3 had been published in 'International Journal of Rock Mechanics and Mining Sciences'.

CHAPTER 4

Self-sealing investigation in pre-cracked claystone using X-ray micro-tomography and digital volume correlation

1 Introduction

As discussed in Chapter 2, the self-sealing capability of COx claystone is of critical importance, allowing partially closed fractures to recover when the crack is subjected to indirect water injection. Several experimental studies using various setups (Zhang, 2011; Auvray et al., 2015; Wang et al., 2024), particularly those employing the X-ray tomography technique (Giot et al., 2019; Agboli et al., 2024), have confirmed the self-sealing behavior. Di Donna et al. (2022) first observed the diffusion deformation mechanism through Digital Volume Correlation (DVC), which is a progressive swelling propagating through the whole sample from the initial central fracture. However, there is very little information on the self-sealing process driven solely by the swelling of the rock matrix expansion without direct water loading to fracture. In this chapter, we discuss the impact of fracture geometry, initial fracture opening and injected pressure on the self-sealing process of artificial fractures in cylindrical COx claystone samples under indirect water injection. The first part introduces the samples characteristics used and the designed model, followed by a detailed description of the designed triaxial compression cell, the experimental device and protocol, and the data processing method. The second part focuses on the analysis and discussion of the experimental results to identify the dominant mech-

anisms and temporal evolution of the self-sealing process. To study this phenomenon, a series of permeability and scanning tests were conducted on COx claystone samples. Gas permeability measurements were continuously taken throughout all tests, while 3D X-ray micro-tomographic scans with high spatial resolution were performed before, during, and after testing. The reconstructed tomographic images were analyzed using Avizo and ImageJ software to visualize and quantify the evolution of fracture opening and sample diameter. In addition, DVC analysis was applied on the tomographic data to evaluate the deformation field for further characterizing the microstructural response under loading. To our knowledge, there are no similar studies in the literature characterizing the self-sealing process of clayey rocks under indirect water injection conditions. The results therefore contribute to a better understanding of the mechanisms governing self-sealing and provide experimental data for future numerical model validation.

2 Sample preparation and equipment

2.1 Materials and model design

The samples used in this work were sourced from the original rock cores EST 66747 and EST 72793. Cylindrical samples were drilled parallel to the bedding plane of the COx claystone layer (see Chapter 2 for details), each with a diameter and length of 20 mm. To simulate through-going fractures, four types of fracture geometry were designed, as illustrated in Fig. 4.1. Crack CG1 was created by initially cutting the sample along the central axis. One of the halves was machined using precision instruments to produce a fracture with a length of one-third of the diameter and a width of 0.4 mm. Crack CG2 was generated using the Brazilian splitting test, making an artificial fracture with an average width of 0.1 mm. Crack CG3 was obtained by cutting the sample into two halves, sealed with silicon on both sides, with the fracture opening controlled at 0.4 mm and the fracture length set to 17 mm. Crack CG4 was created by drilling a cylindrical artificial aperture with a diameter of 1 mm through the sample. These fractures were parallel to the bedding plane. The initial condition of tested samples and their fracture geometry were presented in Table 4.1. Because of an experimental handling error, the initial fracture opening of sample EST 72793-1 was approximately 2 mm. The chemical composition of injected water is similar to that of groundwater in situ, as seen in Table 2.2.

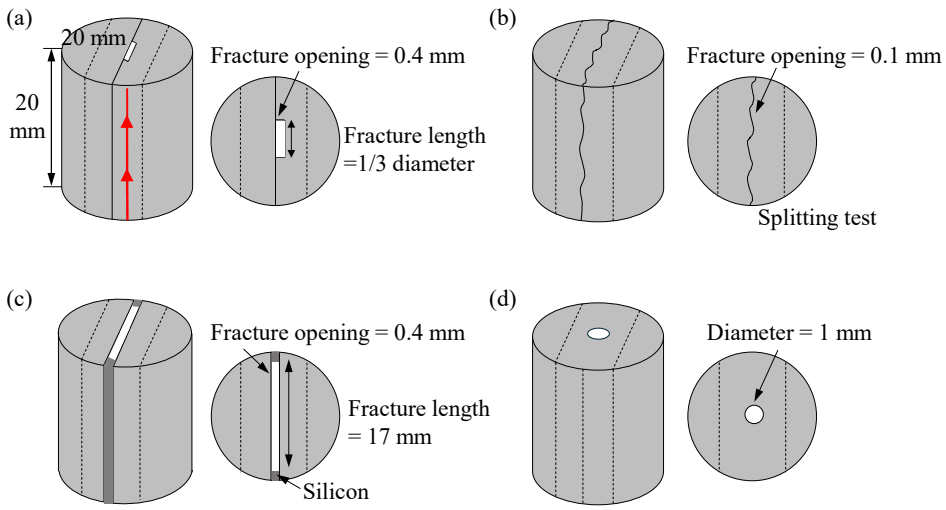

Figure 4.1: Schematic illustration of artificially cracked geometries: (a) crack CG1, (b) splitting crack CG2, (c) cutting crack CG3, and (d) artificial hole CG4.

Table 4.1
Initial conditions and geometric characteristics of testing samples.

Samples reference	Fracture gerometry	Fracture opening (mm)	Water content (%)	Confining pressure (MPa)
EST 66747-2	CG1	0.467	6.75	0.3
EST 66747-3	CG2	0.100	6.75	0.3
EST 66747-4	CG3	0.413	6.75	0.3
EST 72793-1	CG3	2.116	6.40	1.0
EST 72793-2	CG4	0.992	6.40	1.0

In order to follow indirect water injection during the test, a new cylindrical model was designed, featuring two symmetrically distributed circular holes on its lateral wall that served as injection channels. Noting that the two lateral injection holes are perpendicular to the main fracture, preventing water from getting through to them directly. The preparation procedure of this model is presented in Fig. 4.2(a). The sample was placed inside the model with a 37 mm diameter and two plastic cylinders with a diameter of 12 mm and a height of 10 mm were glued to both ends of the sample with silicone adhesive. These plastic cylinders were used only during model preparation, with the primary purpose of ensuring the formation of continuous gas flow pathways in subsequent processing steps. Owing to their brittle properties, they can be easily removed while preventing any disturbance or secondary damage to the sample fracture itself and its fracture geometry during

drilling or machining operations. The remaining void space between the sample and the model was filled with degassed epoxy resin. Before making, a thin layer of silicone was applied over the sample surface and insulating tape was wrapped around both ends to prevent direct contact between the sample and the liquid epoxy resin. The white parts in Fig. 4.2(b) correspond to the insulating tape. After pouring, the epoxy resin was allowed to fully solidify at room temperature for approximately 48 hours. Once fully solidified, the plastic cylinders at both ends were removed and the fracture orientation was masked on the model. Then, two circular holes were symmetrically drilled at the midpoints on both sides perpendicular to the fracture as the injection channels.

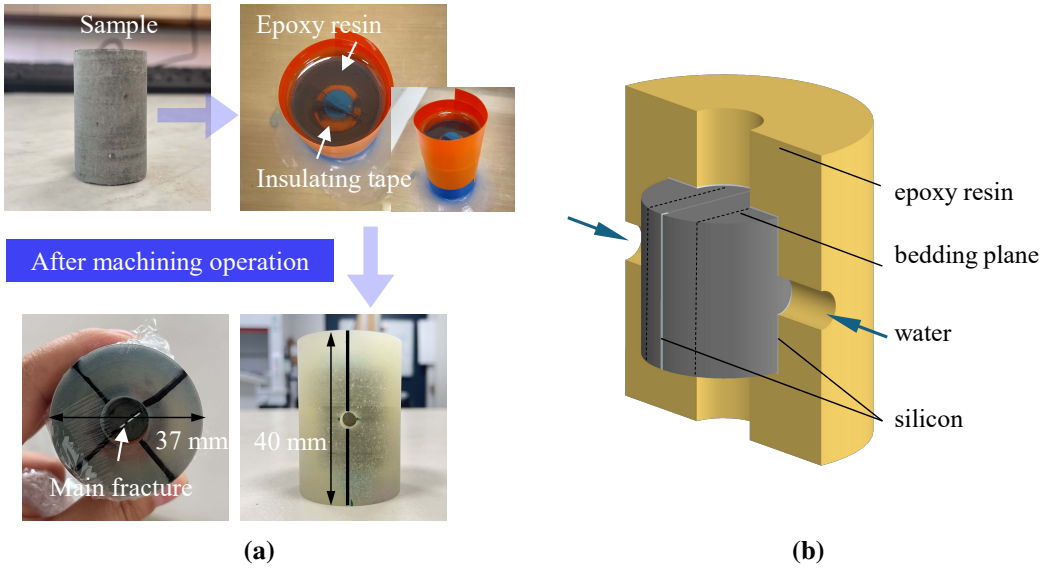

Figure 4.2: Preparation procedure (a) and schematic configuration (b) of the indirectly injected water model.

2.2 Experimental device

An innovative mini-triaxial cell, designed for testing cylindrical models with a diameter of 37 mm, has been developed, as shown in Fig. 4.3(a) and Fig. 4.3(c). The particularity of this design is its polycarbonate construction, which is transparent to X-rays, enabling the tracking of fracture evolution within the same sample at different times under a high-resolution X-ray micro-tomography scanner. This triaxial cell is designed to simultaneously feature confining and gas pressure loading paths. The lateral and lower inlets are used for fluid and gas injection, respectively, both supplied using pressure pumps through flexible connections. The confining pressure chamber is filled with water to en-

sure uniform isotropic confinement around the sample and the pressure can be precisely controlled using a servo pump. The gas–water injection system is illustrated in Fig. 4.3(b). During the tests, water is continuously injected through the side channels to simulate indirect hydration-induced fracture closure, while gas is injected from the bottom to monitor permeability evolution. This configuration allows coupled control of hydraulic and gas conditions while maintaining compatibility with X-ray imaging, thereby enabling in situ characterization of the self-sealing process. Fig. 4.3(d) shows the photograph of experimental setup. It consists of a triaxial compression cell, a water pump with a maximum pressure of 3 MPa, a gas pump and a LabView-based data acquisition system for continuously recording the upstream pressure. The model containing the artificially fractureed sample was placed into the triaxial cell.

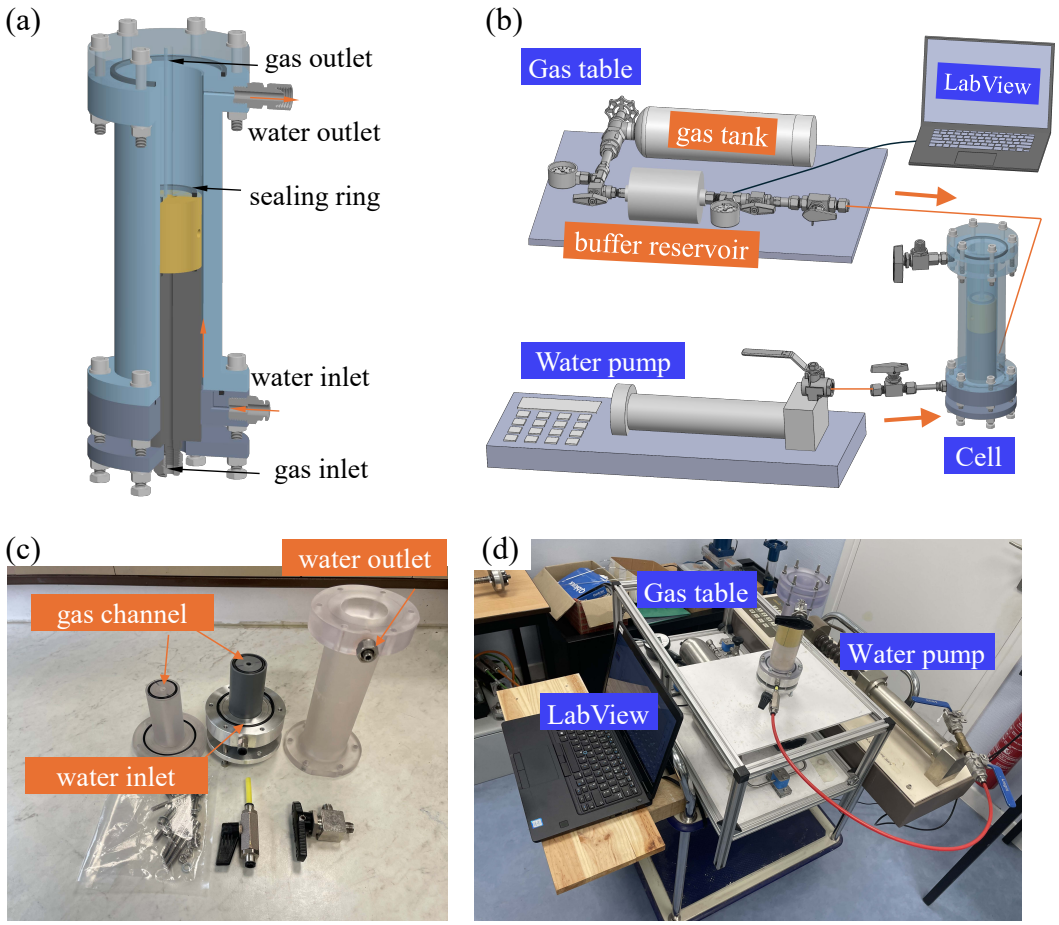

Figure 4.3: Schematic views and photographs of the triaxial compression cell and the gas–water injection system: (a) triaxial compression cell, (b) gas–water injection system, (c) triaxial cell components, and (d) experimental setup.

2.3 X-ray micro-tomography acquisition

The characteristics of claystone fracture evolution during the self-sealing process were conducted on the In-Situ Innovative Setups under the X-ray micro-tomography (ISIS4D) platform using a computational tomography system Ultra TomR from RX Solution (Limodin et al., 2013), as seen in Fig. 4.4. The triaxial cell was placed on a rotating stage in the tomography between the X-ray source and the detector. The X-ray source is a high-resolution X-ray tube, with the acceleration voltage set to 160 kV. A multipurpose flat-plane detector (1874×1496 pixel, pixel size 127 μm) has been selected. To characterize the 3D microstructural evolution of COx samples, X-ray scans with a resolution of 16 μm voxel size were performed on the same area of each sample before and after water injection. For each scan, 1440 projections were acquired as the sample rotated 360° along its vertical axis, with a total acquisition time of 48 min per scan.

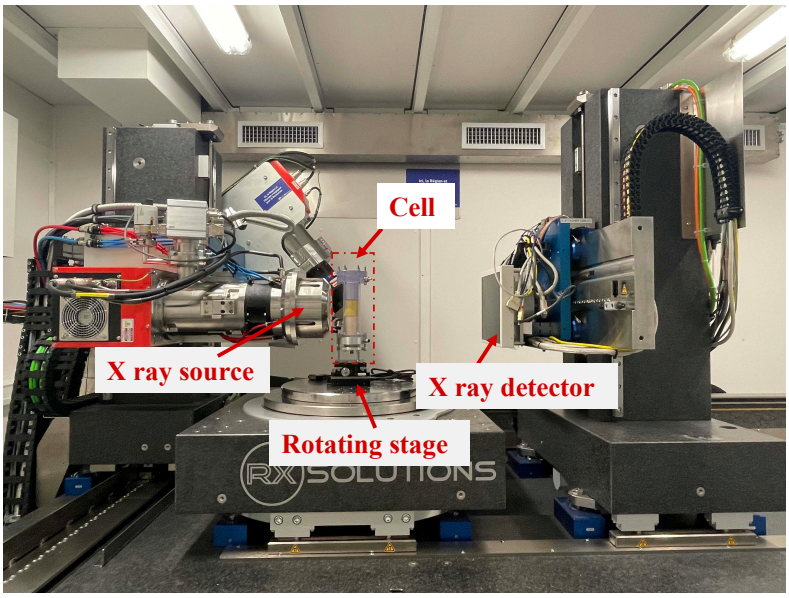

Figure 4.4: The triaxial compression cell enclosed within the X-ray micro-tomography scanner.

The acquired radiographs were reconstructed into each tomogram with a filtered back-projection algorithm (Kak and Slaney, 2001) using the software X-Act UniCT module (version 23.04.01) developed by RX Solutions. During data acquisition, non-uniform detector responses and system geometric deviations may lead to ring artifacts or image blurring (Rashid et al., 2012). To obtain quality images, the reconstruction algorithm incorporates spot correction, geometric correction and ring filtering optimization to remove

artifacts and enhance image clarity. The reconstruction produces tomographic slices in three orthogonal directions, among which the Y-direction slices were selected for output and analysis in this study. The results were exported as 8-bit grayscale raw files. It should be noted that the minimum and maximum gray values of each reconstructed data were set identically to ensure comparability across scans conducted at different times and maintain consistency in image display.

3 Experimental methods and procedure

Prior to testing, gas permeability measurement and X-ray scans were conducted to record the initial shape of the fracture as a reference for the experimental process. Just after, synthetic water is injected from the inlet at a hydrostatic pressure to saturate the sample through the symmetrical holes in the model, simulating the fracture closure process under low confining pressure. In this study, the confining pressure was maintained at 0.3 MPa and 1 MPa. Once the confining pressure has stabilized for several hours, a second X-ray scan and gas permeability measurement are performed to determine the water infiltration pathway. The test continues as long as water does not enter the main fracture directly. The confining pressure was kept constant during the test.All tests are conducted at a room temperature of 21°C.

3.1 Gas permeability measurements

Gas permeability is determined at equilibrium using Darcy's law for gas flow. In this study, argon is used as the injection gas, injected at intervals with an initial upstream pressure of 0.1 MPa, while the downstream remained at atmospheric pressure. As seen in Fig. 4.3(b), pressure measurement is recorded for the pressure variations in the buffer reservoir and connecting tubing based on the steady-state flow method. The calculation of laboratory-measured gas permeability K_g is seen in Section 3.1.

3.2 Data reconstruction and processing

Avizo software was employed to render the 3D reconstruction of samples, as shown in Figs. 4.5 to 4.9, where five horizontal slices (slices 200, 400, 650, 900 and 1100) perpendicular to the sample axis are selected and subsequently analyzed over time. The slices are

numbered from bottom to top, and slice 650 corresponds to the water-injected channels. Prior to image analysis, a media filter was employed to homogenize the images by reducing the amount of noise and preserving structural details. Registration and resampling were essential for the automatic alignment of corresponding slices within the sample, ensuring a consistent spatial reference despite irreversible deformations over time. A 3D mask was applied to distinguish the sample from the background, effectively separating the internal structure from its surroundings. As shown in slice 650 of Figs. 4.5 to 4.9, these slices illustrate the initial fracture geometries and the corresponding fracture openings of each sample. It is worth noting that the fracture type for sample EST 727937-1 was crack CG3. However, during sample preparation, partial epoxy resin blockage occurred within the fracture, and therefore a drill with a diameter of 2 mm was used for secondary processing to ensure proper fracture connectivity.

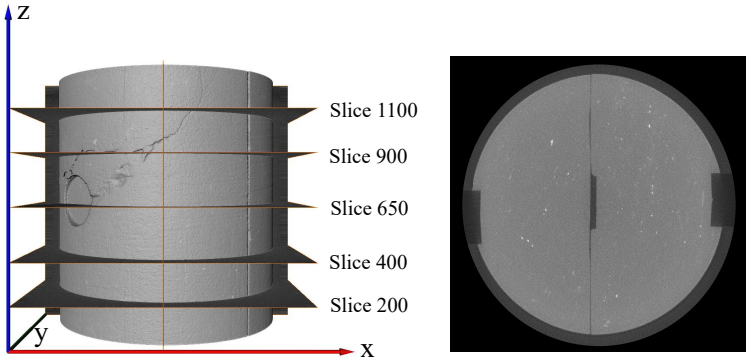

Figure 4.5: 3D reconstruction of sample EST 66747-2 and resampled 8-bit X-ray tomographic image at slice 650.

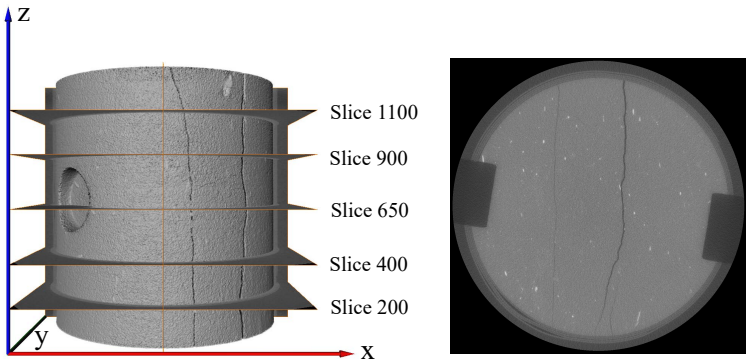

Figure 4.6: 3D reconstruction of sample EST 66747-3 and resampled 8-bit X-ray tomographic image at slice 650.

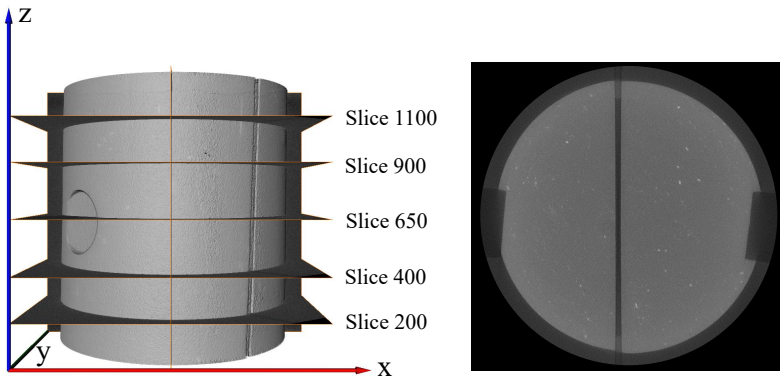

Figure 4.7: 3D reconstruction of sample EST 66747-4 and resampled 8-bit X-ray tomographic image at slice 650.

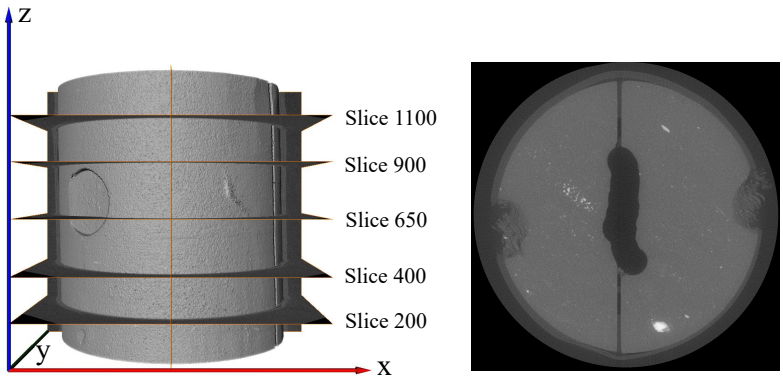

Figure 4.8: 3D reconstruction of sample EST 727937-1 and resampled 8-bit X-ray tomographic image at slice 650.

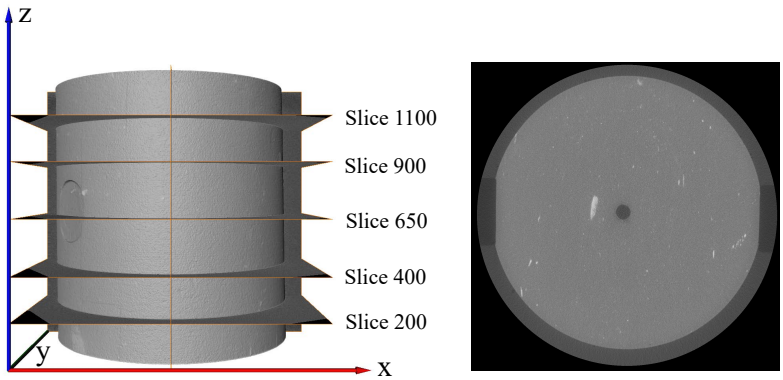

Figure 4.9: 3D reconstruction of sample EST 727937-2 and resampled 8-bit X-ray tomographic image at slice 650.

Fig. 4.10 presents the resampled tomographic images with the gray-level histogram for the selected image, where variations in gray levels observed across different regions reflect presences in claystone composition, fractures or other structural features. The two peaks of the gray level of the average histogram correspond to the epoxy resin around the sample and the COx matrix, respectively. A relatively low grayscale frequency is observed between these two peaks, representing the grayscale values of the fractures. These contrast counts between different materials facilitate their effective differentiation during the image segmentation process, thereby effectively quantifying the evolution of fracture opening and variations in sample diameter.

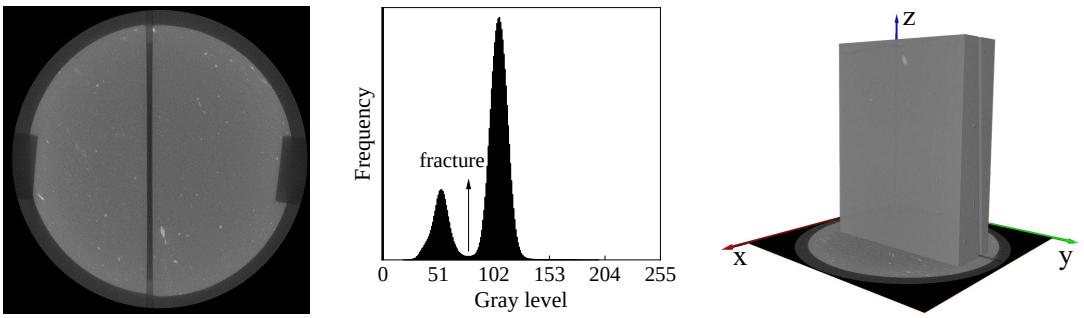

(a) masked image **(b)** gray-level histogram **(c)** fracture ROI

Figure 4.10: Resampled 8-bit X-ray tomography image (a) and gray-level histogram (b) of sample EST 66747-4, with fracture region of interest (ROI) in (c).

To further characterize the fracture evolution, ImageJ software was used for slice visualization and selection of a representative region of interest (ROI) to analyze the changes in fracture opening, as shown in Fig. 4.10(c). Image segmentation was performed using an objective and automated thresholding technique, such as Otsu's method or MinError's method, ensuring higher accuracy and consistency in the segmentation results. The outcome of the segmentation process was the generation of binary images, where the fracture structures were represented as connected regions composed of continuous voxels. The segmentation process generated a binary image in which the fracture structure is represented as a connected region composed of continuous voxels. To quantitatively analyze fracture opening, the BoneJ plugin (Domander et al., 2021) in ImageJ was used, providing a robust measurement of structural thickness at a local scale. The thickness algorithm defines the point thickness as the maximum diameter of the largest inscribed sphere within the binary image, thereby enabling precise determination of fracture opening. Additionally, ParaView software was further employed for three-dimensional reconstruction and

visualization of the fractures. High-resolution 3D rendering techniques provided a detailed representation of the spatial distribution and geometric characteristics of the fractures. This procedure effectively revealed the evolution of fracture morphology, providing valuable information for the mechanical properties and fluid migration behavior of claystone.

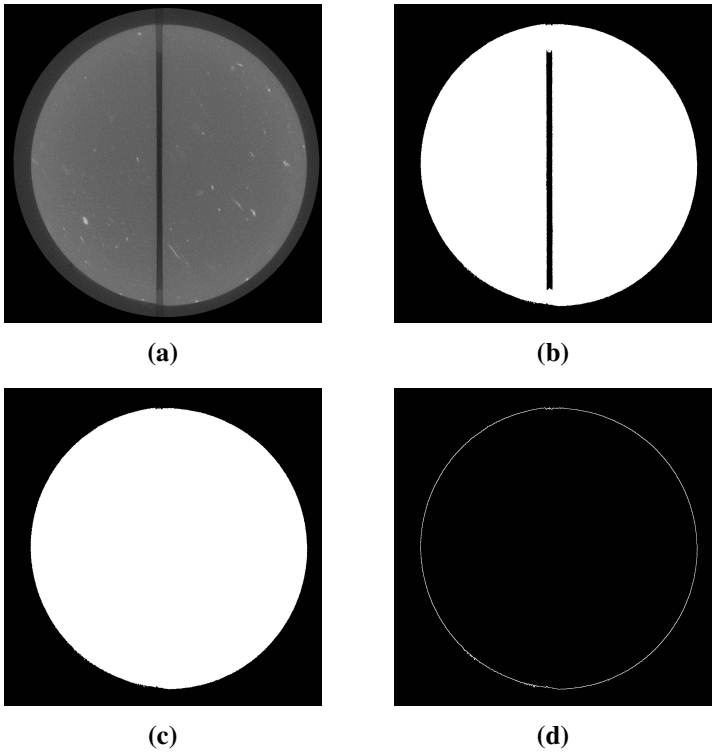

Figure 4.11: The procedure adopted for the edge segmentation from the X-ray 3D image: (a) resampled Image; (b) image segmentation; (c) enclosed holes; (d) sobel edge detection.

The expansion of COx claystone during water saturation was evaluated through quantifying changes in its diameter using a four-step image analysis, as seen in Fig. 4.11. First, image segmentation was applied to separate the sample region from the background, thereby precisely delineating the sample region within the entire image. In this step, the 8-bit image was converted into a binary image. Second, voids caused by imaging noise or material heterogeneity in the binary image were enclosed to ensure continuity in edge detection. To further refine boundary delineation, the Sobel edge detection algorithm was employed, followed by particle analysis to quantify the total area of the identified features, enabling a more comprehensive characterization of its morphology. Lastly, the equivalent average diameter was calculated from the segmented total area as a key parameter to

quantitatively assess the swelling process.

3.3 Digital Volume Correlation (DVC)

To measure the macroscale 3D kinematic field during the self-sealing test, the Digital Volume Correlation (DVC) technique was performed using the YaDICs platform (Yet Another Digital Image Correlation Software) (Seghir et al., 2014), an image processing platform developed in C++ by the Laboratoire de Mécanique Multiphysique Multiéchelle (LaMcube). It is an efficient image analysis platform for 2D and 3D correlation computation and has been widely employed for studying damage evolution and mechanical responses in geomaterials and composites (Hosdez et al., 2017; Berger et al., 2022; Shi et al., 2023). The fundamental principle of DVC is based on the gray-level conservation assumption between a reference image (f) and a deformed image (g). It aims to determine the transformation between these two images by optimizing a correlation metric, under the assumption that gray-level variations at different instants depend only on the displacement field.

$$f(\boldsymbol{x}) = g(\boldsymbol{x} + \boldsymbol{u}(\boldsymbol{x})) \tag{4.1}$$

where $\boldsymbol{u}$ denotes the displacement vector field at posisiton $\boldsymbol{x}$. The objective of DVC is to determine the best displacement field $\boldsymbol{u}$ by minimizing a correlation metric, with the Sum of Squared Differences (SSD) used as the correlation metric in this study.

$$SSD(\boldsymbol{u}, f, g) = \frac{1}{\Omega} \sum\nolimits_{\boldsymbol{x} \in \Omega} (f(\boldsymbol{x}) - g(\boldsymbol{x} + \boldsymbol{u}(\boldsymbol{x})))^2 \tag{4.2}$$

One notices that the optimization rule used herein is a steepest gradient descent algorithm (Cauchy et al., 1847) to easily treat such large volumes with a high degree of freedom, but there is no matrix problem to solve. With YaDICs platform, a set of key parameters needs to be defined, including the correlation metric, sampling strategy, interpolation method, transformation model, optimization algorithm and regularization method (Seghir et al., 2014). Bi-cubic interpolation was used to apply the transformation to the deformed image at each iteration. Additionally, median filtering was applied as a regularization technique at each pyramid level to reduce noise, improve displacement continuity and maintain structural discontinuities. A multi-scale resolution strategy

as a pyramid scheme with the correlation sequence of optical flow integrated (OFI) and optical flow elastic transformation based on finite element methods (OFFEM) was utilized (Li et al., 2017). The image registration scheme is presented in Fig. 4.12. OFI-H is defined by the OFI method and refers to the homogeneous deformation assumption. The multi-scale image pyramid was constructed through progressive down-sampling. The displacement field estimated in a level is thereafter up-sampled and used to initialize the next level. At the coarsest scales, OFI-H algorithms are used to find global transformations for easy and fast convergence, while the more computationally intensive OFFEM algorithm is used to calculate local displacements at the finest scales (Dahdah et al., 2016; Li et al., 2020; Shi et al., 2021). This hierarchical approach significantly enhances algorithmic robustness and convergence efficiency while allowing flexible parameter adjustment across different scales to balance computational accuracy and efficiency.

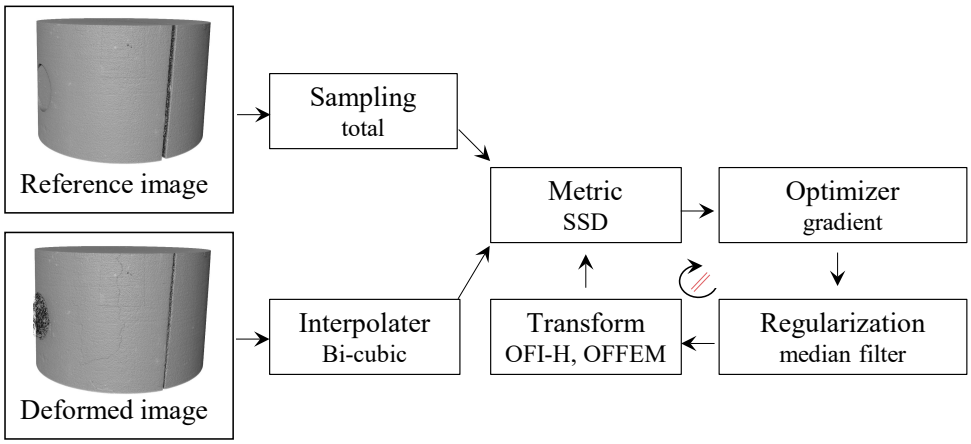

Figure 4.12: The image registration scheme of YaDICs platform.

To effectively capture the main physical processes at a relevant scale, the choice of voxel size is a critical parameter. Considering the average size of mineral inclusions in the sample is on the order of several hundred micrometers, together with the sample dimensions and fracture openings, a voxel size of approximately 16 μm was chosen. Previous research has used mineral inclusions in COx claystone, such as heavy minerals, carbonates, and silicates, as internal markers to characterize the creep strain and cracking process (Robinet et al., 2012; Shi et al., 2021). At this resolution, heavy minerals within the claystone can be clearly identified in grayscale images to characterize the fracture closure process, as seen in Fig. 4.13(a). The spatial distribution of these heavy minerals serves as reliable reference features for DVC analysis, improving the accuracy of displacement

field calculations.

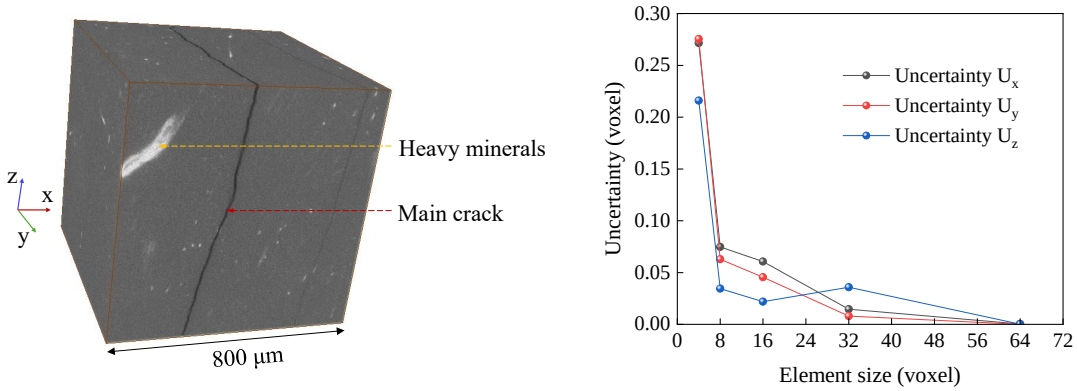

(a) **(b)**

Figure 4.13: Three-dimensional distribution of mineral phases and main fracture (a) and variation of DVC displacement uncertainty as a function of element size for the three displacement components (b).

Standard deviation of the correlation coefficient was used as the key parameter for selecting the optimal mesh size. DVC performance was evaluated based on displacement uncertainty, estimated from the standard deviation between two scans: one at a reference position and another after a controlled 0.25 mm translation along the beam axis. Due to the conical geometry of the lab-based X-ray source, voxel size varied slightly across the field of view, with a nominal resolution of 16 µm at the center. As shown in Fig. 4.13(b), displacement uncertainty in the X, Y, and Z directions ranges from 0 to 0.3 voxels for element sizes between 4 and 64 voxels. This analysis highlights the strong dependence of measurement precision on element size. Balancing accuracy and computational cost, an element size corresponding to 16 µm was selected for all DVC analyses in the self-sealing tests. In addition, due to the computation effect, 800 slices in the middle of images were chosen to analyze.

4 Image-based analysis of sealing processes

This section explores the self-sealing feasibility of pre-cracked claystone under indirect infiltration from several aspects, including the initial fracture geometry, fracture opening, and mechanical loading conditions such as confining stress. The main results focus on the temporal evolution of sample swelling and fracture opening from X-ray im-

ages and gas permeability evolution during the experiment, with particular attention to the deformation under indirect water infiltration.

4.1 Effect of fracture geometry

In the present study, we designed four fracture geometries to investigate the possibility of sealing under indirect water percolation. The fracture geometry is referenced in Fig. 4.2 and Table 4.1, while the 3D reconstruction of samples is presented in Figs. 4.5 to 4.7 and Fig. 4.9, respectively. Of these samples, different fracture types exhibit significantly different closure characteristics under indirect water injection conditions.

Crack CG3 is designed with an opening of 0.4 mm and a length of 17 mm. Sample EST 66747-4 with this type of fracture is presented in Fig. 4.7. The reconstructed tomographic images of slice 650, which is located at the middle height of the sample, are presented in Fig. 4.14. It is noticed that the two water injection inlet holes are also located at this height of sample. The first scan with T= 0h represents the initial state of sample before water injection. One can easily see a quasi-uniform opening of the pre-fracture. It is

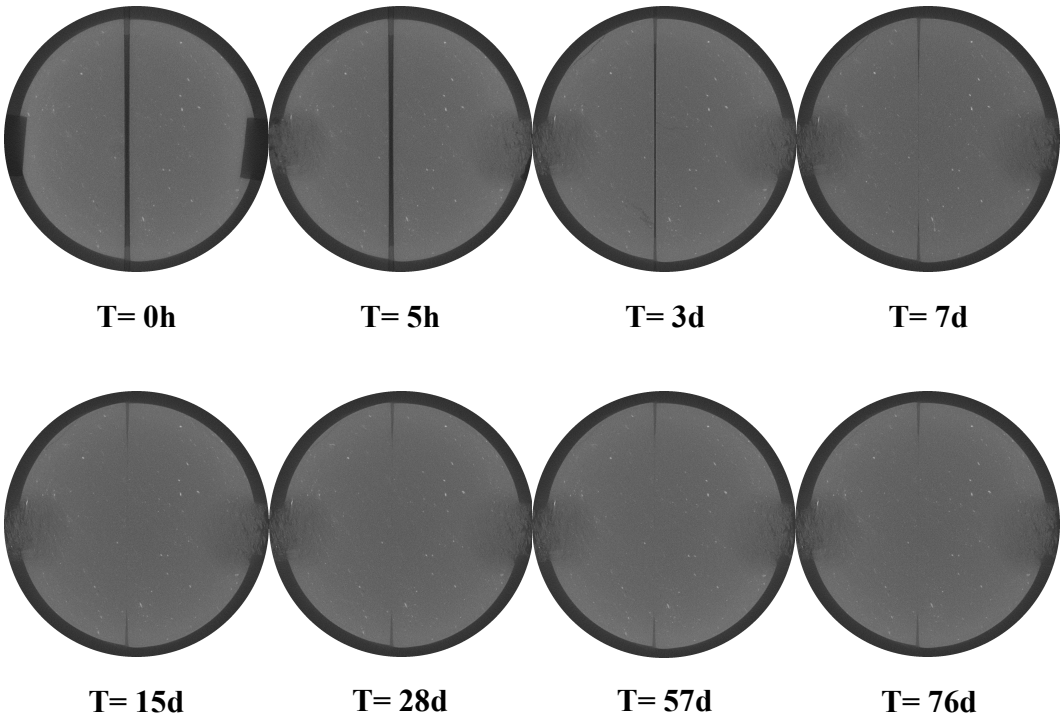

Figure 4.14: Evolution of tomographic reconstructions of selected horizontal (XY) slice 650 under 0.3 MPa confining pressure in sample EST 66747-4.

useful to notice that silicon is injected into the two external ends of pre-fracture to prevent water leak-off along the fracture, as indicated on the scan. Water injection is conducted with a constant pressure of 0.3 MPa. It is useful to notice that this water injection pressure is uniformly applied to the external surface of epoxy resin mold as indicated in Fig. 4.3. The progressive closure of pre-fracture during water injection is very clearly captured. More precisely, the central part of fracture is slightly more quickly closed than the side parts. This is due to the fact that the distance between the central part and injection holes is shortest. After 7 days of water flow, the major part of pre-fracture is almost closed. The closure of whole fracture is observed around 28 days.

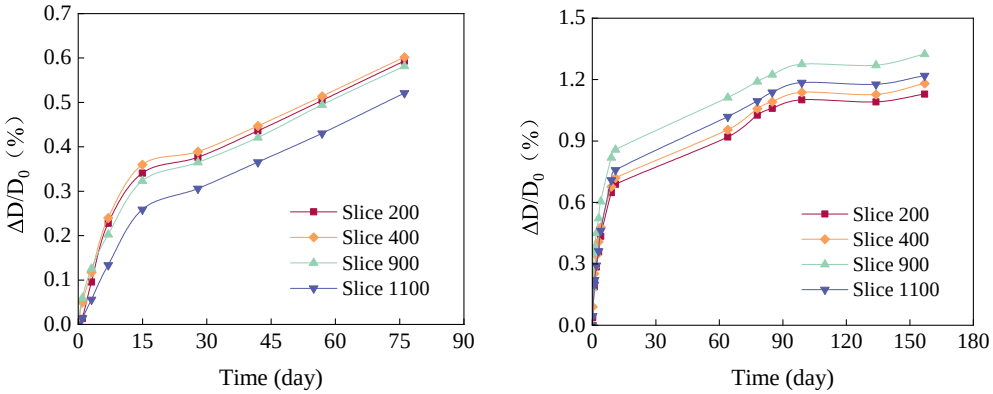

(a) EST 66747-4 **(b)** EST 66747-2

Figure 4.15: Time-dependent relative diameter change ($\Delta D/D_0$) across different slices in sample EST 66747-4 (a) and EST 66747-2 (b).

In order to define the correlation between swelling deformation and pre-fracture closure, we calculate the average variation of specimen diameter by using an edge segmentation procedure. The specific method is described in Section 3.2. The obtained results are presented in Fig. 4.15(a), showing the evolution of relative variation of average diameter with time ($\Delta D/D_0$) for four different slices. In general, there is a systematic increase of diameter, clearly indicating volume expansion of sample due to water injection. Moreover, the diameter evolution curves can be separated into two distinct phases. In the first stage until 15 days, there is a rapid increase in diameter, accompanied by a rapid closure of pre-fracture shown in Fig. 4.14. This indicates that there is an important swelling deformation of claystone during this period due to a rapid decrease of capillary pressure upon water resaturation. The diameter expansion kinetics become much smaller during the second phase between 15 days and the end of test. This is a consequence of the non-

linear hydric behavior of claystone. With the increase of water saturation, the variation of capillary pressure, responsible for swelling deformation, is smaller and smaller. It is further interesting to notice that the diameter expansion is not uniform along the height of sample. Notably, the diameter expansion of slice 1100 is much smaller than three other slices. The main reason is that there is a larger residual aperture of pre-fracture around the upper end zone. Therefore, there is a strong correlation between swelling deformation and pre-fracture closure upon water resaturation.

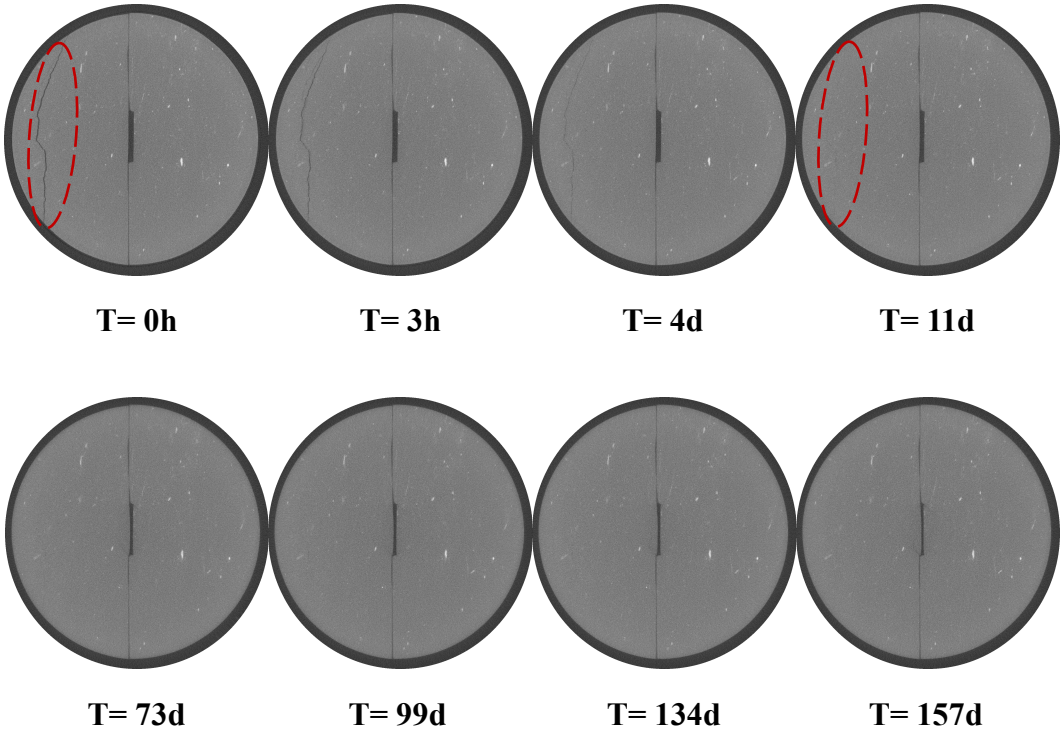

Figure 4.16: Evolution of tomographic reconstructions of selected horizontal (XY) slice 1100 under 0.3 MPa confining pressure in sample EST 66747-2.

Crack CG1 is a main fracture with a length of one-third of the diameter and a width of 0.4 mm. Sample EST66747-2 is with a main fracture (CG1) and microcracks penetrating the water-injected channel, as shown in Fig. 4.5 and Fig. 4.16. Regardless of whether the sample is split or precisely cut, a number of microcracks are inevitably created during main fracture preparation. This sample was injected under a pressure of 0.3 MPa for 157 days, but the main fracture was not completely closed. It can be observed that this microcrack highlighted by the red circle was closed on day 11, but the main fracture was gradually closing but not completely. These microcracks are spatially connected

to the two subsequently drilled water injection channels (see Fig. 4.5), providing potential pathways for localized water infiltration. Fluid may penetrate preferentially along these microcracks, influencing the local and even global swelling behavior of the sample. Here, variations in the measured equivalent diameter were observed across different slices (slices 200, 400, 900 and 1100), as seen in Fig. 4.15(b). Generally, the $\Delta D/D_0$ exhibited a similar trend across different slices. It increased rapidly in the first 15 days because the rapid infiltration of water induced significant expansion. As the process progressed, the swelling rate increased more slowly, with $\Delta D/D_0$ ranging from 1.1% to 1.4% across different slices until day 100. It is noted that the expansion in slices 900 and 1100 was slightly greater than that in the lower slices 200 and 400 in the first 15 days. This discrepancy may be attributed to localized hydration-induced swelling in the upper region where the microcrack is located. The presence of microcracks provides preferential pathways for water infiltration, leading to a greater increase in pronounced localized swelling deformation.

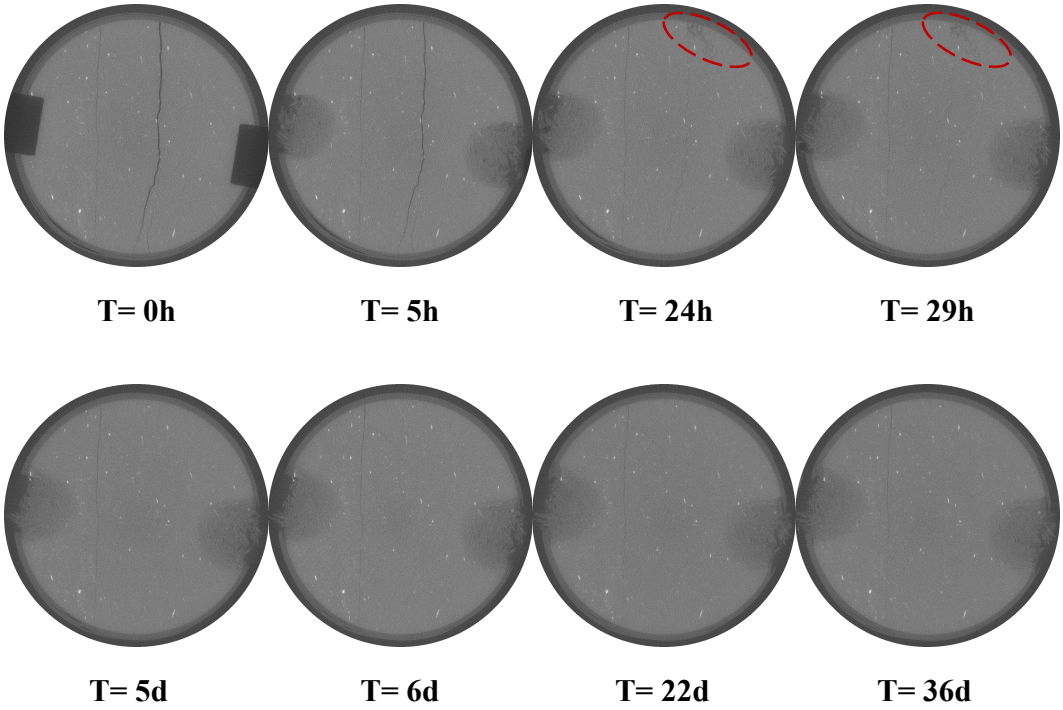

Figure 4.17: Evolution of tomographic reconstructions of selected horizontal (XY) slice 655 under 0.3 MPa confining pressure in sample EST 66747-3.

Furthermore, crack CG2 is obtained through splitting test, the sample EST66747-3 with this type of fracture is presented in Fig. 4.6. This sample contained a main frac-

ture and a microcrack, as shown in Fig. 4.17. After water injection of 0.3 MPa injected pressure, the main fracture was closed progressively. By day 5, the main fracture became blurred, but the microcrack remained partially connected. This sample exhibited a comparatively faster fracture closure because water was able to directly flow into the main fracture. The highlighted circles in the 24-hour and 29-hour images (see Fig. 4.17) clearly represent water. From the $\Delta D/D_0$ curve in Fig. 4.18(a), it was observed that a slower diameter increase occurred in the first 29 hours. This is because clay swelling initially occurs near the main fracture and is mainly consumed in closing the fracture, rather than contributing to a rapid increase in the overall sample diameter. After the main fracture closed, the sample had global swelling and the corresponding $\Delta D/D_0$ increased rapidly. Afterward, the swelling rate slowed and the diameter gradually stabilized, suggesting that the crack-sealing process approached equilibrium and the internal structure reached a new stable state. In addition, the curves corresponding to different slices display similar trends with only slight variations in amplitude, indicating that fracture closure progresses relatively uniformly along this sample.

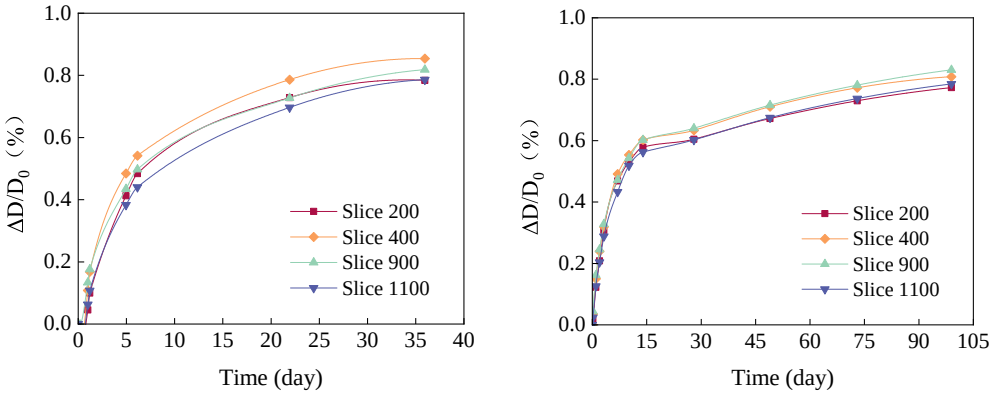

(a) EST 66747-3 **(b)** EST 72793-2

Figure 4.18: Time-dependent relative diameter change ($\Delta D/D_0$) across different slices in sample EST 66747-3 (a) and EST 72793-2 (b).

Additionally, the crack CG4 is a cylindrical aperture with a diameter of 1 mm. Sample EST 72793-2 with this type of fracture is presented in Fig. 4.9, and the X-ray tomographic reconstructions of the same slice 650 at different resaturation times are shown in Fig. 4.19. Before day 3 of 1.0 MPa water injection, internal fracture features were clearly visible in the slice as distinct low-gray-value regions. However, gradual changes in gray values were seen around the main fracture, due to water beginning to infiltrate the rock ma-

trix and cause local microstructural changes. After day 14, fracture boundaries become increasingly blurred and low-gray-value regions shrink significantly. On day 99, some clay surrounding the main fracture separated. This reflects long-term hydration-induced swelling of the clay matrix adjacent to the fracture walls, which promotes gradual fracture closure. Further quantitative insight into the swelling process is provided by the evolution of the relative diameter change for different axial slices, as shown in Fig. 4.18(b). All slices exhibited a rapid radial swelling response within the first 15 days, with a sharp increase corresponding to the initial hydration-induced swelling following water infiltration. Thereafter, the swelling rate gradually decreased, entering a quasi-stable growth phase, and reached approximately 0.7%–0.8% by day 99. The swelling curves for different slices display similar temporal trends, with only limited variations in magnitude, suggesting a relatively homogeneous axial swelling distribution under a confining pressure of 1.0 MPa.

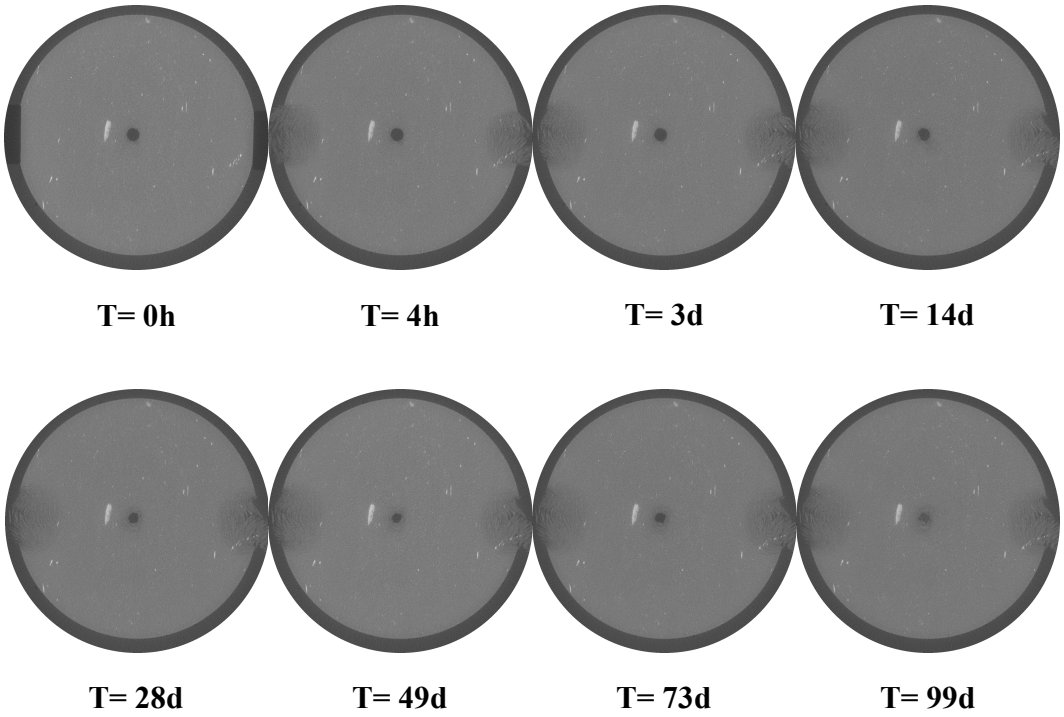

Figure 4.19: Evolution of tomographic reconstructions of selected horizontal (XY) slice 650 under 1.0 MPa confining pressure in sample EST 72793-2.

Among these four fracture geometries in this study, different fracture types exhibited significantly different closure characteristics under indirect water injection conditions. Only the sample with crack CG3 is completely closed under an indirect injection of 3 MPa

pressure. It is satisfied in terms of fracture geometry and water infiltration path. Other samples, except for the sample with crack CG2, are not completely closed. It indicates that with these fracture geometry and aperture, matrix swelling solely is insufficient for complete closure. Sample with crack CG2 obtained by the splitting test has a small main fracture, allowing water to easily enter the main fracture and making it difficult to offer an indirect infiltration path. Thus, crack CG3 is selected as the preferred type for future studies on self-sealing behavior in the presence of fracture opening, injection pressure, and other loading conditions.

4.2 Effect of initial fracture opening

The initial fracture opening is one of the factors that other researchers have proposed as contributing to fracture closure. Here, the influence of different initial fracture openings on closure behavior is also investigated by comparing sample EST 66747-4 (see Fig. 4.14) with an initial fracture opening of 413 μm to sample EST 72793-1 with an initial fracture opening of approximately 2116 μm. Sample EST 72793-1 is presented in Fig. 4.9 and Fig. 4.19. It is worth noting that the fracture type for sample EST 727937-1 has the same fracture geometry (CG3) as sample EST 66747-4. However, during sample preparation, partial epoxy resin blockage occurred within the fracture, and therefore a drill with a diameter of 2 mm was used for secondary processing to ensure proper fracture connectivity. Fig. 4.19 illustrates the evolution of sample EST72793-1 under a confining pressure of 1 MPa at selected slices 200, 650 and 1100 with a maximum duration of 69 days. It was observed that the fracture along the main fracture progressively narrowed within the first 30 days, while the main fracture itself exhibited a slower change. By day 69, the fracture opening of the main fracture was significantly reduced but remained unclosed. There are some microcracks, such as within slice 1100, accelerating local hydration and pronounced localized swelling. Notably, localized clay peel is observed along the main fracture walls, indicating that the sealing process has evolved from matrix swelling to localized structural rearrangement. Under indirect water injection conditions, the fracture closure in COx claystone is primarily driven by matrix swelling but also by clay peeling along the fracture wall during long-term hydration. This phenomenon was only observed in the sample with the large fracture opening in this study.

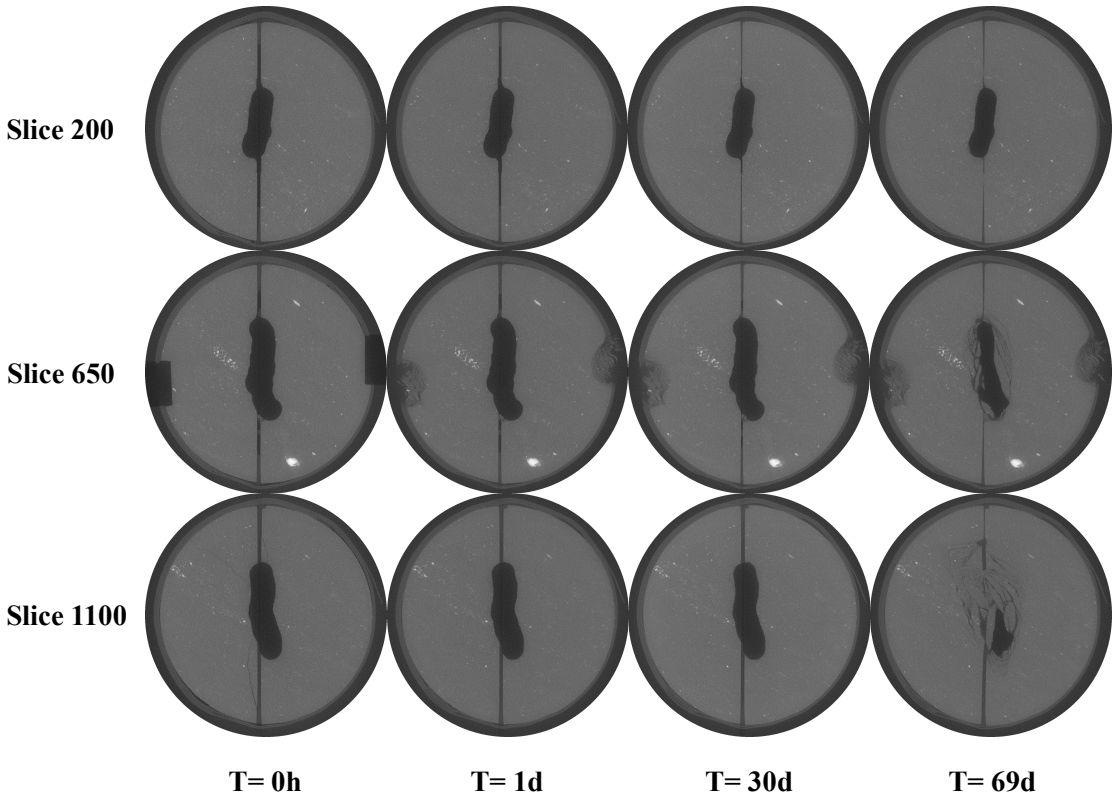

Figure 4.20: Evolution of tomographic reconstructions of selected horizontal (XY) slices 200, 650 and 1100 under 1 MPa confining pressure in sample EST 72793-1.

The microstructure of the cracked sample obtained by means of X-ray tomography also provides more information on the fracture opening and its morphology. Through quantification of fracture opening, the further analysis directly relates to the fracture evolution of sample EST 66747-4 and sample EST 72793-1. This study primarily focuses on the main fracture, selecting a representative region of interest (ROI) to analyze the evolution of fracture closure. The thickness algorithm of ImageJ was used to estimate the average fracture opening (W), where the thickness function defines point thickness as the diameter of the maximum inscribed sphere that fits within the structure at each point (Domander et al., 2021; Gupta et al., 2022). The distribution of fracture opening at different time instances is presented in Fig. 4.21. The initial average aperture of pre-fracture was estimated as equal to 413 μm and used as the reference value before water injection. The water resaturation process induces progressive closure of fracture. More precisely, the closure is faster in the central part of ROI than the outer edge parts. After 7 days, the central part of ROI was almost fully closed, with an average fracture opening of around

100 µm. After 15 days, only small residual opening remained near the edge of ROI. After 28 days, the full fracture was almost closed.

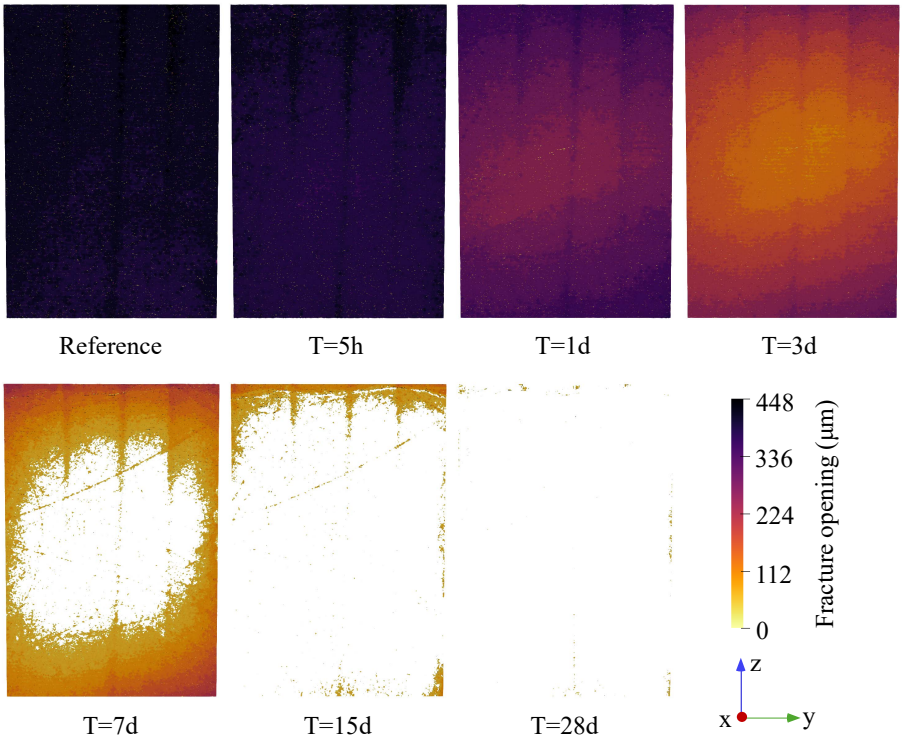

Figure 4.21: 3D fracture opening evolution maps for sample EST 66747-4 over time.

Fig. 4.22 presents the spatial evolution of the 3D local fracture opening in sample EST 72793-1 at different times. In its initial state, the fracture opening exhibited significant spatial heterogeneity, with locally larger openings. During the first 6 days of water injection at 1 MPa pressure, the overall fracture geometry remained clearly visible, but opening reduction began at the fracture edges. As hydration progressed, the opening narrowed and the effect of swelling spread from localized areas to a larger area. By day 30, the average fracture opening had decreased to approximately 2003 µm. By day 69, the fracture edges have nearly closed and the main fracture opening has significantly decreased, with the average opening reduced to approximately 1187 µm. The presence of a residual opening indicated that the shrinkage was not uniform, with notable temporal and spatial variation. Overall, this sample clearly demonstrates that the self-sealing process is progressive and spatially heterogeneous. fracture closure does not occur simultaneously across the entire fracture but rather begins in narrower regions and gradually spreads to larger and more structurally complex areas.

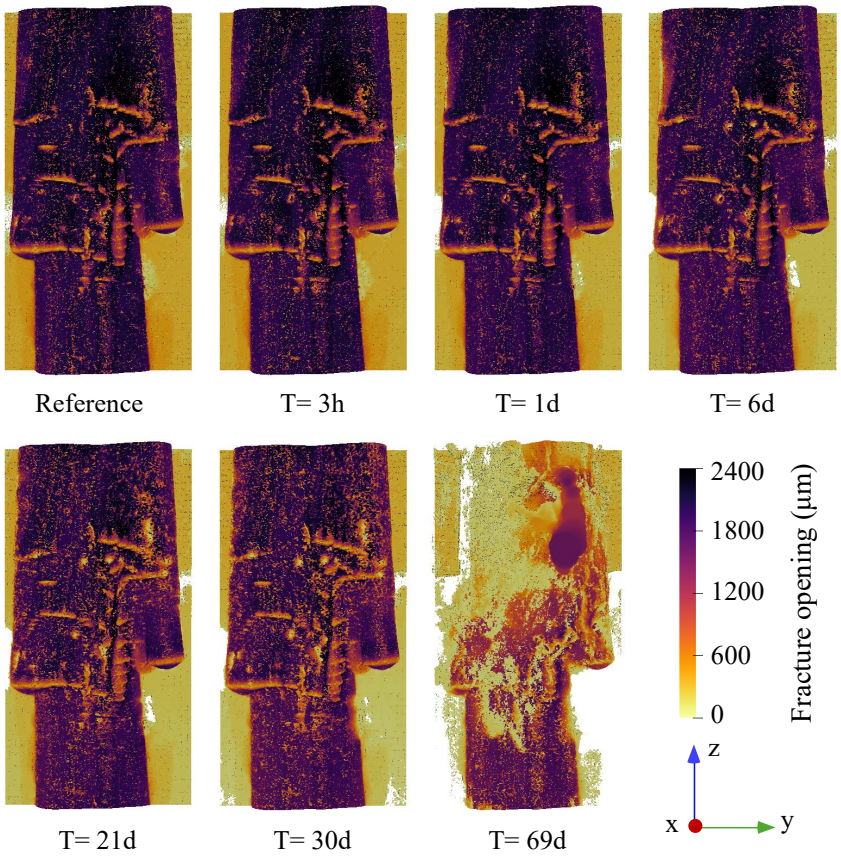

Figure 4.22: 3D fracture opening evolution maps for sample EST 72793-1 over time.

As discussed in Section 4.1, sample EST 72793-2 with crack CG4 was incompletely closed. In addition to fracture geometry, its relatively large initial fracture opening may be another factor contributing to the incomplete closure of sample EST 72793-2. The evolution of main fracture over time is shown in Fig. 4.23. In the initial state, the fracture exhibits a relatively large overall aperture along the axial direction, with an average opening of approximately 992 μm. As water injection proceeds, the fracture opening shows a continuous decreasing trend. In the early stages of water injection, fracture opening changes are limited, with an average opening of 982 μm by day 3. By days 14 and 28, the fracture opening has significantly decreased, particularly along the fracture edges and in the lower part of the sample, indicating that rock matrix swelling has become the dominant mechanism controlling aperture reduction. By day 49, the average fracture opening is reduced to 589 μm, but significant spatial heterogeneity along the sample height remains visible. As water injection continues, the rate of aperture reduction gradually slows. After that, the fracture opening fluctuated slightly but remained stable at 580 μm. The global

swelling rate of the claystone at this stage was relatively low, resulting in a slower re-closure process. In further study, different fracture openings in this fracture geometry will also be investigated to explore complete closure possibility.

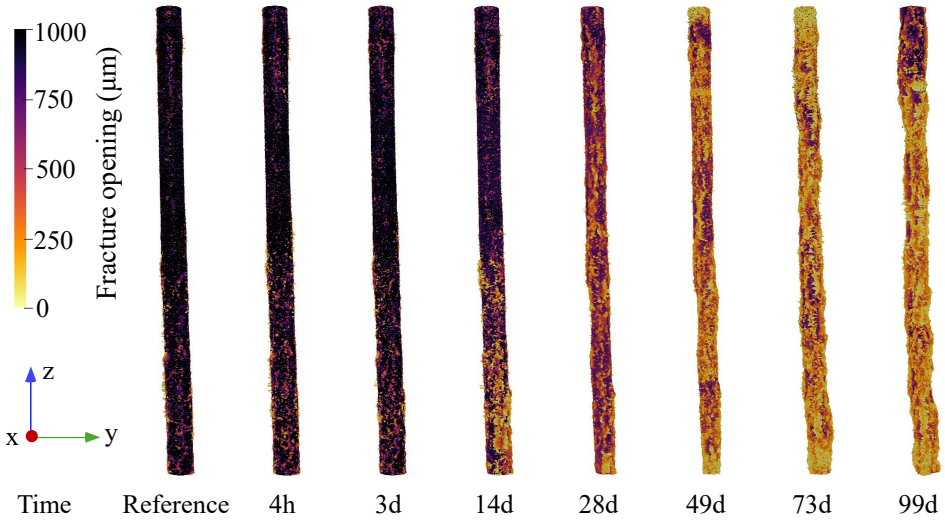

Figure 4.23: 3D fracture opening evolution maps for sample EST 72793-2 over time.

5 Gas permeability results

In these experiments, gas permeability is an important indicator for evaluating the fracture closure and sealing process. The permeability test is conducted before, during and after water injection. Using the aforementioned method, changes in gas permeability in each sample are accurately measured, allowing for a preliminary assessment of fracture closure.

Among these samples, sample EST 66747-4 eventually closed completely from images after being indirectly injected with water. The obtained result of average gas permeability is presented in Fig. 4.24. The initial gas permeability (K_g) stood at 6.15×10^{-12} m^2. There is a continuous decreased with the fracture closure. At 28 days, while the fracture was almost fully closed according to tomographic images, the average gas permeability of sample was about 1.80×10^{-18} m^2, which is much higher than the estimated intrinsic permeability of intact claystone (Davy et al., 2007). That means that at this stage, there is still an important residual hydraulic opening of pre-fracture even if it is mechanically seen as closed. After 76 days, the gas permeability reached 2.53×10^{-20} m^2, which is

close to that of intact claystone sample, indicating a good state of hydraulic sealing of pre-fracture due to swelling deformation of claystone.

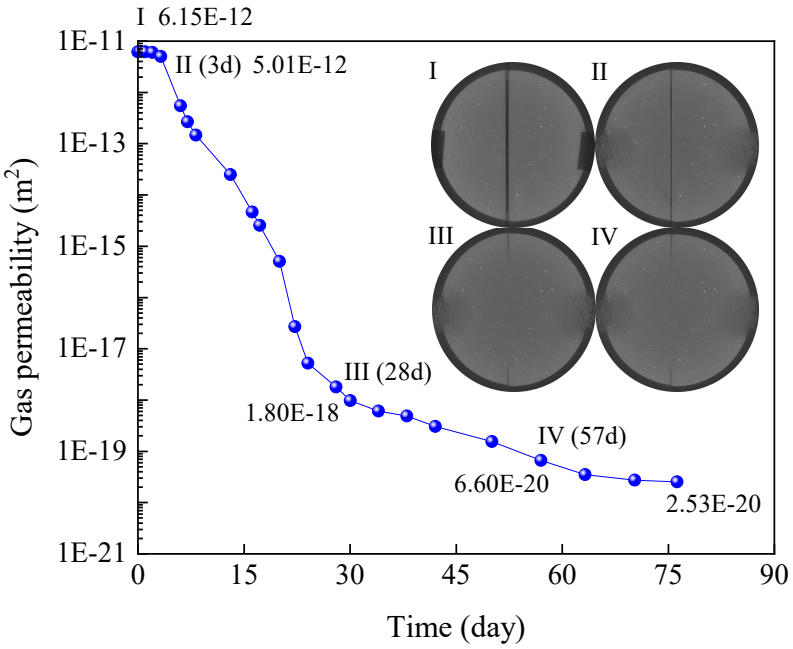

Figure 4.24: Time-dependent evolution of gas permeability in sample EST 66747-4.

More precisely, the decrease curve of gas permeability can be approximately divided into four distinct stages: the initial stage (0-3 days), the rapid decrease stage (3-28 days), the slowed decrease stage (28-63 days), and the quasi-stabilization stage (after 63 days). In the initial stage, although the fracture opening decreases significantly from approximately 413 μm to 198 μm, there is only a very small diminution of gas permeability. This can be explained by the fact that despite important fracture closure, there is a continuous and well-connected gas flow pathway along fracture, and the remaining opening does not reach the critical threshold for a significant closure of gas flow pathway. Referring to Fig. 4.21, a clear fracture closure is observed around day 7, corresponding to a sharp drop in gas permeability in Fig. 4.24. It marks the starting point of the rapid decrease stage, during which the gas permeability is decreased by approximately six orders of magnitude. The gas flow pathways are significantly narrowed, but partial connectivity remains. By Day 28, the fracture is no longer visible in Fig. 4.14, the permeability decrease is clearly slowed down. During this stage, the main connected gas pathways are sealed while important residual gas pathways remain, causing the corresponding permeability to still be much higher than that of intact material. After 63 days, the gas permeability tended to

stabilize, indicating that the fracture was almost completely closed, leading to a quasi-full hydraulic sealing of fracture. From the results obtained here, it is concluded that the gas permeability evolution is well correlated with the fracture closure and provides a quantitative indicator of self-sealing process of fracture.

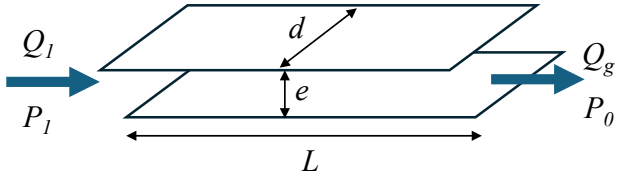

Figure 4.25: Schematic diagram of the flow between two parallel plates.

However, the direct determination of fracture aperture from tomographic images is not an easy task and cannot be easily used in practice. In the present work, an alternative solution is proposed. It consists of calculating an equivalent fracture aperture from gas permeability measurement. Therefore, the gas flow through a fractured porous sample is approximated by that through an equivalent fracture between two parallel plates (see Fig. 4.25). However, in rock-like materials, most fracture surfaces are not smooth but characterized by different types of asperities. In order to account for the effect of asperities on pure Poiseuille type flow, a correction coefficient is generally introduced depending on spatial distribution of asperities (Rastiello et al., 2015). In the present work, we search for an equivalent Poiseuille flow model for the fractured claystone sample for which the spatial distribution of asperities cannot be directly measured. Therefore, a purely macroscopic approach is here by introducing a fitted correction coefficient denoted as $\alpha \geq 1$. Thus, based on the corrected Poiseuille law, the volumetric gas flow rate can be expressed as follows:

$$Q_g = \frac{d \times e^3}{12\mu L} \times \frac{P_1^2 - P_0^2}{2P_0} \tag{4.3}$$

where Q_g is the volume flow rates at the downstream (m^3/s), e is the aperture of equivalent fracture, μ is the gas dynamic viscosity, L is the length of fracture (here height of sample), P_0 and P_1 are the downstream and upstream pressures, respectively. At the same time, the volumetric flow rate of fractured sample is provided by the Darcy law (see Eq. (2.2)). It is noticed that the case $\alpha = 1$ corresponds to the ideal Poiseuille model. By making equivalence between fracture flow and porous medium flow, one gets

the following aperture of equivalent fracture:

$$e = \sqrt[3]{3\mu K_{ag}\pi d} \tag{4.4}$$

The value of α is calibrated from initial value of average opening of pre-fracture determined from the micro-tomographic images (see Fig. 4.21 for reference). One obtains $\alpha = 64$ for the claystone sample studied here. Using this value, the evolution of equivalent fracture aperture is then calculated and presented in Fig. 4.26. Most interestingly, it is compared with the average fracture opening determined from tomographic images. There is a very good qualitative correlation between the equivalent fracture aperture and average fracture opening. This indicates that the gas flow in fractured claystone sample is clearly dominated by the pre-existing fracture and its subsequent evolution. Quantitatively, it seems that during the first period up to 15 days, the decrease of equivalent fracture aperture is delayed with respect to that of average fracture opening. But after 15 days, the equivalent fracture aperture becomes smaller than the average opening. These results indicate that in real material, in addition to the main pre-fracture, there are also a number of microcracks contributing to gas flow in sample. As a consequence, during the first period of 15 days, the gas permeability diminution can be affected and delayed by those open microcracks. The equivalent fracture aperture calculated from the measured gas permeability is therefore higher than the pre-fracture opening estimated from tomographic images. In the second period, those microcracks are almost all closed, the gas

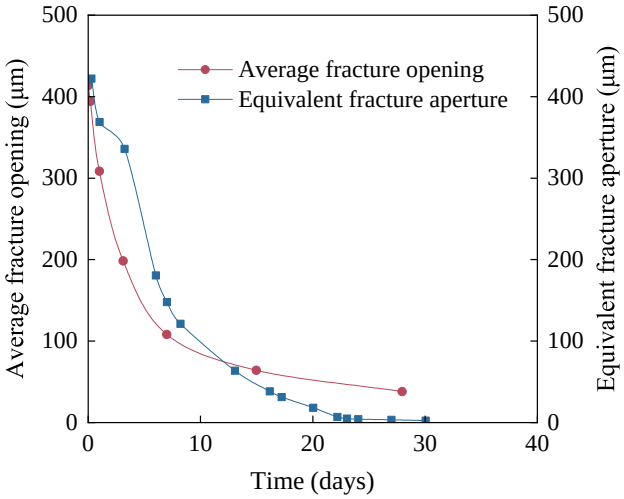

Figure 4.26: Evolution of average fracture opening and equivalent fracture aperture of sample EST 66747-4.

flow is dominated by the remaining opening of pre-fracture. The gas flow through the sample can be well approximated by that of an equivalent single fracture. At the same time, due to the resolution limitation of micro-tomograph used in this work, the estimation accuracy of average fracture opening becomes lower when the fracture is nearly closed during the second stage.

The main fracture aperture of samples EST 66747-2, EST 72793-1 and EST 72793-2 was gradually decreased but incompletely closed. However, the gas permeability (K_g) of these samples exhibited only minor variations in the total process, despite an overall decreasing trend over time, as shown in Fig. 4.27(a). Specifically, the gas permeability of samples EST 66747-2 and EST 72793-1 fluctuated slightly, decreasing by only one magnitude. The initial K_g was 2.20×10^{-12} m^2, which decreased to 10^{-14} m^2 after 157 days of water absorption in sample EST 66747-2. Permeability remained relatively stable in the early stage (0-10 days), owing to the localized closure of microcracks, while the aperture of the main fracture had not yet changed significantly. During 10 to 100 days, there was little change in the permeability. This trend may be attributed to the hardly reduction in the primary fracture aperture and the gas flow pathways retaining total connectivity. After 120 days, permeability dropped from 7.35×10^{-13} m^2 to 3.36×10^{-14} m^2, a sharp reduction of more than one order of magnitude. This significant decline indicates a pronounced self-sealing effect of the fractures, likely associated with clay particle swelling due to water absorption, progressive closure of the pore structure, and localized blockage caused by water filling. This result is identical to the fracture opening, which decreased

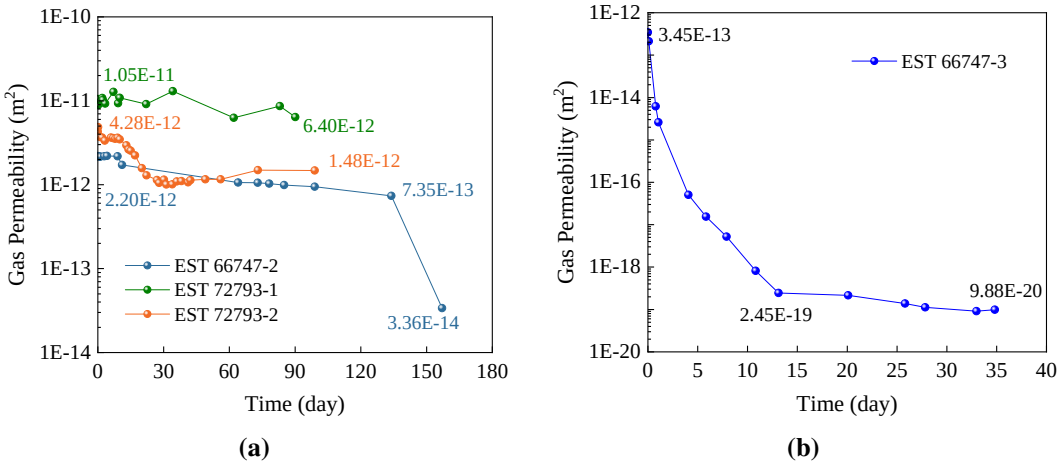

Figure 4.27: Time-dependent evolution of the gas permeability in (a) samples EST 66747-2, EST 72793-1 and EST 72793-2, and (b) sample EST 66747-3.

from 255 μm to 204 μm. Although the initial fracture opening of this sample was not great at 468 μm, this fracture was not completely closed after 0.3 MPa water injection.

However, the gas permeability of samples EST 72793-1 and EST 72793-2 only fluctuated slightly. From Fig. 4.27(a), they have relatively higher initial gas permeability compared to sample EST 66747-2. These higher initial gas permeabilities are attributed to their larger initial fracture openings, with an initial value of 2116 μm for sample EST 72793-1 and 992 μm for sample EST 72793-2. In sample EST 72793-1, the initial K_g was 1.05×10^{-11} m^2, which decreased to 6.40×10^{-12} m^2 after 90 days of water injection under 1 MPa, while fracture opening decreased to 1187 μm. Sample EST 72793-2 also exhibited a smaller change in permeability, decreasing only from 4.28×10^{-12} m^2 to 1.48×10^{-12} m^2 during the resaturation process, while the fracture opening decreased to 580 μm. The differences in permeability between the samples could be attributed to the relatively large fracture opening, which is difficult to completely close and has little effect on gas permeability.

Compared with other samples, sample EST 66747-3 exhibited a rapid permeability decrease. The result is presented in Fig. 4.27(b). The initial K_g was 3.45×10^{-13} m^2, which dropped by approximately two orders of magnitude after only one day of water injection. By day 13, it had decreased to 2.45×10^{-19} m^2 and then gradually stabilized at 9.88×10^{-20} m^2. This pronounced reduction was attributed to its relatively small initial fracture aperture and direct water infiltration into the fracture, leading to nearly complete sealing within a short period. Overall, the permeability evolution can be divided into two stages: an initial rapid decline followed by a stabilization stage. The initial decline is mainly controlled by water adsorption, matrix swelling, and blockage of flow channels, whereas in the stabilization stage the fracture is nearly closed and the permeability reaches a steady state.

6 Deformation field analysis and discussion

X-ray tomography results provide some information on the evolution of fracture opening and its morphology during the self-sealing process. However, image observations are insufficient to explain the differences in closure behavior among the samples. Some samples were completely closed, while others showed only a slight decrease in aperture. With regard to this, digital volume correlation (DVC) was further employed to quantitatively

analyze the three-dimensional deformation fields during self-sealing in order to better understand the mechanical mechanisms that govern the differences in fracture closure behavior.

6.1 Displacement evolution during complete fracture closure

In order to better characterize water-injected induced swelling formation, the local displacement field, in particular the horizontal displacement component along the perpendicular direction to pre-fracture denoted as U_x, is here determined. Among the samples, sample EST 66747-4 had complete fracture closure under indirect water infiltration. In Fig. 4.28, we show three-dimensional fields of U_x for different time instances. Due to the existence of pre-fracture, the displacement field is discontinuous across the fracture central plane. About temporal evolution, during the early period of water injection, for instance until 5 hours, the swelling deformation is very localized around the injection holes and the induced displacement remains very small. With the continuing water injection, the swelling-induced displacement is more and more important.

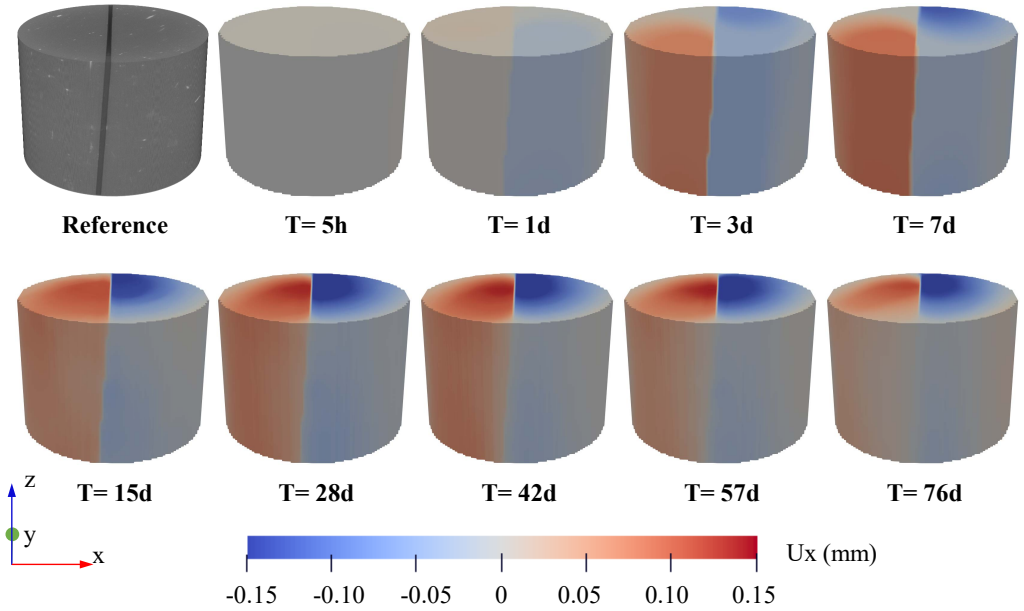

Figure 4.28: Evolution of the 3D horizontal displacements (U_x) measured with DVC in sample EST 66747-4 under 0.3 MPa confining pressure.

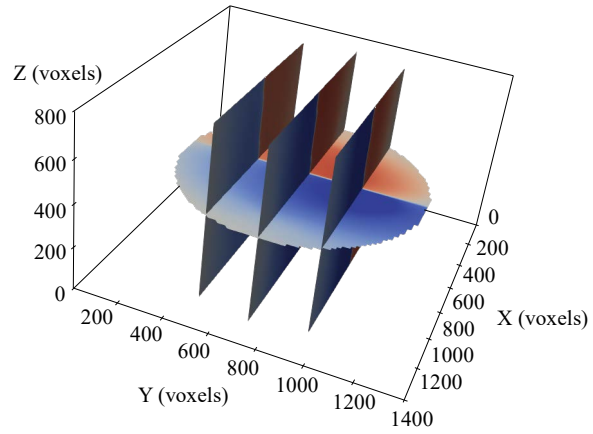

(a) selected three cross-sections

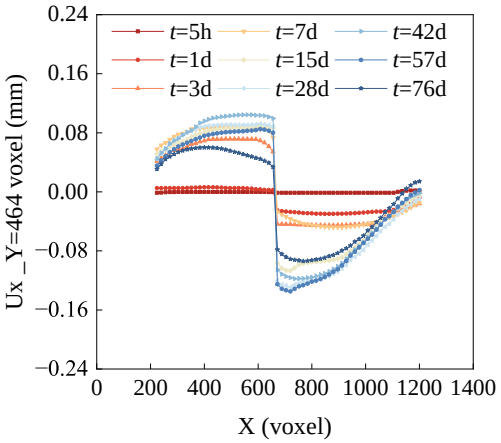

(b) U_x at cross-section $Y = 464$ voxels

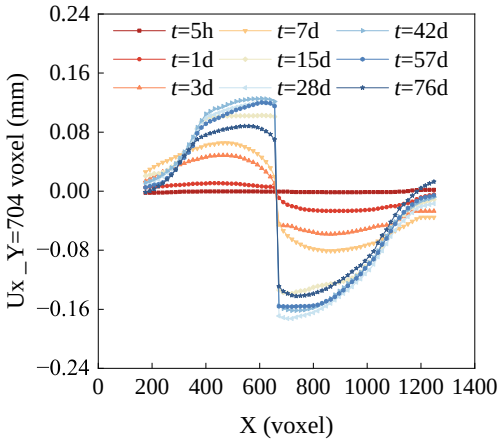

(c) U_x at cross-section $Y = 704$ voxels

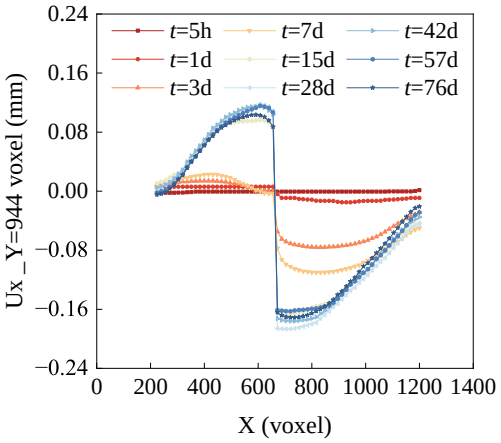

(d) U_x at cross-section $Y = 944$ voxels

Figure 4.29: Spatial distribution and temporal evolution of horizontal displacement U_x at three cross-sections in the middle of the sample EST 66747-4.

In order to get a better quantification, three representative sections along Y axis ($Y = 464, 704, 944$ voxels) are selected, as shown in Fig. 4.29. The distributions of U_x in these three sections at different instances are presented in Fig. 4.29(b), Fig. 4.29(c) and Fig. 4.29(d) respectively. As a primary remark, there are clear differences between three sections, indicating that the displacement U_x is not uniform along Y axis. However, the spatial distribution form and temporal evolution trend of U_x are quite close to each other. At the same time, due to the material heterogeneity of specimen, the displacement field is not symmetrical between two half cylindrical specimens with respect to the pre-fracture plane. As another interesting phenomenon, the values of displacement in the regions near the specimen external surface (the left and right extreme points on the fig-

ures) are significantly smaller than those inside the regions close to the pre-fracture. This clearly indicates that swelling deformation of claystone mainly produces a progressive closure of the pre-fracture rather than a lateral expansion of specimen. The maximum of displacement discontinuity between two lips of pre-fracture is reached around 28 days. This is in perfect correlation with the results presented in Fig. 4.21, indicating that at this time the pre-fracture is almost closed. After the closure of pre-fracture, the continued water injection induces additional swelling deformation of claystone. This leads to an expansive horizontal displacement toward the external surface of specimen between 28 days and 76 days, illustrated by the diminution of both negative displacement in the right part and positive displacement in the left part of the specimen. Therefore, we observe here a very good correlation between the pre-fracture closure and local displacement field due to swelling deformation of claystone specimen.

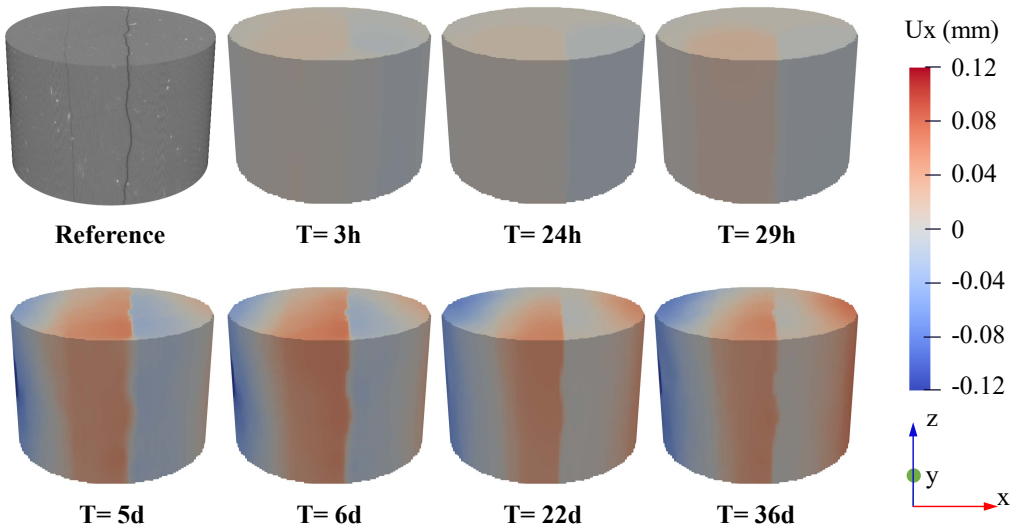

Figure 4.30: Evolution of the 3D horizontal displacements (U_x) measured with DVC in sample EST 66747-3 under 0.3 MPa confining pressure.

In comparison to sample EST66747-4, different deformation of sample EST66747-2 with the splitting fracture under direct water infiltration can be observed. Because the main fracture has a very small initial opening and the space between the tape and the sample provides a convenient pathway for water infiltration (see Fig. 4.17), water can rapidly penetrate along this interface into the main fracture at the early stage of injection. As a result, the main fracture becomes fully closed after approximately 5 days of water injection. This is clearly reflected in the 3D horizontal displacement fields (see Fig. 4.30)

and in the displacement curves of the three cross-sections (see Fig. 4.31), where a noticeable displacement jump appears around day 5. This jump indicates a strong inward movement of the two fracture walls, representing the characteristic signature of rapid fracture closure. In the subsequent stage, the relative displacement at the fracture location gradually decreases, whereas the region near the inlet exhibits continuous outward expansion. These actions result in the asymmetric deformation seen in the Fig. 4.30. In particular, there is a microcrack on the left side of the main fracture, whose walls move in opposing directions, preventing the microcrack from completely closing.

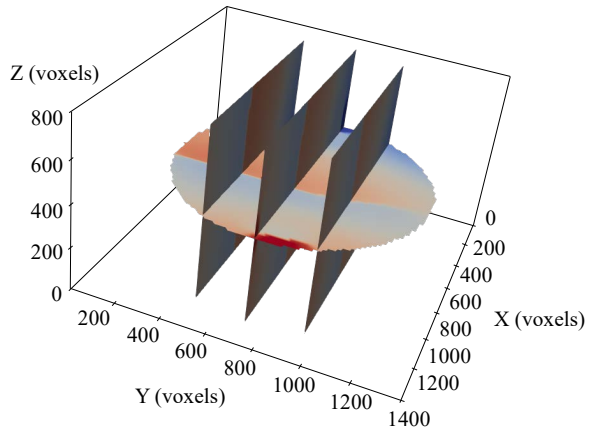

(a) selected three cross-sections

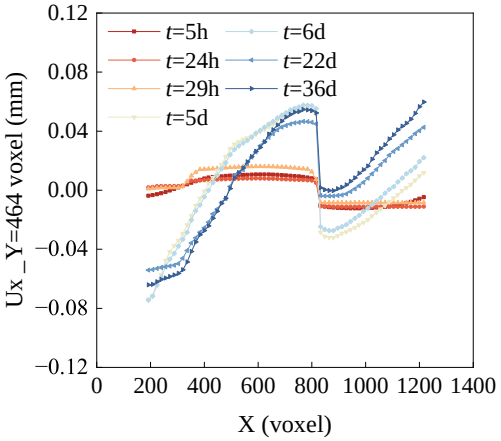

(b) U_x at cross-section $Y = 464$ voxels

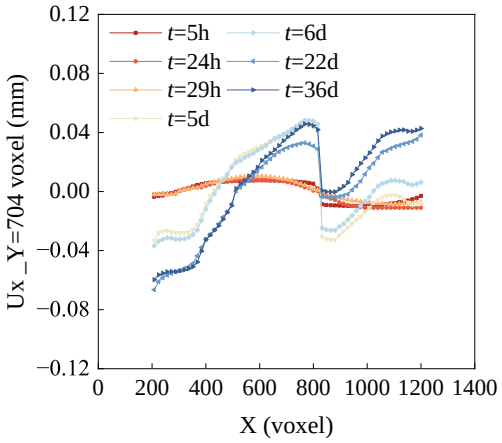

(c) U_x at cross-section $Y = 704$ voxels

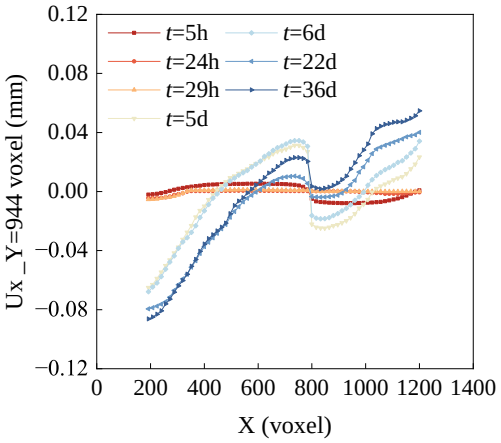

(d) U_x at cross-section $Y = 944$ voxels

Figure 4.31: Spatial distribution and temporal evolution of horizontal displacement U_x at three cross-sections in the middle of the sample EST 66747-3.

6.2 Deformation analysis during partial fracture closure

As discussed in Section 4, the main fractures within neither sample EST 72793-1 with fracture geometry CG3 but a relatively large initial aperture nor sample EST 66747-2 with fracture geometry CG1 were completely closed. Here, the deformation behaviors under initial fracture opening and geometry are analyzed to investigate the mechanisms for the absence of fracture closure. The displacement evolution of sample EST 72793-1 is presented in Fig. 4.32. It shows that the inward deformation is nearly small in the first 30 days, until the relatively large displacement on day 61. The displacement curves taken from the cross-sections at $Y = 704$ voxels and $Y = 944$ voxels in Fig. 4.33 show that by day 61, there is a noticeable displacement increase in the fracture region along with a local misalignment. This feature is effectively illustrated by the tomographic image in Fig. 4.20, where the fracture walls exhibit substantial localized swelling and bulging toward the fracture interior due to clogging. Compared with sample EST 66747-4 (see Fig. 4.28) under a lower confining pressure of 0.3 MPa, this sample exhibits noticeably different fracture closure and swelling behavior due to its larger initial fracture opening. However, the displacement gradients prior to complete fracture closure were still observed in sample EST 72793-1 during re-saturation. The results demonstrate that with an initial fracture opening of approximately 2 mm, complete closure under the higher injection pressure of 1.0 MPa is almost impossible. This emphasizes how the self-sealing

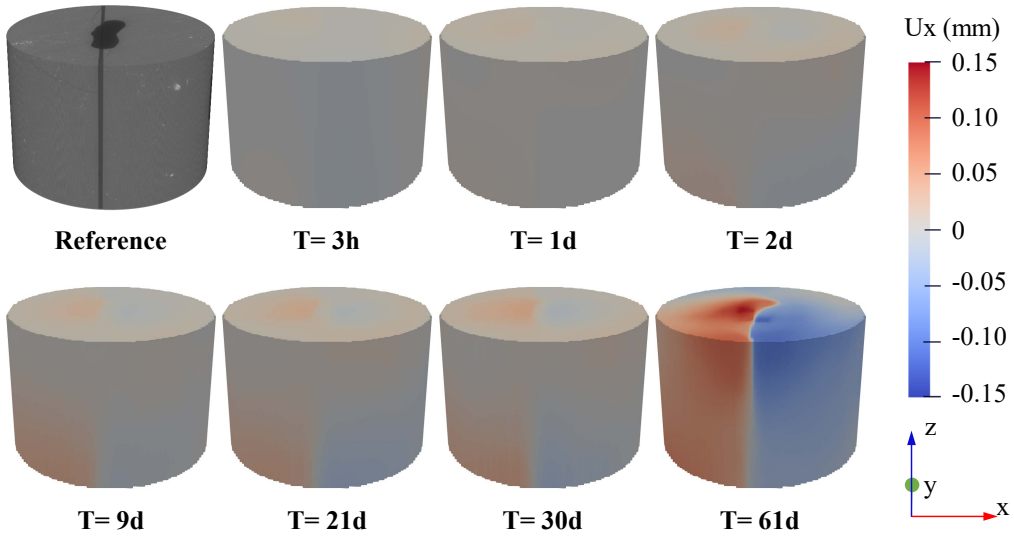

Figure 4.32: Evolution of the 3D horizontal displacements (U_x) measured with DVC in sample EST 72793-1 under 1.0 MPa confining pressure.

ability of COx claystone is influenced by both the initial fracture opening and the injected pressure. In addition to longer hydration and swelling times, larger fracture openings are easily affected by clogging and localized swelling heterogeneity, limiting complete closure ultimately.

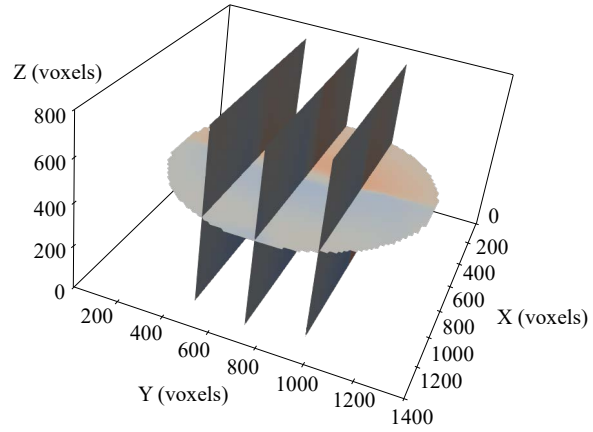

(a) selected three cross-sections

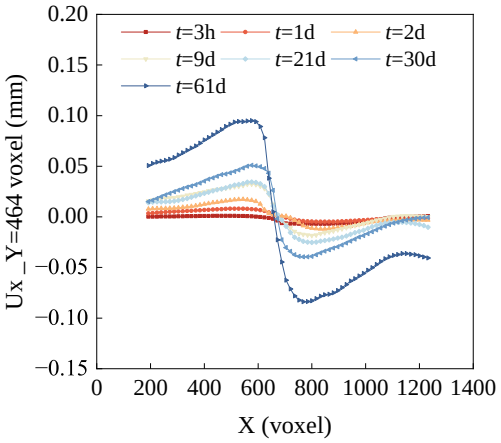

(b) U_x at cross-section $Y = 464$ voxels

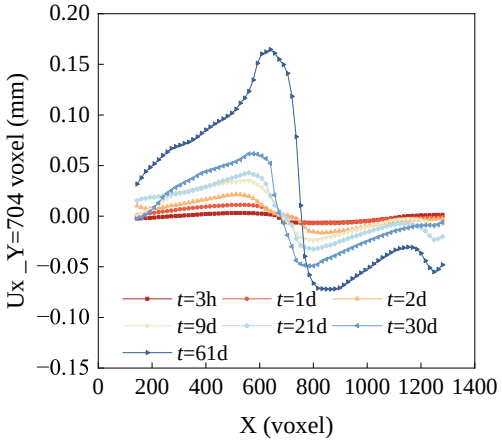

(c) U_x at cross-section $Y = 704$ voxels

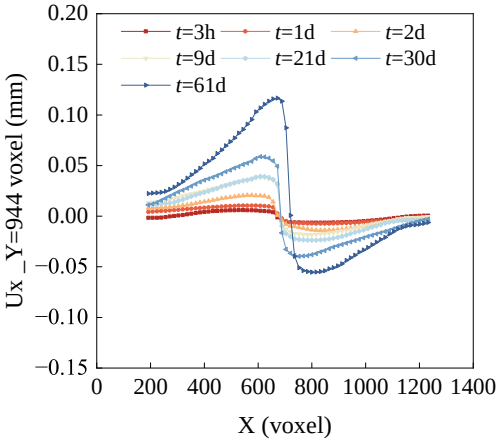

(d) U_x at cross-section $Y = 944$ voxels

Figure 4.33: Spatial distribution and temporal evolution of horizontal displacement U_x at three cross-sections in the middle of the sample EST 72793-1.

In addition to the initial fracture opening, incomplete fracture closure is likely influenced by other multiple factors, including injection pressure, injection duration and fracture geometry. Considering the potential impact of fracture geometry, the emphasis here is put on the U_x displacement evolution of the sample EST 66747-2 with fracture geometry CG1 under injection pressure of 0.3 MPa, as shown in Fig. 4.34. It can be seen that the rock matrix on both sides of the inlet exhibits a noticeable outward expansion in the

first 11 days after water injection, with the sample showing almost no measurable deformation within the first 3 hours. There was a certain delay in the initial swelling response. However, due to the presence of microcracks, localized swelling occurred rapidly once water infiltrated these zones, as illustrated in Fig. 4.16. As water injection continued, by day 73 the microcracks had fully closed, consistent with the observation in Fig. 4.16. The swelling progressively propagated inward, eventually becoming the dominant mechanism governing the closure of main fracture.

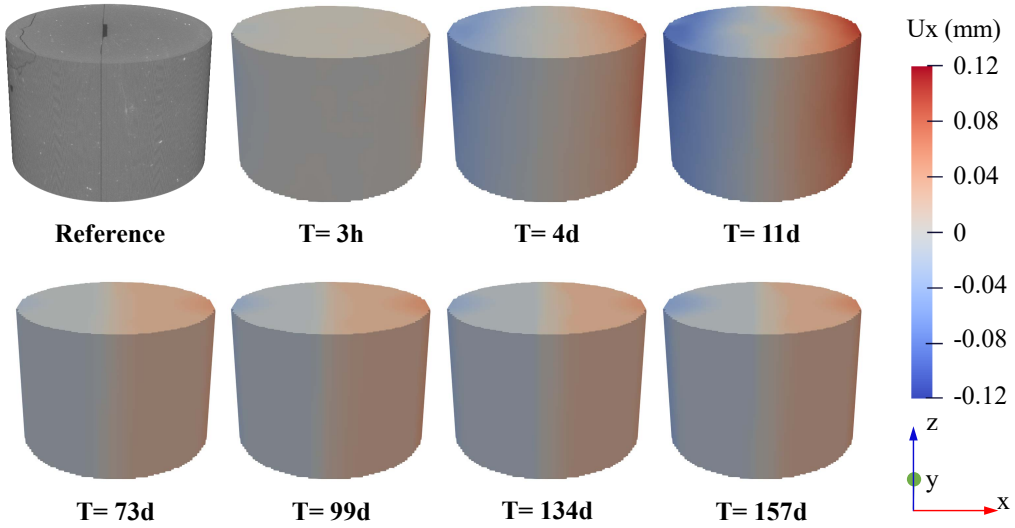

Figure 4.34: Evolution of the 3D horizontal displacements (U_x) measured with DVC in sample EST 66747-2 under 0.3 MPa confining pressure.

The U_x results along three cross-sections (Y = 464, 704 and 944 voxel) in sample EST 66747-2 are presented in Fig. 4.35. It is clear that in the early stages of water injection (before day 11), all cross-sections show gradual outward swelling near the inlet. By day 23, a distinct displacement gradient develops near the main fracture, indicating that matrix swelling driven by water absorption causes relative displacement between the fracture walls. It seems that the swelling begins to propagate into the interior of the sample, accelerating the sealing process. During the intermediate to late stage (T= 85-134 d), the curves gradually flatten and the differences between different observation periods decrease. By day 157, the displacement evolution of the three sections approaches stability. It demonstrated that the local swelling is nearly complete and the internal sealing process has reached equilibrium under a confining pressure of 0.3 MPa. It can be characterized specifically by an early stage dominated by localized outward expansion, followed by

a later stage dominated by localized inward deformation. Local swelling progressively closed local microcracks first and then reduced the main fracture opening. If the injection time is extended, the overall deformation may stabilize.

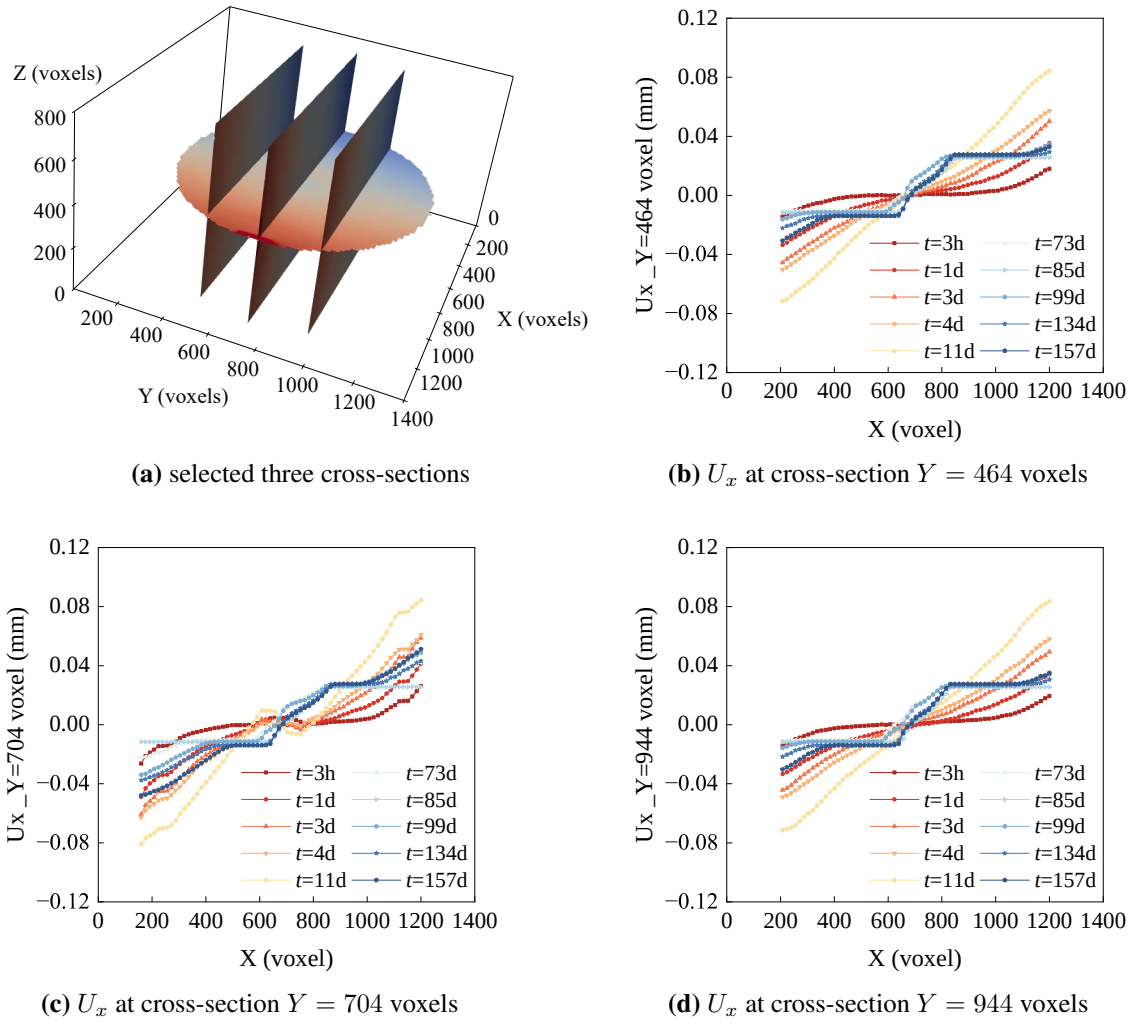

(a) selected three cross-sections

(b) U_x at cross-section $Y = 464$ voxels

(c) U_x at cross-section $Y = 704$ voxels

(d) U_x at cross-section $Y = 944$ voxels

Figure 4.35: Spatial distribution and temporal evolution of horizontal displacement U_x at three cross-sections in the middle of the sample EST 66747-2.

6.3 Analysis of anisotropic swelling results

As previously discussed, sample EST 72793-2 has a cylindrical aperture with a diameter of 1 mm, rather than two parts. It means the claystone will expand around the hole. The bedding plan in this sample is perpendicular to the injected water channel. Hence, the variations of the horizontal displacement U_x and vertical displacement U_y are investigated to understand the mechanics behavior in different directions. Fig. 4.36 and Fig. 4.37

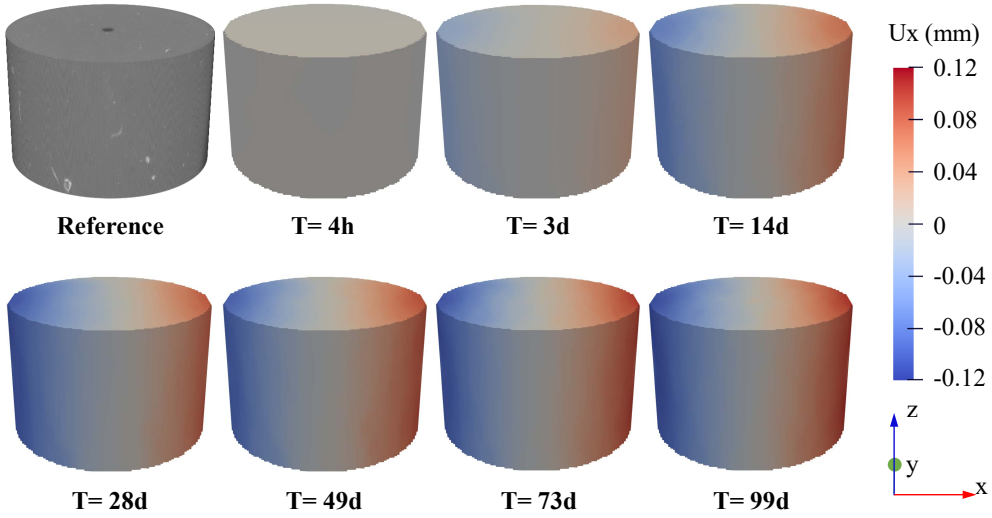

Figure 4.36: Evolution of the 3D horizontal displacements (U_x) measured with DVC in sample EST 72793-2 under 1.0 MPa confining pressure.

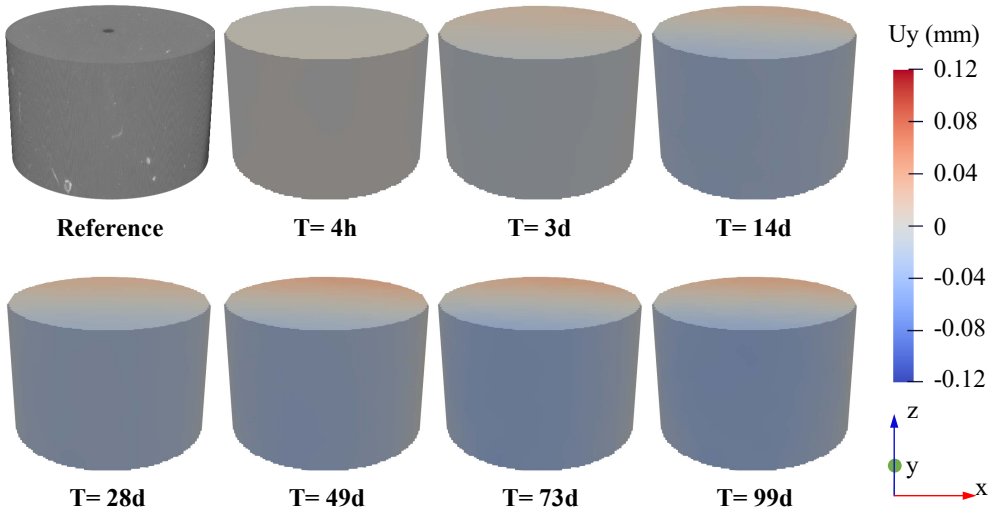

Figure 4.37: Evolution of the 3D vertical displacements (U_y) measured with DVC in sample EST 72793-2 under 1.0 MPa confining pressure.

respectively illustrate the evolution of the three-dimensional horizontal and vertical displacement fields of sample EST 72793-2 under a confining pressure of 1 MPa during resaturation. The results indicate that during the early stage of water injection (the first 3 days), the magnitude of U_x within the sample was relatively small and spatially uniform. After 14 days, a significant displacement gradient demonstrated that hydration-induced matrix swelling led to pronounced lateral deformation. Subsequently, the spatial distribution of displacement tends to stabilize and the displacement growth rate decreases.

The sample started to swell steadily, consistent with the diameter evolution shown in Fig. 4.18(b).

Compared with the horizontal displacement U_x, the vertical displacement U_y exhibits extremely small values, as seen in Fig. 4.37. It shows a clear anisotropic selling behavior between displacements in different directions. It is likely to be associated with the bedding plane of COx claystone, which is perpendicular to the lateral horizontal water injection channels. Thus, deformation perpendicular to the bedding plane strongly occurs as water infiltrates through the claystone matrix, resulting in large U_x. These observations further highlight the important role of bedding planes in influencing deformation properties and swelling anisotropy during the self-sealing process of claystone.

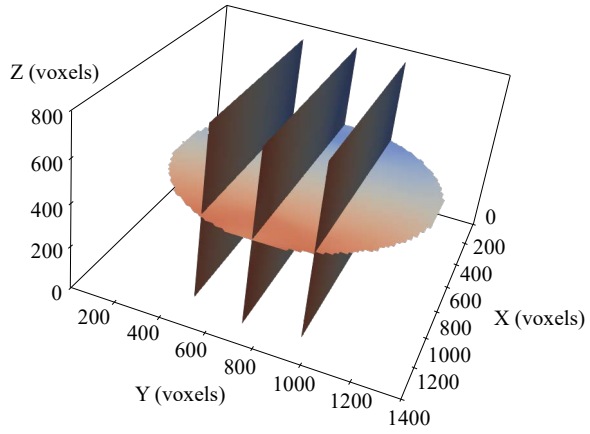

(a) selected three cross-sections

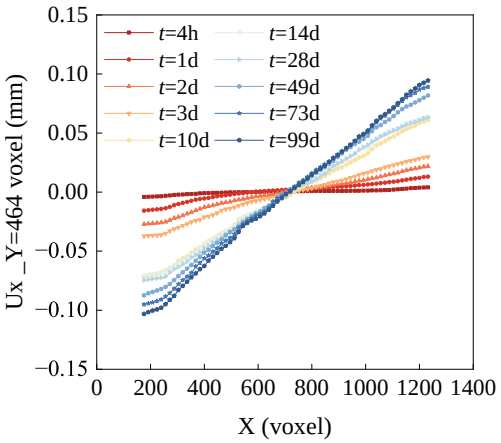

(b) U_x at cross-section $Y = 464$ voxels

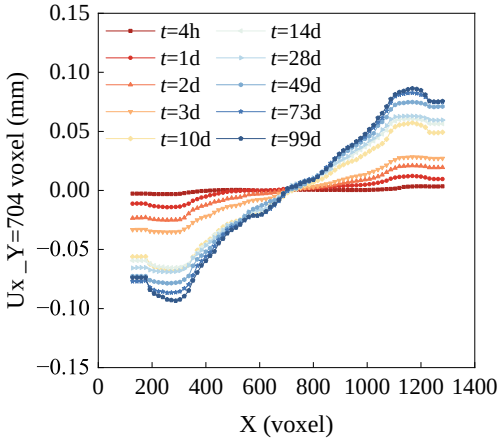

(c) U_x at cross-section $Y = 704$ voxels

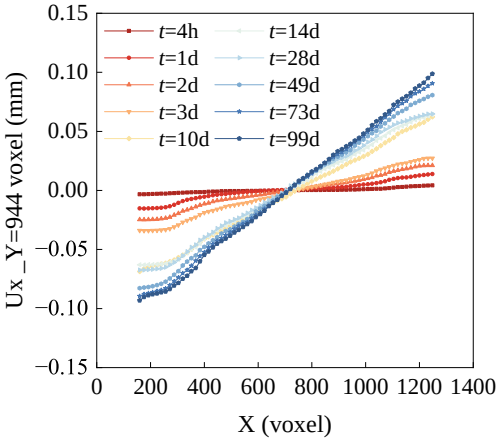

(d) U_x at cross-section $Y = 944$ voxels

Figure 4.38: Spatial distribution and temporal evolution of horizontal displacement U_x at three cross-sections in the middle of the sample EST 72793-2.

Here, horizontal displacement U_x curves in different cross-sections are further studied to explore the difference between the cracked zone and outside the cracked zone. Fig. 4.38 depicted U_x curves at three cross-sections, with the cross-section at $Y = 704$ voxels inside the fracture and the other two cross-sections outside the cracked zone. During early injection, horizontal displacement distributions along the X direction at all cross-sections remain relatively flat, with small displacement magnitudes, indicating that lateral deformation is still limited. After 10 days, the displacements at all cross-sections show a clear gradient and continue to increase in magnitude. The overall similarity in the temporal evolution of displacement across different cross-sections indicates that fracture closure is primarily driven by rock matrix swelling rather than significant material clogging within the fracture. After day 49, the displacement growth rate gradually decreases, and the swelling process begins slowly. These findings show that, under confining pressure, the lateral displacement caused by matrix swelling during the self-sealing process is limited in magnitude.

7 Gas migration behavior after sealing

As discussed in Chapter 3, gas breakthrough pressure (GBP) is most commonly used as a quantitative indicator to evaluate the sealing performance. Hence, the GBP test was

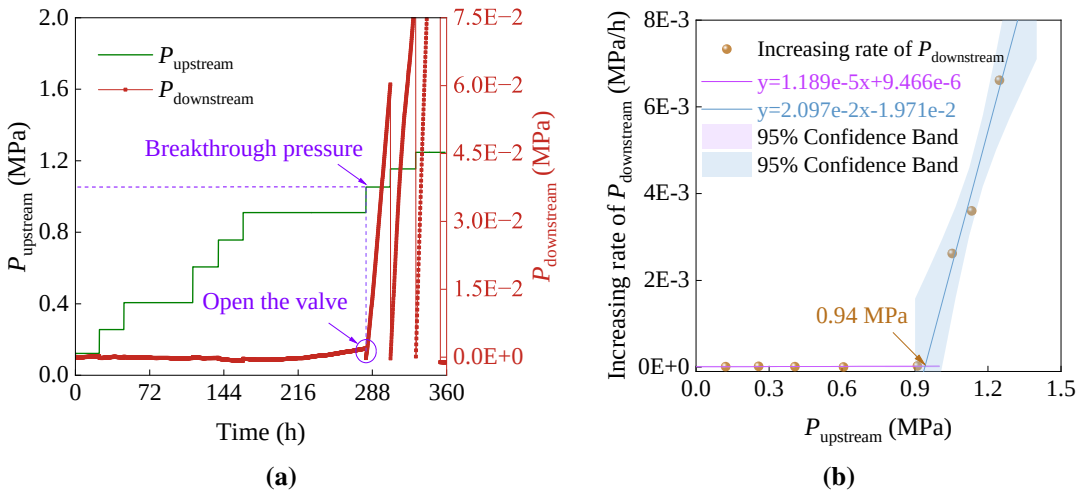

Figure 4.39: Gas breakthrough pressure of sealed sample EST 66747-4 under 3 MPa confining pressure: (a) evolution of $P_{upstream}$ and $P_{downstream}$ over time, (b) relationship between the increasing rate of $P_{downstream}$ and $P_{upstream}$.

conducted on sealed sample EST 66747-4 to evaluate its fracture closure effectiveness. The experiment was carried out under a confining pressure of 3 MPa, with the upstream gas pressure increased step-by-step by 0.1 MPa per increment. Argon is the injection gas. The downstream valve was opened every 24 h to check for continuous gas flow, while the downstream pressure was monitored over time. The specific description is shown in Chapter 3. The results are present in Fig. 4.39. It shows that once the upstream pressure reached the breakthrough threshold, the downstream pressure exhibited a sharp increase, with the observation of a water-gas mixture from the downstream outlet once the valve was opened. Through analyzing the relationship between the increasing rate of $P_{\text{downstream}}$ and P_{upstream}, the gas breakthrough pressure was further determined to be approximately 0.94 MPa. The GBP value of all tested samples is summarized in Fig. 4.40. Although this value is slightly lower than those of other samples mentioned in Zhao et al. (2026) and Chapter 3, it shows that the swelling-induced sealed sample has recovered significant gas barrier capability and can effectively block certain gas pressures. Lower GBP in this sample is associated with several factors, including various experimental models, devices, injection pressures and durations. These issues will be investigated further.

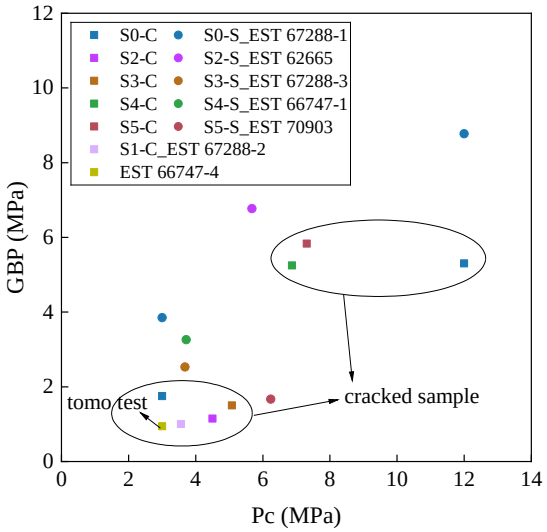

Figure 4.40: Gas breakthrough pressure of all tested samples versus confining pressure.

8 Conclusions

In this chapter, a miniature triaxial testing apparatus based on X-ray micro-tomography was developed to investigate the fracture closure behavior of COx claystone during indirect water injection. Combined with Digital Volume Correlation (DVC), the evolution of fracture closure and water-induced swelling during the re-saturation process was further analyzed. By comparing samples with different fracture geometries and subjected to different initial fracture openings, this chapter clarifies the spatiotemporal evolution characteristics of the self-sealing process in COx claystone and identifies the factors governing its efficiency. The results demonstrate that the self-sealing behavior of COx claystone can be divided into three stages: (i) initial swelling of injected point, (ii) localized matrix swelling on both sides of fracture zone to close fracture, and (iii) global swelling of sample after closure. Samples with small fracture apertures or numerous microcracks causing water infiltration pathways improve fracture closure. Even at relatively high injection pressures, complete fracture closure is challenging for samples with larger initial fracture openings. DVC analyses further reveal that strong local displacement gradients form along the fracture boundaries during the early stages of re-saturation. As the fracture progressively closes, this localized deformation region expands outward and eventually evolves into global swelling. From the deformation behavior of each sample with different geometry, it is characterized by noticeable displacement gradients but different deformation patterns and even spatial heterogeneity.

In general, this chapter clarifies the critical roles of fracture geometry, confining pressure, and water infiltration pathways in governing the self-sealing efficiency of COx claystone during re-saturation. It also reveals the intrinsic coupling between fracture closure and matrix swelling. The findings not only deepen the understanding of the microscale mechanisms associated with fracture closure under indirect re-saturation but also provide important experimental evidence and theoretical support for assessing the long-term sealing performance of COx claystone in geological disposal applications.

Note: This chapter has been written with a purpose of publication and is ready to submit.

CONCLUSIONS AND PERSPECTIVES

1 Conclusions

The Callovo-Oxfordian (COx) claystone, as a key potential host rock for deep geological disposal, is widely present in underground engineering environments such as radioactive waste repositories. Its extremely low permeability and inherent self-sealing capacity make it a critical material for evaluating the long-term safety of engineered barriers. In particular, under indirect water injection conditions, the self-sealing behavior of fractures directly governs the long-term evolution of radionuclide transport pathways. However, the sealing mechanisms induced by hydro-mechanical coupling have not yet been completely understood. Therefore, it is necessary to conduct a series of experiments to investigate these mechanisms. Here, two complementary experimental approaches have been designed and implemented to characterize the self-sealing behavior of cracked COx claystone. The first experiment involves improving three laboratory mock-ups based on hydro-mechanical coupling to analyze the evolution of transport, swelling pressure, and gas migration before and after fracture closure. The second experiment has developed a novel mini-triaxial setup suitable for indirect water injection, combined with X-ray micro-tomography, enabling 3D visible spatial evolution of fracture closure and matrix swelling.The main conclusions of this thesis are as follows:

- Three experimental mock-ups were developed to simulate an indirect percolation pathway, enabling characterization of the self-sealing process without directly injecting liquid water into the fracture. Comparison of the apparent water permeability across the three mock-ups shows highly consistent evolution, as the initial values were measured at about 10^{-19} m^2 and the stable value was close to 10^{-21} m^2. The results further indicated that the apparent water permeability is primarily governed by the saturation degree of the intact sample.

- Under the kinematically constrained condition, the swelling pressure is an efficient indicator of the self-sealing process. The apparent swelling pressure of the intact and cracked samples was simultaneously characterized. It is found that the swelling deformation and the related self-sealing process are strongly affected by the initial state of sample, in particular the initial water content and the distribution of mi-

crocracks and macroscopic fractures. Compared with the sound samples, the set-up of swelling pressure of the cracked samples during the first stage of saturation is slower. However, the experimental results show a significant difference in the cracked sample expansion between mock-ups III and II. In mock-up II, cracked samples had lower swelling pressures than intact samples, owing to direct water penetration into the main fracture and clay particle blockage. But due to deeper water infiltration in mock-up III, there is a higher swelling potential of the cracked sample during a longer swelling period, leading to a higher long-term swelling pressure. Compared with the samples with direct water penetration into the main fracture, the samples with an impermeable joint preventing direct water penetration into the fracture show a larger resaturation extent and then a higher swelling pressure. Furthermore, it has been observed that sample orientation has a significant impact on swelling pressure, but further research is required to provide evidence.

- Gas breakthrough pressure plays an important role in evaluating the sealing capacity of cracked claystone. Therefore, the gas breakthrough test was performed on the resaturated intact samples and the resealed cracked sample after sealing tests. It showed a strong linear relationship between breakthrough pressure and apparent swelling pressure in cracked samples, demonstrating that swelling-driven fracture closure significantly improved gas-sealing capacity. However, this relationship was not observed in intact samples, probably due to damage during the disassembling of the mock-up, resulting in lower measured breakthrough pressures. Finally, the re-sealing tests with water injection demonstrated that the gas-induced pathway would be effectively closed.

- The X-ray micro-tomography experiments using the designed novel triaxial setup show the fracture geometry CG3 is optimal for achieving complete closure, while larger fractures are challenging to seal even under high injection pressure. The fracture with geometry CG3 was closed at a low injection pressure of 0.3 MPa, with an initial fracture opening of about 0.4 mm. In contrast, even with a higher injected pressure of 1 MPa, it was difficult to fully close a large fracture with an initial fracture opening of about 2 mm. This demonstrates that fracture opening is one of the main factors affecting the sealing efficiency. The self-sealing behavior of COx claystone can be divided into three stages: (i) initial swelling of injected

point, (ii) localized matrix swelling on both sides of fracture zone to close fracture, and (iii) global swelling of sample after closure.

- DVC analysis further demonstrated the spatio-temporal evolution of deformation during the self-sealing process. With the resaturation, a noticeable local displacement gradient developed along the fracture boundary. As the fracture gradually closed, this localized deformation zone expanded outward, eventually changing into global swelling. This evolution was consistently observed under various fracture geometries and confining pressures, highlighting the intrinsic mechanisms governing self-sealing in COx claystone.

2 Perspectives

The self-sealing behavior following an indirect percolation path has been studied in the previous chapters and has obtained good experimental results. Nevertheless, the self-sealing process is influenced by multiple coupled factors, and several key scientific issues remain to be explored in greater depth. In future research, we will further improve the experimental design and compare the results with numerical simulations, with a particular focus on the following aspects:

- For the study in Chapter 1, the expansion of cracked samples under low confinement can be captured using a specially designed experimental mock-up and on this basis, the experimental study of swelling behavior in fragmented COx claystone using a stainless steel tube is worth further being investigated and compared.
- The experiments employing X-ray micro-tomography will be further improved, with investigations focusing on key influencing conditions, such as initial water content, the injection pressure, the fracture orientation with the bedding plane, and the temperature effects.
- Based on the experimental model in this study, a phase-field model under coupled hydro-mechanical conditions will be developed to preliminarily simulate the equivalent permeability evolution of claystone, enabling further analysis of the self-sealing effect. This simulation result will then be compared with experimental observations to verify the reliability.

REFERENCES

Agboli, M., Grgic, D., Moumni, M., and Giraud, A. (2024). Study under x-ray tomography of the impact of self-sealing process on the permeability of the callovo-oxfordian claystone. *Rock Mechanics and Rock Engineering*, 57(6):4213–4229.

Al Reda, S. M., Yu, C., Berthe, G., and Matray, J.-M. (2020). Study of the permeability in the opalinus clay series (mont terri-switzerland) using the steady state method in hassler cell. *Journal of Petroleum Science and Engineering*, 184:106457.

Amann, A., Waschbüsch, M., Bertier, P., Busch, A., Krooss, B. M., and Littke, R. (2011). Sealing rock characteristics under the influence of co2. *Energy Procedia*, 4:5170–5177.

Amann-Hildenbrand, A., Bertier, P., Busch, A., and Krooss, B. M. (2013). Experimental investigation of the sealing capacity of generic clay-rich caprocks. *International Journal of Greenhouse Gas Control*, 19:620–641.

Amann-Hildenbrand, A., Ghanizadeh, A., and Krooss, B. M. (2012). Transport properties of unconventional gas systems. *Marine and Petroleum Geology*, 31(1):90–99.

Anandarajah, A. and Chen, J. (1997). Van der waals attractive force between clay particles in water and contaminants. *Soils and foundations*, 37(2):27–37.

Anderson, R. L., Ratcliffe, I., Greenwell, H., Williams, P., Cliffe, S., and Coveney, P. V. (2010). Clay swelling—a challenge in the oilfield. *Earth-Science Reviews*, 98(3-4):201–216.

Andra (2005). Dossier 2005 argile: Synthesis: Evaluation of the feasibility of a geological repository in an argillaceous formation, meuse/haute-marne site.

Andra (2023). Synthesis: National inventory of radioactive materials and waste.

Andrew, M., Bijeljic, B., and Blunt, M. J. (2014). Pore-by-pore capillary pressure measurements using x-ray microtomography at reservoir conditions: Curvature, snap-off, and remobilization of residual co 2. *Water Resources Research*, 50(11):8760–8774.

Armand, G., Bumbieler, F., Conil, N., de La Vaissière, R., Bosgiraud, J.-M., and Vu, M.-N. (2017a). Main outcomes from in situ thermo-hydro-mechanical experiments programme to demonstrate feasibility of radioactive high-level waste disposal in the callovo-oxfordian claystone. *Journal of Rock Mechanics and Geotechnical Engineering*, 9(3):415–427.

Armand, G., Conil, N., Talandier, J., and Seyedi, D. M. (2017b). Fundamental aspects of the hydromechanical behaviour of callovo-oxfordian claystone: from experimental studies to model calibration and validation. *Computers and Geotechnics*, 85:277–286.

Armand, G., Leveau, F., Nussbaum, C., de La Vaissiere, R., Noiret, A., Jaeggi, D., Landrein, P., and Righini, C. (2014). Geometry and properties of the excavation-induced fractures at the meuse/haute-marne url drifts. *Rock mechanics and rock engineering*, 47(1):21–41.

Armand, G., Noiret, A., Zghondi, J., and Seyedi, D. (2013). Short-and long-term behaviors of drifts in the callovo-oxfordian claystone at the meuse/haute-marne underground research laboratory. *Journal of Rock Mechanics and Geotechnical Engineering*, 5(3):221–230.

Auvray, C., Morlot, C., Fourreau, E., and Talandier, J. (2015). X-ray tomography applied to self-healing experiments on argillites. In *13th ISRM International Congress of Rock Mechanics*.

Bandis, S., Lumsden, A., and Barton, N. (1983). Fundamentals of rock joint deformation. *International Journal of Rock Mechanics and Mining Sciences & Geomechanics Abstracts*, 20(6):249–268.

Barshad, I. (1949). The nature of lattice expansion and its relation to hydration in montmorillonite and vermiculite. *American Mineralogist: Journal of Earth and Planetary Materials*, 34(9-10):675–684.

Bastiaens, W., Bernier, F., and Li, X. L. (2007). Selfrac: Experiments and conclusions on fracturing, self-healing and self-sealing processes in clays. *Physics and Chemistry of the Earth, Parts A/B/C*, 32(8-14):600–615.

Benachour, Y., Davy, C. A., Skoczylas, F., and Houari, H. (2008). Effect of a high calcite filler addition upon microstructural, mechanical, shrinkage and transport properties of a mortar. *Cement and concrete research*, 38(6):727–736.

Berger, A., Witz, J.-F., El Bartali, A., Sadat, T., Limodin, N., Dubar, M., and Najjar, D. (2022). Experimental investigation of early strain heterogeneities and localizations in polycrystalline α-fe during monotonic loading. *International Journal of Plasticity*, 153:103253.

Bock, H., Dehandschutter, B., Martin, C. D., Mazurek, M., De Haller, A., Skoczylas, F., and Davy, C. (2010). Self-sealing of fractures in argillaceous formations in the context of geological disposal of radioactive waste. *OECD/NEA Report*, 6184:310.

Bossart, P., Meier, P. M., Moeri, A., Trick, T., and Mayor, J.-C. (2002). Geological and hydraulic characterisation of the excavation disturbed zone in the opalinus clay of the mont terri rock laboratory. *Engineering Geology*, 66(1-2):19–38.

Bossart, P., Nussbaum, C., and Schuster, K. (2019). Generation and self-sealing of the excavation-damaged zone (edz) around a subsurface excavation in a claystone. *Shale: Subsurface Science and Engineering*, pages 125–143.

Bossart, P., Trick, T., Meier, P. M., and Mayor, J.-C. (2004). Structural and hydrogeological characterisation of the excavation-disturbed zone in the opalinus clay (mont terri project, switzerland). *Applied clay science*, 26(1-4):429–448.

Boulin, P., Bretonnier, P., Vassil, V., Samouillet, A., Fleury, M., and Lombard, J. (2011). Entry pressure measurements using three unconventional experimental methods. In *international symposium of the society of core analysts*, pages 18–21.

Boulin, P., Bretonnier, P., Vassil, V., Samouillet, A., Fleury, M., and Lombard, J. (2013). Sealing efficiency of caprocks: Experimental investigation of entry pressure measurement methods. *Marine and Petroleum Geology*, 48:20–30.

Boulin, P. F., Angulo-Jaramillo, R., Daian, J.-F., Talandier, J., and Berne, P. (2008). Pore gas connectivity analysis in callovo-oxfordian argillite. *Applied clay science*, 42(1-2):276–283.

Brisard, S., Serdar, M., and Monteiro, P. J. (2020). Multiscale x-ray tomography of cementitious materials: A review. *Cement and Concrete Research*, 128:105824.

Busch, A. and Amann-Hildenbrand, A. (2013). Predicting capillarity of mudrocks. *Marine and petroleum geology*, 45:208–223.

Busch, A. and Müller, N. (2011). Determining co2/brine relative permeability and capillary threshold pressures for reservoir rocks and caprocks: Recommendations for development of standard laboratory protocols. *Energy Procedia*, 4:6053–6060.

Cauchy, A. et al. (1847). Méthode générale pour la résolution des systemes d'équations simultanées. *Comp. Rend. Sci. Paris*, 25(1847):536–538.

Charlier, R., Collin, F., Pardoen, B., Talandier, J., Radu, J.-P., and Gerard, P. (2013). An unsaturated hydro-mechanical modelling of two in-situ experiments in callovo-oxfordian argillite. *Engineering geology*, 165:46–63.

Chen, B., Li, Q., Tan, Y., Yu, T., Li, X., and Li, X. (2024). Experimental measurements and characterization models of caprock breakthrough pressure for co2 geological storage. *Earth-Science Reviews*, 252:104732.

Chen, G., Maes, T., Vandervoort, F., Sillen, X., Van Marcke, P., Honty, M., Dierick, M., and Vanderniepen, P. (2014). Thermal impact on damaged boom clay and opalinus clay: permeameter and isostatic tests with μct scanning. *Rock mechanics and rock engineering*, 47(1):87–99.

Chen, X., Xie, S., Zhang, W., Armand, G., and Shao, J. (2022). Creep deformation and gas permeability in fractured claystone under various stress states. *Rock Mechanics and Rock Engineering*, 55(4):1843–1853.

Chiarelli, A.-S., Ledesert, B., Sibai, M., Karami, M., and Hoteit, N. (2000). Influence of mineralogy and moisture content on plasticity and induced anisotropic damage of a claystone; application to nuclear waste disposals. *Bulletin de la Société géologique de France*, 171(6):621–627.

Chiarelli, A.-S., Shao, J.-F., and Hoteit, N. (2003). Modeling of elastoplastic damage behavior of a claystone. *International Journal of plasticity*, 19(1):23–45.

Cnudde, V. and Boone, M. N. (2013). High-resolution x-ray computed tomography in geosciences: A review of the current technology and applications. *Earth-Science Reviews*, 123:1–17.

Conil, N., Talandier, J., Djizanne, H., de La Vaissière, R., Righini-Waz, C., Auvray, C., Morlot, C., and Armand, G. (2018). How rock samples can be representative of in situ condition: A case study of callovo-oxfordian claystones. *Journal of Rock Mechanics and Geotechnical Engineering*, 10(4):613–623.

Cui, Y.-J., Nguyen, X.-P., Tang, A. M., and Li, X.-L. (2013). An insight into the unloading/reloading loops on the compression curve of natural stiff clays. *Applied clay science*, 83:343–348.

Cuss, R., Harrington, J., Giot, R., and Auvray, C. (2014). Experimental observations of mechanical dilation at the onset of gas flow in callovo-oxfordian claystone. *Geological Society, London, Special Publications*, 400:507–519.

Cuss, R. J., Harrington, J. F., Noy, D. J., Wikman, A., and Sellin, P. (2011a). Large scale gas injection test (lasgit): Results from two gas injection tests. *Physics and Chemistry of the Earth, Parts A/B/C*, 36(17-18):1729–1742.

Cuss, R. J., Milodowski, A., and Harrington, J. F. (2011b). Fracture transmissivity as a function of normal and shear stress: First results in opalinus clay. *Physics and Chemistry of the Earth, Parts A/B/C*, 36(17-18):1960–1971.

Daab, M., Eichstaedt, N. J., Habel, C., Rosenfeldt, S., Kalo, H., Schießling, H., Förster, S., and Breu, J. (2018). Onset of osmotic swelling in highly charged clay minerals. *Langmuir*, 34(28):8215–8222.

Dahdah, N., Limodin, N., El Bartali, A., Witz, J.-F., Seghir, R., Charkaluk, E., and Buffiere, J.-Y. (2016). Damage investigation in a319 aluminium alloy by x-ray tomography and digital volume correlation during in situ high-temperature fatigue tests. *Strain*, 52(4):324–335.

Dana, E. and Skoczylas, F. (1999). Gas relative permeability and pore structure of sandstones. *International Journal of Rock Mechanics and Mining Sciences*, 36(5):613–625.

Dao, L.-Q., Cui, Y.-J., Tang, A.-M., Pereira, J.-M., Li, X.-L., and Sillen, X. (2015). Impact of excavation damage on the thermo-hydro-mechanical properties of natural boom clay. *Engineering Geology*, 195:196–205.

Davy, C. A., Skoczylas, F., Barnichon, J.-D., and Lebon, P. (2007). Permeability of macro-cracked argillite under confinement: gas and water testing. *Physics and Chemistry of the Earth, Parts A/B/C*, 32(8-14):667–680.

Davy, C. A., Skoczylas, F., Lebon, P., and Dubois, T. (2009). Gas migration properties through a bentonite/argillite interface. *Applied Clay Science*, 42(3-4):639–648.

Davy, C. A., Skoczylas, F., and Talandier, J. (2013). Gas migration through cox claystone and implications for self-healing. In *Poromechanics V: Proceedings of the fifth biot conference on poromechanics*, pages 1615–1624.

Dazas, B., Ferrage, E., Delville, A., and Lanson, B. (2014). Interlayer structure model of tri-hydrated low-charge smectite by x-ray diffraction and monte carlo modeling in the grand canonical ensemble. *American Mineralogist*, 99(8-9):1724–1735.

de La Vaissière, R., Armand, G., and Talandier, J. (2015). Gas and water flow in an excavation-induced fracture network around an underground drift: a case study for a radioactive waste repository in clay rock. *Journal of Hydrology*, 521:141–156.

Desbois, G., Höhne, N., Urai, J. L., Bésuelle, P., and Viggiani, G. (2017). Deformation in cemented mudrock (callovo–oxfordian clay) by microcracking, granular flow and phyllosilicate plasticity: insights from triaxial deformation, broad ion beam polishing and scanning electron microscopy. *Solid Earth*, 8(2):291–305.

Dewhurst, D. N., Jones, R. M., and Raven, M. D. (2002). Microstructural and petrophysical characterization of muderong shale: application to top seal risking. *Petroleum Geoscience*, 8(4):371–383.

Di Donna, A., Charrier, P., Dijkstra, J., Andò, E., and Bésuelle, P. (2022). The contribution of swelling to self-sealing of claystone studied through x-ray tomography. *Physics and Chemistry of the Earth, Parts A/B/C*, 127:103191.

Di Donna, A., Charrier, P., Salager, S., and Bésuelle, P. (2019). Self-sealing capacity of argillite samples. In *7th international symposium on deformation characteristics of geomaterials*.

Domander, R., Felder, A. A., and Doube, M. (2021). Bonej2-refactoring established research software. *Wellcome Open Research*, 6:37.

Duan, Q., Chen, J., and Yang, X. (2020). A comparison of gas and water permeability in clay-bearing fault and reservoir rocks: Experimental results and evolution mechanisms. *Journal of Geophysical Research: Solid Earth*, 125(7):e2019JB018278.

Duan, Q. and Yang, X. (2014). Experimental studies on gas and water permeability of fault rocks from the rupture of the 2008 wenchuan earthquake, china. *Science China Earth Sciences*, 57(11):2825–2834.

Duan, Z., Skoczylas, F., Wang, C., and Talandier, J. (2021). Hydric cycle impacts on cox argillite permeability and young's modulus. *Rock Mechanics and Rock Engineering*, 54(3):1129–1147.

Egermann, P., Lombard, J., and Bretonnier, P. (2006). A fast and accurate method to measure threshold capillary pressure of caprocks under representative conditions. *SCA2006 A*, 46:1–14.

Ezzedine El Dandachy, M., Hassoun, L., El-Mir, A., and Khatib, J. M. (2024). Effect of elevated temperatures on compressive strength, ultrasonic pulse velocity, and transfer properties of metakaolin-based geopolymer mortars. *Buildings*, 14(7):2126.

Ferrage, E., Lanson, B., Malikova, N., Plançon, A., Sakharov, B. A., and Drits, V. A. (2005). New insights on the distribution of interlayer water in bi-hydrated smectite from x-ray diffraction profile modeling of 00 l reflections. *Chemistry of Materials*, 17(13):3499–3512.

Gaucher, E., Robelin, C., Matray, J., Negrel, G., Gros, Y., Heitz, J., Vinsot, A., Rebours, H., Cassagnabère, A., and Bouchet, A. (2004). Andra underground research laboratory: interpretation of the mineralogical and geochemical data acquired in the callovian–oxfordian formation by investigative drilling. *Physics and Chemistry of the Earth, Parts A/B/C*, 29(1):55–77.

Gay, N., Duan, Z., Skoczylas, F., and Briffaut, M. (2026). Measuring low gas permeability of granites: a comparative assessment of quasi-steady-state and pulse-test methods. *European Journal of Environmental and Civil Engineering*, 30(1):2621812.

Ghayaza, M., Skoczylas, F., Robinet, J., and Talandier, J. (2013). Self-sealing capacity of macro-cracked argillite under confinement. In *Poromechanics V: Proceedings of the Fifth Biot Conference on Poromechanics*, pages 1580–1589.

Ghazy, A. and Bassuoni, M. (2017). Resistance of concrete to different exposures with chloride-based salts. *Cement and Concrete Research*, 101:144–158.

Giot, R., Auvray, C., Conil, N., and de La Vaissière, R. (2018). Multi-stage water permeability measurements on claystone by steady and transient flow methods. *Engineering Geology*, 247:27–37.

Giot, R., Auvray, C., and Talandier, J. (2019). Self-sealing of claystone under x-ray nanotomography. *Geological Society, London, Special Publications*, 482.

Gonzalez-Blanco, L., Romero, E., and Levasseur, S. (2024). Self-sealing of boom clay after gas transport. *Rock Mechanics and Rock Engineering*, 57(6):4173–4189.

Grgic, D., Giraud, A., and Schoumacker, L. (2019). Dynamic anisotropic elastic properties of a claystone under variable loading direction and saturation. *Geophysical Journal International*, 216(1):148–163.

Gupta, R., Lukić, B., Tengattini, A., Dufour, F., and Briffaut, M. (2022). Experimental characterisation of transient condensed water vapour migration through cracked concrete as revealed by neutron and x-ray imaging: Effect of initial saturation. *Cement and Concrete Research*, 162:106987.

Hale, S., Ries, X., Jaeggi, D., and Blum, P. (2021). Mechanical and hydraulic properties of the excavation damaged zone (edz) in the opalinus clay of the mont terri rock laboratory, switzerland. *Solid earth*, 12(7):1581–1600.

Hao, J., Ma, L., Hollis, C., Fauchille, A.-L., and Taylor, K. G. (2023). Spatial distribution of mineral development in carboniferous bowland shale, uk at 3d micro-to nano-scales. *International Journal of Coal Geology*, 271:104236.

Harrington, J., Cuss, R., Noy, D., Graham, C., Milodowski, A., Hall, M., and Talandier, J. (2015). Stress coupling in callovo-oxfordian claystone during gas and water flow. In *6th international conference clays in natural and engineered barriers for radioactive waste confinement, Brussels, March*, pages 23–26.

Harrington, J., de La Vaissière, R., Noy, D., Cuss, R., and Talandier, J. (2012). Gas flow in callovo-oxfordian claystone (cox): results from laboratory and field-scale measurements. *Mineralogical Magazine*, 76(8):3303–3318.

Harrington, J. F., Cuss, R. J., and Talandier, J. (2017). Gas transport properties through intact and fractured callovo-oxfordian mudstones. *Geological Society, London, Special Publications*, 454:131–154.

Hassler, G. and Brunner, E. (1945). Measurement of capillary pressures in small core samples. *Transactions of the AIME*, 160(01):114–123.

Hildenbrand, A., Schlömer, S., and Krooss, B. (2002). Gas breakthrough experiments on fine-grained sedimentary rocks. *Geofluids*, 2(1):3–23.

Homand, F., Giraud, A., Escoffier, S., Koriche, A., and Hoxha, D. (2004). Permeability determination of a deep argillite in saturated and partially saturated conditions. *International Journal of Heat and Mass Transfer*, 47(14-16):3517–3531.

Horseman, S., Harrington, J., and Sellin, P. (1999). Gas migration in clay barriers. *Engineering geology*, 54(1-2):139–149.

Hosdez, J., Witz, J.-F., Martel, C., Limodin, N., Najjar, D., Charkaluk, E., Osmond, P., and Szmytka, F. (2017). Fatigue crack growth law identification by digital image correlation and electrical potential method for ductile cast iron. *Engineering Fracture Mechanics*, 182:577–594.

Hu, D., Zhang, F., Shao, J.-F., and Gatmiri, B. (2014). Influences of mineralogy and water content on the mechanical properties of argillite. *Rock mechanics and rock engineering*, 47(1):157–166.

Ibrahim, N. (2008). *Caractérisation des propriétés mécaniques des géomatériaux par technique de micro indentation*. PhD thesis, Lille 1.

Ito, D., Akaku, K., Okabe, T., Takahashi, T., and Tsuji, T. (2011). Measurement of threshold capillary pressure for seal rocks using the step-by-step approach and the residual pressure approach. *Energy Procedia*, 4:5211–5218.

Jougnot, D., Revil, A., Lu, N., and Wayllace, A. (2010). Transport properties of the callovo-oxfordian clay rock under partially saturated conditions. *Water Resources Research*, 46(8).

Kak, A. C. and Slaney, M. (2001). *Principles of computerized tomographic imaging*. SIAM.

Karaborni, S., Smit, B., Heidug, W., Urai, J., and Van Oort, E. (1996). The swelling of clays: molecular simulations of the hydration of montmorillonite. *Science*, 271(5252):1102–1104.

Kawakata, H., Cho, A., Yanagidani, T., and Shimada, M. (1997). The observations of faulting in westerly granite under triaxial compression by x-ray ct scan. *International Journal of Rock Mechanics and Mining Sciences*, 34(3-4):151–e1.

Keller, L. M. and Giger, S. B. (2019). Petrophysical properties of opalinus clay drill cores determined from med-xct images. *Geotechnical and Geological Engineering*, 37(4):3507–3522.

Keller, L. M., Holzer, L., Wepf, R., and Gasser, P. (2011). 3d geometry and topology of pore pathways in opalinus clay: Implications for mass transport. *Applied clay science*, 52(1-2):85–95.

Keller, L. M., Schuetz, P., Erni, R., Rossell, M. D., Lucas, F., Gasser, P., and Holzer, L. (2013). Characterization of multi-scale microstructural features in opalinus clay. *Microporous and mesoporous materials*, 170:83–94.

Keller, W., Reynolds, R., and Inoue, A. (1986). Morphology of clay minerals in the smectite-to-illite conversion series by scanning electron microscopy. *Clays and Clay Minerals*, 34(2):187–197.

Klinkenberge, L. (1941). The permeability of porous media to liquids and gases. *Drilling and production practice*, pages 200–213.

Laird, D. A. (2006). Influence of layer charge on swelling of smectites. *Applied clay science*, 34(1-4):74–87.

Laird, D. A., Shang, C., and Thompson, M. L. (1995). Hysteresis in crystalline swelling of smectites. *Journal of Colloid and Interface Science*, 171(1):240–245.

Lerouge, C., Grangeon, S., Gaucher, E. C., Tournassat, C., Agrinier, P., Guerrot, C., Widory, D., Fléhoc, C., Wille, G., Ramboz, C., et al. (2011). Mineralogical and isotopic record of biotic and abiotic diagenesis of the callovian–oxfordian clayey formation of bure (france). *Geochimica et Cosmochimica Acta*, 75(10):2633–2663.

Li, Z., Limodin, N., Tandjaoui, A., Quaegebeur, P., Witz, J.-F., and Balloy, D. (2017). Influence of fe content on the damage mechanism in a319 aluminum alloy: Tensile tests and digital image correlation. *Engineering Fracture Mechanics*, 183:94–108.

Li, Z., Limodin, N., Tandjaoui, A., Quaegebeur, P., Witz, J.-F., and Balloy, D. (2020). In-situ 3d characterization of tensile damage mechanisms in a319 aluminium alloy using x-ray tomography and digital volume correlation. *Materials Science and Engineering: A*, 794:139920.

Limodin, N., Rougelot, T., and Hauss, G. (2013). Isis4d-in situ innovative set-ups under x-ray microtomography.

Lion, M., Skoczylas, F., Lafhaj, Z., and Sersar, M. (2005). Experimental study on a mortar. temperature effects on porosity and permeability. residual properties or direct measurements under temperature. *Cement and Concrete Research*, 35(10):1937–1942.

Liu, J., Davy, C. A., Talandier, J., and Skoczylas, F. (2014). Effect of gas pressure on the sealing efficiency of compacted bentonite–sand plugs. *Journal of Contaminant Hydrology*, 170:10–27.

Liu, J.-F., Song, S.-B., Ni, H.-Y., Cao, X.-L., Pu, H., Mao, X.-B., and Skoczylas, F. (2018a). Research on gas migration properties in a saturated bentonite/sand mixture under flexible boundary conditions. *Soils and foundations*, 58(1):97–109.

Liu, J.-F., Song, Y., Skoczylas, F., and Liu, J. (2015). Gas migration through water-saturated bentonite–sand mixtures, cox argillite, and their interfaces. *Canadian Geotechnical Journal*, 53(1):60–71.

Liu, J.-f., Wu, Y., Cai, C.-Z., Ni, H.-y., Cao, X.-l., Pu, H., Song, S.-b., Pu, S.-y., and Skoczylas, F. (2018b). Investigation into water retention and gas permeability of opalinus clay. *Environmental Earth Sciences*, 77(5):213.

Liu, Z. and Shao, J. (2016). Moisture effects on damage and failure of bure claystone under compression. *Geotechnique letters*, 6(3):182–186.

Loosveldt, H., Lafhaj, Z., and Skoczylas, F. (2002). Experimental study of gas and liquid permeability of a mortar. *Cement and concrete research*, 32(9):1357–1363.

Marschall, P., Giger, S., De La Vassière, R., Shao, H., Leung, H., Nussbaum, C., Trick, T., Lanyon, B., Senger, R., Lisjak, A., et al. (2017). Hydro-mechanical evolution of the edz as transport path for radionuclides and gas: insights from the mont terri rock laboratory (switzerland). In *Mont Terri Rock Laboratory, 20 Years: Two Decades of*

Research and Experimentation on Claystones for Geological Disposal of Radioactive Waste, pages 175–196. Springer.

Marschall, P., Horseman, S., and Gimmi, T. (2005). Characterisation of gas transport properties of the opalinus clay, a potential host rock formation for radioactive waste disposal. *Oil & gas science and technology*, 60(1):121–139.

Mayer, R. P. and Stowe, R. A. (1965). Mercury porosimetry—breakthrough pressure for penetration between packed spheres. *Journal of colloid Science*, 20(8):893–911.

Menaceur, H., Delage, P., Tang, A. M., and Talandier, J. (2016). The status of water in swelling shales: an insight from the water retention properties of the callovo-oxfordian claystone. *Rock Mechanics and Rock Engineering*, 49(12):4571–4586.

Meyn, V. (1999). Die bedeutung des sperrdrucks (threshold pressure) für den fluidtransport in niedrigstpermeablen gesteinen: Experimentelle und theoretische aspekte. In *DGMK Spring Conference, Celle, Germany*, pages 255–264.

Meziani, H. and Skoczylas, F. (1999). An experimental study of the mechanical behaviour of a mortar and of its permeability under deviatoric loading. *Materials and structures*, 32(6):403–409.

Mitchell, J. and Soga, K. (2005). *Fundamentals of soil behavior*. John Wiley & Sons.

Monfared, M., Sulem, J., Delage, P., and Mohajerani, M. (2012). On the thm behaviour of a sheared boom clay sample: Application to the behaviour and sealing properties of the edz. *Engineering Geology*, 124:47–58.

M'Jahad, S., Davy, C. A., Skoczylas, F., and Talandier, J. (2017). Characterization of transport and water retention properties of damaged callovo-oxfordian claystone. *Geological Society, London, Special Publications*, 443.

Németh, T., Máthé, Z., Pekker, P., Dódony, I., Kovács-Kis, V., Sipos, P., Cora, I., and Kovács, I. (2016). Clay mineralogy of the boda claystone formation (mecsek mts., sw hungary). *Open Geosciences*, 8(1):259–274.

Niandou, H., Shao, J., Henry, J., and Fourmaintraux, D. (1997). Laboratory investigation of the mechanical behaviour of tournemire shale. *International Journal of Rock Mechanics and Mining Sciences*, 34(1):3–16.

Norrish, K. (1954). The swelling of montmorillonite. *Discussions of the Faraday society*, 18:120–134.

Olivella, S. and Alonso, E. (2008). Gas flow through clay barriers. *Géotechnique*, 58(3):157–176.

Ortiz, L., Volckaert, G., and Mallants, D. (2002). Gas generation and migration in boom clay, a potential host rock formation for nuclear waste storage. *Engineering geology*, 64(2-3):287–296.

Pham, Q., Vales, F., Malinsky, L., Minh, D. N., and Gharbi, H. (2007). Effects of desaturation–resaturation on mudstone. *Physics and Chemistry of the Earth, Parts A/B/C*, 32(8-14):646–655.

Pimentel, E. (2015). Existing methods for swelling tests–a critical review. *Energy Procedia*, 76:96–105.

Purcell, W. (1949). Capillary pressures-their measurement using mercury and the calculation of permeability therefrom. *Journal of Petroleum Technology*, 1(02):39–48.

Pusch, R., Ranhagen, L., Nilsson, K., and Geological, S. (1985). Gas migration through mx-80 bentonite. final report. In *NAGRA Technical Report TR-85-36*.

Quacquarelli, A., Talandier, J., Di Donna, A., and Collin, F. (2024). Numerical modeling of self-sealing in fractured clayey materials. *Acta Geotechnica*, 19(6):3785–3803.

Rao, S., Thyagaraj, T., and Thomas, H. (2006). Swelling of compacted clay under osmotic gradients. *Géotechnique*, 56(10):707–713.

Rashid, S., Lee, S. Y., and Hasan, M. K. (2012). An improved method for the removal of ring artifacts in high resolution ct imaging. *EURASIP Journal on Advances in Signal Processing*, 2012(1):93.

Rastiello, G., Tailhan, J. L., Rossi, P., and Dal Pont, S. (2015). Macroscopic probabilistic cracking approach for the numerical modelling of fluid leakage in concrete. *Annals of Solid and Structural Mechanics*, 7:1–16.

Rezaeyan, A., Tabatabaei-Nejad, S. A., Khodapanah, E., and Kamari, M. (2015). Parametric analysis of caprock integrity in relation with co2 geosequestration: capillary breakthrough pressure of caprock and gas effective permeability. *Greenhouse Gases: Science and Technology*, 5(6):714–731.

Rhaiem, H. B., Pons, C., and Tessier, D. (1987). Factors affecting the microstructure of smectites: role of cation and history of applied stresses. *In: Proceedings of the International Clay Conference. Denver: The Clay Mineral Society*, pages 292–297.

Robinet, J.-C., Sardini, P., Coelho, D., Parneix, J.-C., Prêt, D., Sammartino, S., Boller, E., and Altmann, S. (2012). Effects of mineral distribution at mesoscopic scale on solute diffusion in a clay-rich rock: Example of the callovo-oxfordian mudstone (bure, france). *Water resources research*, 48(5).

Rossen, W. R. (2000). Snap-off in constricted tubes and porous media. *Colloids and Surfaces A: Physicochemical and Engineering Aspects*, 166(1-3):101–107.

Rutqvist, J. (2012). The geomechanics of co2 storage in deep sedimentary formations. *Geotechnical and Geological Engineering*, 30(3):525–551.

Sabet, S., Barisik, M., Mobedi, M., and Beskok, A. (2019). An extended kozeny-carman-klinkenberg model for gas permeability in micro/nano-porous media. *Physics of Fluids*, 31(11).

Saiyouri, N., Hicher, P.-Y., and Tessier, D. (2000). Microstructural approach and transfer water modelling in highly compacted unsaturated swelling clays. *Mechanics of Cohesive-frictional Materials: An International Journal on Experiments, Modelling and Computation of Materials and Structures*, 5(1):41–60.

Saiyouri, N., Tessier, D., and Hicher, P.-Y. (2004). Experimental study of swelling in unsaturated compacted clays. *Clay minerals*, 39(4):469–479.

Savoye, S., Goutelard, F., Beaucaire, C., Charles, Y., Fayette, A., Herbette, M., Larabi, Y., and Coelho, D. (2011). Effect of temperature on the containment properties of argillaceous rocks: The case study of callovo–oxfordian claystones. *Journal of contaminant hydrology*, 125(1-4):102–112.

Schlömer, S. and Krooss, B. M. (1997). Experimental characterisation of the hydrocarbon sealing efficiency of cap rocks. *Marine and Petroleum Geology*, 14(5):565–580.

Seghir, R., Witz, J.-F., and Coudert, S. (2014). Yadics-digital image correlation 2/3d software.

Shi, H., Hosdez, J., Rougelot, T., Xie, S., Shao, J., Talandier, J., and Lacidogna, G. (2020). Digital volume correlation applied to x-ray micro-tomography images in uniaxial creep tests on anisotropic clayey rock. *Applied Sciences*, 10(14):4898.

Shi, H., Rougelot, T., Xie, S., Shao, J., and Talandier, J. (2023). Investigation of strain fields and anisotropy in triaxial tests on callovo-oxfordian claystone by x-ray micro-tomography and digital volume correlation. *International Journal of Rock Mechanics and Mining Sciences*, 163:105330.

Shi, H.-L., Hosdez, J., Rougelot, T., Xie, S.-Y., Shao, J.-F., and Talandier, J. (2021). Analysis of local creep strain field and cracking process in claystone by x-ray micro-tomography and digital volume correlation. *Rock Mechanics and Rock Engineering*, 54(4):1937–1952.

Sing, K. S. (1985). Reporting physisorption data for gas/solid systems with special reference to the determination of surface area and porosity (recommendations 1984). *Pure and applied chemistry*, 57(4):603–619.

Song, Y., Davy, C. A., Bertier, P., and Troadec, D. (2016a). Understanding fluid transport through claystones from their 3d nanoscopic pore network. *Microporous and Mesoporous Materials*, 228:64–85.

Song, Y., Davy, C. A., and Skoczylas, F. (2015a). Gas migration through self-sealed or intact claystone. In *International Symposium of the Society of Core Analysts*, Canada. SCA2015-046.

Song, Y., Davy, C. A., and Troadec, D. (2016b). Gas breakthrough pressure (gbp) through claystones: correlation with fib/sem imaging of the pore volume. *Oil & Gas Science and Technology*, 71(4):51.

Song, Y., Davy, C. A., Troadec, D., Blanchenet, A.-M., Skoczylas, F., Talandier, J., and Robinet, J.-C. (2015b). Multi-scale pore structure of cox claystone: Towards the prediction of fluid transport. *Marine and Petroleum Geology*, 65:63–82.

Soomro, A. N., Anioł, Ł., Kudasik, M., Dąbrowski, K., and Nagy, S. (2025). Comparative analysis of capillary threshold pressure measurement techniques: mercury intrusion porosimetry vs. innovative measuring tool for carbon storage. *Frontiers in Energy Research*, 13:1518424.

Sridharan, A., Rao, A. S., and Sivapullaiah, P. V. (1986). Swelling pressure of clays. *Geotechnical Testing Journal*, 9(1):24–33.

Stavropoulou, E., Andò, E., Roubin, E., Lenoir, N., Tengattini, A., Briffaut, M., and Bésuelle, P. (2020). Dynamics of water absorption in callovo-oxfordian claystone revealed with multimodal x-ray and neutron tomography. *Frontiers in Earth Science*, 8:6.

Stavropoulou, E., Andò, E., Tengattini, A., Briffaut, M., Dufour, F., Atkins, D., and Armand, G. (2019). Liquid water uptake in unconfined callovo oxfordian clay-rock studied with neutron and x-ray imaging. *Acta Geotechnica*, 14(1):19–33.

Tanai, K., Kanno, T., and Gallé, C. (1996). Experimental study of gas permeabilities and breakthrough pressures in clays. *MRS Online Proceedings Library*, 465(1):995–1002.

Tang, C., Tang, A. M., Cui, Y.-J., Delage, P., Schroeder, C., and De Laure, E. (2011). Investigating the swelling pressure of compacted crushed-callovo-oxfordian claystone. *Physics and Chemistry of the Earth, Parts A/B/C*, 36(17-18):1857–1866.

Tanikawa, W. and Shimamoto, T. (2006). Klinkenberg effect for gas permeability and its comparison to water permeability for porous sedimentary rocks. *Hydrology and Earth System Sciences Discussions*, 3(4):1315–1338.

Thomas, L., Katz, D., and Tek, M. (1968). Threshold pressure phenomena in porous media. *Society of Petroleum Engineers Journal*, 8(02):174–184.

Tsang, C.-F., Barnichon, J.-D., Birkholzer, J., Li, X. L., Liu, H., and Sillen, X. (2012). Coupled thermo-hydro-mechanical processes in the near field of a high-level radioactive waste repository in clay formations. *International Journal of Rock Mechanics and Mining Sciences*, 49:31–44.

Tsang, C.-F., Bernier, F., and Davies, C. (2005). Geohydromechanical processes in the excavation damaged zone in crystalline rock, rock salt, and indurated and plastic clays—in the context of radioactive waste disposal. *International Journal of Rock Mechanics and Mining Sciences*, 42(1):109–125.

Van Geet, M., Bastiaens, W., and Ortiz, L. (2008). Self-sealing capacity of argillaceous rocks: review of laboratory results obtained from the selfrac project. *Physics and Chemistry of the Earth, Parts A/B/C*, 33:S396–S406.

Villar, M. V. and Lloret, A. (2008). Influence of dry density and water content on the swelling of a compacted bentonite. *Applied Clay Science*, 39(1-2):38–49.

Voltolini, M. and Ajo-Franklin, J. B. (2020). The sealing mechanisms of a fracture in opalinus clay as revealed by in situ synchrotron x-ray micro-tomography. *Frontiers in Earth Science*, 8:207.

Wan, M., Delage, P., Tang, A. M., and Talandier, J. (2013). Water retention properties of the callovo-oxfordian claystone. *International Journal of Rock Mechanics and Mining Sciences*, 64:96–104.

Wang, C. (2021a). *Cicatrisation et colmatage de l'argilite de Bure*. PhD thesis, Centrale Lille.

Wang, C., Briffaut, M., Talandier, J., and Skoczylas, F. (2024). Self-sealing of pre-cracked callovo-oxfordian claystone: Implications for geological disposal of nuclear waste. *International Journal of Rock Mechanics and Mining Sciences*, 175:105678.

Wang, C., Talandier, J., and Skoczylas, F. (2022a). Swelling and fluid transport of re-sealed callovo–oxfordian claystone. *Rock Mechanics and Rock Engineering*, 55(3):1143–1158.

Wang, H. (2021b). *Delayed and swelling behaviour of damaged/fractured Callovo-Oxfordian claystone*. PhD thesis, École des Ponts ParisTech.

Wang, H., Cui, Y.-J., Dangla, P., Vu, M. N., and Talandier, J. (2025). Anisotropic mechanical behaviour of callovo-oxfordian claystone under triaxial lateral unloading. *Journal of Rock Mechanics and Geotechnical Engineering*.

Wang, H., Cui, Y.-J., Vu, M. N., Talandier, J., and Conil, N. (2022b). Fracture effect on the hydro-mechanical behaviour of callovo-oxfordian claystone. *Engineering Geology*, 303:106674.

Wang, H., de La Vaissière, R., Vu, M.-N., La Borderie, C., and Gallipoli, D. (2022c). Numerical modelling and in-situ experiment for self-sealing of the induced fracture network of drift into the callovo-oxfordian claystone during a hydration process. *Computers and Geotechnics*, 141:104487.

Wang, L., Bornert, M., and Chanchole, S. (2013). Micro-scale experimental investigation of deformation and damage of argillaceous rocks under hydric and mechanical loads. In *Poromechanics V: Proceedings of the Fifth Biot Conference on Poromechanics*, pages 1635–1643.

Wang, L., Bornert, M., Yang, D., Héripré, E., Chanchole, S., Halphen, B., Pouya, A., and Caldemaison, D. (2015). Microstructural insight into the nonlinear swelling of argillaceous rocks. *Engineering Geology*, 193:435–444.

Wang, L., Yang, R., Chanchole, S., and Zhang, G. (2017). The time-dependent swelling of argillaceous rock under resaturated conditions. *Applied Clay Science*, 146:186–194.

Wang, Q., Meng, Y., Su, W., Ye, W., and Chen, Y. (2021). Cracking and sealing behavior of the compacted bentonite upon technological voids filling. *Engineering Geology*, 292:106244.

Wang, Q., Tang, A. M., Cui, Y.-J., Delage, P., and Gatmiri, B. (2012). Experimental study on the swelling behaviour of bentonite/claystone mixture. *Engineering geology*, 124:59–66.

Washburn, E. W. (1921a). The dynamics of capillary flow. *Physical review*, 17(3):273.

Washburn, E. W. (1921b). Note on a method of determining the distribution of pore sizes in a porous material. *Proceedings of the National Academy of Sciences*, 7(4):115–116.

Wen, S., Cheng, W.-C., Li, D., and Hu, W. (2023). Evaluating gas breakthrough pressure and gas permeability in a landfill cover layer for mitigation of hazardous gas emissions. *Journal of Environmental Management*, 336:117617.

Wikramaratna, R. S., Goodfield, M., Rodwell, W., Nash, P., and Agg, P. (1993). *A preliminary assessment of gas migration from the copper/steel canister*. Swedish Nuclear Fuel and Waste Management Company.

Wu, T., Pan, Z., Connell, L. D., Liu, B., Fu, X., and Xue, Z. (2020). Gas breakthrough pressure of tight rocks: A review of experimental methods and data. *Journal of Natural Gas Science and Engineering*, 81:103408.

Yang, D., Chanchole, S., Valli, P., and Chen, L. (2013). Study of the anisotropic properties of argillite under moisture and mechanical loads. *Rock mechanics and rock engineering*, 46(2):247–257.

Yuan, H., Agostini, F., Pei, Y., Zhang, M., Zhang, Q., Skoczylas, F., and Talandier, J. (2023). Experimental investigation on the effects of confining pressure and pore pressure on gas/water transport properties of cox argillite. *Applied Clay Science*, 244:107090.

Yuan, H., Agostini, F., Skoczylas, F., and Talandier, J. (2020). About adsorption effects on the poroelastic properties and gas permeability of cox claystone. *European Journal of Environmental and Civil Engineering*, 24(2):267–282.

Yven, B., Sammartino, S., Geraud, Y., Homand, F., and Villieras, F. (2007). Mineralogy, texture and porosity of callovo-oxfordian argillites of the meuse/haute-marne region (eastern paris basin). *Mémoires de la Société géologique de France*, 178(1):73–90.

Zappone, A., Rinaldi, A. P., Grab, M., Wenning, Q., Roques, C., Madonna, C., Obermann, A., Bernasconi, S. M., Soom, F., Cook, P., et al. (2020). Fault sealing and caprock integrity for co 2 storage: an in-situ injection experiment. *Solid Earth Discussions*, 2020:1–51.

Zeng, Z., Cui, Y.-J., and Talandier, J. (2021). Compaction and sealing properties of bentonite/claystone mixture: Impacts of bentonite fraction, water content and dry density. *Engineering Geology*, 287:106122.

Zhang, C., Heemann, U., Schmidt, M. W., and Staupendahl, G. W. (1993). A constitutive model for description of compaction behavior of crushed salt backfill. *In: Proceedings of the ISRM International Symposium - EUROCK 93, Lisboa, Portugal*.

Zhang, C. and Rothfuchs, T. (2004). Experimental study of the hydro-mechanical behaviour of the callovo-oxfordian argillite. *Applied Clay Science*, 26(1-4):325–336.

Zhang, C., Wieczorek, K., and Xie, M. (2010). Swelling experiments on mudstones. *Journal of Rock Mechanics and Geotechnical Engineering*, 2(1):44–51.

Zhang, C.-L. (2011). Experimental evidence for self-sealing of fractures in claystone. *Physics and Chemistry of the Earth, Parts A/B/C*, 36(17-18):1972–1980.

Zhang, C.-L. (2013). Sealing of fractures in claystone. *Journal of Rock Mechanics and Geotechnical Engineering*, 5(3):214–220.

Zhang, C.-L. (2015). Investigation of gas migration in damaged and resealed claystone. *Geological society, London, special publications*, 415(1):75–93.

Zhang, C.-L. (2016). The stress–strain–permeability behaviour of clay rock during damage and recompaction. *Journal of Rock Mechanics and Geotechnical Engineering*, 8(1):16–26.

Zhang, C.-L. (2018). Thermo-hydro-mechanical behavior of clay rock for deep geological disposal of high-level radioactive waste. *Journal of Rock Mechanics and Geotechnical Engineering*, 10(5):992–1008.

Zhang, C.-L., Armand, G., Conil, N., and Laurich, B. (2019). Investigation on anisotropy of mechanical properties of callovo-oxfordian claystone. *Engineering Geology*, 251:128–145.

Zhang, C.-L. and Rothfuchs, T. (2008). Damage and sealing of clay rocks detected by measurements of gas permeability. *Physics and Chemistry of the Earth, Parts A/B/C*, 33:S363–S373.

Zhang, C.-L., Rothfuchs, T., Su, K., and Hoteit, N. (2007). Experimental study of the thermo-hydro-mechanical behaviour of indurated clays. *Physics and Chemistry of the Earth, Parts A/B/C*, 32(8-14):957–965.

Zhang, C.-L. and Talandier, J. (2023). Self-sealing of fractures in indurated claystones measured by water and gas flow. *Journal of Rock Mechanics and Geotechnical Engineering*, 15(1):227–238.

Zhang, F., Cui, Y.-J., Conil, N., and Talandier, J. (2020). Assessment of swelling pressure determination methods with intact callovo-oxfordian claystone. *Rock Mechanics and Rock Engineering*, 53(4):1879–1888.

Zhang, F., Xie, S., Hu, D., Shao, J.-F., and Gatmiri, B. (2012). Effect of water content and structural anisotropy on mechanical property of claystone. *Applied Clay Science*, 69:79–86.

Zhao, X., Briffaut, M., Gay, N., Shao, J., and Talandier, J. (2026). Experimental study of swelling-induced crack self-sealing process in claystone samples with indirect water injection process. *International Journal of Rock Mechanics and Mining Sciences*, 203:106544.

Zheng, L., Rutqvist, J., Liu, H.-H., Birkholzer, J. T., and Sonnenthal, E. (2014). Model evaluation of geochemically induced swelling/shrinkage in argillaceous formations for nuclear waste disposal. *Applied clay science*, 97:24–32.